PL-TR-95-2126

DTIC
SELECTED
NOV 2 8 1995
F

ARC RATE SIMULATION AND FLIGHT DATA ANALYSIS FOR THE PASP PLUS EXPERIMENT

James D. Soldi, Jr.
Daniel E. Hastings

Massachusetts Institute of Technology
Space Power and Propulsion Laboratory
77 Massachusetts Avenue
Cambridge, MA 02139

1 September 1995

19951124 012

Final Report
6 April 1992–1 September 1995
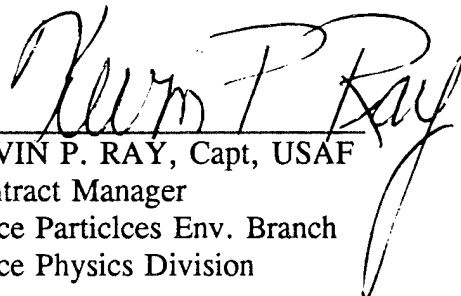
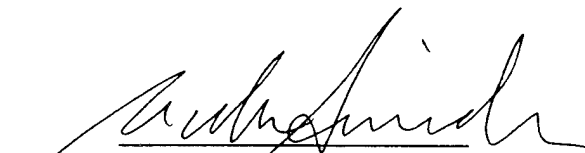Approved For Public Release; Distribution Unlimited

PHILLIPS LABORATORY
Directorate of Geophysics
AIR FORCE MATERIEL COMMAND
HANSCOM AIR FORCE BASE, MA 01731-3010

DTIC QUALITY INSPECTED

"This technical report has been reviewed and is approved for publication"

KEVIN P. RAY, Capt, USAF
Contract Manager
Space Particlces Env. Branch
Space Physics Division

EDWARD G. MULLEN, Chief
Space Particles Env. Branch
Space Physics Division

WILLIAM SWIDER
Deputy Director
Space Physics Division

REPORT DOCUMENTATION PAGE

Public reporting burden for this collection of information is estimated to average 1 hour per response, including the time for reviewing instructions, searching existing data sources, gathering and maintaining the data needed, and completing and reviewing the collection of information. Send comments regarding this burden estimate or any other aspect of this collection of information, including suggestions for reducing this burden, to Washington Headquarters Services, Directorate for Information Operations and Reports, 1215 Jefferson Davis Highway, Suite 1204, Arlington, VA 22202-4302, and to the Office of Management and Budget, Paperwork Reduction Project (0704-0188), Washington, DC 20503.

1. AGENCY USE ONLY (Leave blank)	2. REPORT DATE 1 September 1995	3. REPORT TYPE AND DATES COVERED Final (6 April 1992–1 September 1995)

4. TITLE AND SUBTITLE
Arc Rate Simulation and Flight Data Analysis for the PASP Plus Experiment

6. AUTHOR(S)
James D. Soldi, Jr
Daniel E. Hastings

5. FUNDING NUMBERS
PE 63410F
PR 2822
TA 01
WU PP
Contract F19628–92–K–0016

7. PERFORMING ORGANIZATION NAME(S) AND ADDRESS(ES)
Massachusetts Institute of Technology
Space Power and Propulsion Laboratory
77 Massachusetts Avenue
Cambridge, MA 02139

8. PERFORMING ORGANIZATION REPORT NUMBER

9. SPONSORING/MONITORING AGENCY NAME(S) AND ADDRESS(ES)
Phillips Laboratory
29 Randolph Road
Hanscom AFB, MA 01731–3010

Contract Manager: Kevin Ray, Capt, USAF/GPSP

10. SPONSORING/MONITORING AGENCY REPORT NUMBER
PL–TR–95–2126

11. SUPPLEMENTARY NOTES

12a. DISTRIBUTION/AVAILABILITY STATEMENT

Approved for public release; distribution unlimited

12b. DISTRIBUTION CODE

13. ABSTRACT (Maximum 200 words)

As power demands continue to increase, spacecraft power systems are being designed to operate at higher voltages. When operating at high negative voltages, however, arcing may occur on the solar cells. In this work, a model of the arcing process developed by Cho and Hastings was refined to be more physically accurate and to better simulate experiment operations. The modified computer simulation was then used to predict the arcing rates on the PASP Plus solar cells. Both the pre-flight and post-flight simulations showed good agreement with the flight data. The flight data was then analyzed to examine corrleations between arc rates and the various material, environmental, and operational parameters. Arcing levels were found to depend strongly on the bias voltages, with the scalings suggested by the model proving to accurately relate the arcing rates on the different modules. Cell temperature and ion flux were also found to be important parameters. As expected, a critical tremperature above which no arcing occurs was found to exist.

14. SUBJECT TERMS
Solar array arcing
High voltage solar arrays
Wrap–through–contact solar cells
Space environmental interactions
PASP Plus

15. NUMBER OF PAGES
284

16. PRICE CODE

17. SECURITY CLASSIFICATION OF REPORT	18. SECURITY CLASSIFICATION OF THIS PAGE	19. SECURITY CLASSIFICATION OF ABSTRACT	20. LIMITATION OF ABSTRACT
Unclassified	Unclassified	Unclassified	SAR

Contents

List of Figures

List of Tables

List of Symbols

A	Fowler-Nordheim coefficient $(1.54 \times 10^{-6} \times 10^{4.52\phi_W^{-1/2}}/\phi_W \ \mathrm{A/V^2})$
A'	$A\frac{S_{FN}}{S_{real}}\ (\mathrm{A/V^2})$
A_{array}	solar array area (m^2)
A_{cell}	solar cell area (m^2)
A_{wave}	discharge wave area (m^2)
a_n	coefficients in polynomial fit to η
B	Fowler-Nordheim coefficient $(6.53 \times 10^9 \phi_W^{1.5} \ \mathrm{V/m})$
b_n	coefficients in polynomial fit to d_i/d
C_1, C_2	coefficients to arc rate fits
C_{diele}	capacitance of dielectric $(\mathrm{F/m^2})$
C_{front}	capacitance of coverglass front surface (F)
d	thickness of dielectric (m)
c_n	coefficients in polynomial fit to capacitance matrix diagonal elements
C_s	ion acoustic velocity (m/s)
d_1	thickness of coverglass (m)
d_2	thickness of adhesive (m)
d_{gap}	interconnector length (m)
d_i	distance of electron first impact point from triple junction (m)
e	electron charge
E_e	electric field at emission site (V/m)
E_{e_0}	initial electric field at emission site (V/m)
E_d	neutral adsorbate binding energy (eV)
E_i	electron incident energy on dielectric plate (eV)
E_{max}	electron incident energy for maximum secondary electron yield (eV)
E_{TJ}	electric field at triple junction (V/m)
E_1	electric field of coverglass (V/m)
E_2	electric field of adhesive (V/m)

E_{se} secondary electron energy (eV)

E_{se1} electron incident energy for a secondary electron yield of unity (eV)

ESA electrostatic analyzer

j_{ec} electron current density from conductor (A/m^2)

j_{ee} secondary electron current density from dielectric (A/m^2)

j_{FN} Fowler-Nordheim current density from the conductor (A/m^2)

j_{id} ion ram current density to the dielectric (A/m^2)

j_{m-d} Fowler-Nordheim emission current at metal dielectric interface (A/m^2)

j_{sp} Child-Langmuir space charge limited current density (A/m^2)

n_e plasma number density (m^{-3})

n_{es} emission site number density (m^{-2})

m_e electron mass (kg)

m_i ion mass (kg)

N_{cell} number of solar cells in array

n_n desorbed neutral density (m^{-3})

n_{n_a} ambient neutral density (m^{-3})

n_{n_c} critical desorbed neutral density for breakdown (m^{-3})

N_n number density of neutral particles adsorbed on dielectric side surface (m^{-2})

N_n^* steady state surface neutral density (m^{-2})

N_{n_0} surface neutral density for monolayer coverage (m^{-2})

p neutral pressure (torr)

Q_{ESD} effective electron stimulated desorption cross section (m^2)

QCM quartz crystal microbalance

R arc rate (sec^{-1})

r_{dis} discharge wave radius (m)

r_s sheath radius (m)

S_{FN} emission site area determined from F-N plot (m^2)

S_{real} emission site area determined by accounting for electron space charge effects (m^2)

T_e electron temperature (eV)

T_i ion temperature (eV)

TPM	transient pulse monitor
T_s	cell surface temperature (K)
V_a	voltage at which last arc occurred (V)
V_{bias}	bias voltage of interconnector/conductor (V)
v_d	discharge wavefront velocity (m/s)
V_e	voltage which minimizes arcing time (V)
V_i	initial voltage before solar cell charging (V)
v_{ion}	mean speed of ions entering sheath (m/sec)
v_{orbit}	spacecraft orbital velocity (m/sec)
v_x	electron velocity in the x direction (m/sec)
v_y	electron velocity in the y direction (m/sec)
y	distance of emission site from the triple junction (m)
α	angle of attack - angle between velocity vector and vector normal to array front surface
α_w	wake angle
β	field enhancement factor
ΔQ	charge lost from coverglass by one discharge (C)
ΔV	potential drop across dielectric due to arc discharge (V)
ϵ_{d_1}	dielectric constant of coverglass
ϵ_{d_2}	dielectric constant of adhesive
$\mathcal{E}_1$	energy at $\gamma_{ee} = 1$ (eV)
λ_D	plasma debye length (m)
λ_{mfp}	mean free path (m)
ϕ_c	potential of conductor (V)
ϕ_d	potential of first impact point (V)
ϕ_i	potential of coverglass-adhesive interface (V)
ϕ_w	work function (eV)
γ_{ee}	secondary electron yield
γ_{max}	maximum secondary electron yield at normal incidence
Γ_{ESD}	electron stimulated desorption flux $(/m^2 s)$
Γ_i	ion flux onto array front surface $(/m^2 s)$
$\Gamma_{i_{crit}}$	critical ion flux onto array front surface for arcing $(/m^2 s)$

Γ_n neutral flux onto dielectric side surface ($/m^2s$)

Γ_{TSD} thermally stimulated desorption flux ($/m^2s$)

η factor accounting for difference in electric field at emission site and triple junction

κ Boltzmann constant

σ surface charge density (C/m^2)

τ_{arc} time between arcs (sec)

τ_{chrg} total charging time$=\tau_{ion} + \tau_{efee}$ (sec)

τ_{efee} EFEE charging time (sec)

τ_{ion} ion charging time (sec)

τ_{exp} experiment time (sec)

θ_0 Mach angle

θ_i incident impact angle of electron onto the dielectric surface

ξ factor accounting for difference of dielectric constants between coverglass and adhesive

ξ_0 ξ at the coverglass front surface

Chapter 1

Introduction

Photovoltaic power systems continue to be the most commonly used means of meeting power needs for both DoD and commercial satellites. In the past, most systems operated at low voltage levels, typically -28 volts. Driven by higher power requirements, several current spacecraft designs now utilize a somewhat higher bus voltage, with the Lockheed-Martin A2100 and Hughes HS601 satellites using -33V and -51V bus voltages, respectively[95, 6]. Future space missions, however, will have higher power requirements than current systems, with power levels of 10kW to 1MW needed. To meet these requirements, either high current or high voltage systems can be used. The use of high current is undesirable for two reasons. First, high current systems require more massive power distribution cables, increasing the mass of the spacecraft. And second, high current results in higher resistive losses during the power transmission. Thus, high voltage power generation and transmission at low currents is desirable. For example, the Space Station design calls for power to be provided by high voltage solar cells operating at -160V. Here, the term high voltage means that the absolute value of the bias voltage is on the order of 100V to 1000V. In this work, when discussing negative bias voltages, "low" and "high" voltage refers to the magnitude of the voltage.

A schematic of a conventional geometry solar cell is shown in Figure 1. The solar cell semi-conductor is protected by a coverglass glued to the top surface. This coverglass is used primarily to protect the cell from the radiation environment. The semiconductor itself is composed of two parts: an n-type semiconductor and a p-type semiconductor. A current path is set up between the cells by the use of metal interconnectors from the n-type semiconductor on one cell to the p-type semiconductors of the neighboring cells. Series of solar cells are used to achieve the desired voltage levels and cells connected in parallel give the desired current levels. The conductive interconnects between the cells are exposed

1

to the ambient environment. When the array is generating power, a sheath forms on the interconnects, which expands into space and interacts with the ambient plasma.
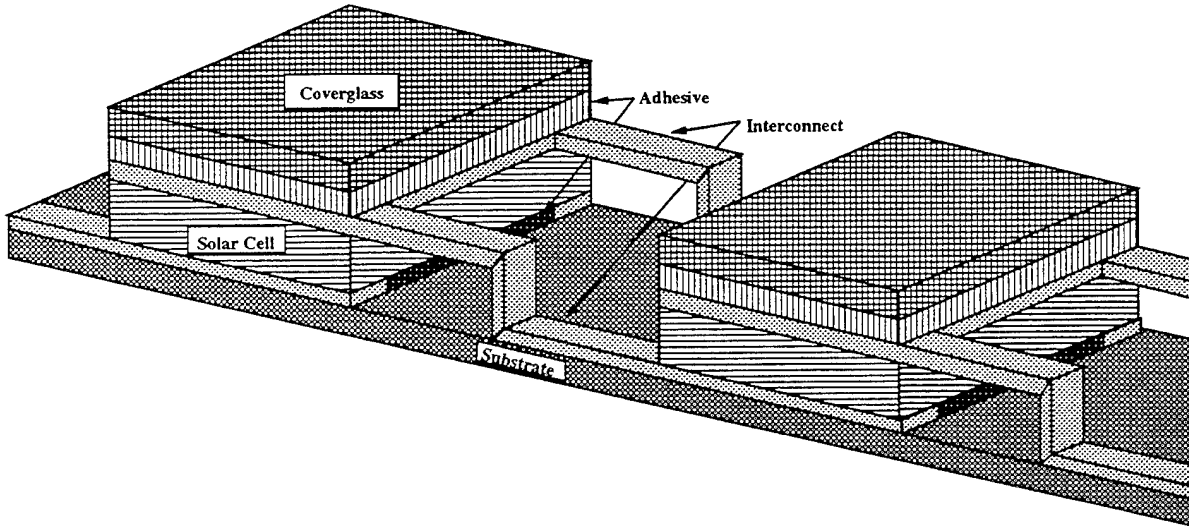
Figure 1: Schematic of a Conventional Solar Cell

The interactions between the high voltage solar arrays and the ambient plasma environment can be strong and could greatly affect the operation of the spacecraft. The steady state current collected by the solar arrays from the plasma must obey the zero net current condition, given by the steady state solution of

$$\frac{\partial \rho}{\partial t} + \nabla \cdot \vec{j} = 0, \tag{1}$$

which is derived from Gauss' and Ampere's Law. This causes part of the array to float positive with respect to the plasma, and thus collect electrons, and the rest to float negative and collect ions. Because electrons have a much higher mobility than the ions, the electron flux is higher than the ion flux. This causes most of the array to float negative with respect to the plasma in order to satisfy the zero net current condition.

High voltage solar arrays have been found to interact with the ambient space plasma environment in several manners, including current leakage[98], arc discharges[40, 93], and enhanced drag due to Coulomb collisions[36]. For positively biased arrays, the current collection

2

can become anomalously large, known as "snap-over". This can result in a significant leakage power loss. For large negative voltages, arc discharges have been found to occur. An arc is typically defined as a sudden current pulse up to the order of an ampere on a timescale of a microsecond or less. The current pulse is often accompanied by a spot of light at the edge of the coverglass, which may interfere with optical systems[24]. Arcing can also result in electromagnetic interference and solar cell damage, thus degrading the operation of both the power subsystem and the spacecraft as a whole. If the EMI generated by the arc couples to the spacecraft power system, it could become significant enough to disrupt communications between spacecraft, or between spacecraft and telerobotic systems[24].

1.1 Background

1.1.1 Ground-Based Experiments

Arcing on high voltage solar arrays has been observed in both ground and space experiments. It was first observed in 1971 by Herron et al.[40] during plasma chamber tests of solar arrays biased between ±16kV. During the tests, arcing was found to occur at bias voltages as low as -6kV with a plasma density of 10^8m^{-3}. Several ground tests examined the role of a dielectric on a conductor in arcing. Miller[61] confirmed arcing on dielectric-conductor systems. Kuninaka[50] tested two tungsten samples. One sample was bare and did not arc down to -3kV. The second plate was partially covered by 1mm thick boron-nitride. This sample arced at -1kV. Another set of tests was conducted by Fujii et al.[28]. These tests consisted of biasing three metal samples to high voltages. One of the metal samples was bare and only showed arcing at -1kV, with arcs occurring to the substrate. The two other samples were partially covered with 200μm thick fused silica, representative of solar array coverglass. These samples showed arcing at the metal/coverglass interface at -450V.

The effect of an arc on the coverglass surface potential was examined by Snyder[88], who found that the potential dropped from near the plasma potential before the arc to on the order of a hundred volts after the arc. This implies that a negative discharge wave is created

by the arc which removes the positive charge accumulated on the surface.

Two separate experiments observed electron emission from solar arrays that could not be accounted for by the ambient plasma. In an experiment by Snyder et al.[90], a grounded probe measured a flowing current well after the plasma source was turned off, indicating electron flow from the array. Inouye and Chaky[47] found that the current from the solar array was greater than that which could be due to photoemission.

In an experiment by Kuninaka[51], luminosity was observed during arc discharges. This luminosity is believed to be due to collisions between electrons emitted from the conductor and neutral gas desorbed from the dielectric. The UV spectrum emitted during arcing was measured by Upschulte et al.[99] and was found to show a strong OH spectrum, indicating that water molecules are among those desorbed from the dielectric and ionized by the electron current.

The electromagnetic waves generated by arc currents were examined by Leung[56], who found that the radiation pattern follows that of a dipole emission, so that the electric field, E, varies with distance as

$$E \alpha \frac{1}{r^n} \tag{2}$$

with n$\approx 2 \sim 3$. The amplitude of the electric field from an arc on a 20 pF solar array, at a distance of one meter, was five orders of magnitude above the allowable level for the space shuttle. Using Eq. (2), this gives a safe distance of on the order of 100 m between the arc site and sensitive electronics. Thus, for nearly all spacecraft, an arc anywhere on the solar arrays could affect electronic equipment operation.

The duration of an arc is typically assumed to be on the order of a microsecond, based on an experiment by Upschulte et al.[99]. This experiment showed a correlation between the UV emission from the arc and the current measured in the circuit, which had a duration on the order of microseconds. This is in opposition to the theory by Stevens et al.[94], who proposed a nanosecond duration for the arc, based on high frequency EM spectra measured by Leung[56]. Experiments by Snyder[89] and Leung[56] measured microsecond long arc currents, supporting the results of Upschulte et al.[99].

4

Several ground experiments measured the effect of operational, environmental, and geometric parameters on the arc rate. Experiments by Kuninaka[37, 50] found that the arc rate increases with voltage and plasma density, and decreases with temperature. Experiments by Grier[30] and Miller[61] also found an increase in arc rates with increasing voltage, and Miller's tests also found an increasing arc rate with plasma density. Upschulte et al. [99] observed that overhanging the coverglass 10-20μm over the adhesive substantially lowers the arc rate. In order to reduce arcing on solar arrays, a new cell design was created, known as the wrap-through-contact cell (see Figure 2). In this design, the metal interconnects are not exposed to the ambient plasma. Instead, the interconnects run underneath the coverglass, down through a hole in the center of the cell, and then under a kapton substrate to the adjacent cell. However, the semiconductor is still exposed to the plasma, leading to a possible arcing site[26]. Leung[56] found that wrap-through-contact cells did arc, although less frequently than conventional geometry cells.
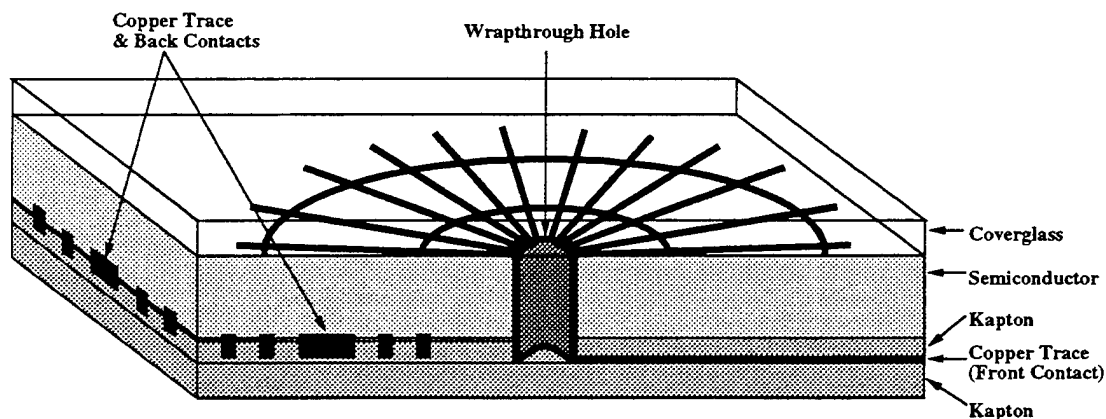
Figure 2: Schematic of a Wrap-Through-Contact Solar Cell

1.1.2 Flight Experiments

The first Plasma Interactions Experiment (PIX)[29], launched in 1978 as an auxiliary payload on Landsat 3's Delta rocket, verified the occurrence of arc discharges in the space environment. The experiment resulted in four hours of data taken in a polar orbit at 920km, during which time a solar array consisting of twenty-four conventional 2cm×2cm silicon solar cells were biased between ±1000 volts. The cells were found to arc at voltages greater than -750

volts.

A more extensive space experiment was conducted in 1983 aboard PIX II[30], which was again launched as an auxiliary payload aboard a Delta launch vehicle into a 900km polar orbit. Approximately 18 hours of data were taken for an array consisting of 500 cells similar to those used in PIX I. During this experiment, arcing was found to occur for voltages as low as -255 volts.

Interpretation of the PIX II data was hampered by unexpected tumbling of the space-craft, resulting in the Langmuir probe being placed in the wake during portions of the experiment, as well as by power supply shutdowns following arcs. The data from the PIX II flight and ground tests were studied by Ferguson[25], who assumed that the arc rate was linearly proportional to the plasma density and found that the arc rate then followed a power law dependence on the bias voltage, given by

$$R = 1.4 \times 10^{-10} \left(-V_{bias}\right)^{3.093} \left(\frac{n_e}{6.3 \times 10^3}\right) \tag{3}$$

for the flight data, and

$$R = 1.82 \times 10^{-18} \left(-V_{bias}\right)^{5.51} \tag{4}$$

for the ground tests at high density, where V_{bias} is the bias voltage and n_e is the plasma density in cubic centimeters.

A more recent space experiment involving high voltage solar array interactions with the space plasma environment was conducted on the NASA Solar Array Module Plasma Interactions Experiment (SAMPIE), conducted aboard the Space Shuttle in March 1994. This experiment tested current collection and arcing characteristics of conventional and wrap-through-contact cells, as well as coupons which were geometrically identical to Cho's model system described in the next section, at bias voltages up to $\pm 600V$. This experiment found that the conventional geometry cells arced in the range of -400V, and that the wrap-through-contact cells exhibited a much lower arcing rate than the conventional cells. A detailed analysis of the SAMPIE flight data was conducted by Perez de la Cruz[79, 80].

6

1.1.3 Arcing Onset Models

There have been three types of theoretical models proposed for the arcing onset mechanism. The first, proposed by Parks et al.[78], based on previous work by Jongeward et al.[48] attributes the arcing onset to the Malter effect[57] at a thin dielectric layer on the conductor surface. The second model, by Thiemann and Schunk, proposes that arcing occurs at the cell side surface, due to secondary electron emission runaway on the Kapton substrate[97]. The third model, by Cho and Hastings[13] based on previous work by Hastings et al.[38], attributes the arc to a gas discharge in neutral gases desorbed from the dielectric surface.

The model by Parks et al.[78] consists of the following scenario:

(1) A dielectric impurity layer is formed on the conductor surface.

(2) Ions attracted to the negative bias of the conductor are accumulated on the dielectric layer and enhance the electric field in the layer.

(3) Fowler-Nordheim field emission causes electrons to be emitted from the conductor into the dielectric.

(4) The electrons emitted from the metal surface have ionization collisions while being accelerated within the dielectric, leaving positive charges behind as they are emitted from the dielectric-vacuum interface.

(5) This remaining positive charge further enhances the electric field within the dielectric layer.

(6) The resulting rate of change of the electric field in the insulating layer is given by

$$\epsilon \frac{d}{dt}(\epsilon_r E_{m-d} - E_{d-v}) = j_i + j_{m-d}e^{\alpha_d d_d}P_{d-v} - j_{m-d}, \tag{5}$$

where ϵ_r is the dielectric constant of the insulating layer, E_{m-d} is the electric field in the dielectric layer, E_{d-v} is the ambient electric field at the dielectric-vacuum interface, j_i is the ion current density, α_d is the ionization rate per unit distance inside the layer, d_d is the dielectric layer thickness, P_{d-v} is the probability that the electrons are emitted from the dielectric-vacuum interface, and j_{m-d} is the Fowler-Nordheim emission current at the

metal-dielectric interface given by

$$j_{m-d} = AE_{ins}^2 e^{-\frac{B}{E_{m-d}}}, \tag{6}$$

where A and B are the Fowler-Nordheim emission coefficients given by

$$A = \frac{1.54 \times 10^{-6} 10^{4.52/\sqrt{\phi_w}}}{\phi_w}, \tag{7}$$

$$B = 6.53 \times 10^9 \phi_w^{1.5}, \tag{8}$$

where ϕ_w is the work function of the metal in eV.

If the factor $e^{\alpha_d d_d} P_{d-v}$ is greater than unity, a positive feedback mechanism is created at the metal-dielectric interface, leading to a runaway of the field and the emission current by increasing E_{m-d} monotonically in time.

The model by Thiemann and Schunk[97] is based on computer simulations and ground experiments. In this model, the arc does not occur at the interconnector. Instead, the arc site is at the edge of the cell at the junction of the cell and Kapton substrate. In this model, ambient ions initially flow to the coverglass surface, producing secondary electron emission and further charging the coverglass, which changes the potential structure on the cell and thus alters the electric field structure in the vicinity. Ions also strike the Kapton and cell, producing secondary electrons. As the charging continues, ions are no longer able to reach the Kapton and are instead drawn to the cell. Secondary electrons released from the cell strike the Kapton and release secondary electrons, further charging the surface. Eventually, the secondary electron emission avalanches, which is believed to be the arc. It should be noted that in neither of these two models should the cell temperature greatly affect the arcing process, which was seen in the ground experiments by Kuninaka[50].

A third arcing onset mechanism was proposed by Cho and Hastings[13], who studied the model system shown in Figure 3. This system was used to study the arc initiation process at the triple junction of the plasma, dielectric, and conductor.

The resulting arcing onset mechanism, used in this research, can be summarized by the
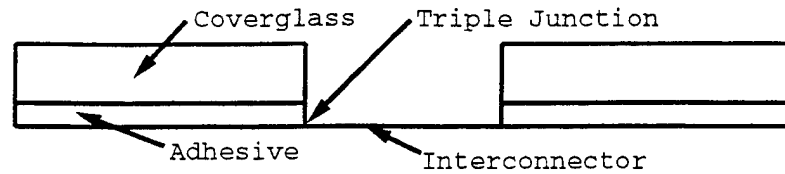
Figure 3: Model of the Conventional Solar Array Used for Numerical Simulations

following sequence, illustrated in Figure 4:

(1) Ambient ions charge the dielectric (i.e. coverglass and adhesive) front surface, but leave the dielectric side surface uncharged.

(2) As the front surface potential approaches zero relative to the plasma, a strong electric field of E=V/d (where V is the bias voltage and d is the dielectric thickness) is formed at the conductor surface, inducing pre-breakdown electron emission due to enhanced field electron emission (EFEE). Electrons are also released due to ion induced emission from ion bombardment of the conductor surface.

(3) Some of the emitted electrons strike the dielectric side surface, inducing the release of secondary electrons and causing electron stimulated desorption of neutrals adsorbed on the dielectric surface. If the secondary electron yield is greater than unity, the side surface charges up positively, providing a positive feedback mechanism to further enhance the electric field at the conductor surface.

(4) As the electric field increases, the electron emission current increases until it is limited by the negative space charge of the emitted electrons.

(5) Once the neutral density becomes high enough, ionization begins due to collisions between electrons and neutrals.

(6) If the neutral density is very high, Townsend breakdown occurs. Even if the density is not high enough for Townsend breakdown to occur, breakdown is still possible if the positive ion space charge can cancel the negative electron space charge and enhance the field at the conductor.

(7) The arcing time is the minimum of the sum of the ion and EFEE charging times for all the emission sites on the conductor.

(8) A discharge wave created by the arc resets the charging process at all of the emission

sites within the area covered by the wave.
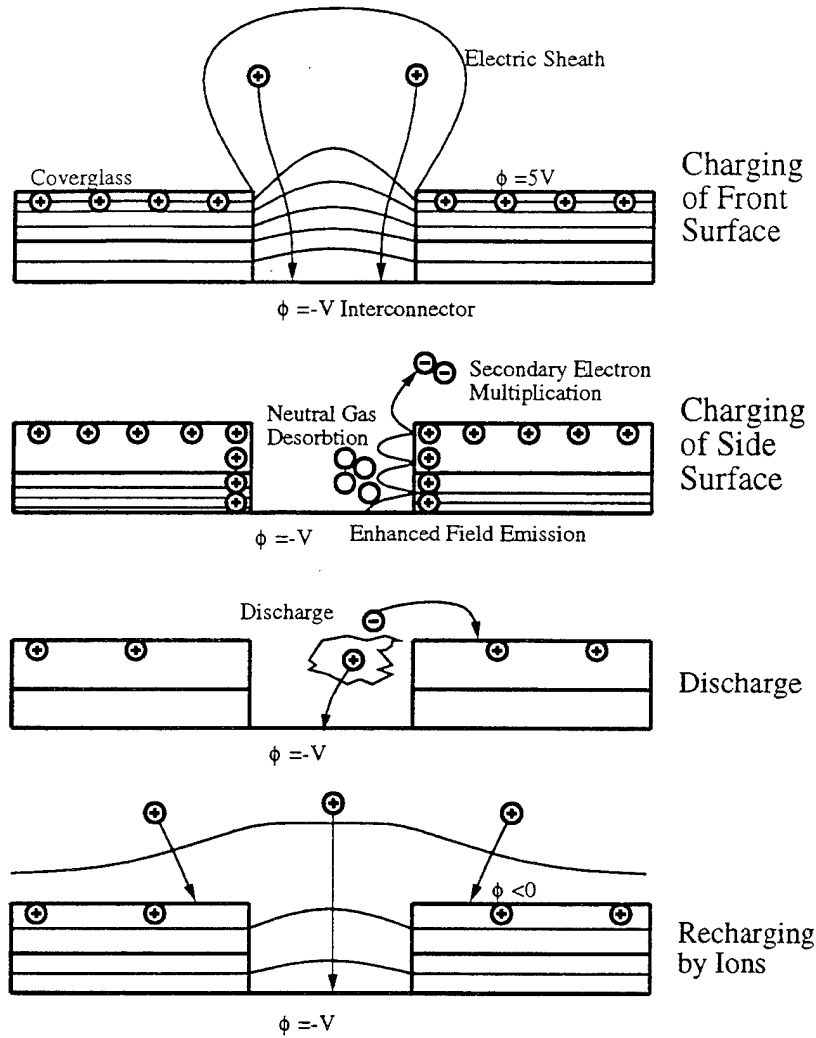
Figure 4: Arcing Sequence of a High Voltage Solar Array

This model was produced through the use of computer particle-in-cell (PIC) and Monte Carlo (MC) simulations of the arc initiation process. These results were then used to develop analytical formulas for the ion charging time τ_{ion} and the enhanced field electron emission charging time τ_{efee}. From this, a semi-analytic computer code was developed to predict the arc rates for high voltage solar arrays placed in a plasma environment. Subsequent work by Mong and Hastings[62] used variations of the particle simulation and semi-analytic codes to explore the arcing characteristics of wrap-through-contact cells and to examine various arc mitigation techniques. In the model developed by Cho, the cell temperature is a critical factor in the arcing process, since the density of neutrals adsorbed on the dielectric side

surface is a strong function of the cell temperature.

1.2 Overview of This Research

As future spacecraft power demands increase, power system designers will need to consider the effect of arcing on the system. To do this, an understanding of the relationship between arcing and cell design, operational parameters and environmental variables needs to be understood. To help gather data for this, the Air Force launched the Advanced Photovoltaic and Electronics Experiment (APEX) satellite, containing the Photovoltaic Array Space Power Plus Diagnostics (PASP Plus) experiment. This experiment is gathering arcing data for various cell materials and geometries in the space environment.

The focus of this research was threefold. First, to modify the semi-analytic simulation to be more physically accurate and create a tool that could be used to predict arcing for any conventional geometry cell under any operating conditions. Next, to use this tool to predict the arc rates for the PASP Plus experiment, and then to analyze the simulated and flight data. The simulation was run before the spacecraft launch using expected environmental and operational parameters for the experiment. Then, the simulation was re-run using actual environmental and operational conditions from the experiment. The data from the experiment was then used, along with the simulations, to determine correlations between arc rate and the various material properties, environmental variables, and experimental parameters.

In Chapter 2 the semi-analytic simulation developed by Cho and Hastings will be outlined, while Chapter 3 will discuss the modifications made to the code to make it more physically and experimentally accurate. A description of the PASP Plus hardware and experiment will be given in Chapter 4. The arc rate simulations for PASP Plus made using the code, and the analysis of the flight and simulated data, will then be discussed in Chapters 5 and 6. Finally, conclusions will be summarized in Chapter 7.

Chapter 2

Semi-Analytic Model

Figure 4 schematically shows the arcing sequence assumed in this research. This chapter will review the semi-analytic model of this sequence developed by Cho and Hastings, and the next chapter will discuss the modifications made to the model.

When an arc discharge occurs, some of the charge stored by the coverglass is lost. Experimentally, coverglass potential drops during discharges of up to several hundred volts from the steady state value have been observed[88]. Before the next arc can occur at the same location, the dielectric must restore some, or all, of the lost charge. It is assumed that the dielectric restores its lost charge through bombardment by the ambient ions since the electric field at the triple junction drops after the discharge and the field emission ceases to charge the dielectric. Once the dielectric charge is recovered so that the electric field induces a significant amount of field emission current, the EFEE charging resumes and leads to the next possible discharge.

For large solar arrays, it can be assumed that arcing can happen independently at separate locations on the array. That is, arcs at one location do not affect the charging processes at sites distant from the arc site. Sites widely separated are thus said to be uncorrelated. The area of correlation is taken to be the area of the discharge wave created by an arc. This area is taken to be $0.012m^2$ based on experimental measurements in Reference 37. When an arc occurs, the resulting plasma cloud discharges an area around the location of the arc, resetting the charging process of all the emission sites within the area. Emission sites outside of this area are unaffected and continue charging. For the simulations, the array area is divided into correlated areas and the arc rates are determined independently for each area. The total arc rate for the array is then taken to be the sum

of the rates for the correlated areas. A more detailed discussion of the discharge wave area is given in Section 2.5.

The time between arcs, τ_{arc}, is the minimum charging time of all the sites on the interconnector within the correlated area, given by

$$\tau_{arc} = min(\tau_{ion} + \tau_{efee}), \qquad (9)$$

where τ_{ion} is the ambient ion charging time and τ_{efee} is the enhanced field electron emission charging time. Numerical results showed that the critical condition for arcing onset after EFEE charging has been initiated is whether the desorbed neutral density is larger than the critical value of approximately 6×10^{21} m^{-3}[13]. If the neutral density is above this value, breakdown occurs. If the density is below this value, the electron current just becomes space charge limited and eventually relaxes without leading to breakdown. In this case, a very short current pulse would be seen, without an arc flash or arc damage. Current pulses such as these, with timescales on the order of a nanosecond, have been detected in many experiments. In previous work by Mong and Hastings[62], it was assumed that the neutral density was always above the critical value, resulting in an upper bound for the breakdown discharges. The next chapter will discuss how the neutral density criterion was incorporated into the simulations.

2.1 EFEE Charging Time

2.1.1 Enhanced Field Electron Emission

The geometry considered for EFEE charging is shown in Figure 5.

As the electric field near the triple junction increases due to the ion charging of the dielectric front surface, electrons are emitted from sites on the interconnect where the electric field has been enhanced due to either dielectric inclusions or microprotrusions on the metal. Some of these electrons escape, while others strike the dielectric side surface
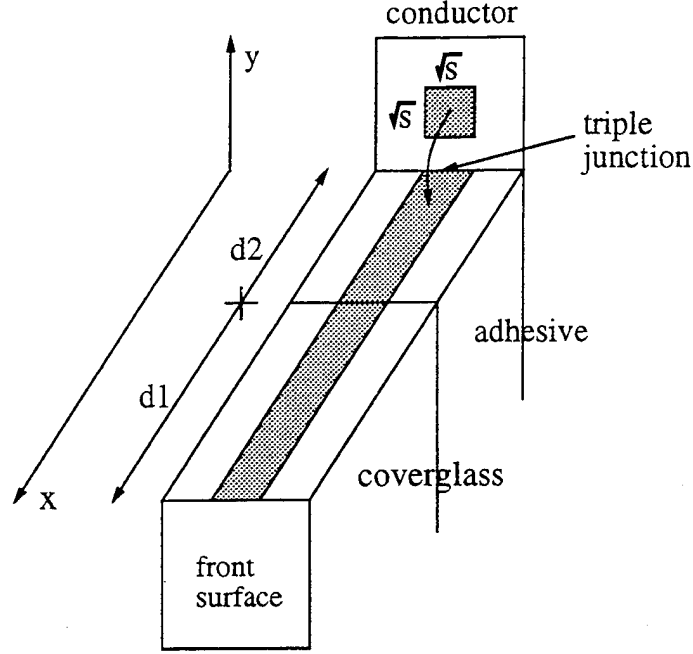
Figure 5: Geometry for EFEE Charging

and induce secondary electrons, charging the surface. The enhanced field electron emission current density from an emission site caused by a dielectric inclusion at location y on the conductor is given by[52]

$$j_{ec}(y) = A \frac{S_{FN}}{S_{real}} \beta^2 E_e^2 \exp\left(-\frac{B}{\beta E_e}\right) = A' \beta^2 E_e^2 \exp\left(-\frac{B}{\beta E_e}\right) \qquad (10)$$

where A and B are the Fowler-Nordheim coefficients given by Eqs. (7) and (8) and E_e is the electric field at the emission site. The factor S_{FN}/S_{real} accounts for the negative space charge effect near the emission site. S_{real} is the area of the dielectric impurity, whereas S_{FN} is the effective emission site area accounting for electron diffusion within the dielectric layer[65]. The factor β is the electric field enhancement factor at the metal-dielectric interface, which can be on the order of 100-1000. A more detailed description of enhanced field electron emission is given in Appendix A.

The secondary electron current density at a point x on the side surface is then given by

$$j_{ee}(x, t) = \int \gamma_{ee}(x, y) P(x, y, t) j_{ec}(y, t) dy + \int \gamma_{ee}(x, x') P(x, x', t) j_{ee}(x', t) dx' \qquad (11)$$

15

where $\gamma_{ee}(x,y)$ is the secondary electron emission at point x due to electrons emitted from point y, and $P(x,y,t)dy$ gives the probability that the electron emitted from y to $y + dy$ on the conductor surface hits the dielectric surface between x and $x + dx$.

The rate of change of the surface charge density σ at position x on the side surface is then given by

$$
\begin{aligned}
\frac{d\sigma(x,t)}{dt} &= -\int P(x,y,t)j_{ec}(y,t)dy - \int P(x,x',t)j_{ee}(x',t)dx' \\
&\quad + j_{ee}(x,t) - j_{en}(x,t) + j_{in}(x,t) + j_{id}(x,t)
\end{aligned}
\tag{12}
$$

The term $j_{id}(x,t)$ gives the ion current density to the side surface due to the ambient plasma. Numerical work by Cho[13] found that this term is much smaller than j_{ec} and j_{ee} and is therefore neglected. The current densities j_{en} and j_{in} are the electron and ion current densities, respectively, due to ionization of neutral gases, which are also neglected. Thus, using Eq. (11), Eq. (12) can be rewritten as

$$
\frac{d\sigma(x,t)}{dt} = \int (\gamma_{ee}(x,y)-1)P(x,y,t)j_{ec}(y,t)dy + \int (\gamma_{ee}(x,x')-1)P(x,x',t)j_{ee}(x',t)dx' \tag{13}
$$

To find the rate of change of the surface charge density at the first impact point, $x = d_i$, on the dielectric side surface, the second term of Eq. (13) is neglected since the contribution due to secondary electrons from the rest of the side surface is negligible at the first impact point. This gives

$$
\int_0^{d_i} \frac{d\sigma(x,t)}{dt}dx = \int [\int_0^{d_i} P(x,y,t)dx](\gamma_{ee} - 1)j_{ec}(y,t)dy \tag{14}
$$

The integral $\int_0^{d_i} P(x,y,t)dx$ is approximately equal to unity since $x = d_i$ is the first impact point of electrons emitted from the conductor. Thus, Eq. (14) reduces to

$$
\frac{d\sigma(x,t)}{dt}dx = (\gamma_{ee} - 1)j_{ec}\frac{\sqrt{S_{real}}}{d_i} \tag{15}
$$

The potential difference between the first impact point, $x = d_i$, and the triple junction, $x = 0$, is related to the surface capacitance, C_{diele}, by $\phi_d = \sigma/C_{diele}$. The electric field at

the triple junction can then be given by

$$E_{T.J.} = \xi \frac{\phi_d}{d_i} = \xi \frac{\sigma}{C_{diele} d_i} \qquad (16)$$

where the factor ξ has been introduced to account for the discontinuity in the electric field due to the difference in the dielectric constants of the adhesive and coverglass in the system shown in Figure 5. In this system, the coverglass thickness is given by d_1 and the adhesive thickness is d_2. If the first impact point is within the adhesive, i.e. $d_i < d_2$, the factor ξ is unity. However, if the impact point is on the coverglass side surface, there is a discontinuity at the dielectric interface, $x = d_2$, and the electric field just within the adhesive is $E_2 = E_1 \epsilon_{d_1} / \epsilon_{d_2}$, where ϵ_{d_1} and ϵ_{d_2} are the dielectric constants of the coverglass and adhesive, respectively. Since $\phi_d = E_2 d_2 + E_1 (d_i - d_2)$, the factor ξ can be written as

$$
\begin{aligned}
\xi &= 1 & (d_i \leq d_2) \\
\xi &= [\frac{d_2}{d_i} + \frac{\epsilon_{d2}}{\epsilon_{d1}} \frac{(d_i - d_2)}{d_i}]^{-1} & (d_i > d_2)
\end{aligned}
\qquad (17)
$$

Because the electric field at the emission site, E_e, can differ from that at the triple junction, a function $\eta(y) = E_e / E_{T.J.}$ must be introduced. Numerical work by Cho found that this factor is only a function of the distance of the emission site from the triple junction[13]. Thus, the electric field at the emission site can be written as

$$E_e = \eta E_{TJ} = \eta \xi \frac{\sigma}{C_{diele} d_i} \qquad (18)$$

Substituting Eq. (18) into Eq. (15) gives a relation for the rate of change of the electric field at the emission site

$$\frac{dE_e}{dt} = \eta \xi \frac{(\gamma_{ee} - 1)\sqrt{S_{real}}}{C_{diele} d_i^2} j_{ec} \qquad (19)$$

where j_{ec} is given by Eq. (10).

2.1.2 Analytic Solution to EFEE Charging Time

The rate of change of the electric field at the emission site on the conductor is given by substituting Eq. (10) into Eq. (19)

$$\frac{dE_e}{dt} = \eta\xi\frac{(\gamma_{ee}-1)\sqrt{S_{real}}}{C_{diele}d_i^2}A'\beta^2 E_e^2 \exp\left(-\frac{B}{\beta E_e}\right) \tag{20}$$

If the secondary electron yield is assumed to be constant, Eq. (20) can be integrated to obtain

$$E_e(t) = \frac{E_{e_o}}{1 + \frac{\beta E_{e_o}}{B}\ln\left(1 - \exp(-\frac{B}{\beta E_{e_o}})(\frac{B}{\beta})Ct\right)} \tag{21}$$

where C is the constant given by

$$C = \eta\xi\frac{(\gamma_{ee}-1)\sqrt{S_{real}}}{C_{diele}d_i^2}A'\beta^2 \tag{22}$$

and E_{e_o} is the initial electric field at the electron emission site on the interconnector, which can be expressed in terms of the potential difference between the coverglass front surface and the triple junction as

$$E_{e_o} = \eta\frac{V}{d}\xi_0. \tag{23}$$

where ξ_0 is the value of ξ found by substituting $d_i = d_1 + d_2$ into Eq. (17). Chapter 3 will discuss the method using a non-constant secondary electron yield. The electric field $E_e(t)$ then has the characteristic shape shown in Figure 6.

The field shows a run-away at a time $t = \tau_{efee}$ when the denominator in Eq. (21) vanishes, which is taken to be the EFEE charging time. Thus, the field emission electron charging time τ_{efee} is given by

$$\tau_{efee} = \frac{1 - \exp(-\frac{B}{\beta E_{e_o}})}{\exp(-\frac{B}{\beta E_{e_o}})}\left(\frac{B}{\beta}\right)C \tag{24}$$

$$\simeq \frac{\beta}{B}\exp\left(\frac{B}{\beta E_{e_o}}\right)\frac{1}{C} \tag{25}$$

$$= \frac{C_{diele}d_i^2}{(\gamma_{ee}-1)\sqrt{S_{real}}\eta\xi A\frac{S_{FN}}{S_{real}}B\beta}\exp\left(\frac{B}{\beta E_{e_o}}\right) \tag{26}$$
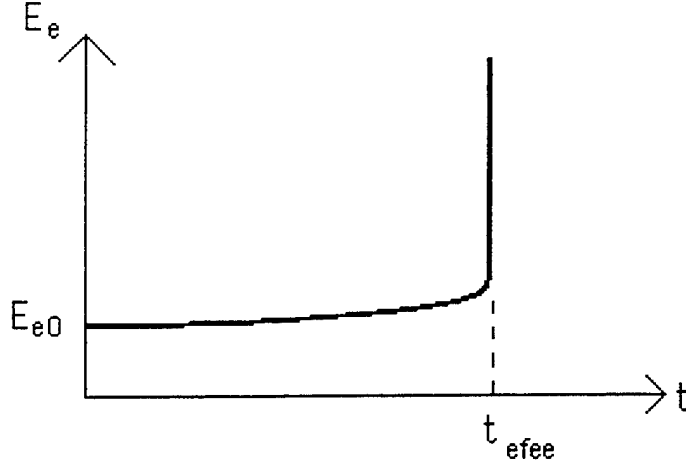
Figure 6: Typical Electric Field Run-Away

Thus, τ_{efee} is given by

$$\tau_{efee}(V) = \frac{C_{diele}d_i^2}{(\gamma_{ee} - 1)\sqrt{S_{real}}\eta\xi A'B\beta} \exp\left(\frac{Bd}{\beta\eta\xi_0 V}\right) \tag{27}$$

The factor η, which was introduced to compensate for the difference in the value of the electric field at the emission site to that at the triple junction, is calculated from the following polynomial fit determined from the numerical schemes

$$\eta = 1 + \sum_{n=1}^{n=4} a_n((\bar{y} - 1)^{2n} - 1), \tag{28}$$

where $\bar{y} = y/(d_{gap}/2)$, y is the distance of the emission site from the triple junction, and d_{gap} is the interconnector length. The first impact point is also calculated from a polynomial fit to numerical results given by

$$\frac{d_i}{d} = \sum_{n=1}^{n=4} b_n \left(\frac{y}{d}\right)^{\frac{1}{2n}} \tag{29}$$

where $d = d_1 + d_2$. The capacitance per unit area of the dielectric side surface, $C_{diele}(d_i)$, is determined from a fifth order polynomial fit to the results of a capacitance matrix scheme[43], discussed in Appendix B. Thus,

$$\frac{C_{diele}(d_i)}{C_{norm}} = \frac{1}{\sum_{n=1}^{n=6} c_n \left(\frac{d_i}{d}\right)^{n-1}} \tag{30}$$

19

where C_{norm} is the capacitance per unit area of the front surface

$$C_{norm} = \frac{1}{\frac{d_1}{\epsilon_{d_1}} + \frac{d_2}{\epsilon_{d_2}}} \tag{31}$$

The term γ_{ee} is the secondary electron yield given by Reference 33 as

$$\gamma_{ee} = \gamma_{max} \frac{E_i}{E_{max}} \exp\left(2 - 2\sqrt{\frac{E_i}{E_{max}}}\right) \exp[2(1 - \cos\theta_i)] \tag{32}$$

Here E_i is the incident energy of the emitted electrons impacting the dielectrics given by

$$E_i = e\phi_d = \frac{E_{TJ}d_i}{\xi} = \frac{\xi_0}{\xi}V\frac{d_i}{d} \tag{33}$$

and θ_i is the incident angle of those electrons at the first impact site given by

$$\theta_i = \arctan\left(\frac{d_i}{y}\right) \tag{34}$$

In Eq. (32), γ_{max} is the maximum secondary electron yield at normal incidence and E_{max} is the electron incident energy for the maximum secondary electron yield.

The implicit assumption in this analysis is that the secondary electron yield is greater than unity. If the yield is less than unity, positive charging of the dielectric side surface will not occur and the field will not run away. However, even when taking into account the oblique incidence of electrons, the incident energy required to give a secondary electron yield of one will be on the order of tens of electron volts, or lower, for typical solar cell dielectric material. Thus, for high negative bias voltages, it is unlikely that the secondary electron yield will become less than unity.

It should also be noted that any changes of the conductor surface work function due to the adsorption of neutral gas on the surface has been neglected. It has been observed that the adsorption of a gas on a metal surface can change the surface's work function[84], and that the change strongly depends on the binding state of the gas. Different adsorbed states for the same gas-metal system can result in both increases and decreases in the work function.

The parameters which affect the EFEE charging, then, are the secondary electron yield, side surface capacitance, Fowler-Nordheim coefficients, emission site parameters, first impact point on the dielectric, and the bias voltage. The Fowler-Nordheim coefficients are functions only of the interconnect work function, and the secondary electron yield and emission site parameters d_i, η, ξ, and C_{diele} are only functions of y, at a given voltage[13].

2.2 Ion Charging Time

The calculation of the ion charging time is simpler than that for the EFEE charging time. If an arc occurs when the potential difference between the front surface and conductor is V_a and the coverglass front surface loses charge ΔQ, then the potential difference drops to $V_a - \Delta Q / C_{front}$, where C_{front} is capacitance of the front surface given by

$$C_{front} = \frac{1}{d_1/(A_{cell}\epsilon_{d_1}) + d_2/(A_{cell}\epsilon_{d_2})} \tag{35}$$

The ambient ion charging time for the voltage to recover to the value V_e is then given by

$$\tau_{ion} = \frac{[V_e - (V_a - \frac{\Delta Q}{C_{front}})]C_{front}}{en_e v_{ion} A_{cell}} \tag{36}$$

where $n_e v_{ion}$ is the ion flux to the coverglass front surface of area A_{cell}. This gives a total charging time of

$$\tau_{chrg} = \frac{(V_e - (V_{arc} - \frac{\Delta Q}{C_{front}}))C_{front}}{en_e v_{ion} A_{cell}} + \frac{C_{diele}d_i^2}{(\gamma_{ee}-1)\sqrt{S_{real}}\eta\xi A\frac{S_{FN}}{S_{real}}B\beta}\exp\left(\frac{Bd}{\beta\eta\xi_0 V_e}\right) \tag{37}$$

2.3 Neutral Desorption

The two possible mechanisms for creating a neutral gas cloud are thermal stimulated desorption (TSD) and electron stimulated desorption (ESD). Cho determined that it is very unlikely that the cloud is created through TSD, due to the temperature rise necessary and

the very short timescale involved[13]. Thus, it is assumed that the neutral gas cloud density is determined by electron stimulated desorption.

ESD can be viewed as an inelastic collisional process between electrons and the adsorbate. The electron impact imparts energy to the adsorbate, and can cause an electronic transition to the excited or ionized state. If the transition is high enough to place the molecule in an antibonding state, the adsorbed particle can leave the surface. The desorption flux due to ESD, Γ_{ESD}, is given by

$$\Gamma_{ESD} = N_n Q_{ESD} \frac{j_e}{e} \tag{38}$$

where N_n is the number of gas particles adsorbed per unit are on the surface, Q_{ESD} is the effective ESD cross section, and j_e/e is the incident electron flux. Typical values of Q_{ESD} range from $10^{-19}m^2$ to $10^{-24}m^2$, depending on the binding state of the adsorbate. Although ESD can also desorb ions, the cross section for this is generally several orders of magnitude smaller than that for neutrals. There is a threshold for the incident electron energy which is about 5 eV for neutrals and 15 eV for ions[22].

To determine the surface neutral density, Cho assumed that the surface was in steady state, such that the thermal desorption flux was balanced by the adsorption flux[13]. In the present work, this was modified to be more time accurate, and will be discussed in the next chapter. The desorption flux due to TSD is given by

$$\Gamma_{TSD} = \frac{dN_n}{dt} = -k_m N_n^m = -N_n^m k_m^0 \exp\left(-\frac{E_d}{\kappa T_s}\right) \tag{39}$$

where m denotes the order of reaction and T_s is the temperature of the surface. In the MC-PIC simulations run by Cho[13], $m = 1$ was used for $A(adsorbed) \to A(gas)$ and $m = 2$ for $2A(adsorbed) \to A_2(gas)$. In the semi-analytic simulations only $m = 1$ was used, since it was assumed adsorbed water molecules are the neutral species. This is an Arrhenius type modeling of the desorption process, with the gas particle trapped in a potential well of depth E_d. The coefficient k_1^0 corresponds to the frequency at which the particle oscillates within the well, which is typically $k_1^0 = 10^{13\pm1}sec^{-1}$. The value of E_d depends on the binding state of the adsorbate. If the binding is due to physical forces, such as van der Waals force

(physisorption), it is on the order of a fraction of an eV. If the binding is due to chemical reactions (chemisorption), the energy is on the order of an eV.

When the residual gas pressure is high, gas molecules can form multiple layers of adsorbed gases on the surface. The lowest layer is due to chemisorption and the upper layers are physisorbed. Under space operating conditions, however, the background neutral pressure is not high enough to prevent the physisorbed layers from disappearing. Therefore, we consider the neutral molecules to be a chemisorbed monolayer. For a monolayer coverage over a flat surface, approximately 10^{19} molecules per m^2 are needed. As the neutral species, H_2O was chosen. During ground testing, UV spectroscopic measurements showed a strong OH spectra when arcs occurred, indicating the involvement of water[99]. Another experiment showed that the major species of outgassed products from dielectric materials typically used on spacecraft, such as Mylar, Teflon, and Plexiglass, was water vapor[60].

The steady state value of the adsorbed neutral density N_n^* is then given by the balance of the desorption flux from Eq. (39) and the adsorption flux, $n_{na}\frac{\bar{c}}{4}s$, where n_{na} is the ambient neutral density and $\bar{c}$ is the thermal speed of the neutral molecules. The term $s = 1 - N_n^*/N_{n0}$ is the probability that a particle striking the surface sticks, where N_{n0} is the surface neutral density for monolayer coverage. The flux balance can then be written as

$$k_1^0 N_n^* exp\left(-\frac{E_d}{\kappa T_s}\right) = n_{na}\frac{\bar{c}}{4}\left(1 - \frac{N_n^*}{N_{n0}}\right), \tag{40}$$

where T_s is the temperature of the dielectric surface. Solving this for N_n^* gives

$$N_n^* = \frac{n_{na}\frac{\bar{c}}{4}}{n_{na}\frac{\bar{c}}{4} + k_1^0 N_{n0} \exp\left(-\frac{E_d}{\kappa T_s}\right)} N_{n0} \tag{41}$$

This is the amount of neutral gas adsorbed on the side surface before the intense outgassing due to EFEE begins.

2.4 Semi-Vacuum Gas Breakdown

As the EFEE charging process occurs, the current density to the side of the dielectric increases dramatically. This intense electron current can desorb a significant amount of neutrals through electron stimulated desorption (ESD). Numerical studies by Cho resulted in neutral densities as high as $10^{23}m^{-3}$[13]. Typical ambient neutral densities in LEO range from $10^{13}m^{-3}$ to $10^{16}m^{-3}$. In the vicinity of spacecraft, however, the neutral density can be significantly increased. For example, neutral densities in the Space Shuttle bay as high as $10^{18}m^{-3}$ have been measured[102]. This section will examine the breakdown mechanism for this neutral density regime.

The length scale for breakdown in the space environment is bound by the size of the electric sheath surrounding the high voltage surface. If there were no plasma present, the discharge would be expected to occur between the two points where the product of the pressure and the distance give the lowest Paschen breakdown voltage, known as a long-path discharge. In the presence of a plasma, however, electrons that are emitted from the negatively biased surface are lost once they leave the sheath, due to Debye shielding. The thickness of the sheath, t, near a biased surface can be calculated from the Child-Langmuir Law[12]

$$\frac{u_0}{(\kappa T_e/m_i)^{1/2}} = \frac{4\sqrt{2}}{9}\frac{(-eV/\kappa T_e)^{3/2}}{t^2}\lambda_D^2 \tag{42}$$

where u_0 is the velocity of the ions entering the sheath, T_e is the electron temperature in eV, and λ_D is the debye length, which is a function of the electron temperature and density, n_e, given by

$$\lambda_D = \sqrt{\frac{\epsilon_0 \kappa T_e}{n_e e^2}} \tag{43}$$

The boundary of the sheath is the point where $u_0 = (\kappa T_e/m_i)^{1/2}$. Using this condition and solving Eq. (42) for t

$$t = \frac{2^{5/4}}{3}(-eV/\kappa T_e)^{3/4}\lambda_D \tag{44}$$

Thus, for negative bias voltages near $\kappa T_e/e$, the sheath thickness is approximately equal to the debye length, and increases with bias voltage. Typical debye lengths in LEO are on the order of a centimeter or less. This derivation, however, assumes a plane biased surface

where the sheath thickness is much less than the size of the surface. This length scale gives an upper bound for the arcing region size. The real size will be smaller, on the order of a millimeter, since the arcing process occurs at localized sites at the interconnect/coverglass junction.

Using these parameters, the product of the pressure and scale length, pd, can range from $1 torr \cdot cm$ to $10^{-8} torr \cdot cm$. The regime were classical Townsend gas breakdown theory holds is at high values of pd, typically above $10^{-2} torr \cdot cm$. Thus, most of the values of pd in the high voltage solar array arcing process fall into the semi-vacuum region between the Townsend breakdown regime, where the ionization mean free path, λ_{mfp}, is smaller than the path length, d, and the vacuum region where $\lambda_{mfp} \gg d$.

In a typical Townsend breakdown[66, 44], ions created by electron-neutral ionization collisions impact the cathode surface and release secondary electrons. Breakdown will occur if the secondary electron current exceeds the original electron current. The secondary electron current is given by $\gamma_{ie} j_i$, where j_i is the ion current to the cathode and γ_{ie} is the secondary electron yield, which is typically less than unity. Therefore, the current returning to the cathode must be greater than the original current, which means that each electron emitted must create more than one ion through collisional ionization of the ambient neutrals before it reaches the anode. So, for Townsend breakdown to occur, the condition $\lambda_{mfp} < d$ must be met. The voltage for breakdown is a function of pd and follows the Paschen Law well.

In vacuum breakdown, the pre-breakdown electron current is emitted from the cathode via field emission. As the current increases, the neutral gas which subsequently breaks down is provided through surface interactions of the electron beam with the electrodes. Voltages for vacuum breakdown are typically on the order of kilovolts to tens of kilovolts, and are independent of the background neutral density, since the neutrals for breakdown are supplied by the surface interactions. However, as the pressure increases, the breakdown voltage shows a sudden drop at around 10^{-3} to 10^{-2} torr and reaches Townsend values.

The solar array arcing problem is closer to vacuum breakdown than Townsend breakdown, in that the neutral source is provided by desorption from the dielectric side surface. However, the resulting neutral density may not be high enough to explain breakdown by the

usual mechanisms. In addition, breakdown voltages on the order of hundreds of volts is typically observed, which is an order of magnitude lower than the typical vacuum breakdown voltages. The current problem also considers the possibility of the residual gas breakdown surrounding the interconnect surface. Thus, the region of pd in the solar array arcing systems corresponds to the transitional region between the vacuum and Townsend regimes, termed the "semi-vacuum" region. In this regime, more than one electron is needed to produce one ion. There is little known of this region compared to the others to due to experimental difficulties in preventing long path discharges.

2.4.1 BKG Breakdown in a One-Dimensional Semi-Vacuum System

In Reference 13, Cho developed a breakdown mechanism for solar array arcing in the semi-vacuum region. The mechanism was first developed for a one-dimensional system, then extended to the two-dimensional system needed for the solar array arcing problem. The one-dimensional system consists of a cathode and anode, and is filled uniformly with neutral gas.

The hypothesis for breakdown in this regime was proposed by Boyle, Kisliuk, and Germer (BKG)[11]. If the distance between the cathode and anode is small enough, there is a pre-breakdown electron current emitted from the cathode due to field emission, with a feedback effect provided by the field enhancement from the positive space charges of the incoming ion current. The resulting secondary electron current is nonlinear with the ion current and the ion current does not have to be larger than the original electron current.

The increment of the electric field at the cathode surface due to returning ion current, j_i, is written as

$$\delta E^+ = C^+ j_i \tag{45}$$

where the constant C^+ will be determined later analytically. In Reference 11, C^+ was given by $C^+ = \frac{10}{3} \frac{d}{\epsilon_o} (\frac{m_i}{2e})^{1/2} \frac{1}{V^{1/2}}$, where V is the voltage across the gap, m_i is the ion mass, and e

is the electron charge. The returning ion current density is given by

$$j_i = (e^{n_n \sigma d} - 1)j_{e0}$$

$$\simeq (n_n \sigma d)j_{e0} \tag{46}$$

where j_{e0} is the initial electron emission current density from the cathode before any ionization occurs, n_n is the neutral density, and σ is the ionization collision cross section. It is assumed that the probability of ionization collisions while one electron travels from the cathode to the anode is very small, that is, $n_n \sigma d \ll 1$. It is also assumed that the neutral density is uniform and independent of the electron current density j_e unless noted otherwise. In Reference 11, the neutral gas was assumed to be a result of the electron impact on the anode surface, which makes the results for the following breakdown condition slightly different.

The field emission current density is given by

$$j_{e0} = A'\beta^2 E_{c.o.}^2 \exp\left(-\frac{B}{\beta E_{c.o.}}\right) \tag{47}$$

where $E_{c.o.}$ is the electric field at the cathode surface without any ion space charge. The current j_{e0} is the emission current from the cathode before any ion is near the cathode surface. If we denote the typical time for an ion to travel across the gap by τ_+, the current j_{e0} is the current flowing in the gap before $t = \tau_+$.

When the group of ions which are created by the initial electrons, j_{e0}, arrives at the cathode at time $t = \tau_+$, the field is enhanced by the ion space charge. The emission current then becomes

$$
\begin{aligned}
j_{e1} &= A'\beta^2 (E_{c.o.} + \delta E)^2 \exp\left(-\frac{B}{\beta(E_{c.o.} + \delta E)}\right) \\
&\simeq A'\beta^2 E_{c.o.}^2 \exp\left(-\frac{B}{\beta E_{c.o.}}\right) \exp\left(\frac{B}{E_{c.o.}}\frac{\delta E^+}{\beta E_{c.o.}}\right) \\
&= j_{e0} \exp\left(\frac{B}{\beta E_{c.o.}}\frac{\delta E^+}{E_{c.o.}}\right) \tag{48}
\end{aligned}
$$

where it has been assumed that $E_{c.o.} \gg \delta E^+$. This assumption is valid because only a small

increase in the electric field is necessary to cause a large increase in the emission current due to its exponential dependence on the field. If $\delta E^+ > E_{c.o.}$, we need to consider a time scale less than τ_+ where the field increment given by $C^+ = n_n \sigma d' j_{e0}$ with $d' \ll d$ is still small compared to $E_{c.o.}$. Using Eqs. (45) and (46), the current density can be rewritten as

$$j_{e1} = j_{e0} \exp \left(\frac{B}{\beta E_{c.o.}^2} C^+ n_n \sigma d j_{e0} \right)$$

Denoting the premultiplier of j_{e0} inside the exponential by a constant M, that is,

$$M = \frac{B}{\beta E_{c.o.}^2} C^+ n_n \sigma d \qquad (49)$$

we can write

$$j_{e1} = j_{e0} \exp(M j_{e0})$$

At time $t = 2\tau_+$, the second group of ions, created by the electrons emitted as j_{e1}, arrives at the cathode and gives the emission current of the next step

$$j_{e2} = j_{e0} \exp(M j_{e1})$$

The emission current density of the following steps are given by

$$\begin{aligned} j_{e3} &= j_{e0} \exp(M j_{e2}) \\ &\vdots \\ j_{en} &= j_{e0} \exp(M j_{en-1}) \end{aligned}$$

This current growth is stable when there is a solution which satisfies

$$j_{en}^* = j_{e0} \exp(M j_{en}^*) \qquad (50)$$

The stable solution j_{en}^* is graphically shown in Figure 7. In this analysis, a discrete treatment of time was used to make the mechanisms of current multiplication clear. If a continuous treatment had been used, the stable condition given by Eq. (50) would still be the same as long as the electric field increment due to j_{en}^* is small compared to $E_{c.o.}$ because Eq. (50)

28

gives a physical condition for the case where the positive ion space charge balances the increment of negative space charge produced by the current increase from the initial current j_{e0}. The curve $j_{e0}\exp(Mj_{en})$ becomes tangential to the line j_{en} when $\partial j_{e0}\exp(Mj_{en})/\partial j_{en} = 1$, that is, $j_{e0}M\exp(Mj_{en}^*) = Mj_{en}^* = 1$. Therefore, breakdown occurs when the initial current density j_{e0} exceeds a critical initial value,

$$j_{e0} \geq j_{e0.cr.} = \frac{1}{M}\exp(-1) \tag{51}$$

This is the point where the positive ion space charge outbalances the increase of negative space charge. Substituting Eqs. (47) and 49 into Eq. (51), the breakdown condition is written as

$$n_n \geq \exp(-1)\frac{1}{C^+\sigma dA'\beta B}\exp\left(\frac{B}{\beta E_{c.o.}}\right) \tag{52}$$

Once we know the constant C^+, we can calculate the breakdown condition for a given set of parameters. To find the ion space charge field enhancement factor C^+, the following system of one-dimensional equations are solved

$$\begin{cases} \frac{\partial}{\partial t}n_e & + & \frac{\partial}{\partial x}(n_e v_e) & = & \nu_{ion}n_e \\ \frac{\partial}{\partial t}n_i & + & \frac{\partial}{\partial x}(n_i v_i) & = & \nu_{ion}n_e \\ \frac{\partial}{\partial t}v_e & + & v_e\frac{\partial}{\partial x}v_e & = & -\frac{e}{m_e}E \\ \frac{\partial}{\partial t}v_i & + & v_i\frac{\partial}{\partial x}v_i & = & \frac{e}{m_i}E \\ & & \frac{\partial}{\partial x}E & = & \frac{e}{\epsilon_o}(n_i - n_e) \\ & & \frac{\partial}{\partial x}\phi & = & -E \end{cases} \tag{53}$$

with the boundary conditions

$$\begin{cases} \phi(x=0) & = & 0 \\ \phi(x=d) & = & V(>0) \end{cases} \tag{54}$$

where n_e, n_i are the electron and ion densities, v_e, v_i are the electron and ion velocities, and ν_{ion} is the ionization collision frequency. Cho determined that for an emission site of size $r_o^2 = 10^{-10}(m^2)$, $\kappa T_e = 1(eV)$, and a gap distance of $d = 0.1mm$, the electron beam broadening can be neglected at a voltage higher than 100 volts[13], making the one-dimensional approach valid.
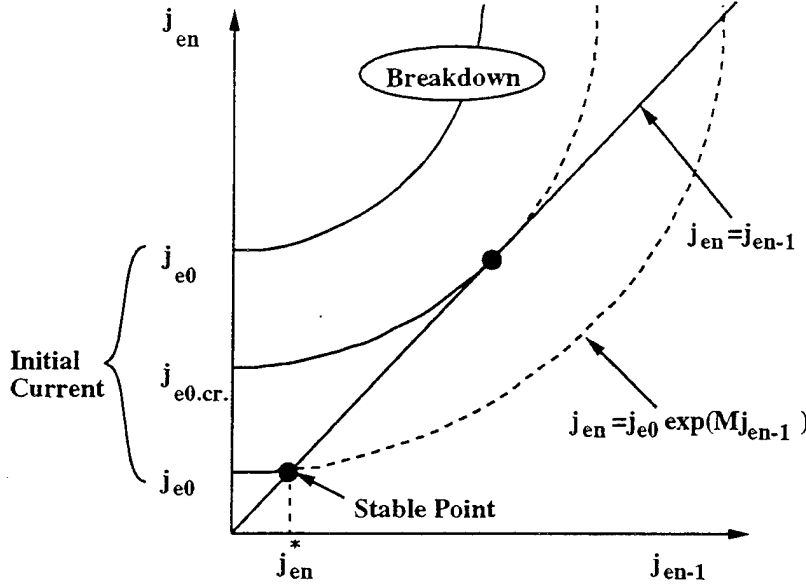
Figure 7: Graphical Description of the BKG Breakdown Condition

Next, the quantities are broken into zeroth and first order terms

$$
\begin{cases}
n_e &= n_{e0}(x) &+ &\delta n_e(x,t) \\
n_i &= n_{i0} &+ &\delta n_i(x,t) \\
v_e &= v_{e0}(x) &+ &\delta v_e(x,t) \\
v_i &= v_{i0}(x) &+ &\delta v_i(x,t) \\
E &= E_0 &+ &\delta E(x,t)
\end{cases}
\tag{55}
$$

The ionization frequency ν_{ion} is given by $\nu_{ion} = v_{eo}/\lambda_{mfp}$. Since the mean free path is very large compared to d, ν_{ion} is regarded as a first order quantity. For the zeroth order, neglecting the unsteady terms and the ionization, the solutions are given by

$$
\begin{cases}
n_{e0}(x) &= \frac{j_{e0}}{e v_{e0}(x)} \\
n_{i0} &= 0 \\
v_{e0}(x) &= \sqrt{-\frac{2e}{m_e} E_0 x} \\
v_{i0}(x) &= -\sqrt{-\frac{2e}{m_i} E_0 (d-x)} \\
E_0 &= \text{const}
\end{cases}
\tag{56}
$$

where the current density j_{e0} is uniform and the electric field E_0 is negative. We consider the

state when the perturbation $\delta n_e(x, t)$ is mainly due to ionization and still small compared to n_{e0}. This corresponds to the state before the emission current from the cathode begins to increase. Since the objective here is to obtain the factor C^+ analytically, not to obtain the growth rate, this approach is justified.

For simplicity, we neglect the unsteady terms to the first order. The first order equations are then written as

$$\begin{cases} \frac{\partial}{\partial x}(\delta n_e v_{e0} + n_{e0}\delta v_e) & = \quad \frac{n_{e0}v_{e0}}{\lambda_{mfp}} \\ v_{e0}\frac{\partial}{\partial x}v_e + \delta v_e \frac{\partial}{\partial x}v_{e0} & = \quad -\frac{e}{m_e}\delta E \\ \frac{\partial}{\partial x}(\delta n_i v_{i0}) & = \quad \frac{n_{e0}v_{e0}}{\lambda_{mfp}} \\ \frac{\partial}{\partial x}\delta E & = \quad \frac{e}{\epsilon_o}(\delta n_i - \delta n_e) \end{cases} \qquad (57)$$

We eliminate δn_e, δv_e, and δn_i and solve for the field δE. After some algebra, the differential equation for δE is obtained

$$[\frac{\partial^3}{\partial \xi^3} + \frac{3}{\xi}\frac{\partial^2}{\partial \xi^2} + (\frac{3}{4\xi^2} + \frac{D}{2\xi^{3/2}})\frac{\partial}{\partial \xi}]\overline{\delta E} = -D\frac{d}{\lambda_{mfp}}[\sqrt{\frac{m_i}{m_e}}\frac{8\xi^2 - 12\xi + 3}{4\xi^2(1-\xi)^{3/2}} - \frac{3}{2\xi^{3/2}}] \qquad (58)$$

where $\xi = x/d$, $\overline{\delta E} = \delta E/E_0$ and the constant D is given by

$$D = \frac{j_{e0}}{\epsilon_o\sqrt{\frac{2e}{m_e}}(-E_0)^{3/2}/\sqrt{d}} = \frac{4}{9}\frac{j_{e0}}{j_{sp}} \qquad (59)$$

with j_{sp} given by the Child-Langmuir space charge limited current for the case of $E_0 = V/d$. Neglecting the fourth term in the LHS because $D \ll 1$ and the second term in the RHS because $\sqrt{m_i/m_e} \gg 1$, Eq. (58) can be approximated by

$$[\frac{\partial^3}{\partial \xi^3} + \frac{3}{\xi}\frac{\partial^2}{\partial \xi^2} + \frac{3}{4\xi^2}\frac{\partial}{\partial \xi}]\overline{\delta E} = -D\frac{d}{\lambda_{mfp}}\sqrt{\frac{m_i}{m_e}}\frac{8\xi^2 - 12\xi + 3}{4\xi^2(1-\xi)^{3/2}} \qquad (60)$$

where $\overline{\delta E}$ must satisfy the condition

$$\int_0^1 \overline{\delta E}d\xi = 0 \qquad (61)$$

31

The solution to Eq. (60) is

$$\overline{\delta E} = \frac{2}{3} D \frac{d}{\lambda_{mfp}} \sqrt{\frac{m_i}{m_e}} [(1 - \xi)^{3/2} - \frac{2}{5}] \tag{62}$$

and at the boundary the field enhancement is given by

$$\frac{\delta E(x = 0)}{E_0} = \frac{8}{45} \sqrt{\frac{m_i}{m_e}} n_n \sigma d \frac{j_{e0}}{j_{sp}} \tag{63}$$

This corresponds to the ion space charge enhancement factor

$$C^+ = 0.4 \frac{d}{\epsilon_o} \left(\frac{m_i}{2e}\right)^{1/2} \frac{1}{V^{1/2}} \tag{64}$$

which is smaller than the one used in Reference 11 by a factor of eight. Substituting Eq. (64) into Eq. (52), the breakdown condition can be written as

$$n_n \geq 0.92 \frac{\epsilon_o V^{1/2}}{\sigma d^2 A' \beta B} \left(\frac{2e}{m_i}\right)^{1/2} \exp\left(\frac{B}{\beta E_{c.o.}}\right) \tag{65}$$

These results were verified by Monte Carlo-PIC simulations by Cho[13]. The results of the simulations agreed very well with experimental data, with a transition from semi-vacuum to vacuum breakdown clearly occurring at $p \sim 10^{-3} torr$.

2.4.2 BKG Breakdown in a Two-Dimensional Semi-Vacuum System

The breakdown neutral density is now determined by modifying the one-dimensional analytical formulas from the previous section. In the two dimensional system, the ion current density to the conductor surface is lower than that given by Eq. (46), since not all of the ions come near the emission site due to the deflection of their paths by the electric field normal to the dielectric side surface. The ion current density in front of the emission site is now given by

$$j_i = \zeta (n_n \sigma d) j_{e0} \tag{66}$$

where ζ is the fraction of the ion current which contributes to the field enhancement at the emission site, and j_{e0} is the current density from the cathode before any ionization begins

and is equal to j_{ec}^* (Appendix A) for the two-dimensional case. Taking into account this factor, the breakdown condition Eq. (51) is rewritten as

$$j_{e0} \geq \frac{1}{M} \exp(-1) = [\frac{B}{\beta E_{c.o.}^2} C^+ \zeta n_n \sigma d]^{-1} \exp(-1) \qquad (67)$$

where the constant M has been corrected to $M = B/\beta/E_{c.o.}^2 C^+ \zeta n_n \sigma d$. The factor C^+ accounts for the increment of the field at the cathode surface due to returning ion current j_i by $\delta E^+ = C^+ j_i$. In the previous section, the one-dimensional equations were solved analytically and C^+ was given by

$$C^+ = 0.4 \frac{d}{\epsilon_o} (\frac{m_i}{2e})^{1/2} \frac{1}{|V|^{1/2}}$$

However, for the present case, we need to modify the above expression by taking into account the fact that the initial electric field along the dielectric surface is not uniform due to the difference of the dielectric properties of the coverglass and adhesive. The factor C^+ is now given by

$$C^+ = 0.4 \frac{d_2}{\epsilon_o} (\frac{m_i}{2e})^{1/2} \frac{1}{|V_{ad}|^{1/2}} \qquad (68)$$

where V_{ad} is the potential difference between the triple junction and the interface between the coverglass and the adhesive, which is given by

$$V_{ad} = V \left(\frac{d_2}{\frac{\epsilon_{d2}}{\epsilon_{d1}} d_1 + d_2} \right)$$

Substituting Eq. (68) into Eq. (67), the breakdown condition can be rewritten as

$$n_n \geq 0.92 \frac{\epsilon_o V_{ad}^{1/2}}{\zeta \sigma (d_1 + d_2) d_2 A' \beta B} \left(\frac{2e}{m_i} \right)^{1/2} \exp \left(\frac{B}{\beta E_{c.o.}} \right) \qquad (69)$$

where the initial cathode field $E_{c.o.}$ and the factor ζ must be calculated numerically. The field $E_{c.o.}$ corresponds to the field at the emission site when the emission current becomes quasi-steady after it is limited by negative space charge before ionization begins. Using

Eq. (143), $E_{c.o.}$ is found by solving the following equation

$$A'(\beta E_{c.o.})^2 \exp\left(-\frac{B}{\beta E_{c.o.}}\right) = 1.05\epsilon_o \sqrt{\frac{2e}{m_e}} \frac{\sqrt{E_{se}}}{\sqrt{S_{real}}d} |V| \tag{70}$$

at a given bias voltage V. Cho approximated the ion concentration factor by $\zeta = 0.1$ from the numerical results of ion current distribution over the conductor surface[13]. From the numerical studies, it was determined that once EFEE charging occurs, arcing onset follows when the desorbed neutral density reaches approximately $3 \times 10^{21} \sim 10^{22} m^{-3}$. In the simulations, a critical neutral density of $6 \times 10^{21} m^{-3}$ was used for breakdown to occur.

For a given bias voltage, the desorbed neutral density depends linearly with the ESD yield $N_n Q_{ESD}$. Since the neutral flow is free molecular, the average neutral density is estimated by

$$n_n = \frac{N_n Q_{ESD}}{\frac{1}{4}\overline{c}} \left(\frac{\overline{j_e}}{e}\right) \tag{71}$$

where $\overline{c}$ is the average speed of neutral $\overline{c} = \sqrt{\frac{8\kappa T_n}{\pi m_n}}$ and $\overline{j_e}$ is the average electron incident current to the side surface defined by Eq. (144). Substituting Eq. (150) into $\overline{j_e}$ in Eq. (71), the neutral density n_n is given by

$$n_n = 2.08 \frac{N_n Q_{ESD}}{\overline{c}} \frac{\epsilon_o}{e} \sqrt{\frac{2e}{m_e}} \frac{\sqrt{E_{se}}}{E_{se1}d^2} |V_e|^2. \tag{72}$$

where N_n is given by Eq. (41), E_{se} is the electron emission energy, E_{se1} is the electron incident energy for a secondary electron yield of unity, and V_e is the potential difference between the conductor and dielectric front surface at the time of the arc. Therefore, once EFEE charging begins, if the desorbed neutral density given by Eq. (72) is greater than a critical neutral density of approximately $6 \times 10^{21} m^{-3}$, breakdown will occur.

Figure 8 shows the time history of the electron emission current for the arcing process created by the full MC-PIC simulation. The current initially increases rapidly until it becomes space charge limited, as discussed in Appendix A. The resulting intense current to the dielectric side surface desorbs neutral gas, creating a dense neutral cloud. If the density of the gas is greater than the critical density, the neutrals are ionized by the electron current flowing through it. The resulting ions move toward the conductor surface, where their

positive space charge partially cancels the negative space charge of the emitted electrons, increasing the electric field at the emission site. This results in an increase in the emission current, and is regarded as the arc onset. The ionized neutral cloud then discharges part of the dielectric surface, as discussed in the next section.
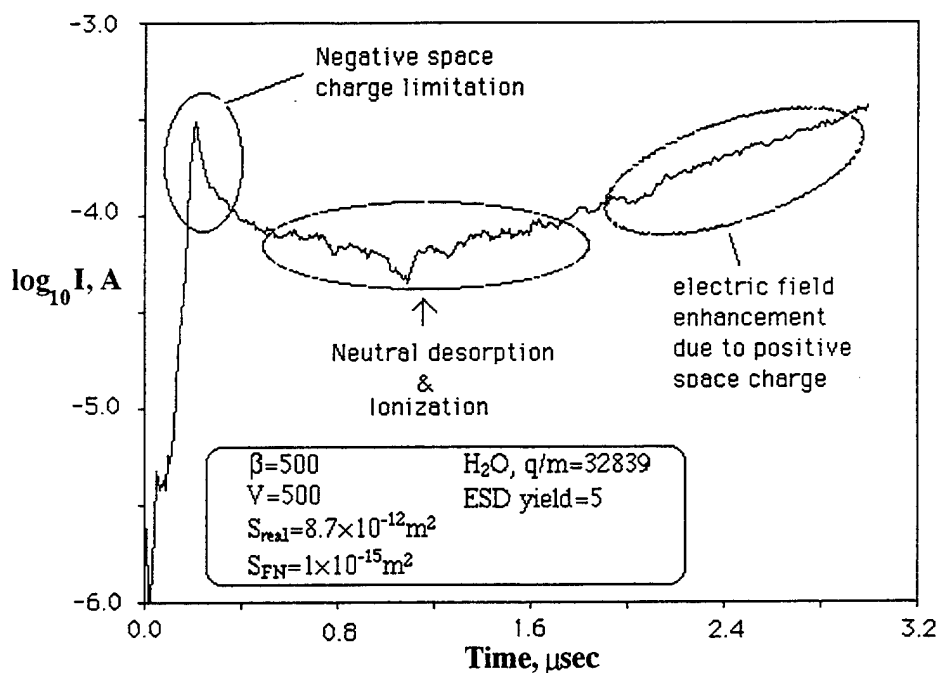
Figure 8: Electron Emission Current from Conductor Surface Calculated by the Full MC-PIC Simulation

2.5 Discharge Wave

When an arc occurs on a solar array interconnect, electrons are emitted from the plasma at the location of the arc. These emitted electrons form part of a plasma cloud over the solar array. Some of the electrons escape, while others strike the coverglass, which has a positive potential near the bias voltage with respect to the interconnect. The impacting electrons produce secondary electrons, and can each easily produce more than one secondary electron due to the high bias voltage. But since the coverglass surface has the highest potential in the region, most of the secondaries are pulled back to the surface. These returning secondary electrons, along with the original electrons from the plasma cloud, causes the balance of the

35

surface charge to go negative, discharging the surface. Because the initial flow of electrons to the surface occurs near the arc site, a potential gradient is created along the coverglass front surface. The resulting electric field causes subsequent secondary electrons to be pulled along the surface instead of returning to their emission sites. By giving secondaries to other parts of the coverglass, the part which emitted the electrons balances the net current across itself and reaches steady state.

This results in the having the discharged portion of the surface expand away from the site of the arc, denoted as a "discharge wave"[13]. The undischarged coverglass capacitance is proportional to the area outside of the area covered by the discharge wave

$$C_g = \frac{\epsilon_d}{d}(N_{cell}A_{cell} - A_{wave}) \tag{73}$$

where N_{cell} is the number of cells in the array, A_{cell} is the cell area, and A_{wave} is the area covered by the discharge wave. Assuming that the wave expands semi-spherically, the speed of the expanding wave front, v_d, is inversely proportional to the area surrounded by the wavefront because of the continuity equation

$$\frac{\partial}{\partial r_{dis}}(r_{dis}^2 v_d) = 0 \tag{74}$$

neglecting the change in the density in time and space, where r_{dis} is the radius of the wavefront. Therefore, the velocity of the wavefront is given by

$$v_d = \frac{dr_{dis}}{dt} \propto \frac{1}{r_{dis}^2} \tag{75}$$

The resulting surface area covered by the discharge wave is found by integrating this to give $A_{wave} = \pi r_{dis}^2 = \pi(3at)^{\frac{2}{3}}$, where a is some proportionality constant. The coverglass capacitance that survives an arc can therefore be given by

$$C_g = \frac{\epsilon_d}{d}N_{cell}A_{cell} - \frac{\epsilon_d}{d}\pi(3a)^{\frac{2}{3}}t^{\frac{2}{3}} \tag{76}$$

From experimental data, Cho determined the wavefront speed to be $v_d = 6.0/r_{dis}^2 m/sec$, where r_{dis} is in meters[13]. Thus, assuming a $10\mu sec$ arc current duration, the wavefront can

discharge an area of $0.01m^2$. When an arc occurs, the charging process at each emission site within the discharged area, referred to as the correlated area, is reset, while the sites outside the area are unaffected.

The above analysis for the area covered by the discharge wave assumes that the wave expands semi-spherically, and that the entire wave remains on the coverglass surface. In most cases, these will be valid assumptions. However, a few cases exist where this will overestimate the area that is discharged, illustrated in Figure 9. Figure 9a shows the case where an arc occurs at least r_{dis} away from an edge of the array and the entire discharge wave remains on the array. If an arc occurs near an edge, however, the area discharged will be lower than that given above, apparent in Figure 9b. However, since most the interconnects lie away from the edges of the array, the above assumptions result in only a slight overestimation in total discharge of the array after many arcs. Also, the area between the cells has been neglected, since this area is typically a very small fraction of the array area.

2.6   Arc Rate Code

Using the semi-analytic model above, a computer code was written by Cho[13] to determine the arc rate for high voltage solar cells operating in a plasma environment. A slightly modified version of this code, which neglected the effects of neutral density on the arc rate, was used by Mong and Hastings to predict arc rates for the PASP Plus experiment[62]. A description of this program will be given here, while the next chapter will discuss modifications made to the code. A flow chart of the code written by Cho is shown in Figure 10.

The program first reads in the input data. This includes the information about the cell dimensions and materials, the experimental parameters (i.e. bias voltage, experiment duration, cell temperature, environmental parameters, etc.), as well as the ranges of the parameters S_{real}, S_{FN}, ΔQ, etc. The emission site density is read in at this point, which will set the number of sites on the conductor. The array is then divided into correlated areas based on the discharge wave area.

Next, the distributions of η, ξ, d_i, and C_{diele} are calculated using Eqs. (28) - (30). Uniform distributions of S_{real}, S_{FN}, and the electron stimulated desorption cross section Q_{ESD} in $log_{10}S_{real}$, $log_{10}S_{FN}$, and $log_{10}Q_{ESD}$ are calculated between minimum and maximum values read in from the input data. The distribution of ΔQ is calculated as a linear distribution between minimum and maximum values. The distribution of the field enhancement factor β is calculated from $f(\beta) = f_0 exp(-\beta/\beta_0)$, where f_0 is a constant determined from the normalization condition $\int f(\beta)d\beta = 1$ and β_0 is a constant which determines the shape of the distribution.

The code then loops through the correlated areas. For each area, a loop is made through the emission sites within the area. All the parameters needed for Eq. (37) are then chosen randomly from the distributions previously calculated or determined using the equations listed above. To determine the charging time for the site using Eq. (37), the term V_e needs to be determined. This is the potential difference between the coverglass and the conductor when the EFEE charging is initiated. It is not necessarily equal to the bias voltage. This is due to the fact that after an arc occurs, as the dielectric recovers its lost charge through ion charging and the electric field at the conductor begins to increase, EFEE charging can start as soon as the conductor surface feels a strong enough electric field. Therefore, the voltage V_e is found by finding the minimum of Eq. (37), which assumes that the secondary electron yield is constant (see Figure 11). This is done by solving the differential equation

$$\frac{d\tau_{arc}}{dV_e} = 0 \qquad (77)$$

using a Newton-Raphson scheme. The arcing time for the site is then calculated using this value of V_e. This is done for each site in the correlated area, and the site with the minimum charging time is the one that arcs. An arc counter is then incremented and the charging time is added to a running timer. The process is then repeated until the timer exceeds the experiment duration. The arc rate is then found by summing the arc counts from all the correlated areas and dividing by the experiment duration. Hastings et al. used the code to predict the arcing rates for the PIX II flight and ground tests[37]. The results of the simulations showed excellent agreement with both sets of experiments, as shown in Figure 12.

2.7 Proposed Arcing Mechanism for Wrap-Through-Contact Solar Cells

The above model was created for the arcing process on conventional geometry solar arrays. Because of the importance of the exposed interconnect in arcing process, the wrap-through-contact (WTC) solar cell was developed to try to mitigate arcing. In this design, the interconnects pass under a kapton substrate between adjacent cells, and are therefore not exposed to the ambient plasma, as shown in Figure 2. However, the solar cell semiconductor is still exposed to the plasma along it's edge, and can participate in the arcing process in a manner similar to the interconnects in the conventional cell system. The WTC cells have been found to arc in both ground and flight tests[56, 23] (although at much lower rates than conventional geometry cells), and an onset mechanism for arcing on WTC cells was proposed by Font et al.[26]. The mechanism can be summarized by the following sequence, illustrated in Figure 13:

(1) Ions from the ambient plasma charge the coverglass front surface and substrate surface between the cells. The region of the substrate immediately adjacent to the cell is charged to a significant positive voltage, producing a strong electric field near the triple junction of the cell, substrate and space.

(2) As the electric field increases, enhanced field electron emission (EFEE) from the semiconductor side surface is initiated. These emitted electrons are attracted to the substrate because of the potential structure in the gap region. The impacting electrons will induce secondary electron emission (SEE) from the substrate surface. The SEE electrons will be unable to climb the potential well and will return the substrate surface, inducing further secondaries. The electron bombardment of the substrate will also desorb neutral molecules through electron stimulated desorption.

(3) Because the electrons can't escape the potential well, the electron current will become space charge limited. If the electron current and desorbed neutral density become sufficiently large before the EFEE emission becomes limited, ionization and discharge will occur.
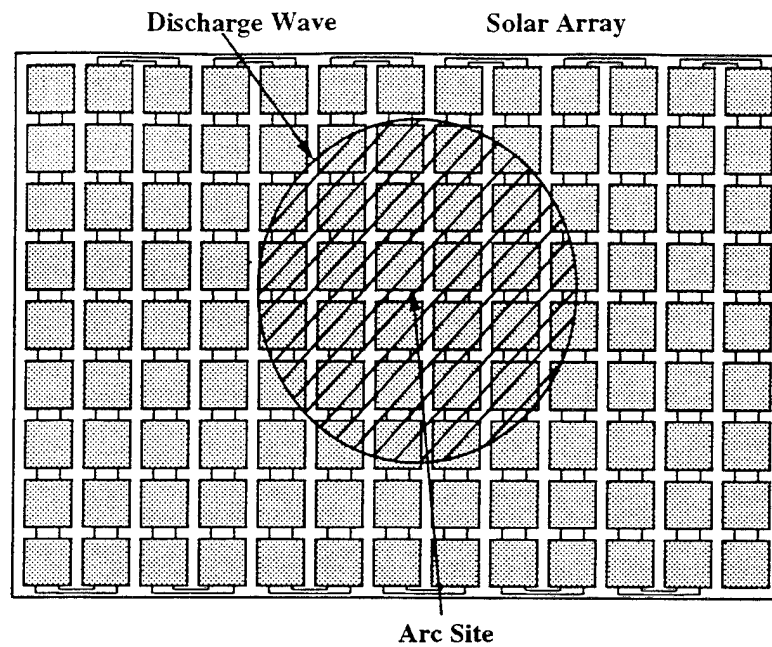
a. Arc Site Away From Array Edge
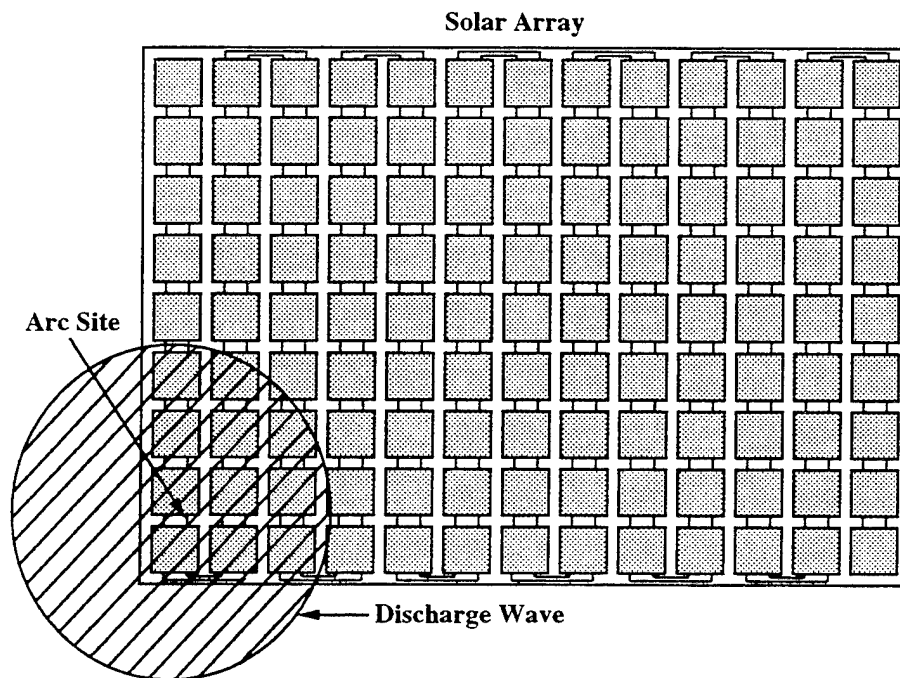
b. Arc Site Near Array Edge

Figure 9: Discharge Wave
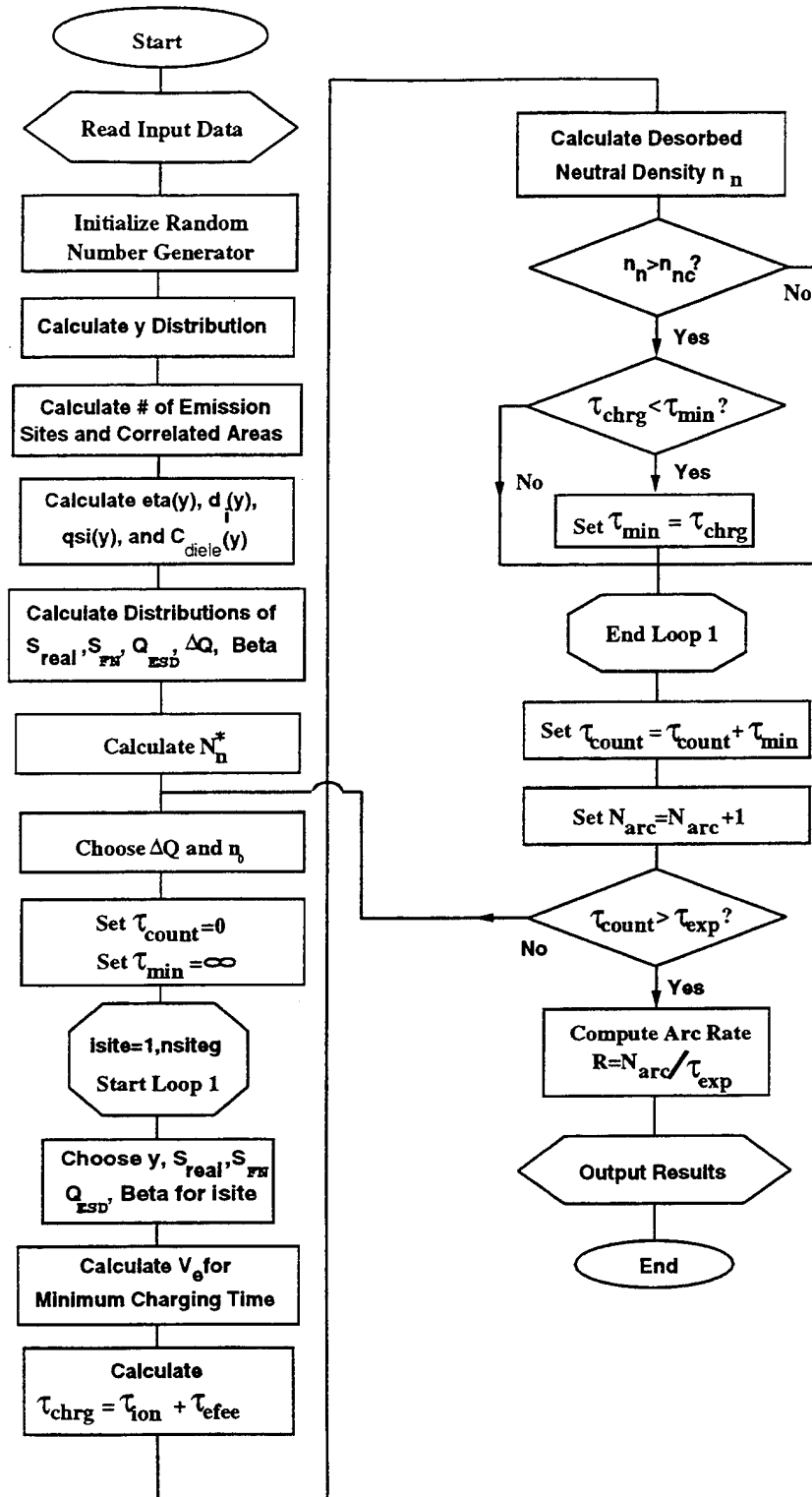
Figure 10: Flow Chart of the Semi-Analytic Arc Rate Code
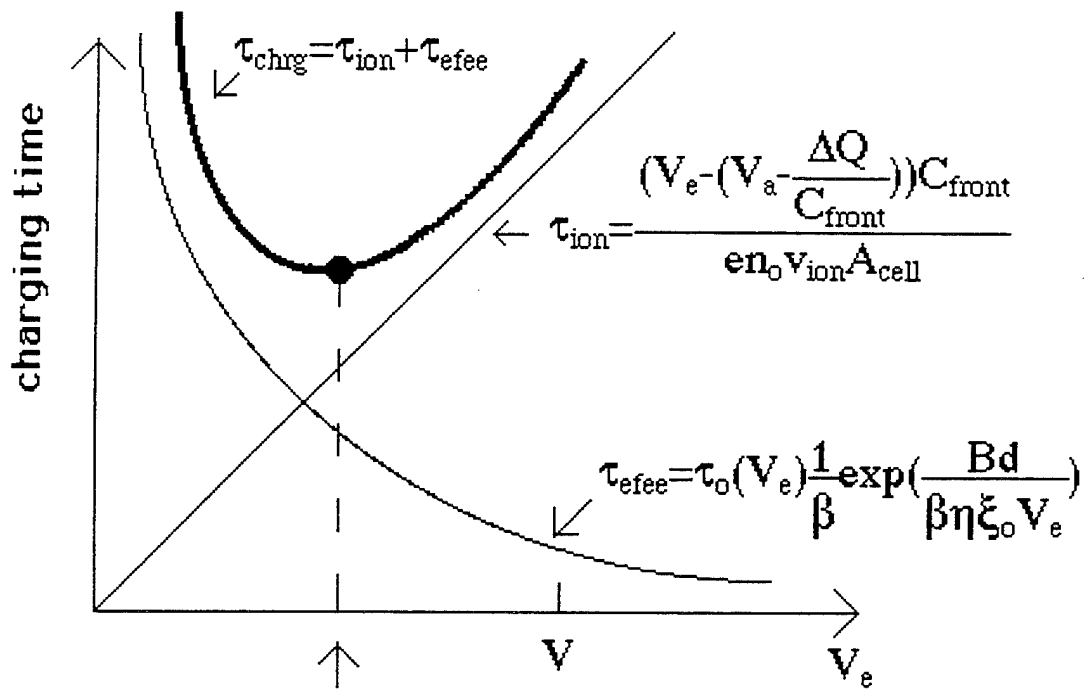
Figure 11: Minimum Charging Time
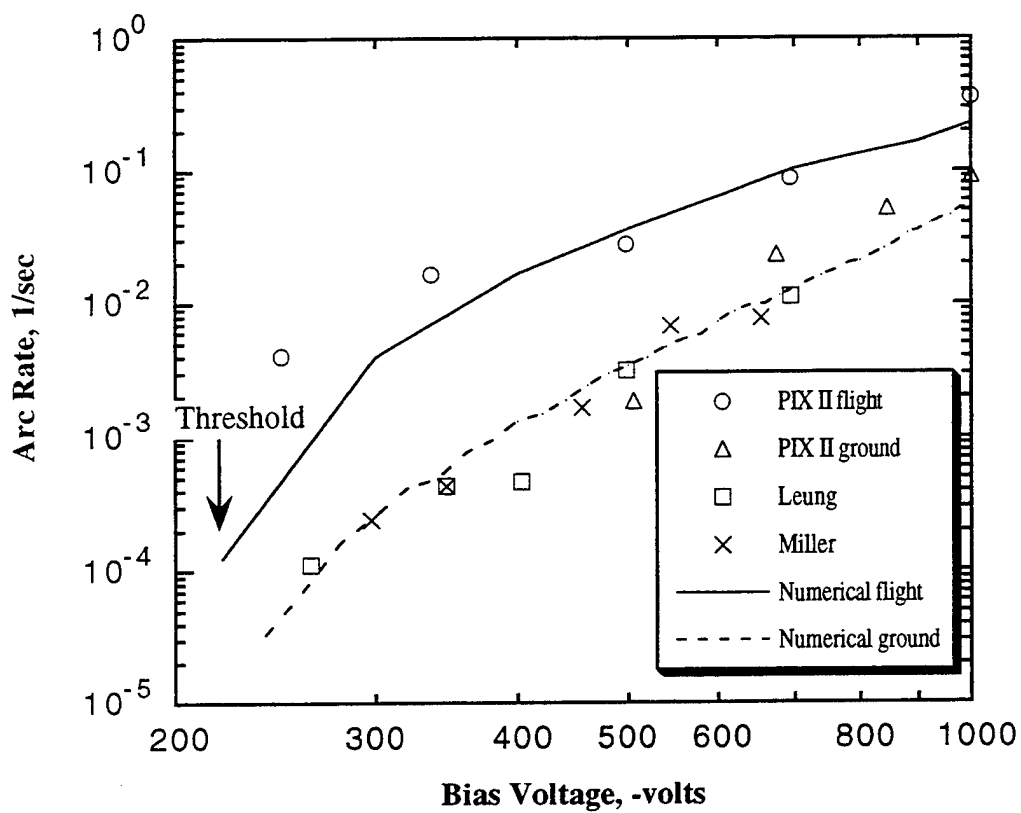
Figure 12: Experimental and Numerical Data for PIX II Flight and Ground Experiments
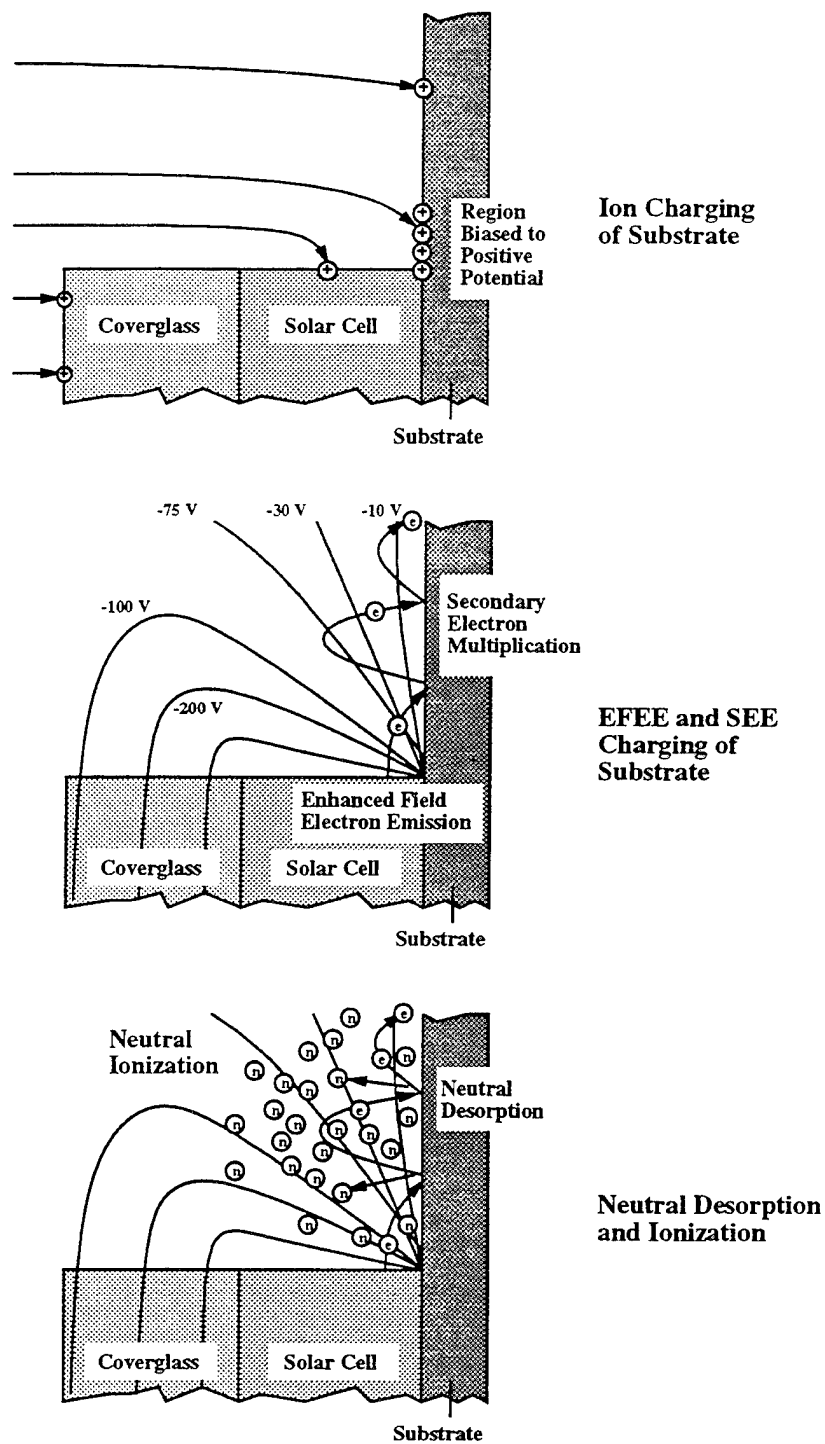
Figure 13: Proposed Arcing Sequence on a High Voltage Wrap-Through-Contact Solar Cell

Chapter 3

Modifications to Semi-Analytic Arc Rate Code

3.1 Arc Rate Code

In the previous chapter, the arc rate code developed by Cho and Hastings was described. This chapter will discuss modifications made to this code to make it more physically accurate and to allow it to accurately model the PASP Plus experiment as the satellite moves through the changing environment of its orbit. A flow chart of the modified code is shown in Figure 14.

The code now has a driver at the front end of the program. This allows the environmental parameters to be defined at one second intervals during the experiment. Thus, when simulating arcing on orbiting spacecraft, the environmental data for the orbit can be set at one second intervals based on either actual data or data generated using environmental models. The bias voltage, experiment time, and cell type are also set in the driver. Output files are then opened. Data from the arc rate simulation can be dumped to these files for one second intervals during the experiment. This was done to match the format of the data for the PASP Plus experiment. This information is then passed to the arcrate subroutine.

The cell data, consisting of cell dimensions and material properties are then read in. Next, the distributions of η, d_i, ξ, C_{diele}, S_{real}, S_{FN}, Q_{ESD}, and β are calculated as before. The distribution of the amount of charge lost from an arc, ΔQ, is now a linear distribution of the percent of charge stored by the dielectric instead of a distribution between two fixed values. The array is then divided into correlated areas based on the discharge wave area.

45
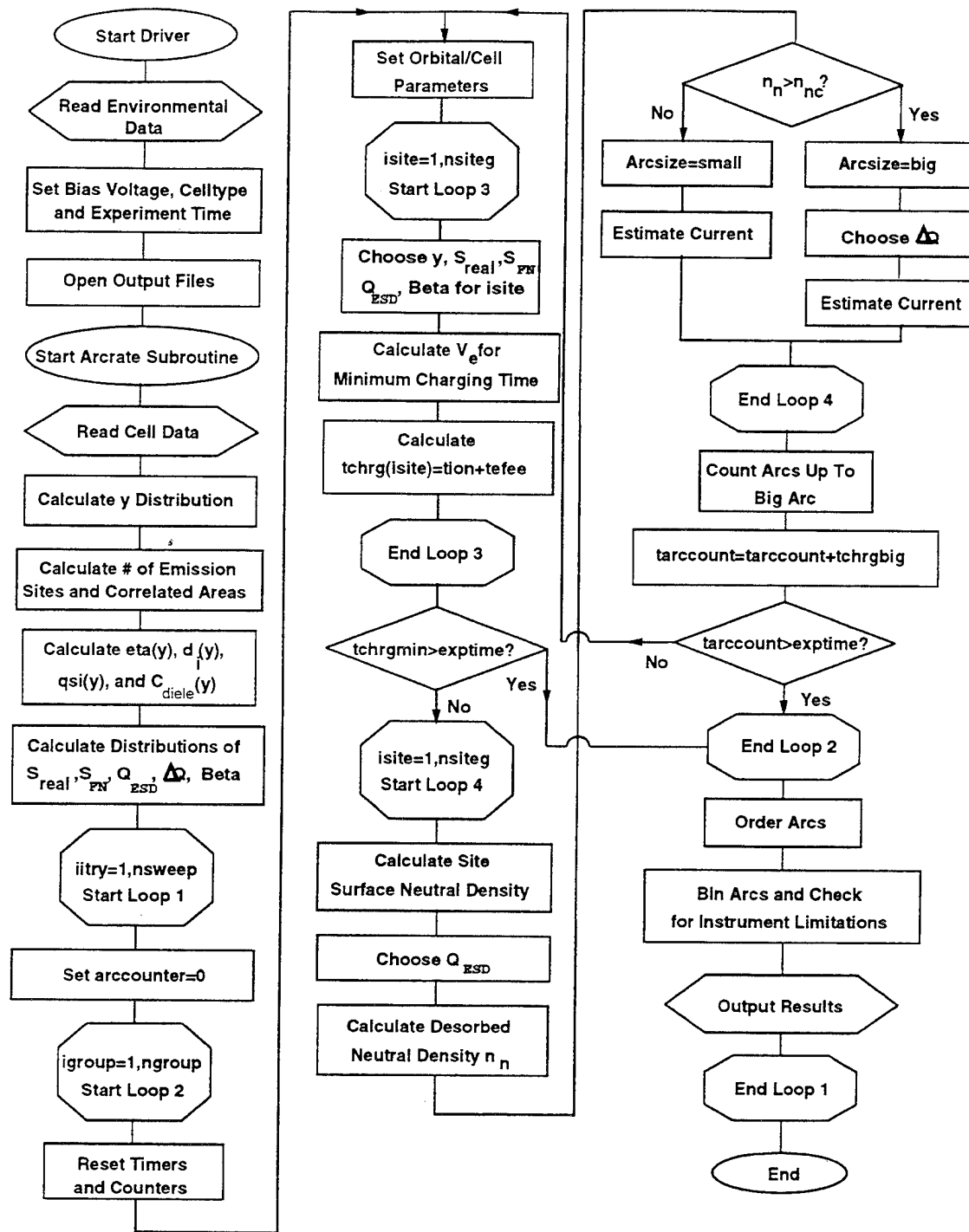
Figure 14: Flow Chart of the Modified Arc Rate Code

The code then loops through these correlated areas. The occurrence of a breakdown discharge at a site in an area will reset the charging process of all other emission sites within that area, but will not affect the charging at sites in the other areas. However, as discussed in Chapter 2, if the desorbed neutral density at the site is not greater than the critical neutral density, breakdown will not occur. A small current pulse, hereafter referred to as a "small arc" will be generated, but no discharge wave will be created. Thus, the charging at the other sites will continue until one of the sites experiences breakdown ("big arc"). Previously, either the small arcs were ignored and only the big arcs were counted, or, as in the work done by Mong and Hastings[62], the neutral density criterion was ignored, resulting breakdown in every case. Now, both big and small arcs are counted, with the sum giving the total arc rate. The results from numerical simulations showed that the current seen from a small arc is on the order of microamps to a few milliamps. Big arcs are typically current pulses on the order of amps. An input current threshold was added to the code to screen out arcs that would be below the level detectable by equipment used in an experiment. For example, the recently flown shuttle based SAMPIE experiment had a detectable current threshold of 20-100 mA[41]. Thus, only big arcs would be seen by this experiment.

3.2   Charging Time Calculation

The charging time for each emission site within the correlated area is then calculated. In previous work by Cho[13] and then by Mong[62], the secondary electron yield of the dielectric was assumed to be constant. This allowed Eq. (20) to be integrated, resulting in a closed form solution for the EFEE charging time given by Eq. (27). The assumption that the secondary electron yield is constant, however, is not physically accurate. As the electric field builds up, the emitted electrons are accelerated to a higher velocity before striking the dielectric surface. This increased velocity results in a higher secondary electron yield. Thus, the secondary electron yield will increase as the EFEE charging takes place. When the equation for the secondary electron yield as a function of the electric field, Eq. (32), is inserted in Eq. (20), a non-linear differential equation results. This equation can not be solved in a closed form as was possible for the case when the secondary electron yield

was assumed to be constant. Thus, the EFEE charging time must now be calculated numerically, using a Runge-Kutta scheme with adaptive stepping[82]. The total charging time for the emission site, τ_{chrg}, is determined by numerically finding the minimum of

$$\tau_{chrg} = \tau_{ion} + \tau_{efee} \tag{78}$$

where τ_{ion} is given by Eq. (36) and τ_{efee} is found by numerically integrating Eq. (20) with the boundary conditions

$$E_{e_{initial}} = \frac{\eta \xi_0 V_e}{d_1 + d_2} \tag{79}$$

and

$$E_{e_{final}} = 2E_{e_{initial}} \tag{80}$$

The choice of the final boundary condition comes from the fact that the field runaway follows the characteristic shape shown in Figure 6, where the field remains almost constant until the runaway time. At the runaway time, the slope of dE/dt becomes nearly infinite. Thus, the final condition for the integration can be assumed to be when the electric field has doubled.

3.3   Neutral Density Criterion

Once the charging time has been calculated for all the emission sites, the breakdown criterion must be judged. To do this, the desorbed neutral density n_n at the site is compared to the critical neutral density n_{n_c}, which was determined by Cho[13] to be approximately $6 \times 10^{21} m^{-3}$. The desorbed neutral density is given by[13] as

$$n_n = 2.08 \frac{N_n Q_{ESD}}{\bar{c}} \frac{\epsilon_0}{e} \sqrt{\frac{2e}{m_e}} \frac{\sqrt{E_{se}}}{E_{se1} d^2} V_e^2 \tag{81}$$

where N_n is the adsorbed neutral density on the dielectric surface before the intensive outgassing due to the EFEE begins, ϵ_0 is the dielectric constant of vacuum, e is the electron charge, m_e is the electron mass, E_{se} is the secondary electron emission energy in eV, E_{se1} is the energy for a secondary electron yield of unity, $d = d_1 + d_2$ is the total dielectric

48

thickness, and $\bar{c}$ is the average speed of the desorbed neutrals, which are assumed to be at the temperature of the dielectric surface T_s, so that

$$\bar{c} = \sqrt{\frac{8\kappa T_s}{\pi m_n}} \tag{82}$$

where m_n is the mass of the neutrals which are assumed to be water. In the previous work by Cho, the adsorbed neutral density N_n was assumed to be at the steady state value determined by the balance of the thermal stimulated desorption of neutrals to the flux of ambient neutrals onto the dielectric surface, found by solving the following equation for N_n

$$k_1^0 N_n exp\left(-\frac{E_d}{\kappa T_s}\right) = n_{na}\frac{\bar{c}}{4}\left(1 - \frac{N_n}{N_{n0}}\right), \tag{83}$$

where k_1^0 is the neutral thermal desorption coefficient, E_d is the adsorption energy, n_{na} is the ambient neutral density, and N_{n0} is the neutral surface density for monolayer coverage of the surface. The term $1 - N_n/N_{n0}$ is an approximation for the probability that a neutral striking the surface will stick. The flux of neutrals onto the surface was assumed to be only due to the thermal flux of ambient neutrals.

In this research, however, the steady state surface neutral density is not assumed, since an arc could occur at a site before the steady state could be reached. Once an arc occurs at a site, the neutrals adsorbed onto the surface must be recharged. Therefore, the change in the surface neutral density with time is given by the difference between the flux of the neutrals from the surface and the flux of neutrals onto the surface that stick

$$\frac{dN_n}{dt} = \left(\Gamma_n + n_{na}\frac{\bar{c}}{4}\right)\left(1 - \frac{N_n}{N_{n0}}\right) - k_1^0 N_n exp\left(-\frac{E_D}{\kappa T_s}\right), \tag{84}$$

where Γ_n is the component of the neutral flux onto the side surface due to the orbital velocity. Since the array may be at a non-zero angle of attack, this is given by

$$\Gamma_n = n_{na}v_{orbit}\sin\alpha, \tag{85}$$

with v_{orbit} being the orbital velocity and α the angle of attack of the arrays to the ram (an angle of attack of 0 corresponds to the spacecraft velocity vector and the vector normal to

the array front surface being parallel). Solving Eq. (84), the surface neutral density, as a function of time, is therefore given by

$$N_n(t) = \frac{C_1}{C_2}\left(1 - e^{-C_2 t}\right) \tag{86}$$

where C_1 and C_2 are given by

$$C_1 = \Gamma_n + n_{na}\frac{\bar{c}}{4} \tag{87}$$

$$C_2 = \frac{C_1}{N_{n0}} + k_1^0 exp\left(-\frac{E_D}{\kappa T_s}\right). \tag{88}$$

The surface neutral density at the time of the arc is calculated from Eq. (86) with the time set to the difference between the time of the arc and the time of the previous arc at that site. This time is the time for which the neutrals have been recharging the surface. If there was no previous arc at the site, the recharging time was set to 1×10^{30}, resulting in the steady state surface neutral density. The ambient neutral density n_{na} was taken to be 100 times the actual ambient density based on numerical work by Cho[13] which found that the neutral gas pressure over the solar cell after an arc was as high as 20 torr when the background density was on the order $< 10^{-3}$ torr, and also due to the neutral density around a spacecraft typically being enhanced by the spacecraft itself.

From Eqs. (86) and (81), it can be seen that the desorbed neutral density is a function of the ambient neutral density, cell temperature, voltage, and electron stimulated desorption cross section Q_{ESD}. Thus, for a given voltage and value of Q_{ESD}, the critical ambient density n_{na_c} needed to result in the desorbed neutral density exceeding the critical density can be determined for various cell temperatures by substituting Eq. (86) into Eq. (81) and solving for n_{na} in steady state, giving

$$n_{na_c} = \frac{k_1^0 N_{n0}\exp(-\frac{E_D}{\kappa T_s})}{(2.08 N_{n0}\frac{Q_{ESD}}{n_{nc}\bar{c}}\frac{\epsilon_0}{e}\sqrt{\frac{2e}{m_e}}\frac{\sqrt{E_{se}}}{E_{se1}d^2}V_e^2 - 1)(v_{orbit}\sin\alpha + \bar{c}/4)} \tag{89}$$

As can be seen, the critical ambient neutral density is a strong function of both cell temperature and bias voltage, as well as the cell thickness and secondary electron emission properties, electron stimulated desorption cross section Q_{ESD}, and the orbital velocity and

angle of attack. Figure 15 shows the critical ambient neutral density needed for breakdown at bias voltages of -100V to -500V and a Q_{ESD} of $1 \times 10^{-19} m^2$ for the APSA solar cells used in the PASP Plus experiment at zero angle of attack. The value of $1 \times 10^{-19} m^2$ for Q_{ESD} was chosen to have the ESD yield $N_n Q_{ESD}$ match experimental values[22]. As can be seen, the ambient neutral density needed to allow breakdown is a strong function of temperature. Conversely, the cell temperature needed to allow a sufficiently large surface neutral density to lead to breakdown can be seen to be a function of ambient neutral density, as well as of voltage and Q_{ESD}. Thus, there exists a critical ambient neutral density above which breakdown will occur at a given cell temperature, and a critical cell temperature above which breakdown will not occur at a given ambient neutral density. The figure also shows that for a given cell temperature, the critical ambient neutral density for breakdown increases with voltage, typically by 1-2 orders of magnitude over the voltage range covered by the PASP Plus experiment. Also apparent is that the critical cell temperature, at a fixed neutral density, also increases substantially with voltage. For the PASP Plus experiment voltages, the critical temperature for arcing could be expected to vary by as much as 50K due to the voltage alone.

Figure 16 shows a comparison of the critical ambient neutral density variation dependence on cell temperature between the different cells biased in the PASP Plus experiment. It shows a slight increase in the critical density with cell thickness, and an increase in critical temperature with decreasing thickness. This assumes, however, that all of the other parameters are equal, which may not be the case. As seen in Figure 17, a change in the ESD parameters can change the critical neutral density by an order of magnitude, or more, and can change the critical cell temperature by tens of degrees. Similarly, from Eq. (89), changes in the secondary electron emission properties or the adsorption properties will also greatly affect the critical neutral density and temperature.

When the solar cells are cold and there is a high ambient neutral density, there is a higher surface neutral density, and therefore a higher desorbed neutral density, which results in a larger probability of breakdown, and thus a larger arc rate. In the limit, all of the possible arcs will have a desorbed neutral density greater than the critical density and will result in breakdown. This is the limit used in the earlier work by Mong[62]. However, when the cells
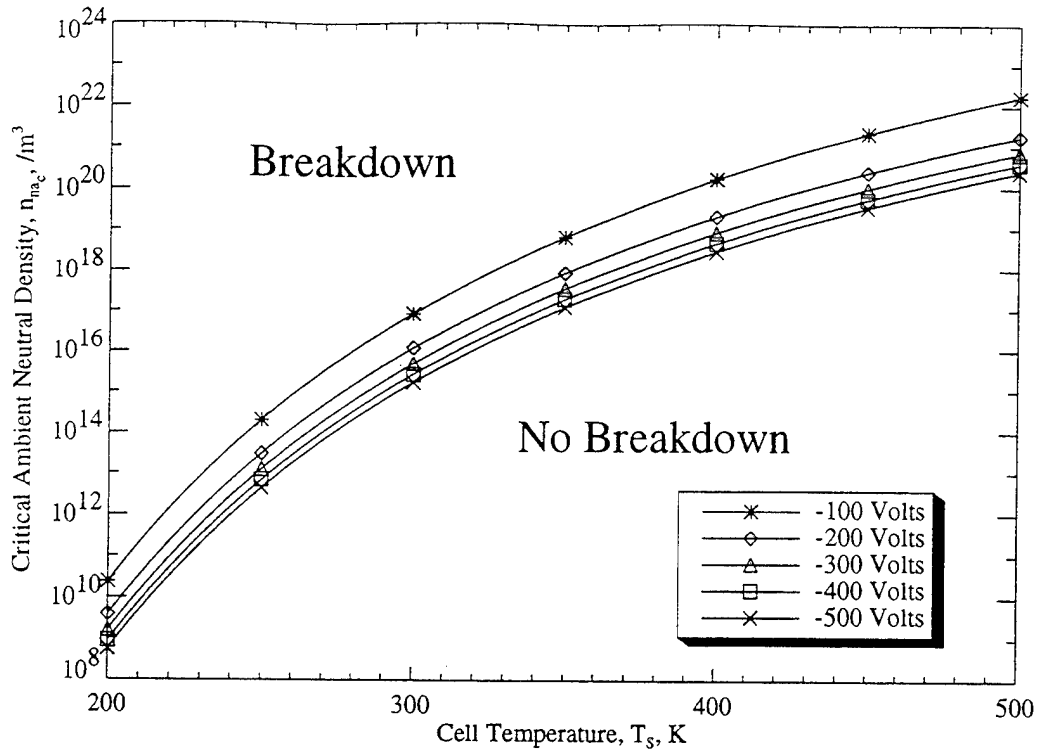
Figure 15: Critical Ambient Neutral Density Variation with Temperature for Varying Bias Voltage

are warm and/or the ambient neutral density is low, many, or all, of the possible arcs will not have a sufficiently large desorbed neutral density to allow breakdown to occur, resulting in a lower arc rate. Figure 18 shows the variation in the simulated average arc rate with temperature for the APSA array on the PASP Plus experiment. The simulation was run with a bias voltage of -300V, a plasma density of $1 \times 10^{10} m^{-3}$, and ambient neutral densities of $3 \times 10^{12} m^{-3}$, $3 \times 10^{13} m^{-3}$, and $3 \times 10^{14} m^{-3}$. At the low cell temperatures, the neutral density has no affect on the arc rate. However, as temperature increases, the arc rate quickly drops for the case with a neutral density of $3 \times 10^{12} m^{-3}$ at a temperature of approximately 260K, becoming zero at 300K. Thus, for this case the critical cell temperature is 300K. As the ambient neutral density increases, the critical temperature increases, reaching 350K at a neutral density of $3 \times 10^{14} m^{-3}$. Thus, while a critical cell temperature is expected for all cells, determining this temperature accurately is difficult without knowing all of the parameters involving in the process.

In the simulation, once the surface neutral density at the arc site is known, a value for Q_{ESD} is randomly chosen from the distribution of Q_{ESD} and the desorbed neutral density is
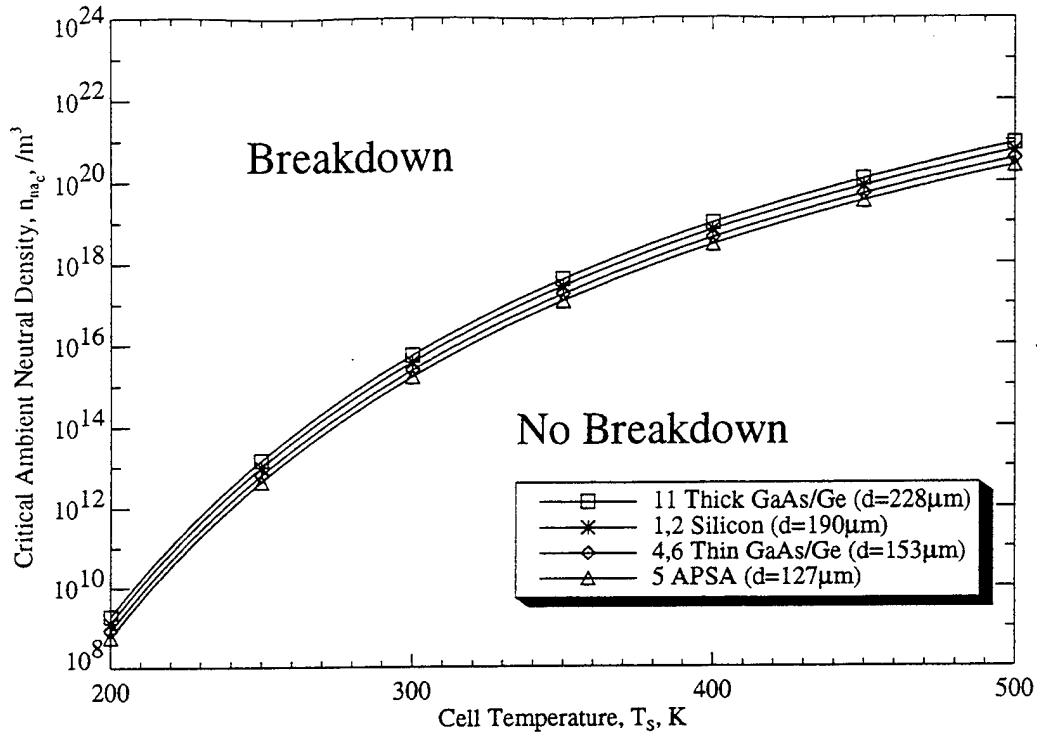
Figure 16: Critical Ambient Neutral Density Variation with Temperature for Varying Cell Thickness

calculated using Eq. (81). This is then compared to the critical neutral density to determine if breakdown occurs (i.e. whether a small or big arc occurs at the site). After the arc size has been determined for all the sites within the correlated area, along with the time of the arcs, all the small arcs up to the first big arc are counted, along with the big arc. Since this big arc resets the charging process at all the sites within the correlated area, the arcs that would have occurred after this first big arc are disregarded and the process is repeated until the time exceeds the experiment duration.

3.4 Total Arc Rate

The arcs from all the correlated areas are then summed to give the total arc count. The code has also been modified to be able to include arc count limitations within the experimental equipment. For example, the PASP Plus transient pulse monitors have an upper count limit of fifteen arcs per second due to software constraints. The final simulated results are
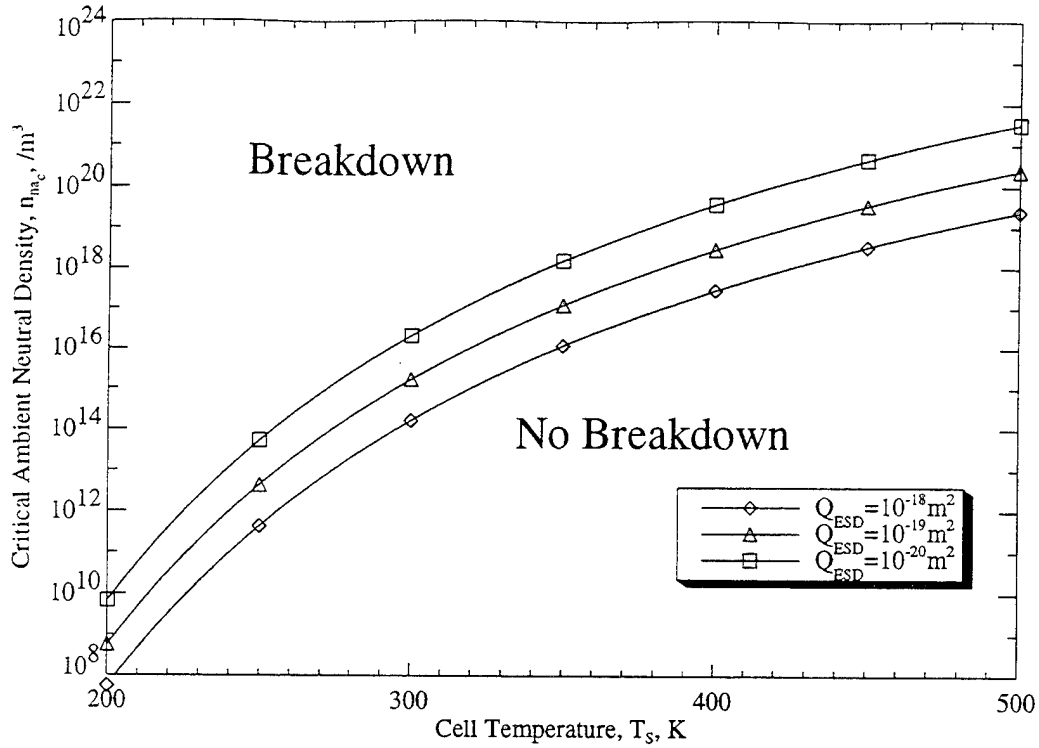
Figure 17: Critical Ambient Neutral Density Variation with Temperature for Varying Q_{ESD}

then output after screening for arc current and arc rate limitations within the experimental equipment. The stochastic nature of the arcing process is represented by the random selection of the parameters during the simulations. Thus, multiple runs of the simulation results in different arc rates. Simulations are typically run one hundred times, giving minimum, maximum, and average arc rates, along with the expected scatter in the data.

This semi-analytic arc rate code can be used to predict the arcing activity of any conventional geometry solar cell in a plasma environment. In the Chapter 5, the results of predictions using this code for the PASP Plus experiment will be discussed. The code was also recently used to predict the arcing on the SAMPIE experiment, with experimental values falling either within or very near the predicted values [92, 79].
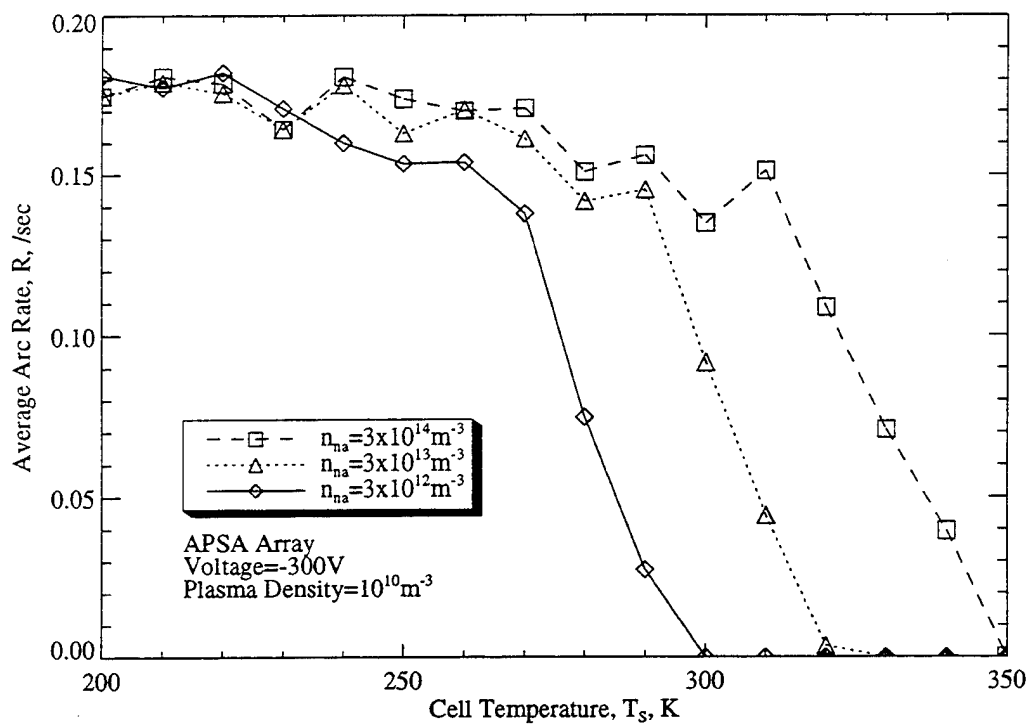
Figure 18: Simulated APSA Array Arc Rate Variation with Cell Temperature at -300V

Chapter 4

PASP Plus Experiment Description

4.1 Background

Spacecraft designers anticipate that future missions will require more survivable, higher powered space systems. This requirement demands more efficient, survivable, and radiation hardened solar array systems operating at higher voltages to minimize the mass requirements and resistive losses in the power distribution subsystem. The interactions of these high voltage arrays with the space plasma and radiation environments need to be clearly understood in order to improve the reliability of the future systems. Because of the complex nature of these interactions, ground simulations are inadequate to accurately quantify the effects of the space environment on the solar array systems. Thus, the Photovoltaic Array Space Power Plus Diagnostics (PASP Plus) experiment was designed by the U.S. Air Force to gather a large base of flight test data to be used to develop an understanding of the interaction of both highly positive and negative biased solar arrays. The experiment was designed to systematically investigate the effects of the space environment on advanced solar arrays.

Initially, PASP Plus was to test only high voltage solar array interactions with the ambient space plasma. Then, in early 1990, the Space and Missile Systems Center's Space Test Program offered the PASP Plus experiment a flight on the Advanced Photovoltaic and Electronics Experiment (APEX), to be launched by a Pegasus launch vehicle. This satellite also has two secondary experiments to study the effects of radiation on electronics: Cosmic Ray Upset Experiment/Cosmic Radiation Effects and Dosimetery Experiment (CRUX/CREDO) and Thin Film Ferroelectric Experiment (FERRO). A description of the

CRUX/CREDO and FERRO experiments is given in Reference 49. Because the APEX satellite was to be placed in a highly elliptical orbit passing through the bottom of the radiation belts, with a one to three year lifetime, the PASP Plus experiment goals were changed to include long term radiation effects on solar arrays[32].

PASP Plus has four main objectives[68]:

(1) Characterize the electrical performance and environmental interaction of a set of advanced solar arrays operating at high voltages in the natural space environment. The plasma leakage current for the arrays at high positive voltages (up to +500V) and the arcing characteristics of the arrays operating at high negative voltages (up to -500V) are to be examined.

(2) Characterize the long-term radiation degradation effects of several advanced solar arrays operating in a harsh space radiation environment.

(3) Determine an environmental cause-and-effect relationship for the impact of the space environment on the operation of solar arrays.

(4) Obtain flight performance data for advanced array designs never before flown.

4.2 Hardware Description

4.2.1 APEX Satellite

The deployed configuration of the APEX satellite is shown in Figure 19. The body of the satellite is a hexagonal cylinder 60 inches tall and 38 inches across (or 44 inches from corner to corner). The top Payload Shelf contains eight solar array modules, three electric field transient pulse monitors (TPMs), the APEX sun sensor, one calorimeter and two quartz crystal microbalances (QCMs). Extending up from the Payload Shelf are two 2-foot booms. On one boom is the langmuir probe head, and on the other is APEX magnetometer, which is used for satellite attitude control. Under the Payload Shelf is the Avionics Shelf, which contains electronics boxes and the CRUX/CREDO and FERRO experiments. The satellite

has four deployed panels attached to the top shelf. Three of these panels contain the solar arrays used for spacecraft power, while the fourth Deployed Panel contains the remaining PASP Plus solar array modules and diagnostic sensors. There is one TPM, one calorimeter, one QCM, and the PASP Plus sun sensor on the Panel. The satellite is three-axis stabilized and is sun pointing to within ±0.5 degrees. Thus, the solar arrays are at varying angles of attack to the ram plasma flux as the satellite moves around it's orbit. Because the langmuir probe head is two feet away from the shelf, the plasma density recorded by the probe while the array modules are in wake does not match that at the location of the modules[32].

4.2.2   Diagnostic Equipment Description

The PASP Plus experiment is controlled by a microprocessor controller, which contains all of the electronics for the solar cell biasing and data acquisition and telemetry. The controller distributes power and commands from APEX to all of the instruments, except for the dosimeter, and receives, processes, and sends the data from the instruments to the satellite. The data is then stored for later transmission to a ground station, or sent down real-time. The dosimeter has its own interface for power, command, and data transmission to and from the satellite[32].

Diagnostic sensors for the PASP Plus experiment include[86]:

(1) Sun sensor to measure the incident angle of the solar energy.

(2) Langmuir probe to measure the plasma temperature and density. The probe also has a potential sensor (SENPOT) to sense and compensate for the vehicle frame potential, which may be more negative than the space plasma potential. The Langmuir probe can measure plasma densities of 10^8 to $10^{12} m^{-3}$, and plasma temperatures of 1000° to 8000° K, with debye lengths of 2.2 mm to 62 cm, at spacecraft potentials of 2 V to -30 V[21].

(3) Four transient pulse monitors (TPMs) to detect and fully characterize (amplitude, rise time, integral, and number of pulses per second) the arc discharges that occur during the negative biasing portion of the experiment[18]. These monitors have a rate limitation of 15 arcs/second. There is also one sensor on the high voltage power line inside the controller.

59

Table 1: PASP Plus TPM Settings

Setting	Telemetry Counts	E-Field Threshold	In-Line Sensor Threshold
0	5	10 V/m	6 mA
1	55	45 V/m	30 mA
2	105	225 V/m	140 mA
3	155	700 V/m	420 mA

The minimum electric field pulse counted by the TPMs can be chosen from the levels in Table 1. The TPMs can measure peak electric fields from $10V/m$ to $5000V/m$, with rates of rise from $3 \times 10^9 V/sm$ to $1 \times 10^{12} V/sm$, and integrals of $8 \times 10^{-6} Vs/m$ to $6 \times 10^{-3} Vs/m$. The peak currents detectable are $3mA$ to $1.4A$, with rates of rise of $7 \times 10^5 A/s$ to $3 \times 10^8 A/s$, and integrals of $2 \times 10^{-9} As$ to $2 \times 10^{-6} As$. The approximate pulse width limits are $5ns$ to $5\mu s$ with rise time limits of $1ns$ to $2\mu s$, and an effective bandwidth of approximately 200 MHz.

(4) Electrostatic analyzer (ESA) to measure the 30 eV to 30 keV electron/ion spectra and detect the passage of the spacecraft through the auroral region. The ESA has four heads: two for ions and two for electrons. The instrument can measure one ion and electron spectrum per second, with an energy resolution of 10%. The number flux range measurable is 10^5 to $10^{10}/cm^2 \cdot s \cdot ster$, integrated, at integrated energy fluxes of 10^5 to $10^{10} keV/cm^2 \cdot s \cdot ster$[21].

(5) Dosimeter to measure the short and long term ionizing particle (electron and ion) radiation flux and dosage.

(6) Contamination monitors to measure the amount and effect of molecular and particulate contamination on the array surfaces. Two types of monitors will be used. Quartz Crystal Microbalances (QCMs) will be used to measure the mass of contamination being deposited on the surface, while Thermal Coated Calorimeters will determine the optical degradation of the coverglass through α/ϵ measurements.

(7) Temperature sensors to measure the temperature of the arrays.

In addition, an electron emitter will be available to emit a stream of electrons to alter the spacecraft potential. This will allow the experiment to more accurately simulate the positive bias voltage operation of large functional arrays.
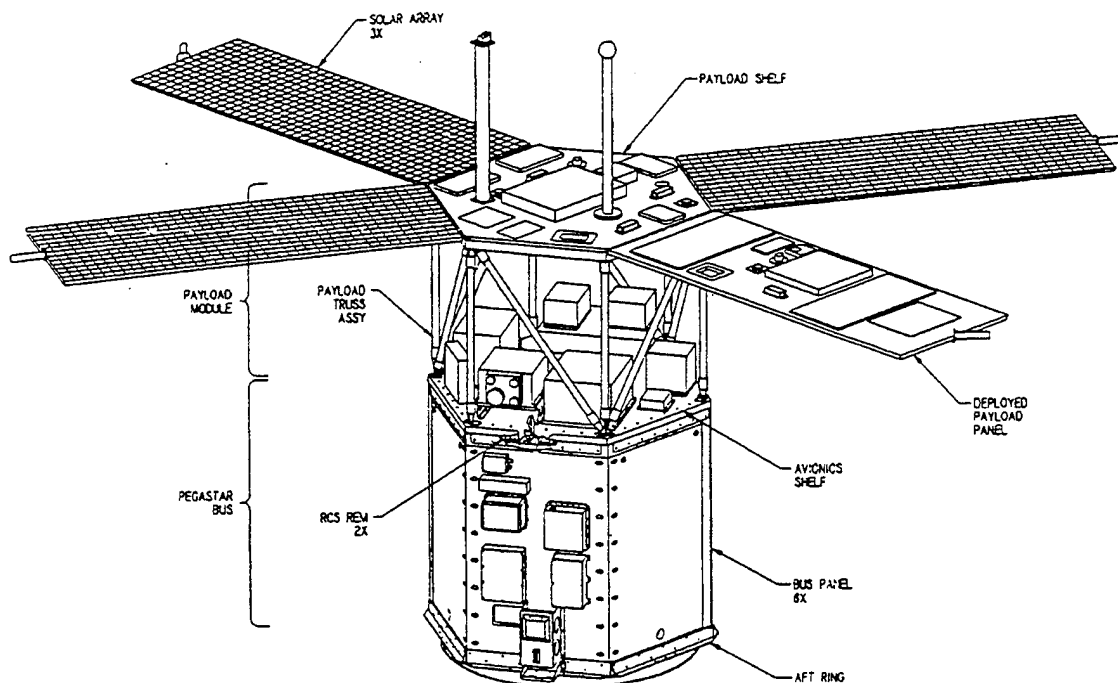
Figure 19: Deployed Apex Spacecraft with PASP Plus Experiment

4.2.3 Solar Array Module Descriptions

There are seventeen arrays of twelve different types being flown on the Payload Shelf and Deployed Panel of the spacecraft. Since there are only sixteen electrical channels, one of the arrays is not being used. Ten of these arrays are subject to high voltage biasing. The information for these arrays are taken from References 1 and 62. The array modules are numbered from 0 to 15 for identification. Arrays #0, #1 and #2 are conventional silicon solar cells. Module #3 is made up of silicon wrap-through-contact (WTC) cells designed for the Space Station. Arrays #4 and #6 are Applied Solar Energy Corporation's (ASEC) gallium arsenide/germanium (GaAs/Ge) conventional cells. TRW's APSA cells make up array #5 (previously labeled array #36). The advanced solar cells of AlGaAs/GaAs Monolithic MBG are on array #7. Array #8 is made of Spectrolab's GaAs/Ge WTC cells. Amorphous silicon cells developed by TRW and Solarex are located in module #9. Array #10 contains advanced indium phosphate (InP) cells. Spectrolab's conventional GaAs/Ge
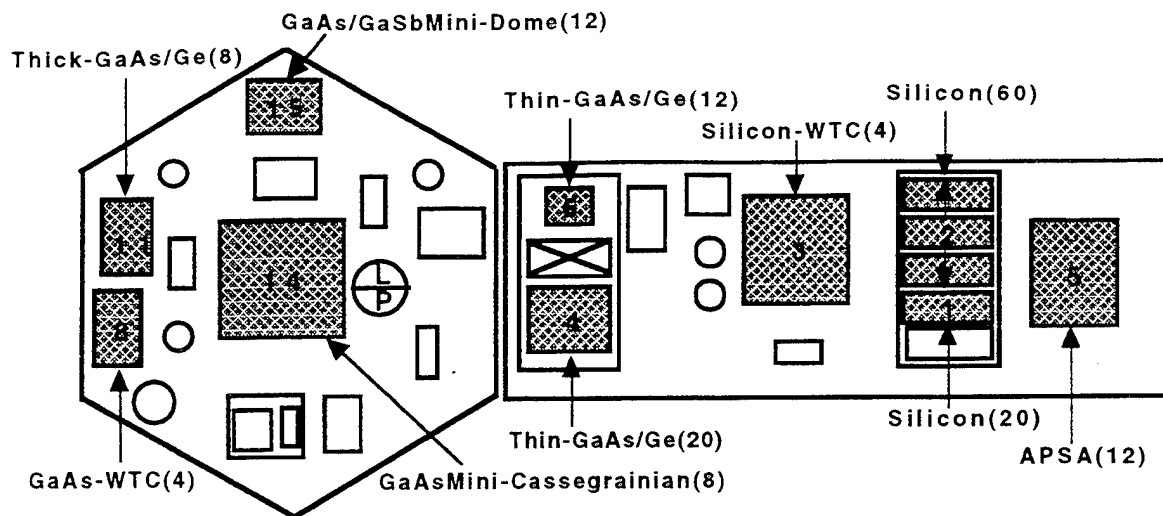
Figure 20: PASP Plus Solar Array Module Locations

cells are in array #11. Modules #12 and #13 are made up of Boeing's GaAs/CuInSe MBG cells. Two concentrator designs are being flown in modules #14 and #15. Module #14 is the Mini-Cassegranian GaAs cell from TRW, while module #15 contains the Boeing Mini-Dome Fresnel Concentrator. Of these, modules #1, 2, 3, 4, 5, 6, 8, 11, 14, and 15 are the arrays subject to high voltage biasing. Figure 20 shows the location of each module on the Payload Shelf and Deployed Panel. The number in parentheses beside the array name is the number of cells in the module. The arc rate simulation was run for the conventional geometry cells (arrays #1, 2, 4, 5, 6, and 11), and will be discussed in the next two chapters.

The biased conventional silicon cell arrays #1 and #2 are representative of virtually all of the arrays flying on DoD, NASA, and commercial spacecraft today. The cells were manufactured by Spectrolab Inc. and incorporated into an array by RCA in 1984. In addition to the objectives stated above, these cells will also be compared to the well documented degradation characteristics of Si to insure the accuracy of the dosimeter readings. The silicon cells are 2cm×4cm and 203μm thick. The coverglass is fused silica bonded to the cell with Dow Corning adhesive DC-93500, with estimated thicknesses of 153μm and 37μm, respectively. The interconnector is assumed to be Kovar with an estimated work function of 4.76 eV. The cells are bonded to a layer of Kapton atop a thin metallic foil interlayer. The substrate is a 0.5" thick 10"×20" aluminum honeycomb structure with graphite/epoxy face sheets. The string measured efficiency, based on cell area, is 14.4% AM0. Array #1

62

contains twenty cells in series, while array #2 has sixty cells contained in three strings of twenty. Thus, differences in the arc rates between these arrays will help give the relationship between arcing and the number of cells. Both of these modules are located next to each other on the Deployed Panel, with module #1 located near the center of the panel, and module #2 located near the side edge.

A much thinner conventional geometry silicon cell design is being tested by the TRW Advanced Photovoltaic Solar Array (APSA) cells in module #5. The thin cells hold a large promise for future use due to the mass cost savings they yield. The beginning-of-life (BOL) specific power and area density performance of a 5.8kW APSA wing, including everything from the gimbal out, are 138 W/kg and 135 W/m^2. The cells are 2.6cm×5.1cm with a thickness of only 63.5μm (2.5 mil) thick. More importantly for arcing considerations, the CMX coverglass thickness is only 51μm (2 mil) and the DC-93500 adhesive is estimated to be 76μm thick. The interconnector is silver plated invar, so the relevant work function is that of silver, which is 4.26 eV. The cells are bonded to a flexible Kapton substrate, which has a 1500 angstrom coating of germanium for atomic oxygen protection. The module is mounted over a cutout on the Deployed Panel, in the center of the panel near the outer edge. This position makes this module the farthest from any TPM, which may result in fewer of its arcs being detected by the monitors. The measured efficiency of the array is 12.9% AM0. The module is made up of twelve APSA cells. Examination of the arc rate of these cells will give insight into the relationship between arcing and cell thickness for silicon cells.

Modules #4 and #6 contain thin GaAs/Ge conventional geometry cells, which are high efficiency, radiation resistant cells produced by the Applied Solar Energy Corporation. These contain 4cm×4cm, 76μm (3.5 mil) cells with 102μm (6 mil) thick CMX coverglasses. The DC-93500 adhesive thickness is estimated to be 51μm thick. The interconnector is also silver plated invar. The advantage of this type of cell arises from the ability to make the inactive germanium substrate thin while maintaining adequate strength. Germanium has a minimum fracture toughness twice that of gallium arsenide. The measured string efficiency for these modules is 19.1% AM0. Array #4 contains four parallel strings of five cells, while array #6 has three parallel strings of four. Thus, these modules will also allow

the dependence of arcing on array area to be examined. Both of these modules are located on the Deployed panel, near the Payload Shelf.

Module #11 has thick GaAs/Ge conventional geometry cells made by Spectrolab Inc. These cells are 4cm×4cm, $178\mu m$ (7 mil) thick, with $152\mu m$ (6 mil) thick coverglasses. The adhesive thickness is estimated to be $76\mu m$ (3 mil). Thus, these cells have a much thicker dielectric layer than the GaAs/Ge cells in modules #4 and #6. The measured performance of the module is 19.2% AM0. There are two strings of four cells each in the module, which is located on the Payload Shelf. By comparing the results from this module with modules #4 and #6, the relationship between arcing and dielectric thickness for the GaAs/Ge cells can be examined.

There are also two modules of wrap-through-contact (WTC) cells being subjected to high voltage biasing in the PASP Plus experiment. Module #3 contains silicon WTC Space Station cells manufactured by Spectrolab Inc. These large (8cm×8cm) cells are mounted on a flexible Kapton blanket and placed over a cutout on the Deployed Panel, similar to the configuration to be used on the Space Station. The Kapton blanket is used to ease manufacturing, reduce array cost in terms of dollars/watt, and results in relatively high specific power (66W/kg). The Space Station array design calls for a beginning-of-life operation at 161.1 V, which shows the need for investigation of the interactions of high voltage solar arrays with the space environment. The measured module performance of the silicon WTC module based on cell area is 13.0% AM0 efficiency.

The second type of wrap-through-contact solar cell being tested on PASP Plus is the GaAs/Ge WTC cell in module #8, also manufactured by Spectrolab Inc. The cell design is identical to that of the GaAs/Ge cells in module #11, with the exception of the wrap-through contacts (see Figures 1 and 2). This module contains four cells in series, with a measured performance of 17.2% AM0, and is located on the Payload Shelf. As discussed in Section 2.7, the wrap-through-contact design is expected to show less arcing than the conventional geometry cells, although it still has a possible arcing mechanism and has been seen to arc on other experiments.

PASP Plus is also biasing two concentrator modules. Concentrator arrays show promise

for use on satellites experiencing high radiation exposure and/or require small solar array areas. The concentrators shield the photovoltaic material from radiation flux and also improve cell performance and cost efficiency. As the concentration of solar illumination is increased, the cell current increases proportionally and the open circuit voltage, V_{oc}, increases slightly. This increase in V_{oc} results in an increased cell efficiency. Because the cells are covered by the concentrators, and thus not directly exposed to the space plasma, it is expected that concentrator arrays would not be susceptible to arcing at high voltages.

Module #14 has eight GaAs mini-Cassegrainian concentrators, one of which was bypassed due to intermittent cell interconnect problems. The mini-Cassegrainian is a double-pass reflective concentrator, which focuses sunlight onto the GaAs cells with an effective concentration ratio of approximately 90x. The concentrator is made up of a group of shallow elements whose height yields a concentrator panel thickness that corresponds to that of a conventional rigid planar solar array. The optical elements include a primary parabolic reflector, a secondary hyperbolic reflector and a conical reflector surrounding the cell to focus any deviant light, shown in Figures 21 and 22. Development of a hardened version of the mini-Cassegrainian concentrator was discontinued by the Air Force and SDIO in 1990, so the are no plans to deploy this specific design. However, the module is being flown and biased to test the interaction of mirror concentrator arrays, in general, with the space environment. When tested in 1985, this module had a maximum power of 2.2W at 7.0V. The intermittent electrical problems with the module made it difficult to accurately state a conversion efficiency. The module is located on the Payload Shelf.

The second concentrator array being flown is the GaAs/GaSb mini-dome Fresnel lens concentrator module #15. The multi-junction GaAs/GaSb cells hold promise for increased performance and reduced cost. The module contains 12 cells and is located on the Payload Shelf. This module has a measured efficiency based on the total module area of 20.9% AM0.

Other solar array modules that are being flown on PASP Plus to test long-term radiation effects only, and thus will not be biased, include a monolithic AlGaAs/GaAs module (#7), amorphous silicon module (#9), indium phosphide module (#10), and two GaAs/CuInSe$_2$ mechanical stack modules (#12 and #13).
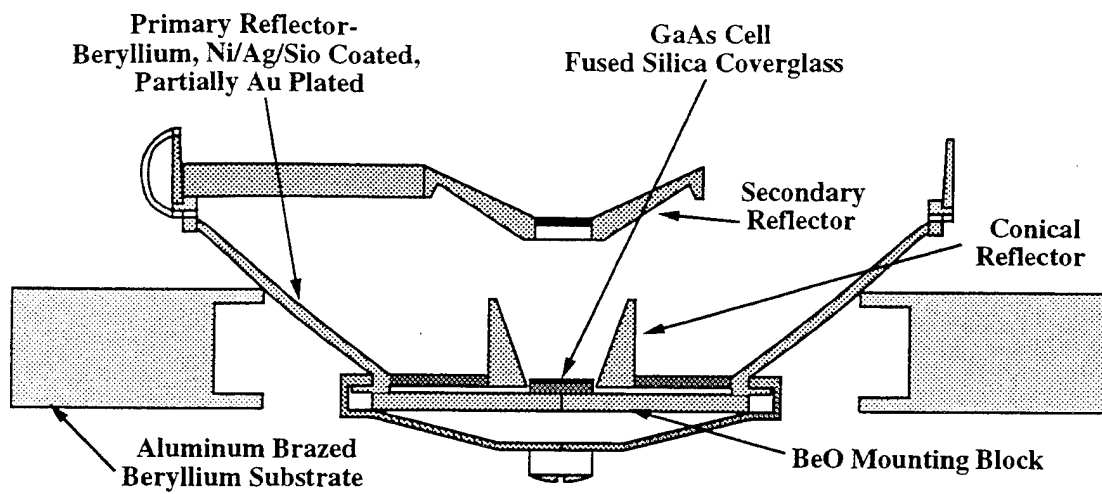
Figure 21: Cross Section of GaAs Mini-Cassegrainian Concentrator Module #14
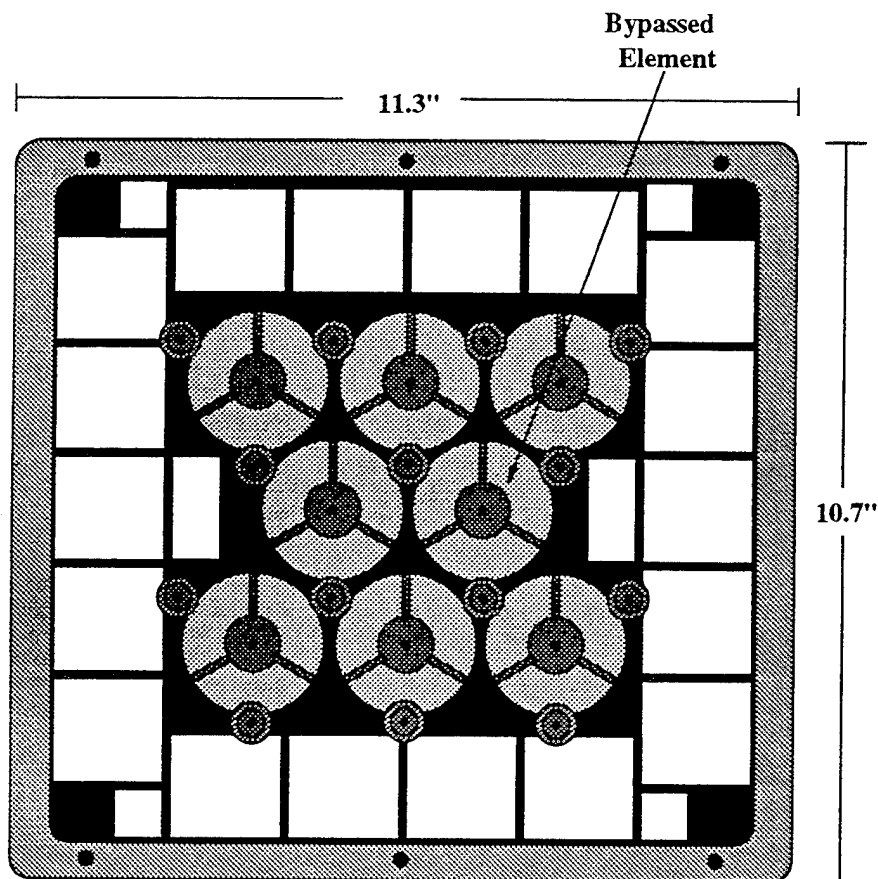
Figure 22: Plan View of GaAs Mini-Cassegrainian Concentrator Module #14

Table 2: PASP Plus Cell Data

Instrument No.	1, 2	3	4, 6	8	11	5 (36)
Cell Type	Si	Si WTC	GaAs/Ge	GaAs/Ge WTC	GaAs/Ge	APSA
Manufacturer	RCA	NASA	ASEC	Spectrolab	Spectrolab	TRW
Cell Size (cm^2)	2x4	8x8	4x4	4x4	4x4	2.6x5.1
No. of Cells	20, 60	4	20, 12	4	8	12
Cell Gap (μm)	500	1000	500	1000	500	635
d_{cell} (μm)	203	203	89	178	178	56
d_1 (μm)	153	203	102	152	152	51
d_2 (μm)	37	N/A	51	N/A	76	76
ϵ_{d_1}	3.5	4	4	4	4	4
ϵ_{d_2}	2.7	3	2.7	3	2.7	2.7
γ_{max_1}	3.46	4	4	4	4	4
γ_{max_2}	3	2	3	2	3	3
E_{max_1} (eV)	330	400	400	400	400	400
E_{max_2} (eV)	300	200	300	200	300	300
ϕ_w (eV)	4.76	4.85	4.26	4.5	4.26	4.26

Table 2 summarizes the given and assumed cell properties for the conventional and wrap-through-contact cells biased during the PASP Plus experiment.

4.3 PASP Plus Testing and Satellite Integration

The PASP Plus solar array modules were integrated into the Payload Shelf and Deployed Panel by NASA Lewis Research Center. Thermal-vacuum tests with simulated-sun illumination of the Shelf and Panel were conducted at the Boeing large-chamber test facility at Kent, WA, in June/July 1992[32]. During the tests, current-voltage (I-V) curves were obtained for the arrays under simulated coming out of eclipse temperature and solar illumination conditions[15]. The entire PASP Plus experiment was then sent to Orbital Sciences Corp.(OSC), who built the APEX satellite, in July 1992. Integration of the PASP Plus experiment onto the satellite was delayed until the spring and summer of 1993 because of various APEX fabrication and software problems[32].

Extensive environmental and performance testing of the spacecraft and experiments were then carried out. After integration of the PASP Plus hardware onto the APEX satellite, comprehensive performance tests were run on all of the hardware in the clean room at

OSC on March 26, 1993[69]. The dosimeter was tested separately from the the rest of the equipment. Pre-environmental testing comprehensive performance tests were conducted December 4, 1993[70]. Pre-pyro-shock limited performance tests were done on January 20 and 21, 1994[72]. Pre-thermal-vacuum limited performance tests were conducted on the satellite without the deployed panel on February 15, 1994[73], and pre-vibration limited performance tests were done on the entire satellite on March 12 and 14, 1994[74]. The final comprehensive performance tests at OSC were conducted on April 8, 1994[71].

The satellite was then shipped to Edwards AFB, CA, where it was integrated into a standard Pegasus launch vehicle. Limited performance tests were conducted on the hardware, as received, on May 26, 1994[75]. The dosimeter then received limited performance testing on June 23, 1994 and the rest of the PASP experiment underwent limited performance testing on June 25, 1994[75]. The launch failure of the first Pegasus XL, carrying the STEP-1 satellite, from the OSC L-1011 aircraft delayed the launch of the APEX satellite through July[32].

Some ground testing of the arcing onset voltages of the PASP Plus modules was performed by Norm Grier at NASA Lewis[31]. Testing was done both with the array back plate grounded and floating. On January 29, 1993, modules #3, #5, #11, and #14 were tested with two plasma conditions. The first was at a density n_e of $5 \times 10^{11} m^{-3}$, electron temperature T_e of 0.7eV and ion temperature T_i of 0.2eV. Module #3 arced at -500V both when grounded and floating. Module #5 arced at -210V when grounded and -250V when floating. Array #14 arced at -350V when grounded and -450V when floating, and array #11 arced at -200V when grounded and -320V when floating. Modules #3, #8, #11, and #14 were then tested on February 12, 1993, with a plasma density of $4 \times 10^{11} m^{-3}$, electron temperature of 0.5eV and ion temperature of 0.1eV. Array #3 then arced at -500V, array #8 at -316V, array #11 at -490V and array #14 at -215V. The last set of tests were conducted on February 18, 1993, on modules #1, #2, #4, #5, #6 at four different conditions: 1) $n_e = 5 \times 10^{11} m^{-3}$, $T_e = 0.7eV$, and $T_i = 0.2eV$, 2) $n_e = 5 \times 10^{11} m^{-3}$, $T_e = 0.6eV$, and $T_i = 0.1eV$, 3) $n_e = 2 \times 10^{12} m^{-3}$, $T_e = 0.9eV$, and $T_i = 0.2eV$, and 4) $n_e = 4 \times 10^{11} m^{-3}$, $T_e = 0.8eV$, and $T_i = 0.2eV$. In these tests, module #1 arced at -141V, module #2 arced at -175V, module #4 at -215V, module #5 at -300V, and module #6 at -168V. These results

show the difficulty in achieving good results from ground testing. Module #1, which has one third as many cells as module #2, arced at a bias voltage 34V lower than module #2, and array #6, which is just over half as large as array #4, arced at a voltage 47V lower than array #6.

4.4   APEX Launch and Orbit

On August 3, 1994, the APEX satellite was launched into orbit by a three-stage solid-fuel Pegasus rocket released from the NASA B-52 aircraft within the Western Test Range off of the coast of California. The launch occurred without problems, as did the satellite's lock onto the sun and the deployment of the four panels. The satellite was placed into a 70° inclination, 363×2550 km orbit, which has an apogee higher than the baselined 1950 km apogee. This higher altitude allows the satellite to traverse farther into the radiation belts, allowing the radiation effects portion of the experiment to be performed in roughly half of the time originally needed[32]. The orbital parameters, as of February 9, 1995, are as follows:

Epoch :	1995+40+13:11:29.00
Semi-Major Axis:	2.566E+7 ft
Eccentricity:	0.1392
Inclination:	69.97^o
Right Ascension:	275.9^o
Argument of Perigee:	318.4^o
Mean Anomaly:	144.4^o

This corresponds to a perigee altitude of 353.82 km, apogee altitude of 2530.9 km, and an orbital period of 114.71 minutes. After 150 days on orbit, it was noticed that the perigee of the orbit was increasing and the apogee was decreasing. Analysis and simulations were performed by Radex, Inc., and it was determined that this was due to the third geopotential

Table 3: PASP Plus Bias Sequences

Seq No.	Step 0	Step 1	Step 2	Step 3
0	safe	safe	safe	safe
1	75	100	125	150
2	200	240	280	320
3	360	400	450	500
4	200	300	400	500
5	160	180	200	220
6	240	260	280	300
7	prog.	prog.	prog.	prog.

term, J_3, which tends to make the altitude go slightly higher in the south and lower in the north. The combination of the J_3 effect with effects from variations is the earth ellipsoid, which are of about the same magnitude, results in the orbital altitudes having a strange pattern in time, producing the noticed effect[59].

4.5   PASP Plus Experiment Operations

After the turn-on and checkout of the APEX spacecraft after launch and initial I-V curve measurements, PASP Plus experimental operations began on August 8, 1994 (day 94220), with positive biasing of the solar array modules. In both the positive and negative biasing, each array to be tested is biased in a sequence of four bias steps each lasting 23 seconds, with each step preceded by an I-V curve measurement on the module being tested, an I-V curve of one of the other 16 modules, and a Langmuir probe measurement of the plasma density and temperature[32]. The modules to be tested are biased in descending numerical order using one of the sequences shown in Table 3. Sequence 0 is no biasing ("safe mode") and sequence 7 is programmable. The biased arrays can be either shorted or at optimum load. The other mode of experimental operation is the I-V Curves Only mode, which produces one I-V curve for each of the modules in 8 minutes.

Positive biasing was conducted from August 8 until August 18 (day 94230) on all of the arrays with voltages from +75V to +500V, except for the APSA arrays, which are not to exceed ±300V. In this phase of the experiment, biasing was carried out ±20 minutes around

70

perigee in order to have a high plasma density during the experiments, and the electron emitter was turned on every third orbit. The positive biasing was followed by three days of I-V Only operations, from August 19-21, 1994.

Negative biasing of the modules to be tested began on August 22, 1994 (day 94234). This initial negative biasing phase continued until September 3, 1994 (day 94246), with biasing from -75V to -450V being done on all arrays except #5, which was biased up to -300V. The negative bias schedule for these days is shown in Table 4. The biasing up to -220V (days 94234-94237) was done from ± 20 minutes of perigee. At this point, high levels of arcing were seen, especially on the APSA module #5, while in eclipse when the cells were cold[76]. As discussed in Section 3.3, this was expected, since the cold cells have a higher surface neutral density, which results in a higher desorbed neutral density and higher probability of breakdown. Because of concerns over damaging the PASP Plus experiment in this early phase, the decision was made to continue performing negative biasing only from 15 minutes after exiting penumbra to 1 minute prior to entering penumbra[76]. Thus, the negative biasing from -240V to -450V (days 94240-94246) was conducted only in sunlight, when the cells were hot. Upon biasing at -450V, the transient pulse monitors became saturated. It was decided that this was due to fluctuations in the power supply and not arcing, and therefore biasing was continued only up to -430V[76].

PASP Plus was set to operate in I-V Curves Only mode from September 4 to October 10, 1994, since this period had the modules in wake while at low altitude (where the plasma density is high). Positive biasing was then continued from October 10-16, 1994, at +100V to +300V, where it was thought that the most interesting aspects of snapover were occurring. At the low positive voltages, current leakage is confined to the interconnects. At higher positive voltages, electrons striking the coverglass produce secondary electrons, causing the coverglass to become positively charged. The coverglass then attracts and collects more electrons, increasing the leakage current. Eventually, leakage current collection takes place over the entire array front surface[32].

Negative biasing was then carried out from October 17-22, 1994 (days 94290-94295), with the arrays biased from -160V to -400V, shown in Table 5. The APEX orbit during this time

Table 4: PASP Plus Bias Sequences for Days 94234-94246

Day	Sequence	-Voltage	Arrays
94234	-Seq 1, Short	75,100,125,150	1,2,4,6,11
94235	-Seq 1, Short	75,100,125,150	3,5,8,14,15
94236	-Seq 5, Short	160,180,200,220	1,2,4,6,11
94237	-Seq 5, Short	160,180,200,220	3,5,8,14,15
94240	-Seq 6, Short	240,260,280,300	1,2,4,6,11
94241	-Seq 6, Short	240,260,280,300	3,5,8,14,15
94242	-Seq 7, Short	320,340,360,380	1,2,4,6,11
	-Seq 6, Short	240,260,280,300	1,2,4,6,11
94243	-Seq 7, Short	320,340,360,380	3,8,14,15
	-Seq 7, Short	250,270,290,300	5
94244	-Seq 7, Short	320,340,360,380	4,6,11
	-Seq 7, Short	270,290,310,330	1,2
94245	-Seq 7, Short	390,410,430,450	3,8,14,15
	-Seq 7, Short	250,270,290,300	5
half	-Seq 7, Short	320,340,360,380	4,6,11
	-Seq 7, Short	270,290,310,330	1,2
half	-Seq 7, Short	390,410,430,420	3,8,14,15
	-Seq 7, Short	250,270,290,300	5
94246	-Seq 7, Short	390,410,430,420	4,6,11
	-Seq 7, Short	340,350,360,370	1,2
	-Seq 7, Short	340,350,360,370	1,2,4,6,11

Table 5: PASP Plus Bias Sequences for Days 94290-94295,94304-308

Day	Sequence	-Voltage	Arrays
94290	-Seq 5, Short	160,180,200,220	1,2,4,6,11
94291	-Seq 5, Short	160,180,200,220	1,2,4,6,11
	-Seq 6, Short	240,260,280,300	3,5,8,14,15
94292	-Seq 6, Short	240,260,280,300	1,2,4,6,11
	-Seq 6, Short	240,260,280,300	3,5,8,14,15
94293	-Seq 6, Short	240,260,280,300	1,2,4,6,11
	-Seq 7, Short	310,330,350,370	3,8,14,15
	-Seq 7, Short	290,290,290,290	5
94294	-Seq 7, Short	310,330,350,370	3,8,14,15
	-Seq 7, Short	290,290,290,290	5
	-Seq 7, Short	320,340,360,380	1,2,4,6,11
94295	-Seq 7, Short	320,340,360,380	1,2,4,6,11
	-Seq 7, Short	340,360,380,400	3,8,14,15
	-Seq 6, Short	240,260,280,300	5
94304	-Seq 5, Short	160,180,200,220	4,5,6,11
94305	-Seq 5, Short	160,180,200,220	1,5,6,11
	-Seq 5, Short	160,180,200,220	2,3,8
94306	-Seq 5, Short	160,180,200,220	1,2,3,8
	-Seq 6, Short	240,260,280,300	4,5,6,11
94307	-Seq 6, Short	240,260,280,300	4,5,6,11
	-Seq 6, Short	240,260,280,300	1,2,3,8
94308	-Seq 6, Short	240,260,280,300	1,2,3,8
	-Seq 7, Short	310,330,350,370	4,6,11

was in a non-eclipse orientation, so the cells were always hot when biased, gathering a large number of data points at the high temperatures. Because arcing data was desired during eclipse times, positive biasing was resumed from October 24-30, 1994, while the satellite remained in a sunlight-only orbit. Negative biasing was then continued from October 31 to November 4, 1994 (days 94304-94308), when the APEX orbit contained portions of eclipse. The bias voltages in this portion of the experiment were predominantly from -160V to -300V, with a few points from -310V to -370V. On November 4, 1994, as the negative biasing beyond -300V was being conducted, a problem developed on APEX, causing the spacecraft to go into Contingency Mode and shut off the experiments.

The problem that developed was in the Battery Control Regulator. Each battery on the spacecraft was monitored by two pressure gauges and two temperature sensors. The data from each of the sensors went through one multiplexer. A short on one of the pressure sensors

resulted in a single point failure at the multiplexer. Therefore, the pressure and temperature data was no longer available for use in regulating the battery charging. A solution to the problem was developed by OSC using the battery voltage and battery radiator temperature to regulate the charging. Software using this scheme was written and tested and then uploaded to the spacecraft, allowing experimental operations to resume on January 14, 1995. Since the software patch was not part of the spacecraft's intrinsic software, it had to be reloaded anytime the system was rebooted, which occurred, for example, after single event upsets (SEUs). Because of this, operations were not conducted above 1200km or near the South Atlantic Anomaly. The requirements for going into Contingency Mode, which then required a system reboot, were then changed to decrease the number of reboots. This, however, is more dangerous since possible problems could arise and the spacecraft may not go into a safe mode.

With PASP Plus once again operational, positive biasing was conducted from January 14-17, 1995. Negative biasing was then performed from January 18 to February 11, 1995 (days 95018-95042). Because of high levels of noise in the TPM data[76], the TPM threshold was increased to level 1 on February 2, 1995 (day 95033). Previously, the TPM setting had always been level 0. The counts detected on these days are believed to be noise (not arcs) for several reasons. First, the counts are an order of magnitude higher than the previous data, and are independent of which cell is biased or what bias voltage is used. Also, although the counts show up, there is no amplitude measured, indicating low-level noise and not arcing. Figures 23 and 24 show the arc rate (actually, TPM pulse detection rate) variation with cell temperature for the thin GaAs/Ge module #4 on day 95032. The first figure shows the rates at a constant bias voltage of -350V and an ion flux of $5 \times 10^{14}/m^2s$, while the second shows the rates for the voltages of -350V, -370V, -390V, and -410V, with no constraint on the ion flux. First, it is clear that the noise level is not a function of either bias voltage or ion flux, since the first graph is just a subset of the second. It is also clear that the noise level increases at times when the cells are warmer. As the cells heat up, so does the rest of the spacecraft, including the transient pulse monitors themselves. The noise is possibly due to a problem in the TPMs as they heat up, or with some other piece of equipment emitting electric field pulses at high temperatures. This effect is currently under examination by the TPM supplier.
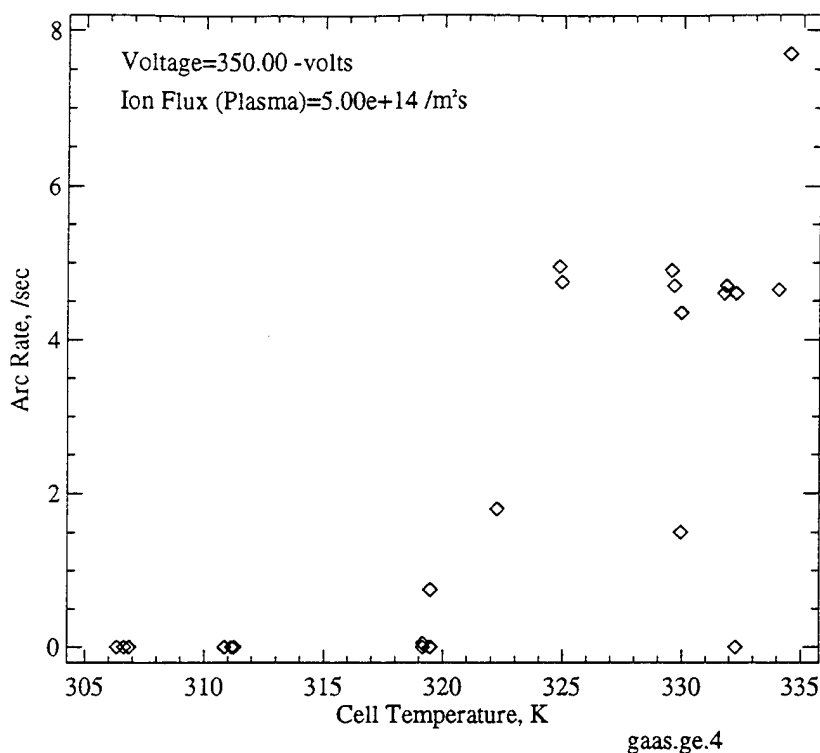
Figure 23: TPM Noise on GaAs/Ge Module #4 at -350V and $5 \times 10^{14} m^{-3}$

Because of the high noise in the data for days 95018-95031, this data will not be used in this work. The biasing sequences used for days 95033-95042 are shown in Table 6. In this set of biasing, one module was biased repeatedly for four consecutive orbits, then the next module was biased for four orbits, etc. This was done to try to get data at continuous points in the cell temperature and plasma density ranges seen throughout the orbit. Biasing was conducted in both sunlight and eclipse, although the modules were in wake during the eclipse portions of the orbit at this time.

The next phase of negative biasing was performed from March 3 to April 1, 1995 (days 95062-95091), when there were portions of the eclipse that had the modules in ram. The same scheme was used as in the last phase: biasing one array at a time repeatedly for several orbits, then moving on the next array to be tested. The biasing of the modules during this period is summarized in Table 7. This portion of the experiment yielded a large amount of data for the variation in the arc rates with cell temperature, which had not been available from the previous data.
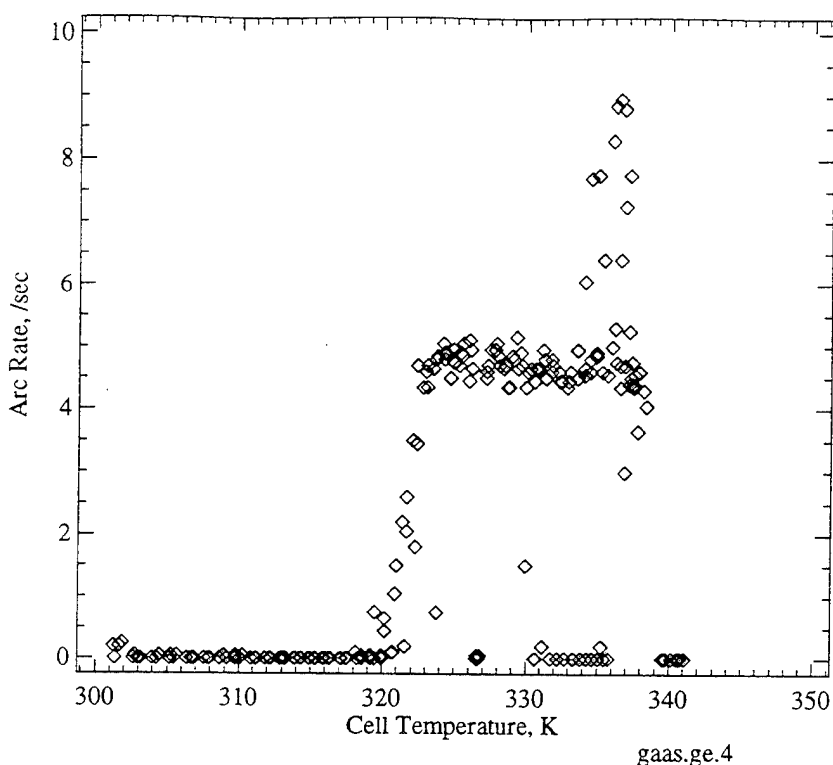
Figure 24: TPM Noise on GaAs/Ge Module #4 at -350V,-370V,-390V, and -410V

The last set of negative biasing took place from April 13 to April 18, 1995 (days 95103-95108). The biasing sequences used during this portion of the experiment are shown in Table 8. Appendix C summarizes the number of times each module was biased at each voltage for every day that negative biasing was conducted. Table 9 lists the total number of times each module was biased to each negative voltage through day 95141.

On May 16, 1995 at 20:31Z, when the APEX spacecraft was located at geodetic latitude 4, longitude 289, altitude 2316 km (near the edge of the South Atlantic Anomaly), there was a failure in the housekeeping interface unit (HIU). Because of this, the HIU heaters are no longer operational, so the vehicle's transmitter is being used as a heat source during sunlight operation. This also caused the battery radiator temperatures to no longer be available for use in regulating the battery charging, so the regulating is now being done based only on the battery voltage and current. PASP Plus is now powered off during eclipse and South Atlantic Anomaly crossings, and is able to collect approximately twelve hours of data per day. The dosimeter is on only during sunlight, which is approximately fifteen hours per day, depending on the date[3].

Table 6: PASP Plus Bias Sequences for Days 95033-95042

Day	Sequence	-Voltage	Arrays
95033	-Seq 6, Short	240,260,280,300	1,2
	-Seq 7, Short	360,380,400,420	14
95034	-Seq 7, Short	360,380,400,420	6,8,11,14
95035	-Seq 7, Short	360,380,400,420	4,6
	-Seq 7, Short	290,310,330,350	2,3
95036	-Seq 7, Short	290,310,330,350	1,2
95037	-Seq 7, Short	330,350,370,390	3,8,11,15
95038	-Seq 7, Short	330,350,370,390	3,8,11,15
	-Seq 7, Short	330,350,370,390	1,2,4,6,11
95039	-Seq 7, Short	330,350,370,390	1,2,4,6
	-Seq 7, Short	380,400,420,440	11,14,15
95040	-Seq 7, Short	380,400,420,440	11,14,15
	-Seq 7, Short	380,400,420,440	4,6,8
95041	-Seq 7, Short	380,400,420,440	3,4,6,8
	-Seq 7, Short	280,300,320,340	1,2
95042	-Seq 7, Short	280,300,320,340	1,2
	-Seq 7, Short	380,400,420,440	3

On June 3-4, 1995, a failure caused all of the heaters to turn on for fifteen hours, heating the TPMs to 100°, which were not designed to be heated above 60°. This caused the TPM sensors #3 and #4, located on the Payload Shelf, to fail. Thus, only one TPM on the Shelf, the TPM on the Deployed Panel and the sensor on the high-voltage power line inside the controller remain operational[83].

4.6 PASP Plus Data

As of May 21, 1995, the PASP Plus experiment had returned approximately 1.37 gigabytes of data. The raw data was processed by software written by Boston University[20], and then distributed to the PASP Plus Science Team. This data includes the satellite housekeeping and ephemeris data, environmental data, and the positive and negative biasing data. Figures 25 and 26 show examples of the plasma density and temperature data measured by the langmuir probe, in this case on day 94235. Figure 27 shows the ram angle, α, of the modules corresponding to times for Figures 25 and 26, and Figure 28 shows the orbital velocity of the spacecraft, which is the velocity at which the ambient plasma ions are striking

Table 7: PASP Plus Bias Sequences for Days 95062-95091

Day	Sequence	-Voltage	Arrays
95062	-Seq 6, Short	240,260,280,300	1,4,6
95063	-Seq 6, Short	240,260,280,300	1,2,3,4,5,6
95064	-Seq 6, Short	240,260,280,300	3,5
	-Seq 7, Short	320,340,360,380	3
95065	-Seq 6, Short	240,260,280,300	5
	-Seq 7, Short	320,340,360,380	3
	-Seq 7, Short	370,390,410,430	4,6,8,11
95066	-Seq 7, Short	370,390,410,430	4,6,8,11
	-Seq 7, Short	370,390,410,430	1,2,3,14
95067	-Seq 7, Short	370,390,410,430	4,6,8,11
	-Seq 7, Short	370,390,410,430	1,2,3,14
95068	-Seq 7, Short	370,390,410,430	4,6,8,11
	-Seq 7, Short	370,390,410,430	1,2,3,15
95069	-Seq 7, Short	370,390,410,430	1,2,3,15
	-Seq 7, Short	400,410,420,430	8,14
95070	-Seq 7, Short	400,410,420,430	8,14,15
	-Seq 7, Short	400,410,420,430	4,6,11
95071	-Seq 7, Short	400,410,420,430	4,6,11
	-Seq 7, Short	400,410,420,430	1,2,3
95072	-Seq 7, Short	400,410,420,430	1,2,3
95073	-Seq 6, Short	240,260,280,300	1,2,4,5,6
95074	-Seq 6, Short	240,260,280,300	4,5,8,11,14,15
95075	-Seq 6, Short	240,260,280,300	8
	-Seq 7, Short	320,340,360,380	1,2,3
95076	-Seq 6, Short	240,260,280,300	5
	-Seq 7, Short	320,340,360,380	1,4,6
95077	-Seq 6, Short	240,260,280,300	3
	-Seq 7, Short	320,340,360,380	8,11,14,15
95078	-Seq 6, Short	240,260,280,300	1,2,3,5
	-Seq 5, Short	160,180,200,220	5
95079	-Seq 5, Short	160,180,200,220	5
	-Seq 6, Short	240,260,280,300	5,6
95080	-Seq 6, Short	240,260,280,300	4,5,6,11,14,15
95081	-Seq 6, Short	240,260,280,300	8,11,14,15
	-Seq 7, Short	320,340,360,380	1,2,3
95082	-Seq 7, Short	320,340,360,380	1,2,3,4,6
	-Seq 6, Short	240,260,280,300	5
95083	-Seq 7, Short	320,340,360,380	4,6,8,11,14,15
	-Seq 6, Short	240,260,280,300	5
95084	-Seq 7, Short	320,340,360,380	8,11,14,15
	-Seq 6, Short	240,260,280,300	5
	-Seq 5, Short	160,180,200,220	5
95085	-Seq 6, Short	240,260,280,300	1,2,3,5
	-Seq 5, Short	160,180,200,220	5
95089	-Seq 6, Short	240,260,280,300	1,2,3,5
95090	-Seq 6, Short	240,260,280,300	1,2,3,5
95091	-Seq 6, Short	240,260,280,300	1,2,3,5
	-Seq 6, Short	240,260,280,300	4,6,15

Table 8: PASP Plus Bias Sequences for Days 95103-95108

Day	Sequence	-Voltage	Arrays
95103	-Seq 6, Short	240,260,280,300	4,5,6
95104	-Seq 6, Short	240,260,280,300	8,11,14,15
95105	-Seq 5, Short	160,180,200,220	5
	-Seq 7, Short	320,340,360,380	1,2,3
95106	-Seq 5, Short	160,180,200,220	5
	-Seq 6, Short	240,260,280,300	5
	-Seq 7, Short	320,340,360,380	4,6
95107	-Seq 6, Short	240,260,280,300	5
	-Seq 7, Short	320,340,360,380	4,6,14,15
95108	-Seq 7, Short	320,340,360,380	8,11,14,15

Table 9: Total Bias Steps for PASP Plus Modules

Voltage	Module									
	1	2	3	4	5	6	8	11	14	15
-75.00	53	53	46	53	46	53	46	53	46	46
-100.00	53	53	46	52	46	53	46	53	46	46
-125.00	52	53	45	53	46	53	46	53	46	46
-150.00	49	53	44	53	46	53	46	53	46	46
-160.00	397	384	204	339	711	373	192	407	30	30
-180.00	397	383	203	338	704	374	192	407	30	30
-200.00	395	381	203	337	697	372	191	406	30	30
-220.00	393	382	201	337	695	372	190	404	30	30
-240.00	837	861	1092	830	1979	731	742	666	529	575
-260.00	836	858	1090	827	1971	724	738	663	529	561
-280.00	1038	1049	1082	821	1962	723	734	661	527	556
-290.00	292	316	186	0	281	0	0	0	0	0
-300.00	1030	1040	1074	816	2077	716	729	656	523	549
-310.00	284	313	334	3	0	1	151	2	152	152
-320.00	622	596	559	569	0	568	321	479	320	320
-330.00	451	455	505	158	0	157	292	151	152	299
-340.00	629	602	594	560	0	569	363	477	360	361
-350.00	349	338	502	237	0	198	292	154	152	301
-360.00	428	411	596	579	0	747	528	516	398	357
-370.00	348	329	477	400	0	359	452	314	233	410
-380.00	412	395	793	783	0	947	727	720	601	550
-390.00	337	318	381	398	0	360	355	320	132	280
-400.00	108	108	366	345	0	494	522	358	393	235
-410.00	279	284	327	361	0	317	327	280	241	243
-420.00	108	108	370	355	0	504	526	366	397	349
-430.00	275	281	326	280	0	274	320	279	240	242
-440.00	0	0	206	206	0	205	196	206	200	190
-450.00	0	0	6	0	0	0	6	0	6	6

the arrays when they are in ram. From this, the ion flux to the arrays can be calculated, when the arrays are in ram (i.e. $\alpha \leq 90^o$), from

$$\Gamma_i = n_i v_{orbit} \cos \alpha \qquad (90)$$

where n_i is the ion density, which is equal to the electron density measured by the langmuir probe because of quasineutrality. As the ram angle approaches 90°, the flux of ions to the surface is dominated by the bohm flux, given (to first order) by

$$v_{bohm} = \sqrt{\kappa T_e / m_i} \qquad (91)$$

so that

$$\Gamma_{i_t} = n_i \sqrt{\kappa T_e / m_i} \qquad (92)$$

where T_e is the plasma electron temperature and m_i is the ion mass. In this work, the ion flux was taken to be the greater of the fluxes given by Eqs. (90) and (92), since the fluxes are not additive. Thus, Figure 29 shows the ion flux to the cells during the orbit, which is a key factor in the charging time for arcing. The portions where the flux drops off the graph are wake periods of the orbit. The plasma densities were measured twice for each bias step: once with a sweep up on the Langmuir probe bias and once by a sweep down. The values for the two sweeps varied by as much as 50%. Thus, in the data analysis done in Chapter 6, a 50% tolerance was used when finding points of constant ion flux. Although the Langmuir probe was rated for densities up to $10^{12} m^{-3}$, the data above 2×10^{11} is inaccurate because of large changes in the spacecraft potential at high densities, and thus points above this value were flagged as bad and are not used in this work.

Unfortunately, the ambient neutral density was not measured, which is also an important factor in the arcing process, as discussed in the previous two chapters. However, because of the highly elliptical orbit of APEX, the neutral density will generally be relatively higher at times of high plasma density. Figure 30 shows a comparison of neutral and plasma densities around one APEX orbit generated by EWB using the MSIS and IRI models. This shows a general correlation between neutral and plasma densities. Therefore, in the analysis of the arcing data, it will be assumed that the neutral flux will be higher at points of high ion

Table 10: Environmental Parameter Ranges for PASP Plus

	Plasma Density	Electron Temperature	Ion Velocity	Ram Angle	Ion Flux
Minimum	$1.005 \times 10^8 m^{-3}$	0.0232 eV	6195 m/s	0.276°	$1.64 \times 10^{11}/m^2 s$
Maximum	$> 2 \times 10^{11} m^{-3}$	0.8542 eV	8211 m/s	179.57°	$2.03 \times 10^{15}/m^2 s$

flux. The ranges in the environmental parameters are listed in Table 10, which were then used as inputs to the arc rate simulation.
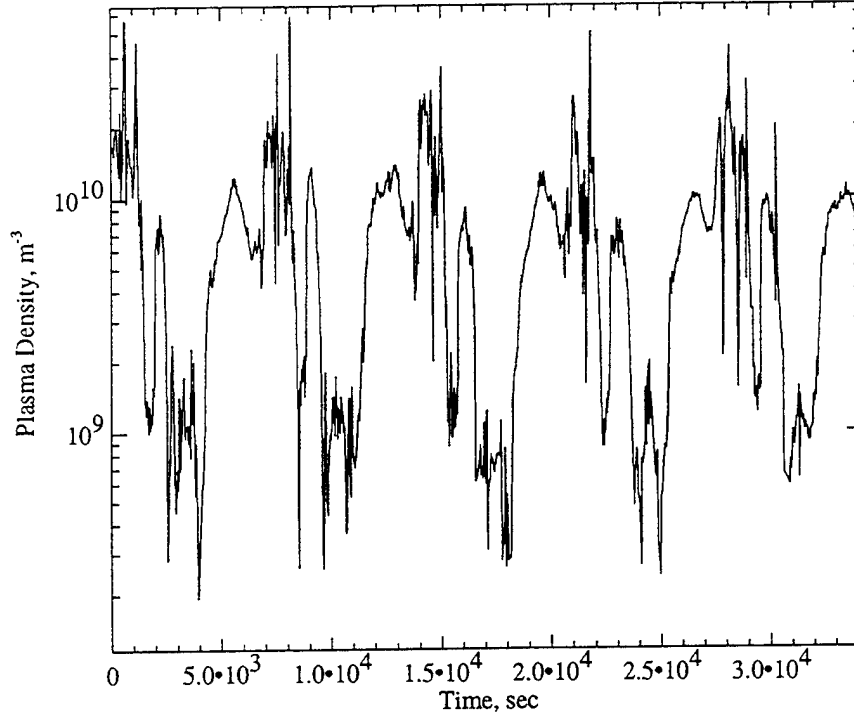
Figure 25: PASP Plus Plasma Density During Five Orbits on Day 94235

The temperature of the modules were also measured throughout the orbit, with an example shown in Figure 31. The cell temperatures quickly drop upon entering eclipse, and then quickly rise again upon entering sunlight, followed by a longer period of near steady state temperature while in sunlight. The two modules located over cutouts on the Deployed Panel (modules #3 and #5) show the quickest temperature drops and reach the coldest temperatures. The temperature ranges of the cells are given in Table 11. Of important note is that the conventional silicon modules #1 and #2 have a maximum temperature that is significantly cooler than the other conventional geometry cells. During the mission, it was noticed that the spacecraft was slowly heating up, thought to be due to changes in the optical properties of the white paint on the satellite. Thus, Tables 12 and 13 list the cell temperature ranges for the early days (94234-94308) and the later days (95033-94108),
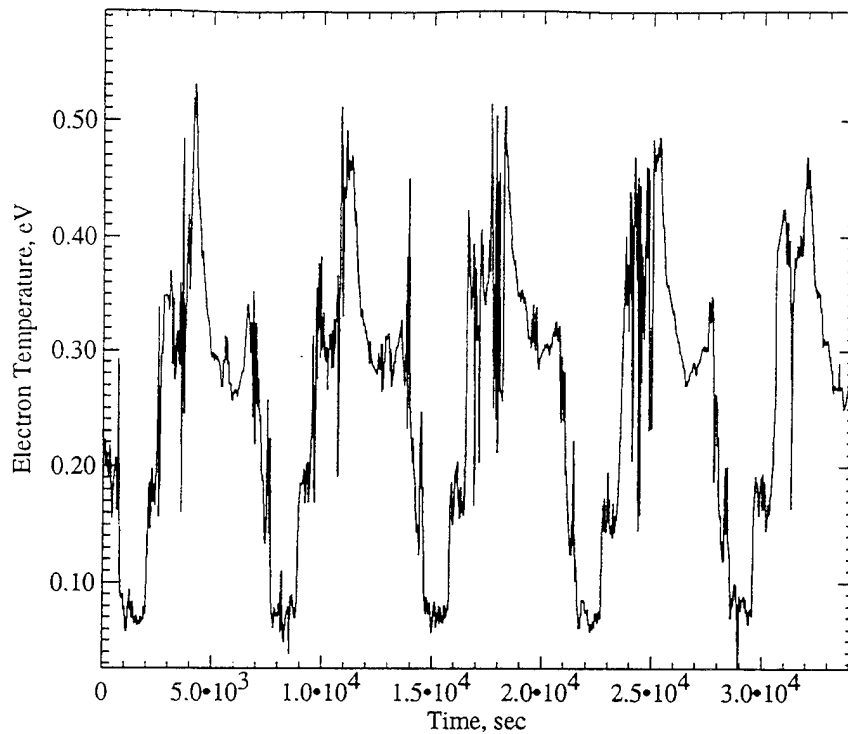
Figure 26: PASP Plus Electron Temperature During Five Orbits on Day 94235

Table 11: Temperature Ranges of Biased PASP Plus Cells

Module	#1	#2	#3	#4	#5	#6	#8	#11	#14	#15
Minimum, K	225	225	186	250	193	250	199	248	273	255
Maximum, K	329	329	358	365	356	365	331	339	342	335

respectively.

The 30 eV to 30 keV ion and electron spectra seen by the APEX spacecraft are measured by the electrostatic analyzer (ESA). The ESA has four detectors: one each for low energy ions, high energy ions, low energy electrons and high energy electrons. Because of the ellipticity of the orbit, the particle fluxes to the spacecraft can vary greatly. Figure 32 shows an example of the data from the ESA for one orbit on day 95235.

The arcing activity on the modules biased to high negative voltages is monitored by the

Table 12: Temperature Ranges of Biased PASP Plus Cells on Days 94234-94308

Module	#1	#2	#3	#4	#5	#6	#8	#11	#14	#15
Minimum, K	230	230	186	254	196	254	254	251	273	258
Maximum, K	323	323	339	343	346	343	331	338	342	332
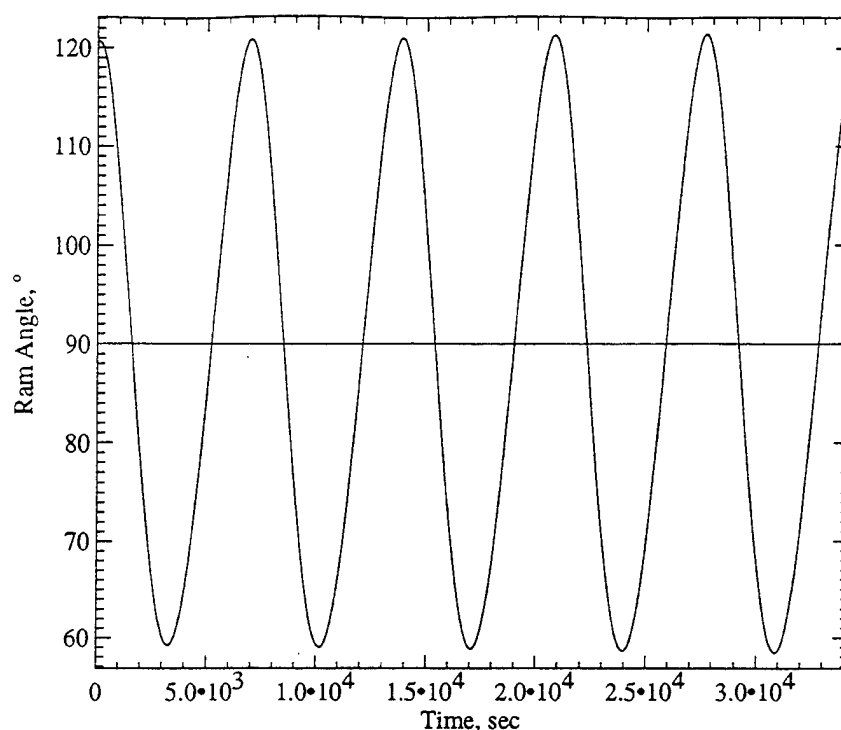
Figure 27: PASP Plus Ram Angle During Five Orbits on Day 94235

Table 13: Temperature Ranges of Biased PASP Plus Cells on Days 95033-95108

Module	#1	#2	#3	#4	#5	#6	#8	#11	#14	#15
Minimum, K	225	225	187	250	193	250	199	248	273	255
Maximum, K	329	329	358	365	356	365	330	339	342	335

four electric field transient pulse monitors and one in-line current sensor. The data from these monitors is returned for one second intervals. The number of pulses in each second are counted, and the pulse with the largest amplitude is characterized in terms of maximum positive and negative amplitudes, derivatives, and integrals. Because the rise and fall of the bias on the cells show up in the first and last seconds, the first two and last seconds of bias were not considered during the data analysis. Further discussion of the data will be conducted in Chapter 6.
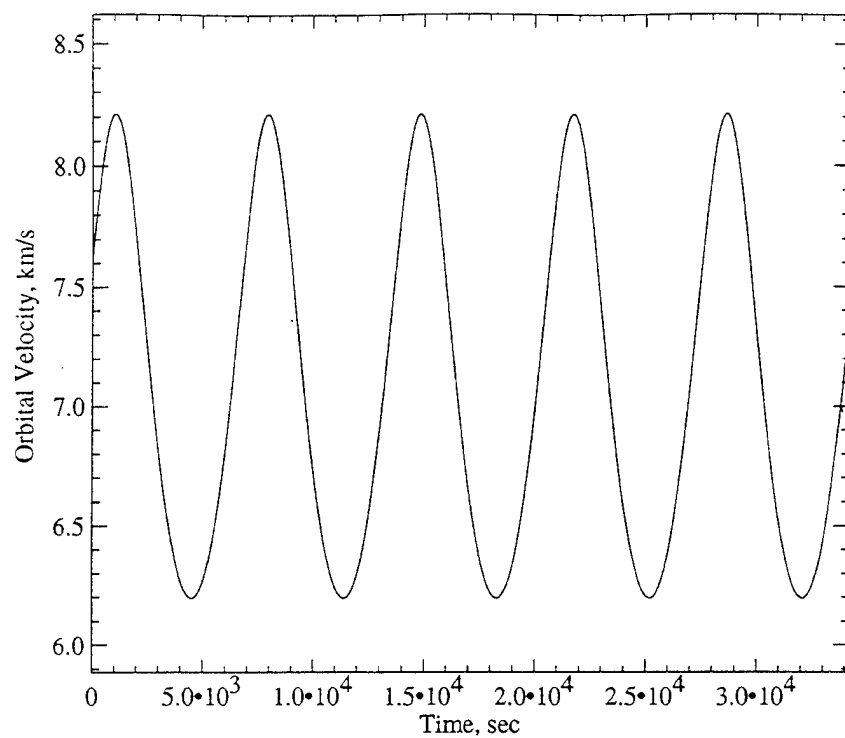
Figure 28: APEX Orbital Velocity During Five Orbits on Day 94235
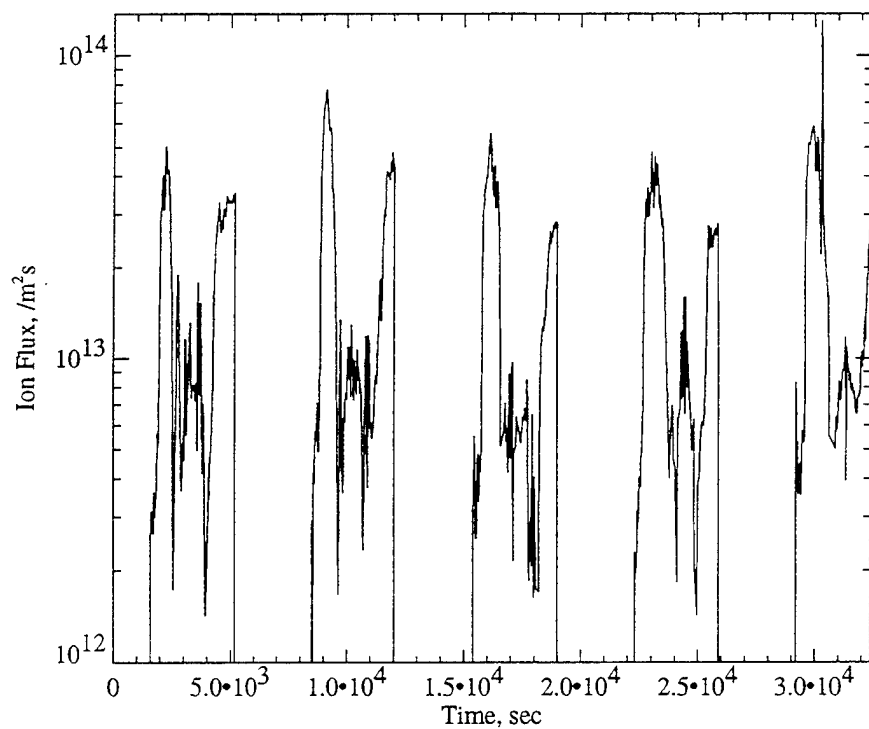
Figure 29: PASP Plus Ion Flux During Five Orbits on Day 94235
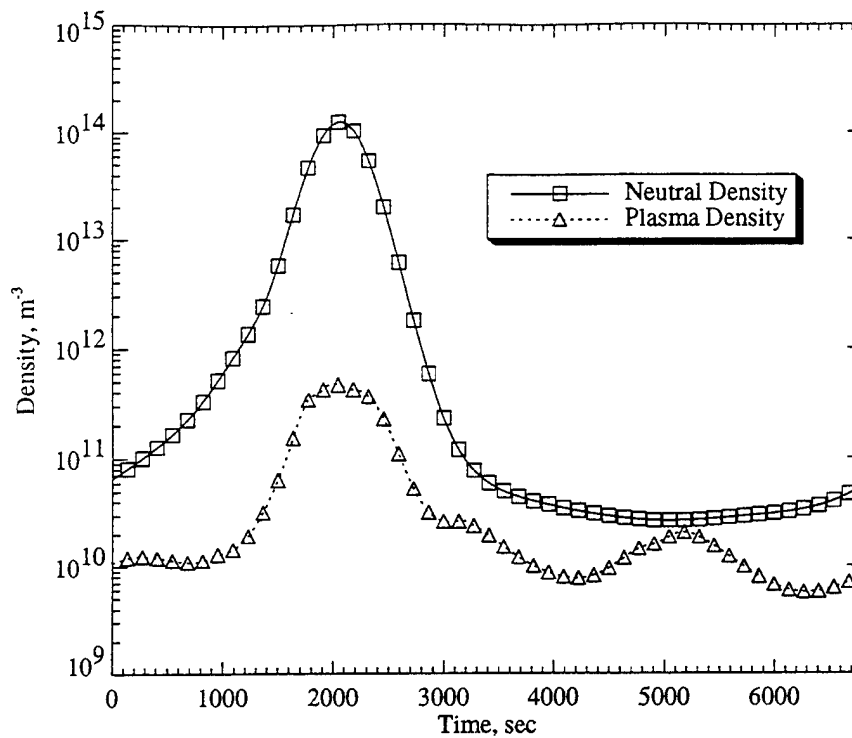
Figure 30: EWB Simulated Plasma and Neutral Densities
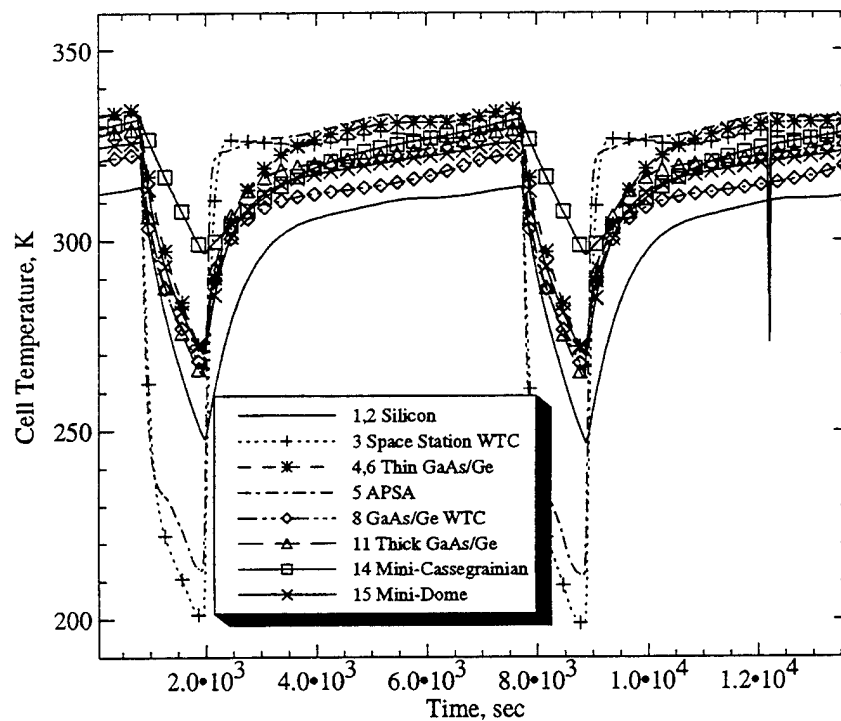
Figure 31: PASP Plus Cell Temperatures During Two Orbits on Day 94235
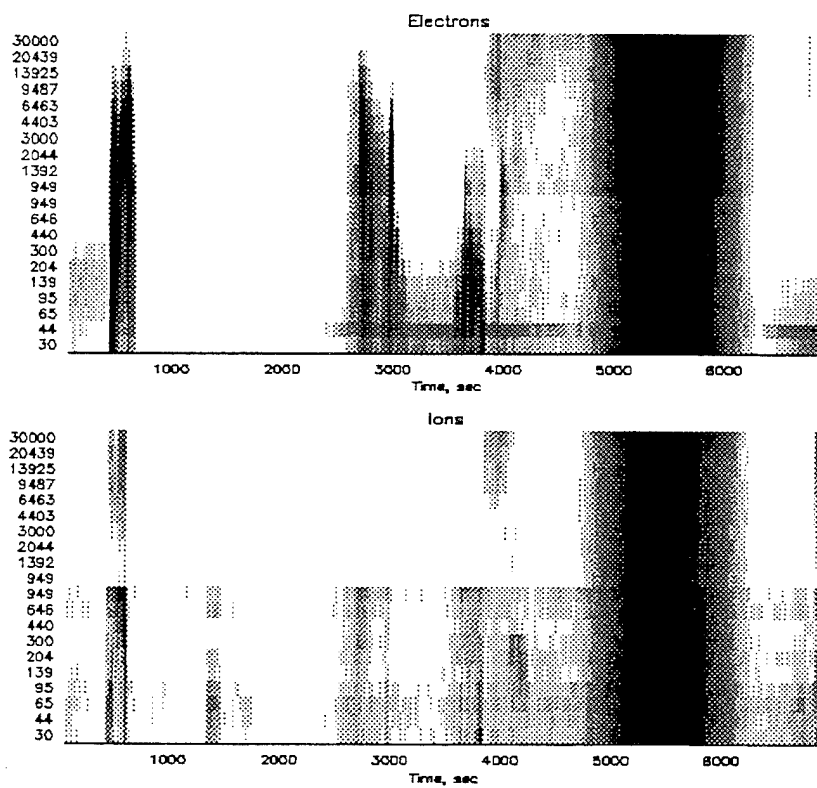
Figure 32: PASP Plus ESA Flux During One Orbit on Day 94235

Chapter 5

PASP Plus Arc Rate Simulations

The arc rate simulation described in Chapters 2 and 3 was run both pre- and post-flight for the conventional geometry solar cell modules on PASP Plus. The pre-flight simulations were conducted using environmental parameter values generated using the Environmental Workbench (EWB) software from S-cubed, assuming the 360x1950 km, 70° baseline orbit. The cell temperature range used was 215 K to 285 K, which had a much lower maximum temperature than was seen during the actual experiment. The simulation was run using the values for the environmental parameters that were either most or least conducive to arcing, listed in Table 14. The values of the parameters used were for ram, since the initial plan was to first bias only within ±20 minutes of maximum ram conditions. Two sets of simulations were run: one using the minimum and maximum conditions, and one set using EWB generated data for one second intervals. The second set was done to simulate the actual experiment throughout the first eight days of negative biasing, at ±20 minutes of ram.

The simulations were then re-run post-flight as soon as the initial negative biasing data was processed, using the environmental parameters and cell temperatures measured during the experiment, where available, listed in Table 15. The EWB generated values of ion mass, neutral density, and neutral temperatures were again used, since they were not measured during the experiment. A maximum plasma density of $3.5 \times 10^{11} m^{-3}$ was used, since the

Table 14: Pre-Flight Environmental Parameters for Minimum/Maximum Arcing

Condition	Plasma Density	Electron Temp.	Ion Mass	Orbital Velocity	Neutral Density	Cell Temp.
Minimum	$2.8 \times 10^{8} m^{-3}$	0.0715 eV	2.64×10^{-26} kg	6536.79 m/s	$6.85 \times 10^{9} m^{-3}$	285.0 K
Maximum	$3.5 \times 10^{11} m^{-3}$	0.347 eV	2.21×10^{-27} kg	8083.78 m/s	$3.18 \times 10^{14} m^{-3}$	215.0 K

Table 15: Post-Flight Environmental Parameters for Minimum/Maximum Arcing

Condition	Plasma Density	Electron Temp.	Ion Mass	Orbital Velocity	Neutral Density
Minimum	$1. \times 10^{8} m^{-3}$	0.023 eV	2.64×10^{-26} kg	6195 m/s	$6.85 \times 10^{9} m^{-3}$
Maximum	$3.5 \times 10^{11} m^{-3}$	0.85 eV	2.21×10^{-27} kg	8211 m/s	$3.18 \times 10^{14} m^{-3}$

Table 16: Temperature Ranges of Biased PASP Plus Conventional Cells

Module	#1	#2	#4	#5	#6	#11
Minimum, K	231	231	255	205	255	253
Maximum, K	311	311	329	333	329	323

experimental data above $2 \times 10^{11} m^{-3}$ is unreliable. The cell temperatures used are given by Table 16, which are the ranges seen during the first day of negative biasing (day 94234). The maximum temperature corresponds to the minimum arcing condition, and vice versa.

5.1 Pre-Flight Simulations

The pre-flight simulations were run using the parameters described above and the bias sequences given by Table 3[91]. Simulations were run to find the maximum and minimum arc rates expected during the initial phase of negative biasing, as well as to simulate the actual experimental operations of PASP Plus.

5.1.1 Pre-Flight Arcing Ranges

A set of simulations were run to determine the expected arcing of the conventional geometry cells under the orbital conditions for maximum and minimum arcing in ram. The parameters used are listed in Table 14.

In the simulations, 100 trials were run at each bias voltage for the two sets of conditions. The resulting range of arc rates for the conventional cells are shown in Figure 33. The upper curves show the maximum rates seen, while the lower curves show the minimum. For each

cell, minimum rates of at or near zero arcs/second occurred for the entire voltage range, while the maximum rates varied from 0.56 to 4.3 arcs/second. The large area between the two curves represents the high scatter that was anticipated in the data. The data points in the graphs are all of the actual flight data (approximately 4000-5000 points per module). The points were plotted regardless of ion flux or cell temperature in order to show the total range of arc rates seen in the experiment. Figure 35 shows the effect of the emission site density on arcing levels. Simulations were run with all parameters identical to the those for the pre-flight simulations, except the emission site density was increased by a factor of three, on the standard silicon module #2. As seen, this results in a much higher arc rate. The standard silicon modules on PASP Plus were manufactured in 1984 and are suspected of having a higher emission site density than newer cells. This could explain the slight underprediction of the arcing for these modules. Considering this effect, as well as the fact that all of the pre-flight environmental parameters were estimated, the simulations predicted the arcing on PASP Plus fairly well. For example, the bulk of the flight data lies within the predicted range for module #1, with only 42 out of 4972 points (less than 1%) outside the range.

In the pre-flight simulations, the thin cells (APSA and thin GaAs/Ge) showed the highest rates, as expected. The predictions for the silicon cells in modules #1 and #2 show that the arc rate should depend on the number of cells, which is expected since more cells results in a larger number of correlated areas in which arcs can occur independently. This is also evident by examining the rates from the two thin GaAs modules #4 and #6. In these simulations, as well as the second set of simulations conducted to represent the actual on-orbit experiment, it was found that at low cell temperatures, most of the arcs were big arcs, while at high temperatures they were mostly, or solely, small arcs. This is expected since at the high temperatures there is not a sufficient surface neutral density to be desorbed to lead to breakdown, whereas at low temperatures there is. The pre-flight simulations did a reasonable job of predicting the experimental arcing activity, considering that all of the parameters used in the simulation were estimates. The analysis of the flight data will be conducted in the next chapter, where the influence of voltage, ion flux, and cell temperature will properly be taken into consideration.

Table 17: PASP Plus Conventional Cell Pre-Flight Simulated Onset Voltages

	Module 1	Module 2	Module 4	Module 5	Module 6	Module 11
Onset Voltage	-180	-180	-125	-125	-125	-200

Figure 34 show the range of probability of arcs occurring that was expected for the experiment. These probabilities are the percentage of trials in which at least one arc occurred. The upper curves show the probability of arcing under maximum conditions, while the lower curve shows the probability under minimum conditions. Thus, the actual probability of arcs occurring during the experiment lie between these curves, depending on the actual environmental conditions. During the actual experiment at voltages for which the probability is greater than zero but less than one, it is expected that arcing may occur in some trials and not in others. For a given bias voltage, it can be seen that the environmental conditions can greatly affect the chance of arcing. For example, at -500V the thick GaAs/Ge cells (module #11) experienced arcing in nearly 100 percent of the trials under maximum conditions, but arced in less than 60 percent of the trials under the minimum expected conditions. The thinner cells showed higher probabilities of arcing than the thick cells in addition to having higher arc rates.

By examining the results from the trials at maximum arcing conditions, expected onset voltages could be found. The voltages represent the level at which arcing was first seen to occur on the cells. Below these levels, no arcs occurred in any of the trials. The simulated arcing onset voltages for the cells are shown in Table 17. Again, it should be emphasized that these simulations assumed ram conditions. In the wake, the much lower ion and neutral densities would result in no arcing until the ram angle approached 90°.

5.1.2 Pre-Flight Orbital Simulation

The next set of simulations consisted of simulating the actual experimental operation of the PASP Plus conventional cells during the initial biasing phase. Using the sequencing listed in Table 18, along with orbital data generated with EWB, the cells were biased for ±20 minutes of ram. With approximately thirteen orbits per day, this resulted in a database
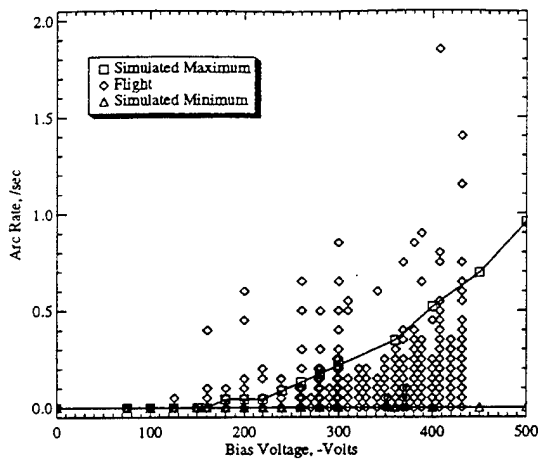
a: Module #1 Silicon
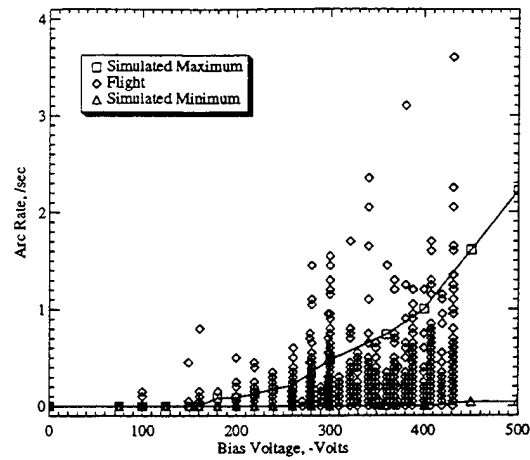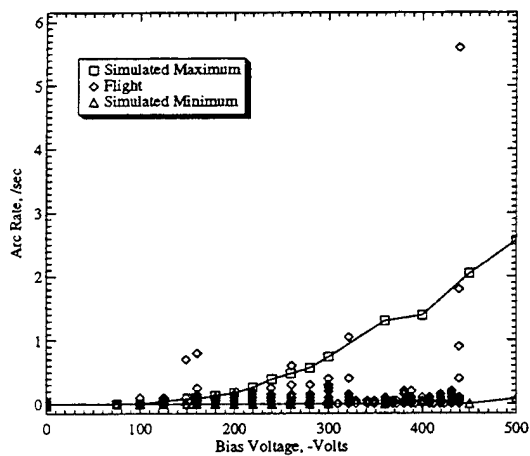
b: Module #2 Silicon

c: Module#4 Thin GaAs/Ge
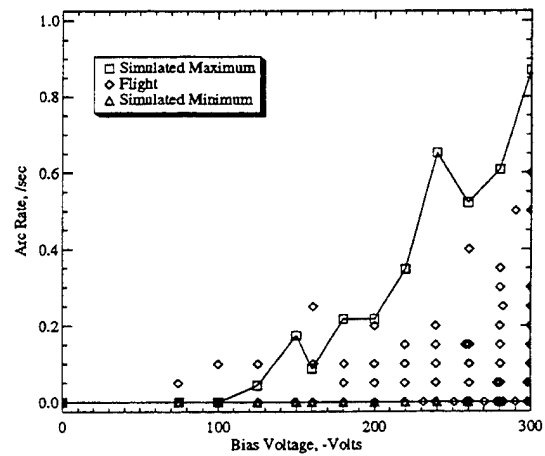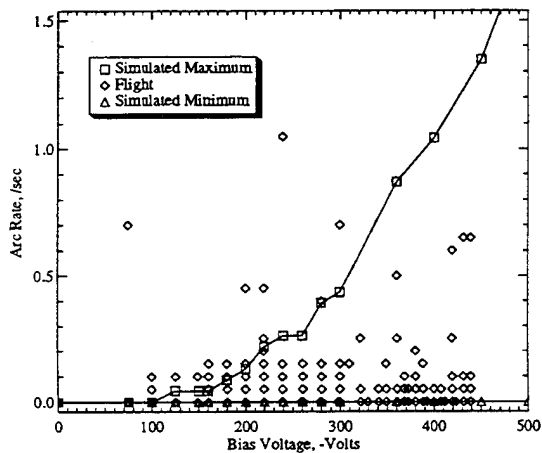
d: Module #5 APSA

e: Module #6 Thin GaAs/Ge
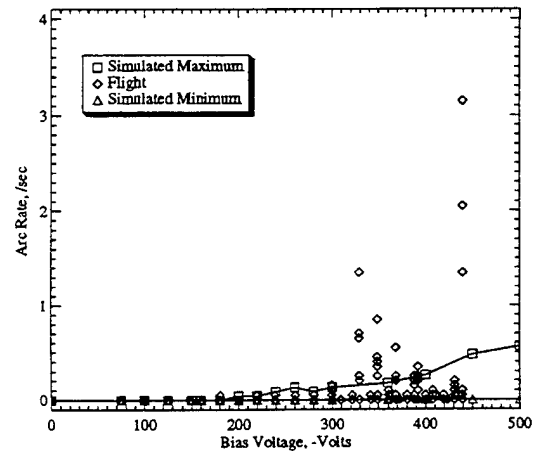
f: Module #11 Thick GaAs/Ge

Figure 33: Pre-Flight Simulations and Flight Data for Conventional Cells
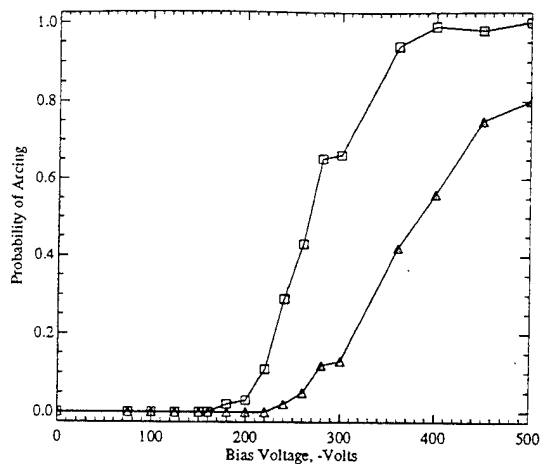
a: Module #1 Silicon
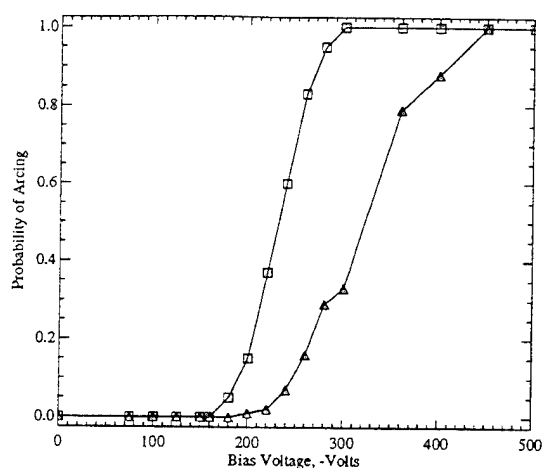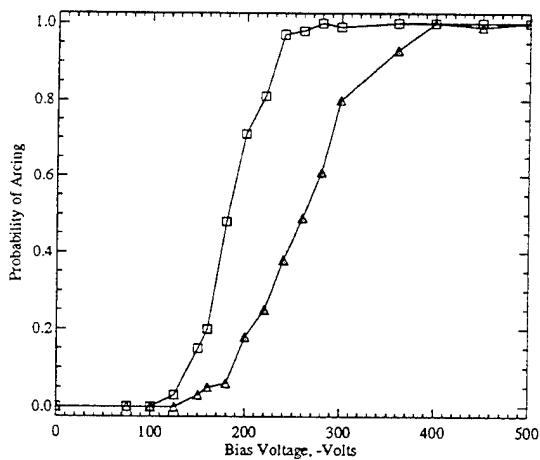
b: Module #2 Silicon

c: Module#4 Thin GaAs/Ge
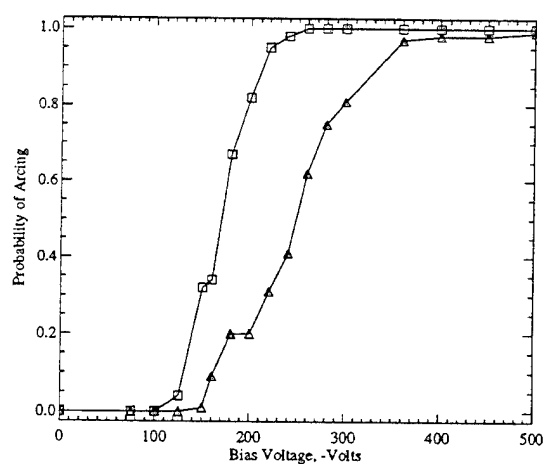
d: Module #5 APSA
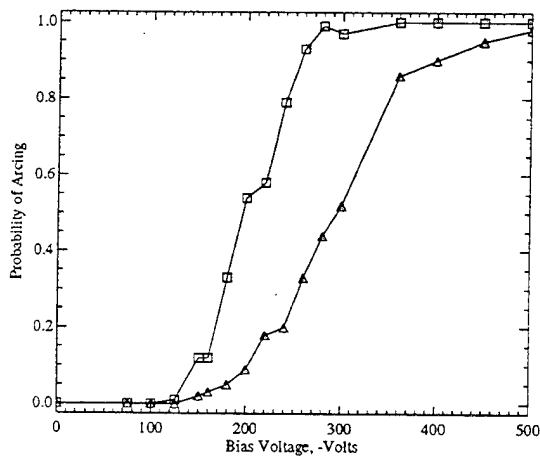
e: Module #6 Thin GaAs/Ge
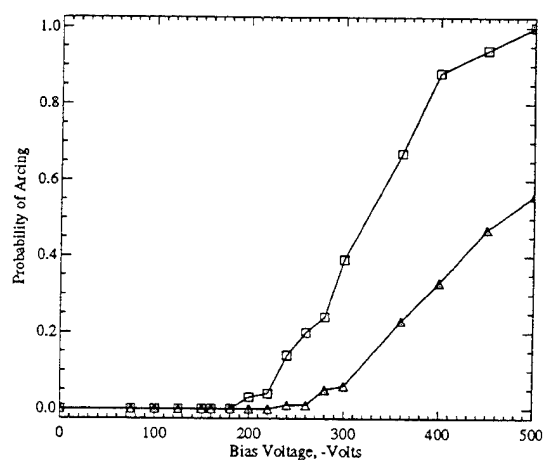
f: Module #11 Thick GaAs/Ge

Figure 34: Probability of Arcing in Pre-Flight Simulations
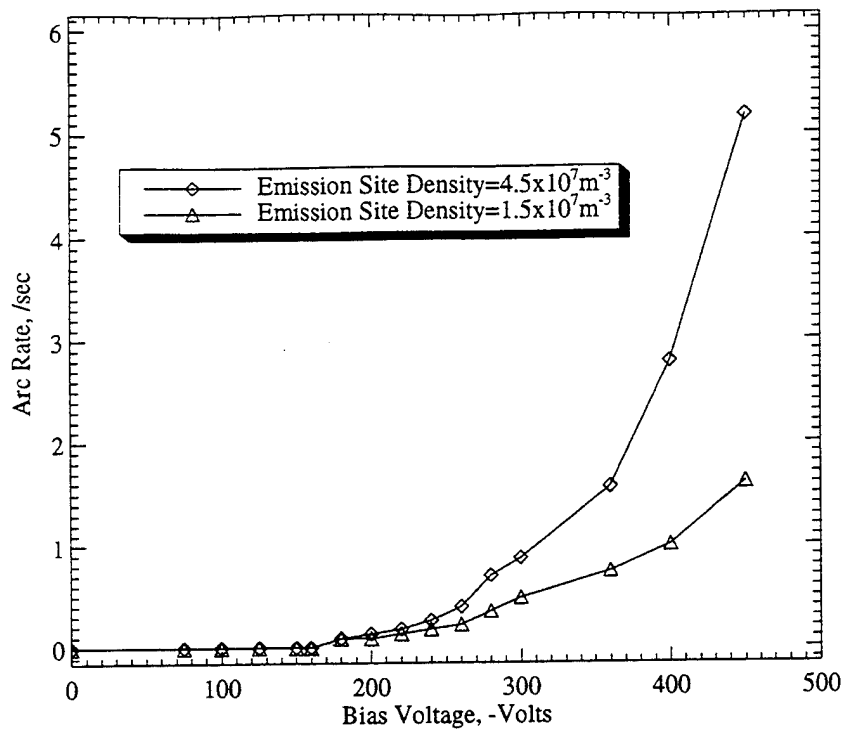
Figure 35: Effect of Emission Site Density on Arcing on Silicon Module #2

Table 18: PASP Plus Pre-Flight Simulation Bias Sequencing

Seq No.	Step 0	Step 1	Step 2	Step 3
1 (Days 1,2)	-75	-100	-125	-150
5 (Days 3,4)	-160	-180	-200	-220
6 (Days 5,6)	-240	-260	-280	-300
3 (Days 7,8)	-360	-400	-450	-500

of approximately 1000 simulated bias steps being conducted each day. Each of these step simulations were done using the environmental data generated for the appropriate portion of the orbit. This database was then used to develop software using the Interactive Data Language from Research Systems, Inc. to be used to find correlations between arc rates and the various environmental and operational parameters.

For example, by scanning through the data for points of constant ion density, neutral density and cell temperature, a fit to the arc rate versus voltage similar to that found by Ferguson for the PIX II data [25], discussed in Chapter 1, was done, given by the equation

$$R = C_1 n_e \left(-V\right)^{C_2} \tag{93}$$

93

where n_e is the plasma density and C_1 and C_2 are coefficients found by the fit. An example of this is shown in Figure 36 for the silicon cells in array #2, which had approximately the same cell area as the PIX II cells. In the fits, the power of the voltage is on the order of 3, matching the results found by Ferguson, and the premultiplier from the fit was 9.71×10^{-20}, compared to 2.22×10^{-20} for the PIX data.
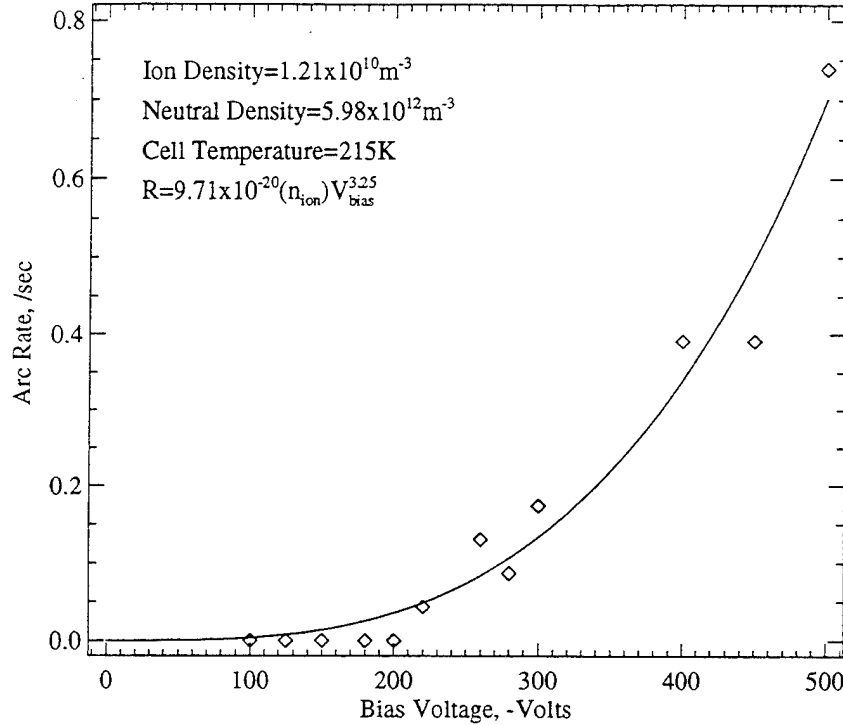
Figure 36: Voltage Power Law Fit to Array #2 Pre-Flight Arc Rate

Another type of correlation between arc rate and voltage is motivated by the model used in the simulations. Because of the need to numerically calculate the charging times for the arcs, a closed form equation for the arc rate is not given by the model. However, by assuming a constant secondary electron yield, a form of the solution is implied by Eq. (37). It should be noted that this equation is combination of a linear function of V_e and an exponential function of V_e, where V_e is the voltage which the dielectric charges up to when EFEE charging is initiated, and not explicitly a function of the bias voltage. Neglecting this, and assuming that the exponential term of the equation was dominating for low voltages, fits were made to the data with the form

$$R = C_1 \exp(C_2/V_{bias}) \tag{94}$$

where C_1 and C_2 are the coefficients found by the fit. Based on the typical values of the parameters in Eq. (37), C_1 is expected to be on the order of 10^{-15}, while C_2 is expected to be on the order of -10000. An example of this fit, using the same simulated data as for the fit above, is shown in Figure 37, with a resulting fit of $R = 5.97\exp(-1100.7/V_{bias})$. The coefficients found from the fit do not match those expected from Eq. (37). This is because the fit is done assuming these coefficients are constant with respect to voltage, which is not the case. For example, the average value of the factor β of the sites that arc, which appears in both coefficients, is a function of voltage, since at higher voltages sites with lower enhancement factors will show EFEE runaway. Figure 38 shows the variation in the average enhancement factor value with bias voltage from simulations for the standard silicon and APSA cells on PASP Plus. Both of these clearly show a decrease in average β as voltage increases. Also, because the form of the fit is exponential, the first coefficient is extremely sensitive to the coefficient within the exponent. Thus, a change in an order of magnitude in C_2 would cause C_1 to differ by many orders of magnitude.
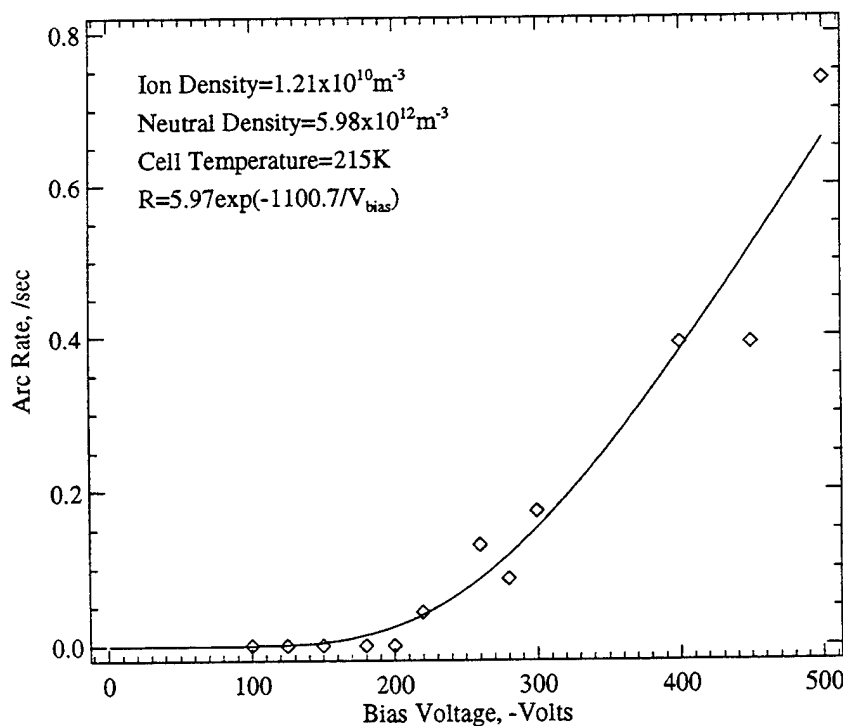
Figure 37: Voltage Exponential Fit to Array #2 Pre-Flight Arc Rate
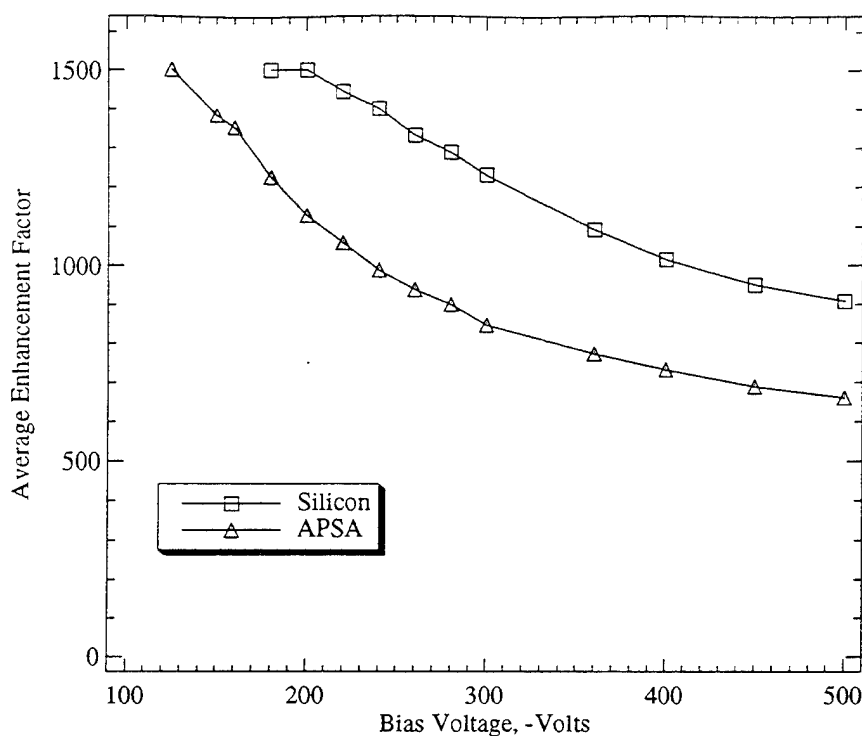
Figure 38: Average Enhancement Factor of Emission Sites That Arc

5.2 Post-Flight Simulations

A set of simulations were run after experimental data had been returned, using environmental parameters seen by PASP Plus, given in Table 15. And, more importantly, the cell temperatures of the cells during the experiment were used as inputs for the simulations, listed in Table 16. For the minimum temperatures, the APSA array was 10 K colder than the pre-flight estimate of 215 K, while the remaining cells were from 16 to 40 K hotter. In sunlight, however, all of the cells were much warmer than the pre-flight simulation's 285 K. The standard silicon cells were coolest in sunlight, at 311 K, whereas the remaining modules ranged from 323 to 333 K. As seen in Figure 18, at 285 K the APSA cells would be expected to arc at even relatively low neutral densities, whereas arcing would only be expected at very high ambient neutral densities for a cell temperature of 333 K. From Figure 15, the temperature effect on arcing levels of the remaining cells is similar than that of the APSA cells. During these simulations, only big arcs were counted, since it is believed that the TPMs would most likely not be able to detect small arcs. Figure 39 shows the results of the post-flight simulations with the cells at the maximum temperatures in Table 16. The

neutral density for the maximum arcing condition in these simulations was $3.18 \times 10^{14} m^{-3}$, which is the maximum density from the EWB generated environmental data for the APEX orbit. As discussed in Section 3.3, as the neutral density is decreased, lower arcing would be expected at the higher cell temperatures. Also shown in the graph are the flight data points with temperatures four degrees colder than the temperatures in the simulations, $\pm 3\%$, since there are very few data points at the temperature extremes themselves. Figure 40 shows the results of the post-flight simulations using the minimum temperatures from PASP Plus in Table 16, along with flight data points four degrees warmer than the temperatures in the simulations, $\pm 3\%$. In both cases, the simulations predict the arcing activity well. The thin GaAs/Ge modules showed less arcing than expected, however. This could possibly be due to a lower emission site density, which the arcing rate was shown above to be very sensitive to. Also, the arcing levels near the critical temperature are more difficult to predict, since at this point the arcing becomes very sensitive the parameters such as neutral density and the desorption yield.

In the next chapter, a detailed analysis of the flight data will be conducted. The correlations between arcing and the environmental and operational parameters will be examined for each of the modules, and further comparisons to simulated results will be made.
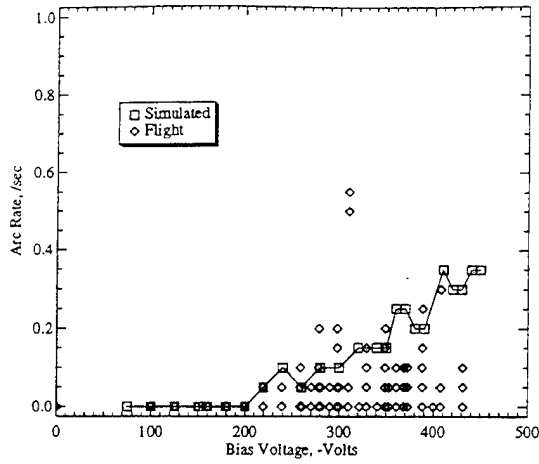
a: Module #1 Silicon
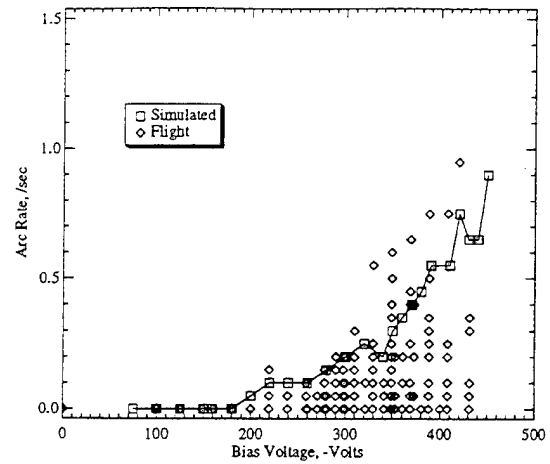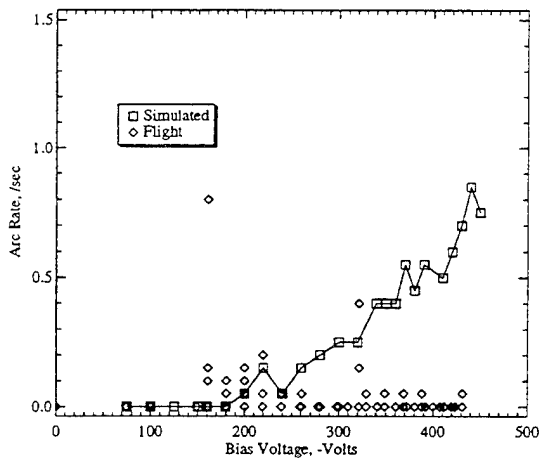
b: Module #2 Silicon

c: Module#4 Thin GaAs/Ge
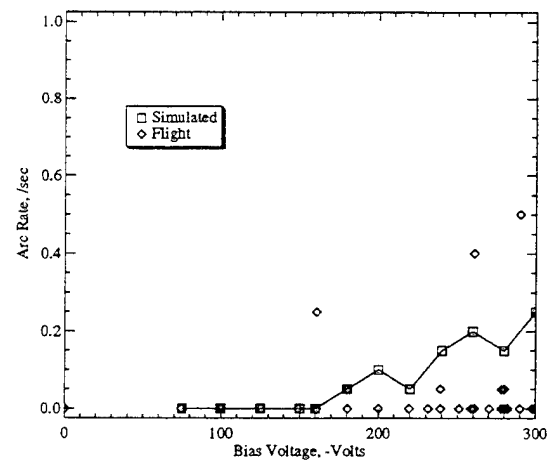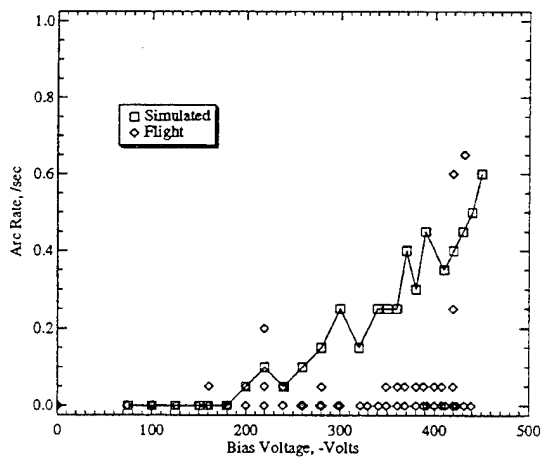
d: Module #5 APSA

e: Module #6 Thin GaAs/Ge
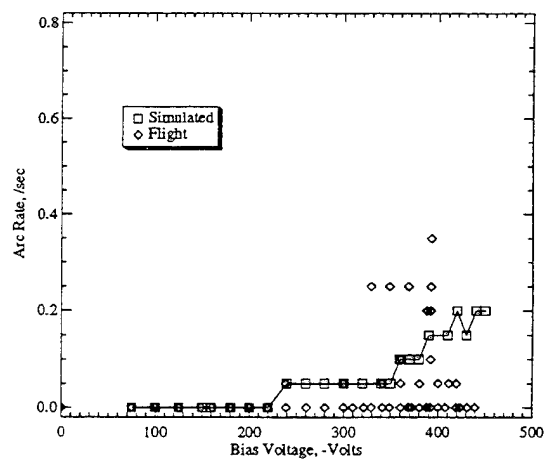
f: Module #11 Thick GaAs/Ge

Figure 39: Post-Flight Simulations and Flight Data for Conventional Cells at High Cell Temperature
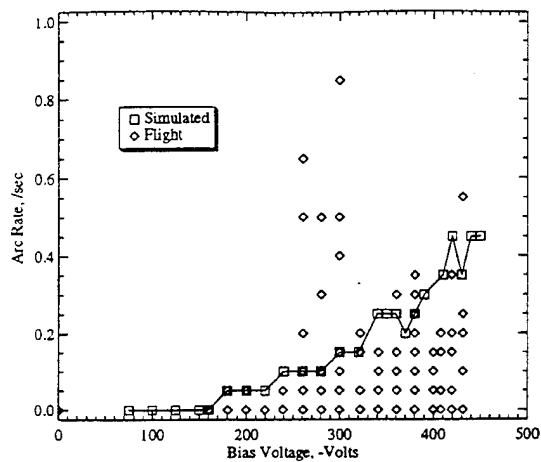
a: Module #1 Silicon
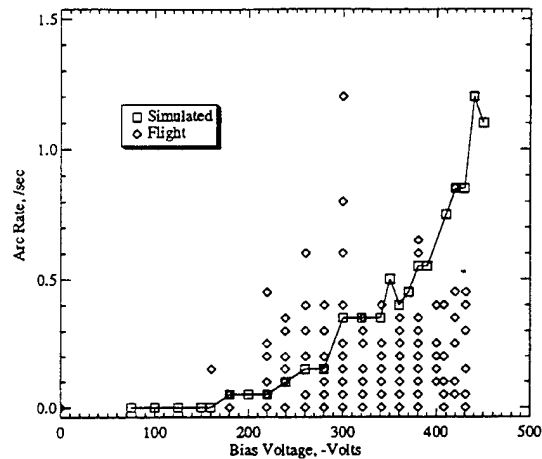
b: Module #2 Silicon
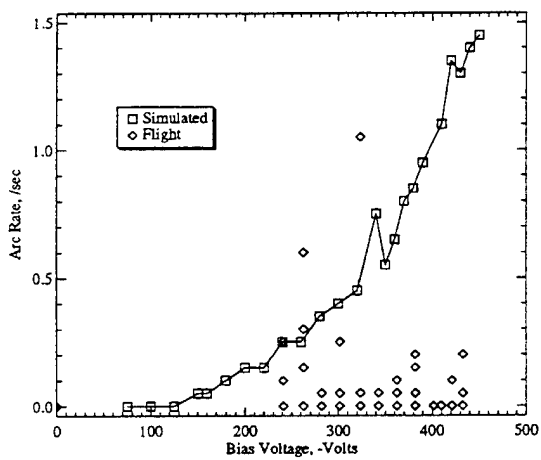
c: Module#4 Thin GaAs/Ge
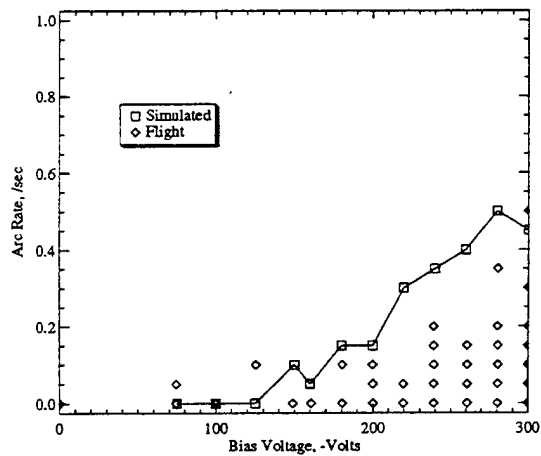
d: Module #5 APSA
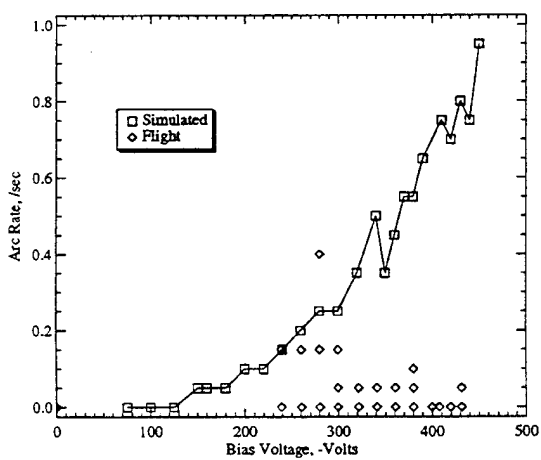
e: Module #6 Thin GaAs/Ge
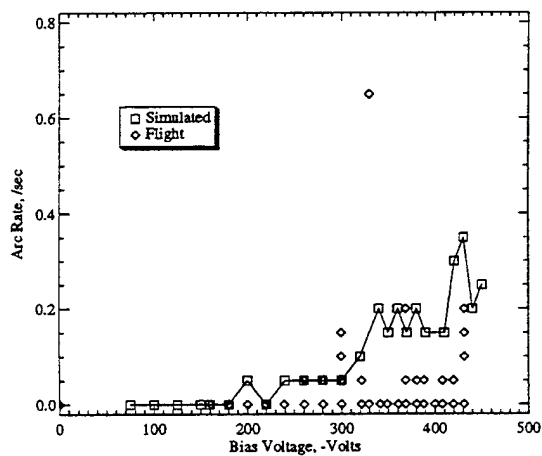
f: Module #11 Thick GaAs/Ge

Figure 40: Post-Flight Simulations and Flight Data for Conventional Cells at Low Temperature

Chapter 6

PASP Plus Flight Data Analysis

In this chapter, the PASP Plus flight data will be examined to determine correlations between the arcing rates of the various modules with the environmental variables, operational parameters, and cell properties that are known for the experiment. From the model used in this work, the arc rate, defined as the inverse of the charging time, is expected to be a function of bias voltage, array area, dielectric thickness, ion flux, neutral flux, and surface temperature, as well as the various EFEE parameters. Thus, the arc rate can be expressed as $R = R(V_{bias}, A_{array}, d, \Gamma_i, \Gamma_n, T_s, EFEE)$. Correlations with these parameters will be examined, as well as possible dependencies on radiation flux, ram angle (which affects the ion flux), and transition into and out of eclipse. For a description of the experimental results regarding the positive biasing operation and the radiation degradation of the solar cells, the reader is referred to References 16, 17, 58, 23, 19.

6.1 Statistics and Uncertainty

In the PASP Plus experiment, the modules to be tested were individually biased to fixed voltages for 23 second periods. Because the step up and down in voltage was detected by the sensors, the pulses in the first two seconds and last one second were not counted. Thus, twenty seconds of TPM data were attained for each bias step. Only pulses detected by the TPM nearest the biased module were counted as arcs. The arc rate for the step was then found by dividing the sum of arcs counted during the step by the twenty second experiment duration. Much of the analysis in this chapter will be done on averaged arc rates. When examining arc rate variation with bias voltage, the arc rates at each of the fixed voltages can

be averaged. However, when examining arc rate variation with ion flux or cell temperature, which could not be set to distinct fixed values during the experiment, the data is first binned and then averaged. On all of the graphs involving averaged data, the mean and associated error bars are shown. Two methods were used for determining the values for the error: Gaussian statistics and Poisson statistics. Both of these methods assume that statistical fluctuations, rather than uncertainties in the TPMs themselves, dominate the dispersion of the measured arc counts. Because the pulse counts, and not arc rates, are the measured values, the statistical analysis must be done on the count measurements first, which can then be divided by the experiment duration to give values in terms of arc rate.

If more than one data point is present at a given value for the independent parameter, Gaussian statistics were used to determine the average (i.e. mean) and standard deviation. For N measurements of a parameter x taken from a Gaussian parent distribution, the mean of the measurements is given by[10]

$$\bar{x} = \frac{1}{N} \sum x_i \tag{95}$$

and the appropriate measure of dispersion of the observations is given by the standard deviation

$$\sigma = \sqrt{\frac{1}{N-1} \sum (x_i - \bar{x})^2} \tag{96}$$

Thus, the average arc count can first be determined, along with the associated standard deviation. These values are then divided by the experiment duration t_{exp} to give an average arc rate and corresponding standard deviation in the rate.

If there is only one data point at a given value of the independent parameter, the error cannot be given by Eq. (96) because of the factor $N - 1$ in the denominator. For this case, Poisson statistics can be used for small numbers of counts. For a statistical process, random measurements can be expected to distribute themselves in a Poisson distribution. As the number of measurements becomes infinitely large, the Poisson distribution becomes indistinguishable from the Gaussian distribution. The mean of the measurements from a Poisson distribution is also given by Eq. (95), while the standard deviation is given by $\sigma = \sqrt{\bar{x}}$. If only one measurement x is available, we are forced to use $\sqrt{x}$ as an estimate for the standard deviation. Thus, while the uncertainty increases with the measured value,

Table 19: 68% Confidence Intervals on Small Numbers

x	m_{min}	m_{max}
0	0	1.14
1	0.16	1.80
2	0.70	3.30
3	1.30	4.60
>3	$x - \sqrt{x}$	$x + \sqrt{x}$

the relative uncertainty, $\sigma/x = 1/\sqrt{x}$, decreases with increasing x. For very low arc counts, the method used by Ferguson in the analysis of the PIX II flight data was used to 68% confidence intervals for the error bars when only one data point was available, given in Table 19[25]. As the measured value increases above 10, the relative uncertainty from Poisson statistics becomes small and no longer accurately represents the uncertainty in the experiment. However, most of the counts in the PASP Plus experiment were small, so Poisson statistics were used when necessary. In the graphs, error bars calculated using Gaussian statistics are shown as solid lines, while error bars found using Poisson statistics are shown dashed.

The second type of uncertainty in experiments is instrument uncertainty. As noted above, it has been assumed that the instrument uncertainty in the TPMs is small compared to the statistical uncertainty, so that the standard deviation given by either Gaussian or Poisson statistics gives a 68% confidence level for the arc counts. Examination of the Langmuir probe data showed differences as much as 50% in density between two consecutive measurements, so a 50% tolerance was placed on both ion density and ion flux, assuming that the uncertainty in the ram angle was relatively small, when searching for points of constant ion density or ion flux. When finding points of constant cell temperature, a tolerance of 3% was used. This tolerance was not based on the uncertainty of the temperature measurements, which is assumed to be small, but on the sensitivity of the arcing activity to cell temperature. The tolerance on the bias voltage was set to 2% based on the accuracy of the power supply in biasing to the predetermined voltages in the bias sequences. The ambient neutral density, which is a key parameter in determining the arc rate, was not measured during the PASP Plus experiment. This results in an extra uncertainty in the data analysis, since points that are being compared may have been taken at significantly

different neutral densities.

6.2 Arc Rate Dependency on Bias Voltage

The arc rate of solar arrays biased to high negative voltages is given by the inverse of the charging time, given by Eq. (37), times the ratio of array area to discharge wave area. The arc rate expected for an array can then be given by

$$R = \frac{A_{array}/A_{wave}}{\frac{(V_e - (V_{arc} - \frac{\Delta Q}{C_{front}}))C_{front}}{e n_e v_{ion} A_{cell} \cos \alpha} + \frac{C_{diele} d_i^2}{(\gamma_{ee}-1)\sqrt{S_{real}} \eta \xi A \frac{S_{FN}}{S_{real}} B\beta} \exp\left(\frac{Bd}{\beta \eta \xi_0 V_e}\right)} \tag{97}$$

Thus, setting all parameters but the bias voltage constant, the arc rate can be written as

$$R = \frac{1}{f_0 C_0 V_{bias} + f_1 C_1 \exp(f_2 C_2/V_{bias})} \tag{98}$$

where C_0 contains the premultiplier in the ion charging time and the array area/discharge wave area ratio, C_1 contains the premultiplier in the EFEE term and the array area/discharge wave area ratio, C_2 contains the premultiplier of V_e inside the exponent in the EFEE term, f_0 relates the voltage drop across the dielectric after an arc to the bias voltage, f_1 relates the variation of the terms in the EFEE premultiplier (primarily β) to bias voltage, and f_2 relates βV_e to bias voltage. If it is assumed that the potential across the coverglass drops by a constant fraction C_3 of the bias voltage, the premultiplier of the EFEE term is constant, and $V_e = C_4 V_{bias}$, Eq. (98) can be rewritten as

$$R = \frac{1}{C_0 V_{bias} + C_1 \exp(C_2/V_{bias})} \tag{99}$$

where C_0 has incorporated C_3 and C_2 has incorporated C_4. At low bias voltages, the EFEE term will dominate the charging process and the ion charging term can be neglected, further simplifying the equation for arc rate to

$$R = \frac{1}{C_1 \exp(C_2/V_{bias})} \tag{100}$$

104

Figures 41-50 show the variation in arc rate with bias voltage for each of the biased modules in the experiment, with eclipse temperatures. Because the TPM threshold was changed, the data for days 94234-94308 are shown separately from the data for days 95033-95108. The data for the low days are points at an ion flux of $1 \times 10^{14}/m^2 s$ (except for the concentrator modules, which have an ion flux of $1 \times 10^{13}/m^2 s$, since there were no data at the high flux). The data for the high days are at an ion flux of $1 \times 10^{13}/m^2 s$. The data for the conventional cells was fit using a non-linear least squares method with Eq. (100). While the shape of this form fits the data well and models the onset characteristics accurately, the coefficients do not match those expected from the model. This is because in performing a fit, all other parameters are assumed to be constant. This, however, is not the case, since parameters such as the enhancement factor are seen to vary greatly with bias voltage in the simulations.

The standard silicon arrays #1 and #2 show the highest arcing activity. As mentioned previously, these arrays were produced in 1984 and may have a much higher emission site density than the newer cells. The wrap-through-contact modules #3 and #8 show some arcing activity, although less than the conventional geometry cells. The concentrator modules #14 and #15 also show a small amount of arcing activity, although at rates low enough to possibly be noise. On all of the conventional geometry cells, there is a definite increase in arc rate with increasing bias voltage.
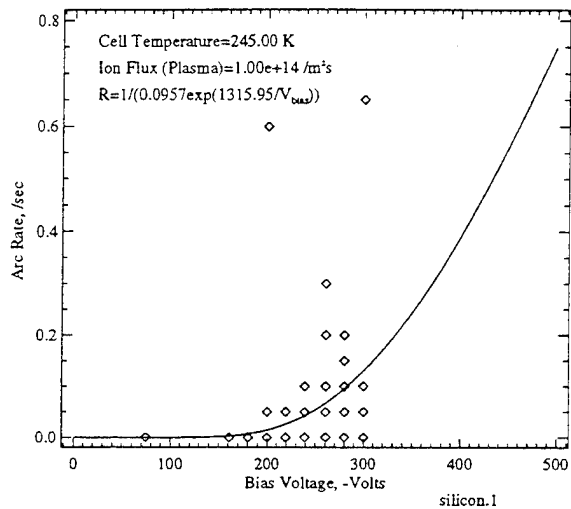
a: Low Days (94234-94308)
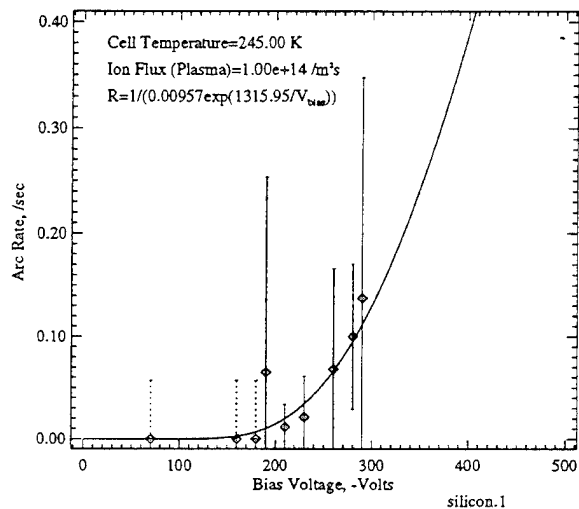
b: Low Days (94234-94308) Average
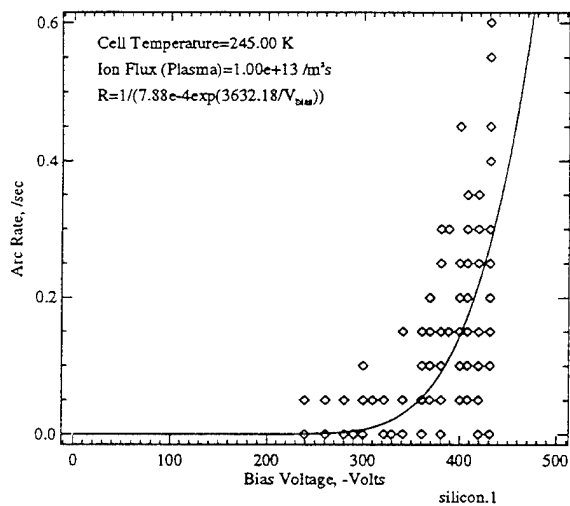
c: High Days (95038-95108)

d: High Days (95038-95108) Average

Figure 41: Arc Rate Variation with Voltage for Silicon Module #1
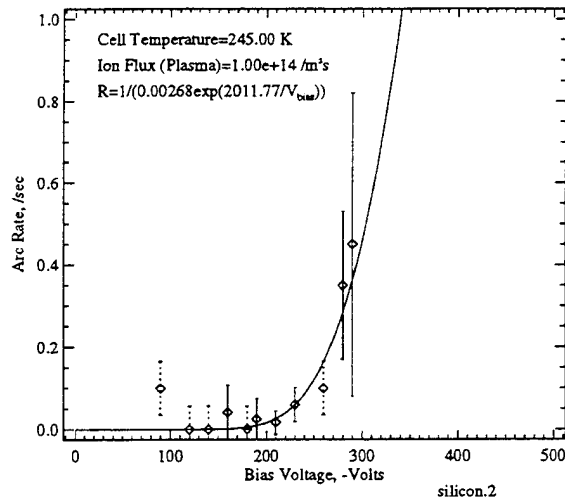
106

a: Low Days (94234-94308)

b: Low Days (94234-94308) Average
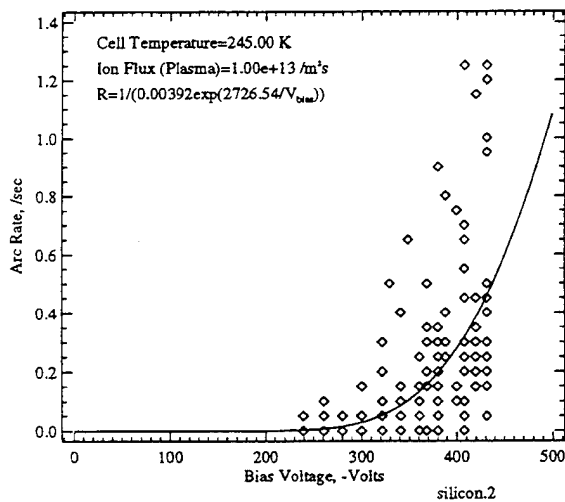
c: High Days (95038-95108)
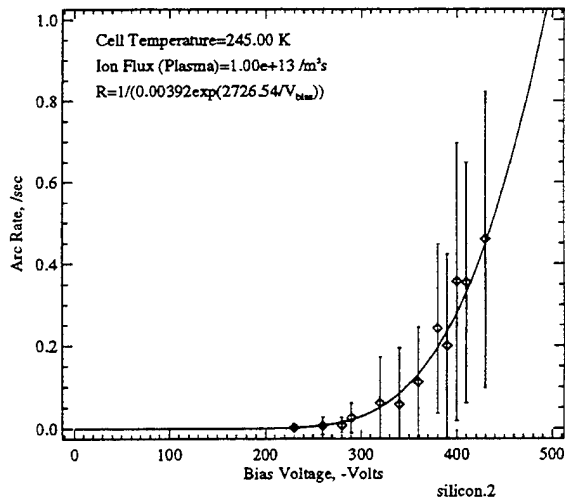
d: High Days (95038-95108) Average

Figure 42: Arc Rate Variation with Voltage for Silicon Module #2
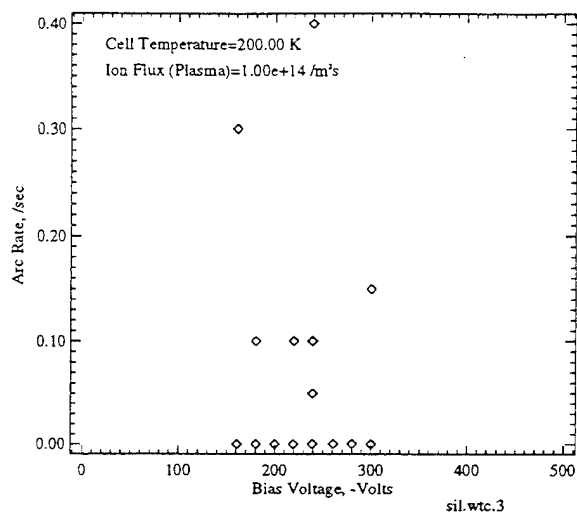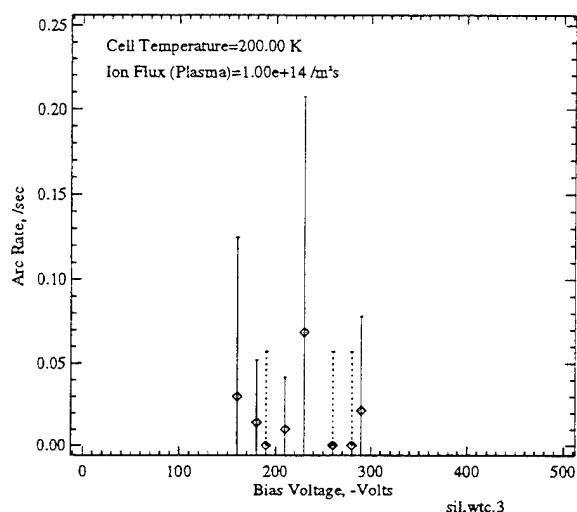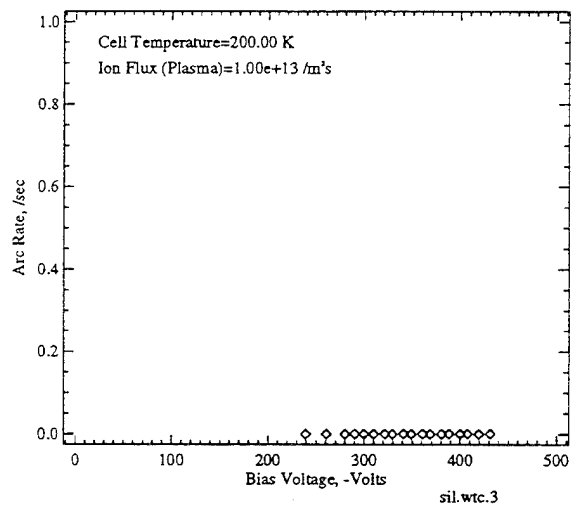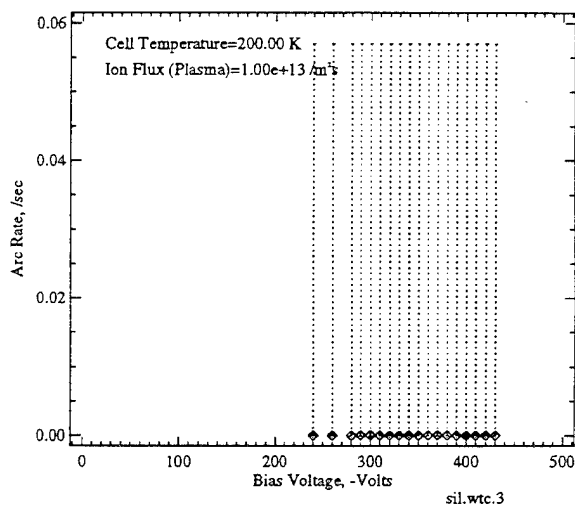
Figure 43: Arc Rate Variation with Voltage for Silicon WTC Module #3
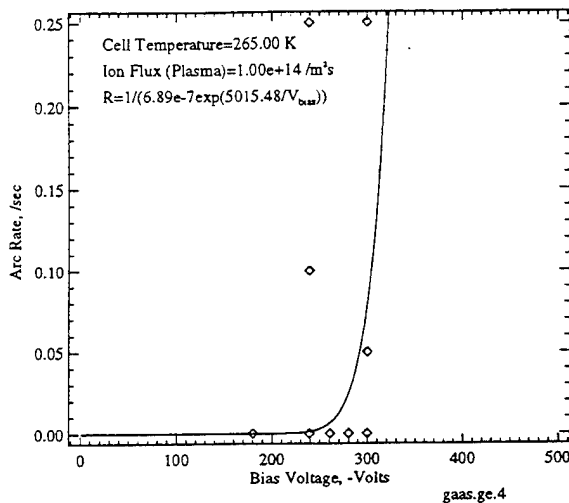
a: Low Days (94234-94308)
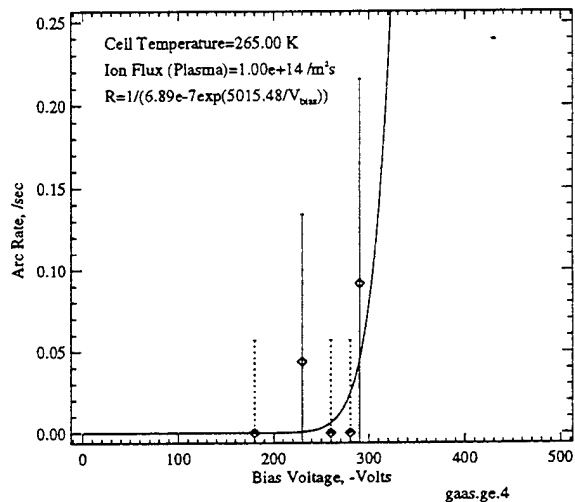
b: Low Days (94234-94308) Average
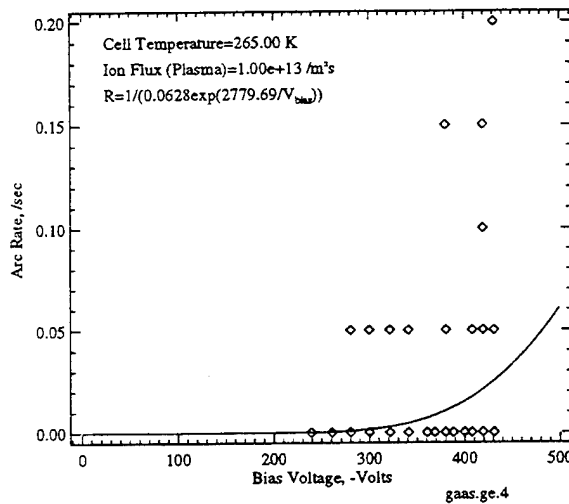
c: High Days (95038-95108)
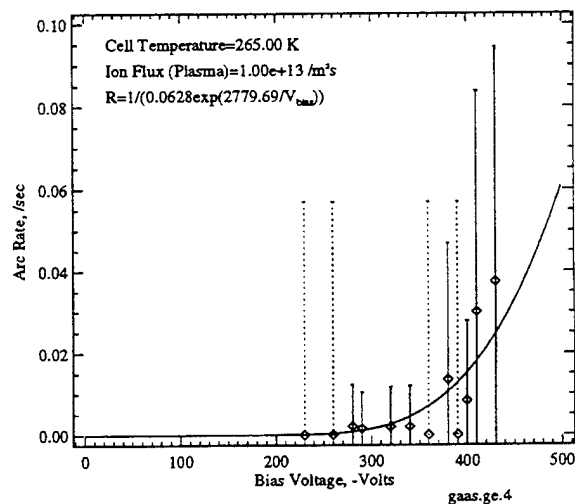
d: High Days (95038-95108) Average

Figure 44: Arc Rate Variation with Voltage for Thin GaAs/Ge Module #4
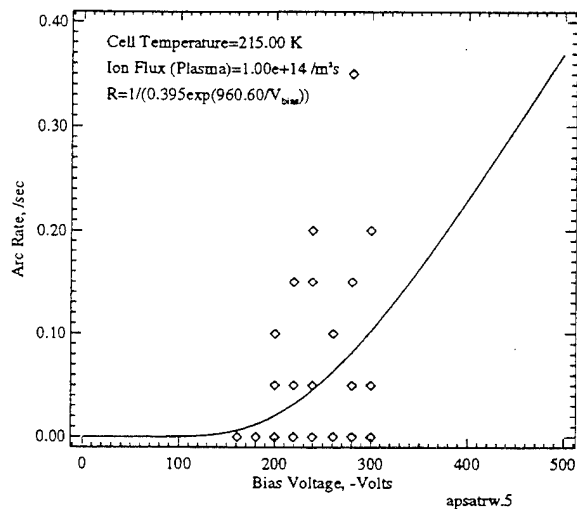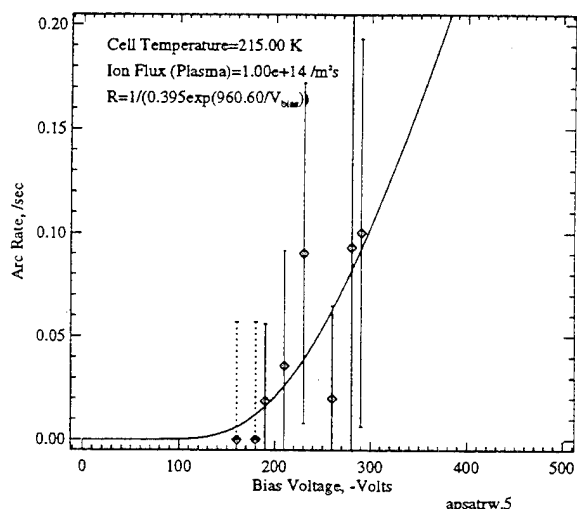
109

a: Low Days (94234-94308)

b: Low Days (94234-94308) Average
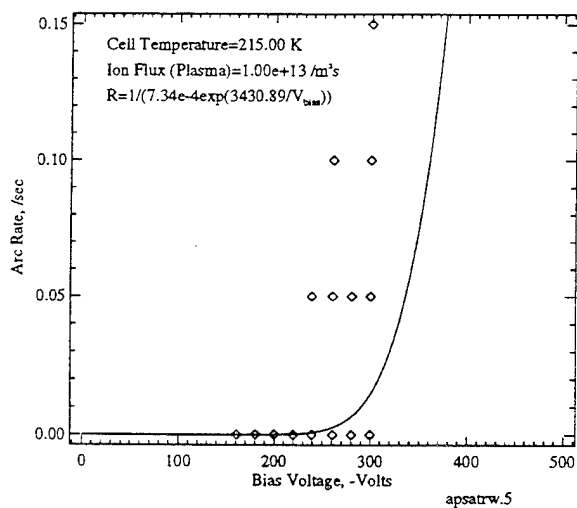
c: High Days (95038-95108)
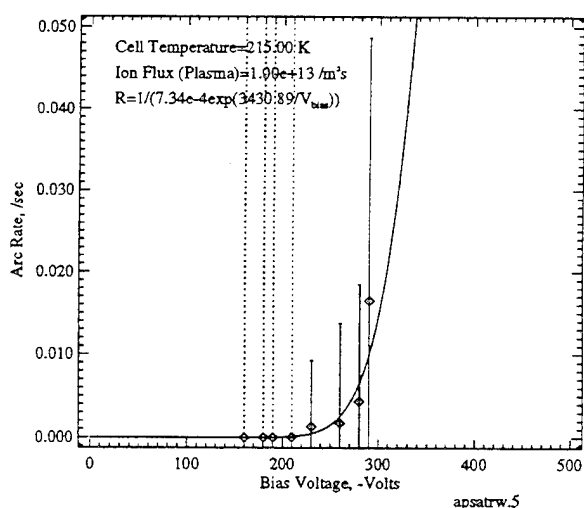
d: High Days (95038-95108) Average

Figure 45: Arc Rate Variation with Voltage for APSA Module #5
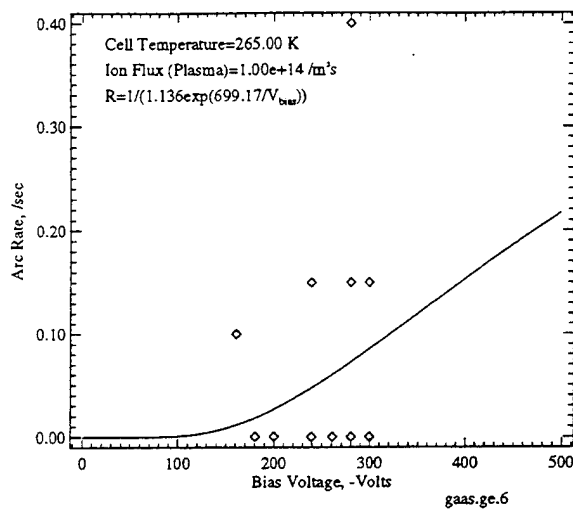
a: Low Days (94234-94308)
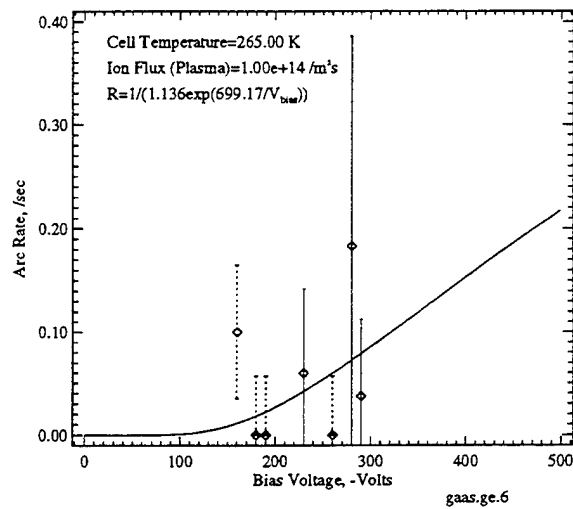
b: Low Days (94234-94308) Average
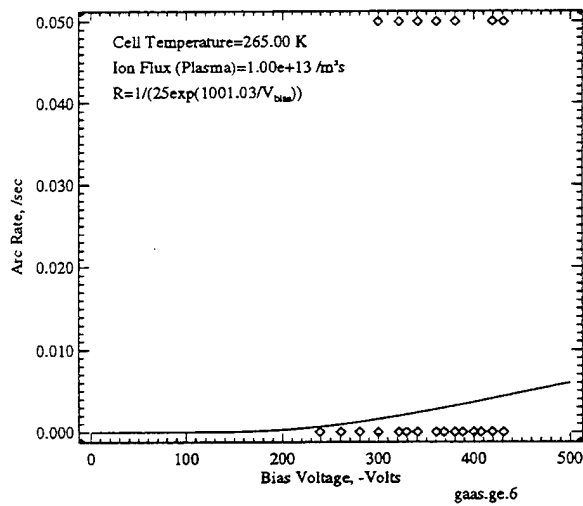
c: High Days (95038-95108)
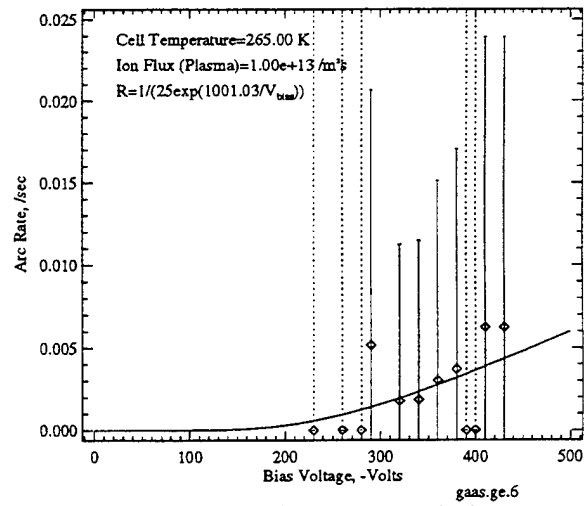
d: High Days (95038-95108) Average

Figure 46: Arc Rate Variation with Voltage for Thin GaAs/Ge Module #6
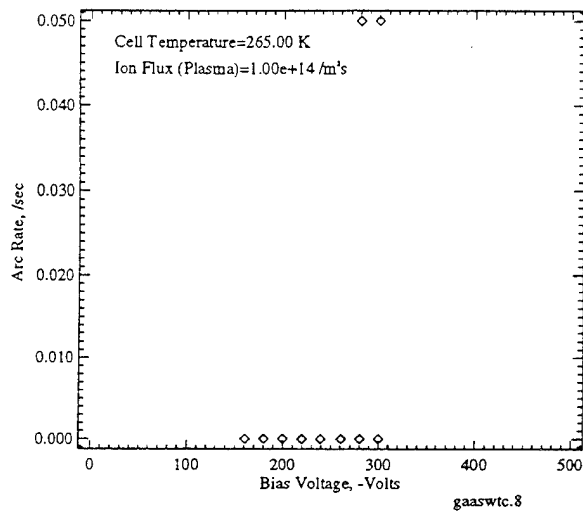
a: Low Days (94234-94308)
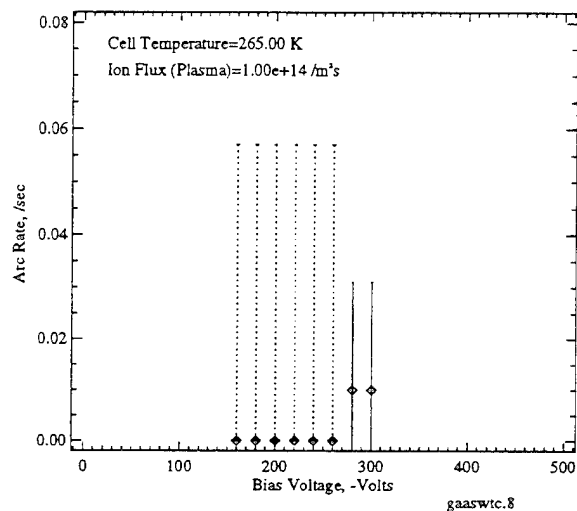
b: Low Days (94234-94308) Average
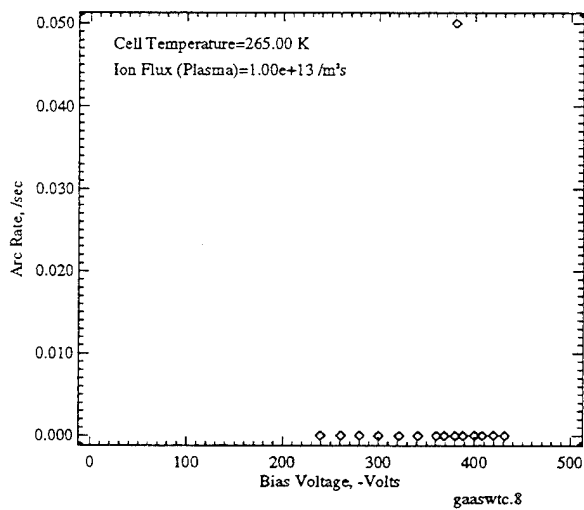
c: High Days (95038-95108)
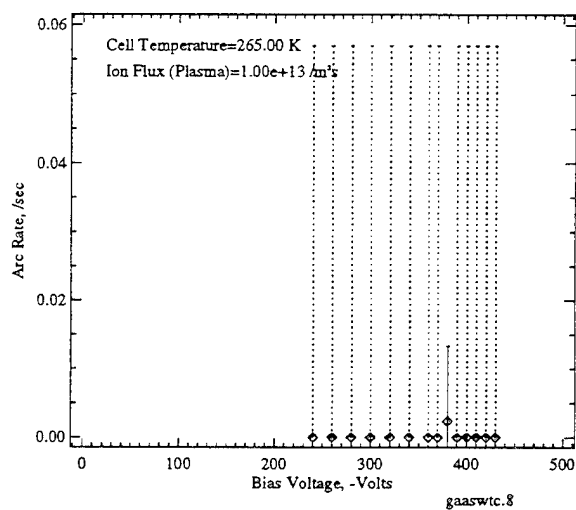
d: High Days (95038-95108) Average

Figure 47: Arc Rate Variation with Voltage for GaAs/Ge WTC Module #8
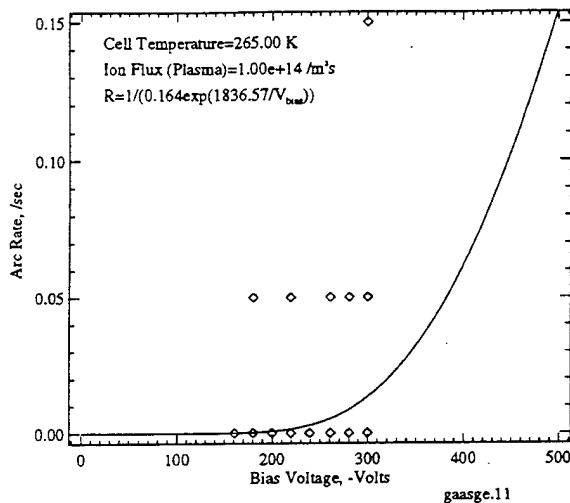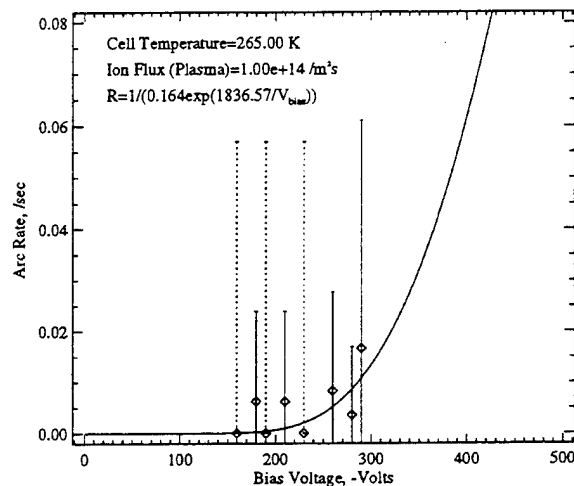
112

a: Low Days (94234-94308)

b: Low Days (94234-94308) Average
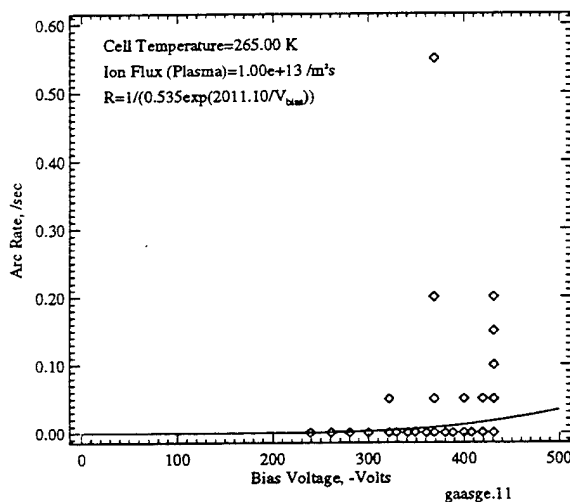
c: High Days (95038-95108)
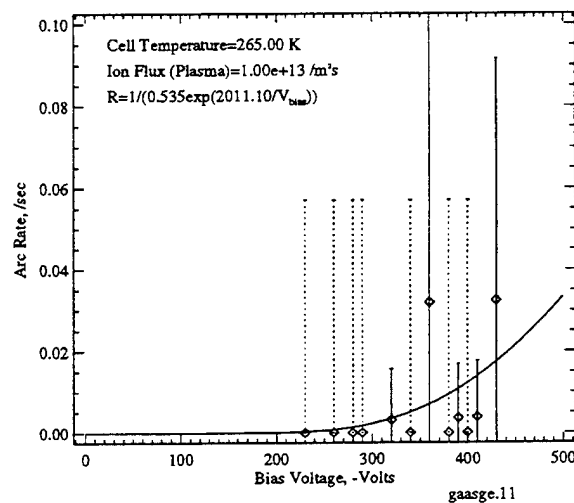
d: High Days (95038-95108) Average

Figure 48: Arc Rate Variation with Voltage for Thick GaAs/Ge Module #11
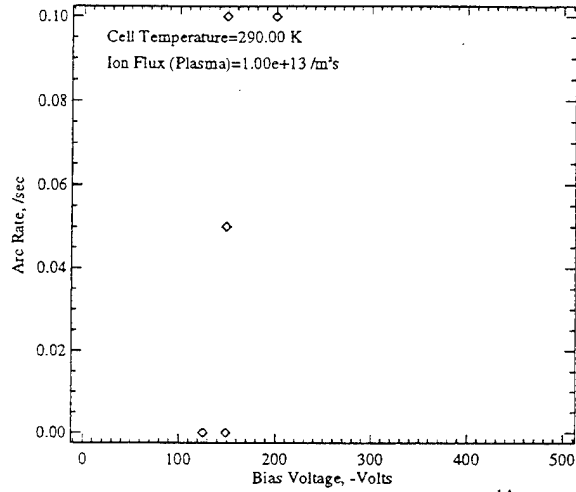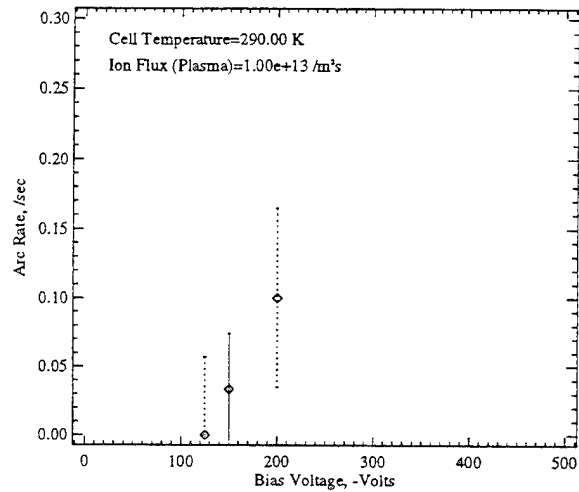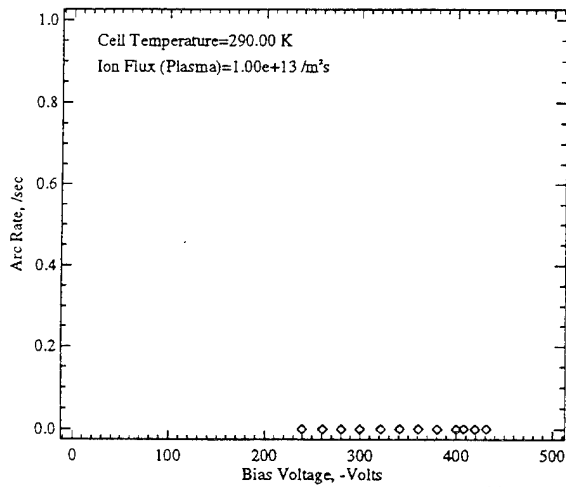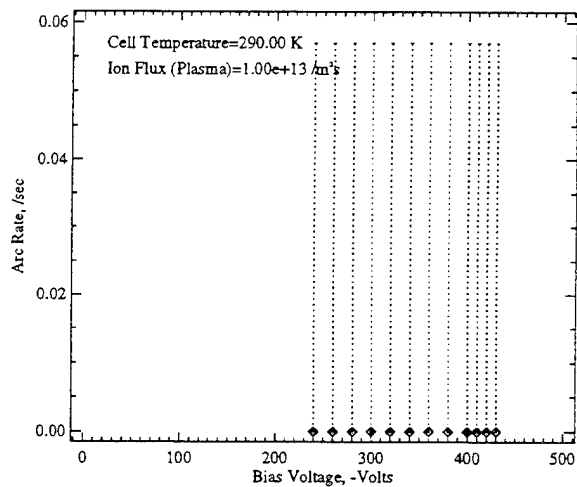
Figure 49: Arc Rate Variation with Voltage for Mini-Cassegrainian Module #14
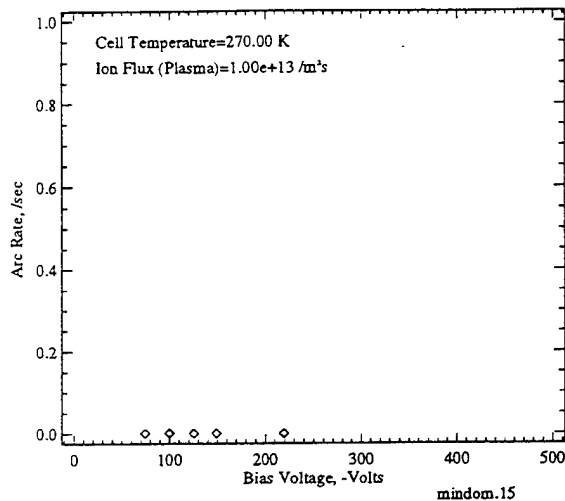
a: Low Days (94234-94308)
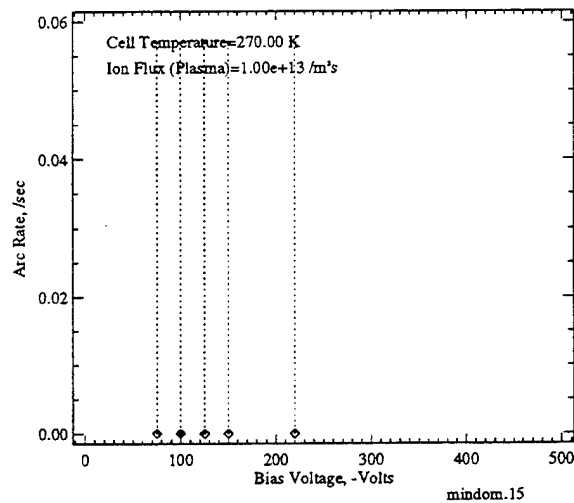
b: Low Days (94234-94308) Average
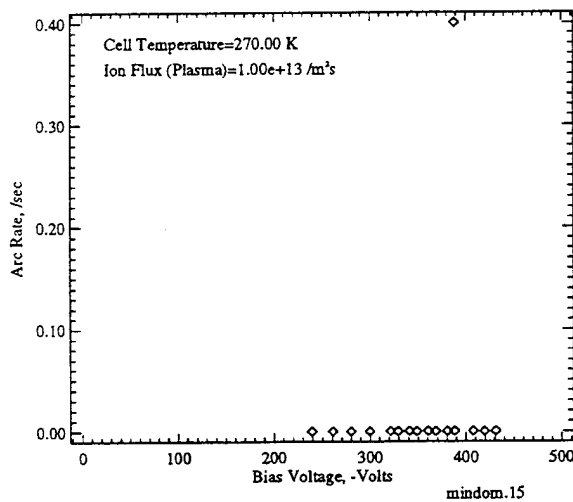
c: High Days (95038-95108)
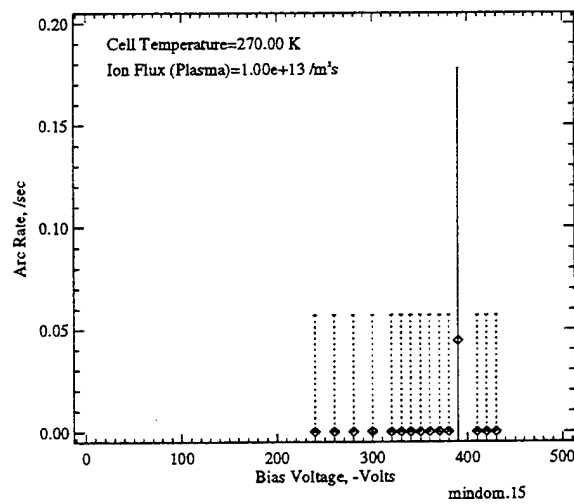
d: High Days (95038-95108) Average

Figure 50: Arc Rate Variation with Voltage for Mini-Dome Module #15

Table 20: Simulated and Experimental Arcing Onset Voltages

Array	Simulated Onset Voltage	Experimental Onset Voltage
(1,2) Standard Silicon	-160V	-160V
(3) Silicon WTC	N/A	-160V
(5) APSA	-100V	-75V to -125V
(4,6) Thin GaAs/Ge	-120V	-125V
(8) GaAs/Ge WTC	N/A	-260V to -300V
(11) Thick GaAs/Ge	-180V	-180V

6.2.1 Onset Voltage

At high ion fluxes, the total charging time will be dominated by the EFEE charging time, and the arc rate can be given by Eq. (100). The EFEE charging time will then determine the threshold voltage at which arcing will begin. The charging time, as a function of bias voltage, is given by the form

$$\tau_{chrg} = C_1 \exp(C_2/V_{bias}) \qquad (101)$$

For any finite experiment duration, there will exist a voltage below which the charging time exceeds the experiment duration, at which point no arcing will be seen. This is illustrated in Figure 51, with the experiment duration of 20 seconds chosen to match the length of the biasing steps on PASP Plus. Onset voltages were found using both the flight data and the simulations, which are summarized in Table 20. Simulated onset voltages could be found only for the conventional geometry cells. To find onset voltages in the simulations, a cell temperature of 200 K, an ion flux of $3.5 \times 10^{11}/m^2 s$, and an experiment duration of 60 minutes were used as extreme values. The very low arcing activity on the concentrator arrays makes determining an onset voltage problematical. As seen from the table, the simulations predict the onset voltages very accurately. The onset voltages observed during the experiment are a significant finding by the PASP Plus experiment, since previously it was believed by the space power community that solar arrays could be operated up to -300V before arcing would become a concern[23]. This experiment has shown that arcing is an issue at much lower voltages, which are at the level of current designs for the Space Station.

116
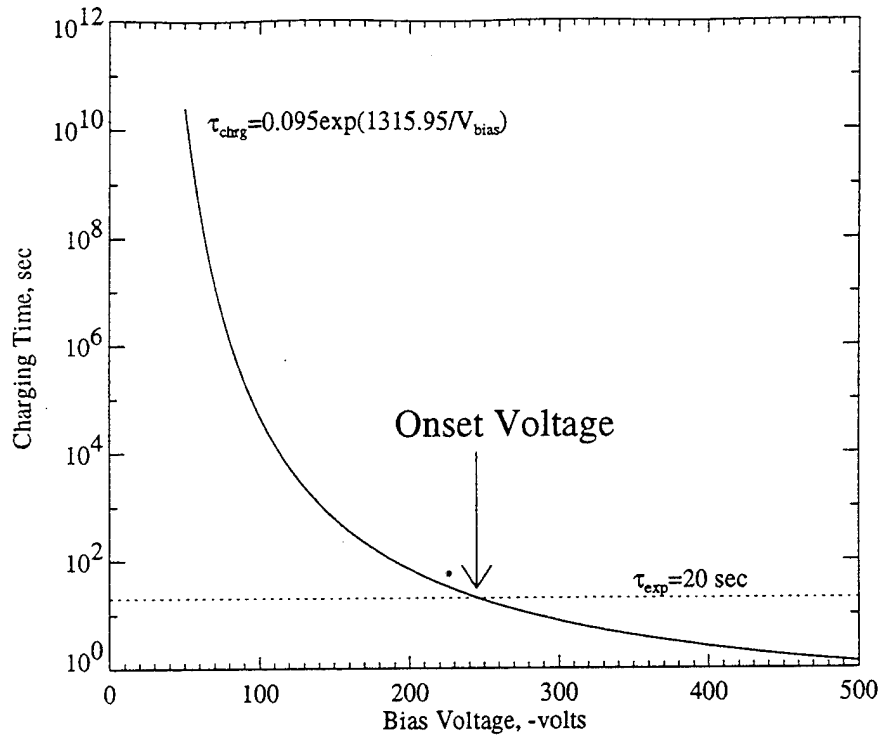
Figure 51: Onset Voltage Based on Experiment Duration and EFEE Charging Time

6.2.2 Area Scaling

From Eq. (97), it can be seen that all else being equal, the arc rate is expected to scale linearly with array area. Thus, it would be expected that module #1 would have an arc rate one third that of module #2. If the arc rate for an array of area A_i is fit using Eq. (100), the scaled rate for a similar array of area A_j would be given by

$$R_j = \frac{A_j}{A_i} R_i = \frac{A_j}{A_i} \frac{1}{C_{1_i} \exp(C_{2_i}/V_{bias})} \tag{102}$$

Figure 42b shows the fit to the arc rate of the silicon module #2, which results in coefficients of $C_1 = 0.002677$ and $C_2 = 2011.77$. The scaled equation for silicon module #1 is then

$$R_1 = \frac{160cm^2}{480cm^2} \frac{1}{(0.002677 \exp(2011.77/V_{bias}))} = \frac{1}{0.008031 \exp(2011.77/V_{bias})} \tag{103}$$

Figure 52 shows the fit to the arc rate data of silicon module #1, along with the scaled fit from Eq. (103). The solid line is the fit to the data for module #1, while the dashed line shows the scaled curve from module #2 given by Eq. (103). Both curves fit the data

equally well, confirming the linear area scaling. Thus, once the arc rate is known for given solar array, the expected rate for a similar array of different size can be determined from a simple area ratio scaling. A similar scaling was conducted on the two thin GaAs/Ge arrays (modules #4 and #6), which had an area ratio of 20 to 12. Scaling the fit to the data for module #4 in Figure 44d using Eq. (102) results in an expected rate on module #6 of

$$R_6 = \frac{192cm^2}{320cm^2} \frac{1}{(0.0628\exp(2779.69/V_{bias}))} = \frac{1}{0.105\exp(2779.69/V_{bias})} \tag{104}$$

Again, the scaled curve fits data as well as the curve found by fitting the data directly.
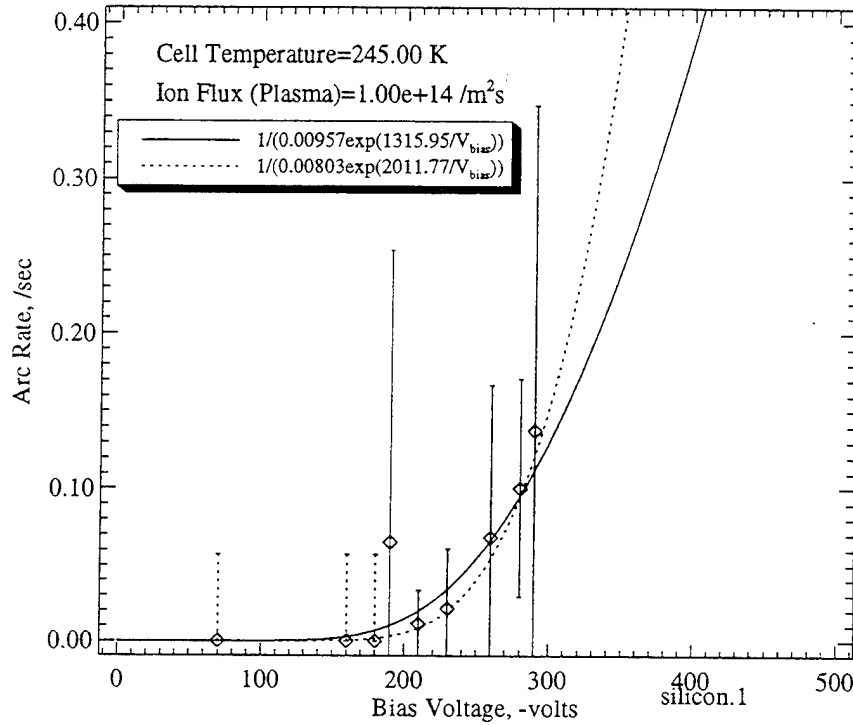
Figure 52: Area Scaling on Silicon Module #1

6.2.3 Dielectric Thickness Scaling

The thickness d of the solar array dielectric layer (i.e. coverglass and adhesive) is expected to be a key parameter in determining the arc rate. As the dielectric thickness is increased, the arcing rate is expected to decrease, since it is this thickness that determines the strength of the electric field in the region of the triple junction ($E = -\phi/d$). However, a thicker
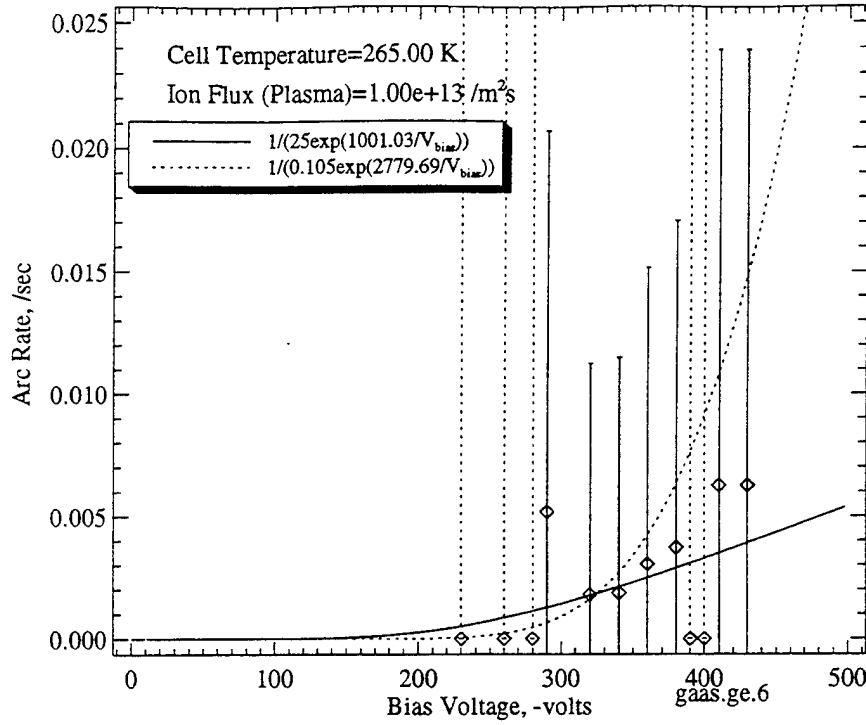
Figure 53: Area Scaling on GaAs/Ge Module #6

dielectric also results in an increased mass. Thus, there exists a trade-off between an acceptable level of arcing and solar cell mass. The coefficients in Eq. (100) are both functions of the dielectric thickness d, with C_1 being related to d through d_i given by Eq. (29). The coefficients for a cell of dielectric thickness d_1 can be scaled to a cell of thickness d_2 by

$$
\begin{aligned}
C_{1_2} &= \frac{d_1 \sum_n b_n \left(\frac{y}{d_1}\right)^{1/2n}}{d_2 \sum_n b_n \left(\frac{y}{d_2}\right)^{1/2n}} C_{1_1} \\
C_{2_2} &= \frac{d_2}{d_1} C_{2_1}
\end{aligned}
\tag{105}
$$

This scaling, however, assumes that the other parameters in Eq. (97) remain constant between the two cells. Unfortunately, this is not necessarily the case. In particular, the average value of the enhancement factor β of the emission sites that arc varies between cells. Since this parameter appears within the exponential term, it will strongly affect the arcing rate, and must be accounted for in order to scale between cells of differing dielectric thickness. Figure 54 shows the variation of β with bias voltage for the thin and thick GaAs/Ge modules obtained through the simulation. This shows that the average enhancement factor decreases with bias voltage for both arrays, and the average enhancement factor on the

119

thick cell is approximately 1.25 times that of the thin cell. Thus, the coefficients C_1 and C_2 can be scaled by this factor, β_f, to take into account the difference in the enhancement factor between the two cells. Scaling the coefficients from the fit to the thin GaAs/Ge
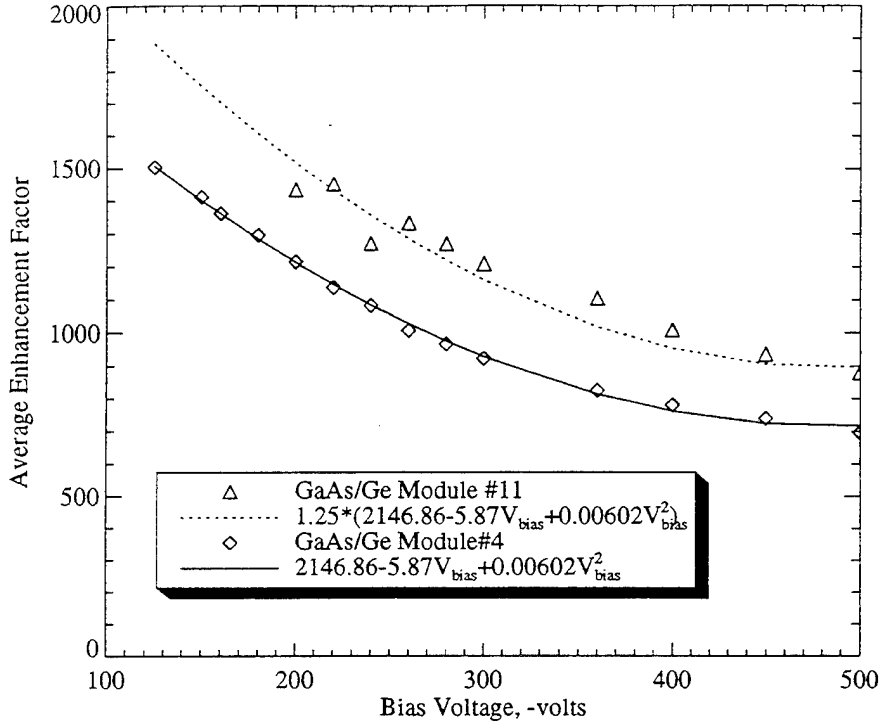
Figure 54: Average Field Enhancement Factor Variation on GaAs/Ge Modules #4 and #11

module #4 in Figure 44d using Eq. (105) and adjusting for the variation in the field enhancement factor yields coefficients for the thick GaAs/Ge module #11 of $C_1 = 0.0176$ and $C_2 = 3313.39$. Figure 55 shows a comparison of the scaled fit and the fit to the data itself. The scaled fit is somewhat lower than the fit to the data, but is still within the error bars. The large scatter in this data set makes the results somewhat inconclusive, but the dielectric scaling does appear valid. Unfortunately, in order to perform this scaling, the simulation must be run in order to determine the relationship between the average β values for the cells being examined. Once this relationship is known, empirical data from a cell of one dielectric thickness can be scaled to predict arcing rates for a similar array with a different dielectric thickness. Thus, the trade between arcing and mass can be conducted either using the simulation itself to predict arcing rates, or by measuring arcing on one cell and then scaling for varying dielectric thicknesses.
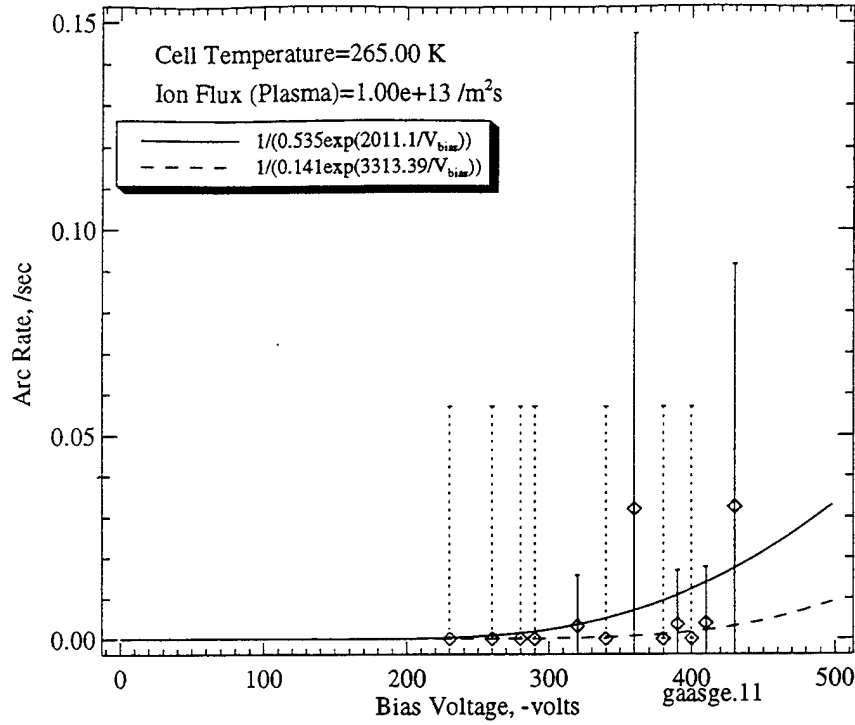
Figure 55: Dielectric Thickness Scaling on GaAs/Ge Module #11

6.2.4 Work Function Scaling

The work function ϕ_w of the interconnector determines the magnitude of enhanced field electron emission. Thus, cells will a lower work function will exhibit higher electron emission and, thus, have a higher arc rate. The work function affects the Fowler-Nordheim coefficients A and B in Eqs. (7) and (8). The coefficients from the fit using Eq. (100) can thus be scaled for cells with a different work function by

$$
\begin{aligned}
C_{1_2} &= 10^{(4.52/\sqrt{\phi_{w_2}} - 4.52/\sqrt{\phi_{w_1}})} \sqrt{\frac{\phi_{w_2}}{\phi_{w_1}}} C_{1_1} \\
C_{2_2} &= \left(\frac{\phi_{w_2}}{\phi_{w_1}}\right)^{1.5} C_{2_1}
\end{aligned}
\tag{106}
$$

Because no two modules on PASP Plus differ only in work function, this scaling cannot be tested independently. Instead, this scaling, along with the area and dielectric thickness scalings, were applied to scale the silicon module #1 fit to the APSA module #5 data. The cell properties for these modules are listed in Table 2. As well as having different thicknesses and work functions, these cells also have different dielectric constants and secondary electron yield characteristics. Also, as noted previously, the silicon cells are believed to have a higher

121

emission site density, which would result in a different β variation between the two modules than was determined from the simulations. Thus, the scaling, which assumes that these properties are the same, are expected to yield somewhat incorrect results. Applying the scalings from Eqs. (102), (105), and (106) to the coefficients from the fit shown in Figure 41b yields coefficients for the APSA module of $C_1 = 0.168$ and $C_2 = 1043.02$. In performing these scalings, a value of 1.4 was used for β_f based on the simulation results shown in Figure 38. Figure 56 shows the scaled curve, along with the fit to the data itself. The scaled curve (shown as a dashed line) is somewhat higher than the fit, but still reasonably represents the arcing activity. The scalings were also applied to the silicon module #1 fit in Figure 41d. The resulting coefficients were $C_1 = 0.00138$ and $C_2 = 2878.86$. The scaled curve (dashed) and actual fit (solid) are shown in Figure 57. Again the scaled curve is somewhat high, but still reasonably describes the arcing rate. Thus, all of the scalings can be applied to the results of testing a single module to estimate the arcing rates on arrays with different areas, dielectric thicknesses, and interconnect work functions.
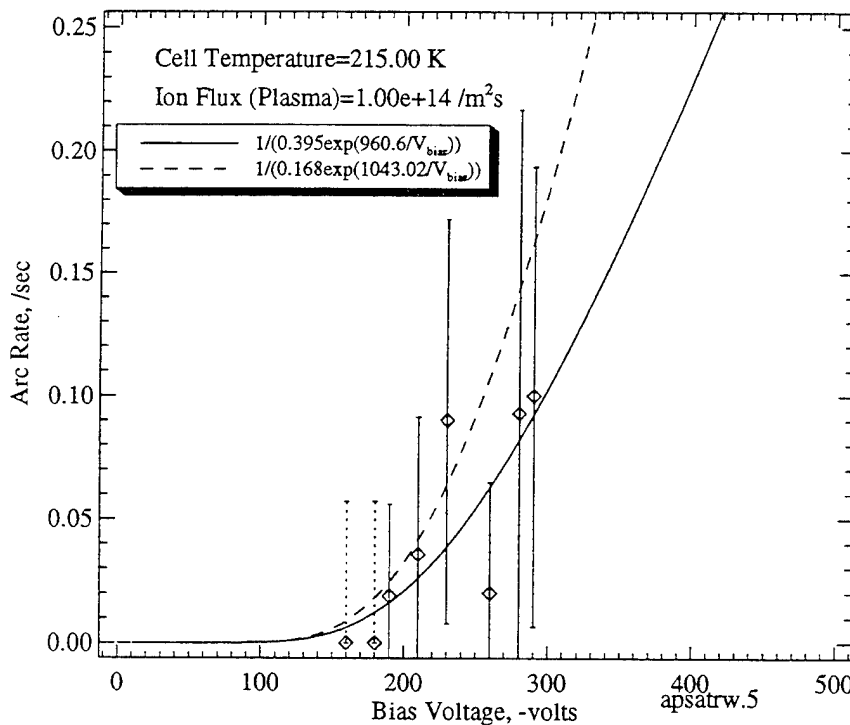
Figure 56: Dielectric Thickness, Area, and Work Function Scaling on APSA Module #5 (Days 94234-94308)
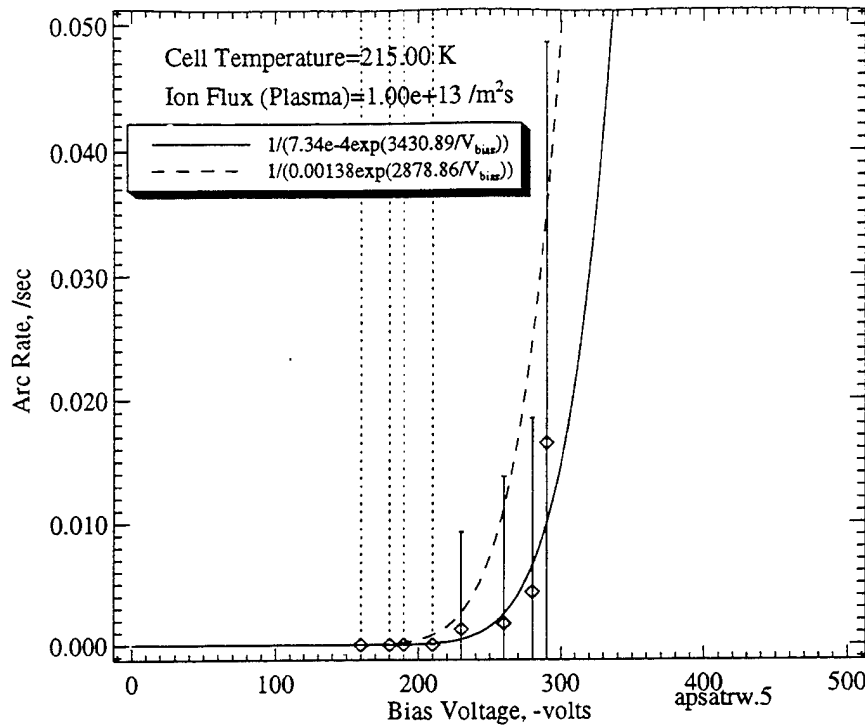
Figure 57: Dielectric Thickness, Area, and Work Function Scaling on APSA Module #5 (Days 95033-95108)

6.3 Arc Rate Dependency on Cell Temperature

As discussed in Section 3.3, the cell temperature is a critical factor in determining the possibility of breakdown and arcing once EFEE runaway has occurred. Shown in Figure 18, high levels of arcing are expected when the cell is coldest and there is a large adsorbed neutral density. As the cell temperature increases, the arcing will sharply decrease until at some critical temperature there will not be a sufficient neutral density to allow breakdown and the arcing rate will drop to zero. This critical temperature is a strong function of the ambient neutral density and bias voltage. Because the neutral density was not measured during the PASP Plus experiment, the effect of neutral density cannot be examined directly. However, the ambient neutral density and plasma density are roughly correlated, as shown in Figure 30. Thus, it will be assumed that the neutral density will be higher at points of high ion flux. The importance of the neutral density is shown in Figure 58, which shows the critical ambient neutral density needed for breakdown at various bias voltages and cell temperatures, with an assumed desorption cross section Q_{ESD} of $1 \times 10^{-19} m^2$,

123

for the APSA cells. The horizontal dashed lines show the maximum and minimum neutral density for the APEX orbit generated using the EWB software. This shows that the cell temperature and expected neutral density regime of the experiment are in the area where neutral density and cell temperature dependencies would be expected. If, for example, data was gathered over the entire density range at -300V and 220K temperature, it would be expected that there would be arcing only above a density of approximately $1 \times 10^{11}/m^3$, while at 250K arcing would only be expected to occur at points above $1 \times 10^{13}/m^3$. At approximately 275K, the neutral density needed for breakdown exceeds that expected for the experiment, at which point no further arcing would be expected at increasing cell temperatures. In this chapter, the method of analysis is to examine the variation of arc rate with one parameter while keeping the remaining parameters constant. Because points of constant neutral density cannot be found, the varying neutral density for the points of constant voltage, cell temperature and/or ion flux examined in this chapter can result in a large scatter in the data.
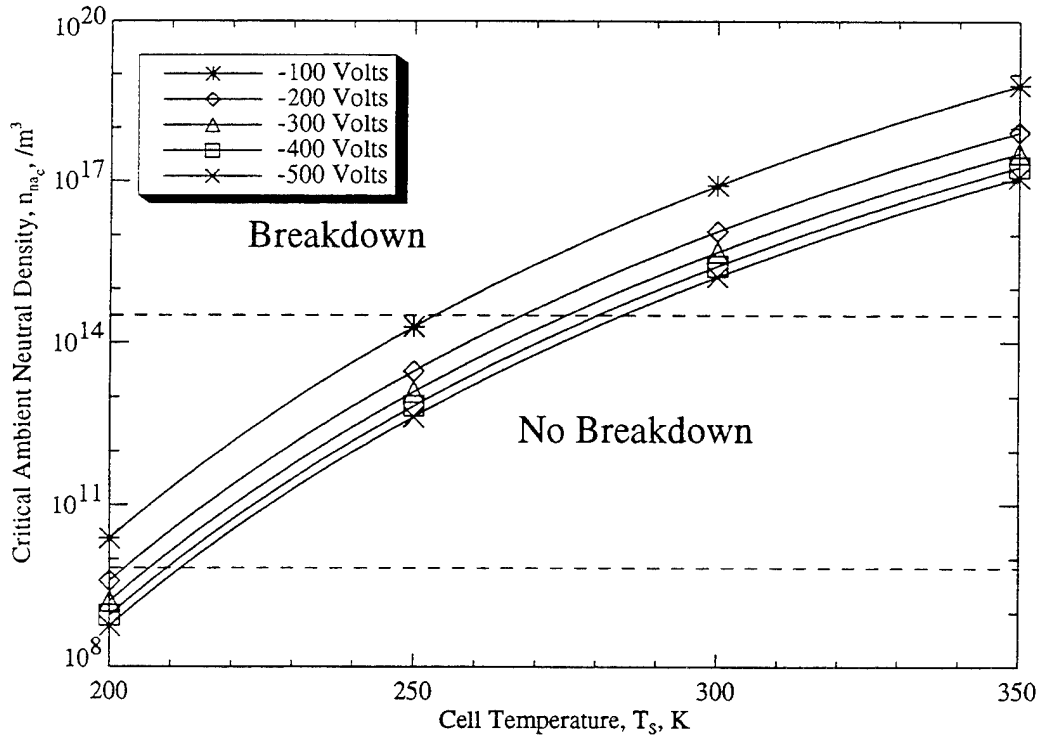
Figure 58: Expected Critical Ambient Neutral Density Variation with Temperature for Varying Bias Voltages for the APSA Module #5

Figures 59 and 60 show the variation in arc rate with cell temperature for the silicon module #1 during days 94234-94308. In Figure 59a, which is at -300V and an ion flux

of $1 \times 10^{13}/m^2 s$, there is some arcing up to approximately 270K, beyond which no arcs occurred. In Figure 59b at the same voltage and an order of magnitude higher ion flux, some arcs occur at the high temperatures, although most of the data points show no arcs. Figure 59c, which is at another order of magnitude higher ion flux, there is only data present at the high temperatures, since the ion density is highest during sunlight. At this point, most of the trials still show no arcs occurring.

In Figure 59d, the bias voltage is now -340V. Again, at the low ion flux, arcing occurs only at the cold temperatures. Once the high ion flux is reached, arcing is occurring in over half of the trials. Figures 60a-c show the arcing variation with cell temperature at -380V. At this voltage, arcing occurs often at the low temperatures. At the high ion flux, which in this case is only $5 \times 10^{14}/m^2 s$, arcing occurs in almost every trial at the high temperatures.

Figures 60d-f show the data at the highest voltage, -430V. At the low ion flux, arcing occurs in all but one trial below 270K, but only once (possibly) above 270K. However, at only half an order of magnitude higher ion flux, large amounts of arcing occur over the entire temperature range. And at an ion flux of $1 \times 10^{14}/m^2 s$, arcing occurs during every trial regardless of temperature. Thus, there is clearly a dependence of arcing on cell temperature, which is also dependent on both the ion flux and bias voltage. As bias voltage and/or ion flux increases, so too does the critical cell temperature and the possibility of breakdown.

The APSA module #5 has shown the highest sensitivity to cell temperature during the experiment. Figure 61 shows the arc rate variation with cell temperature for the APSA module at -300V and an ion flux of $1 \times 10^{13}/m^2 s$ on days 95033-95108. Arcing activity is seen only at the low temperatures. Because the APSA cells are thin, and the module was mounted over a cut-out on the Deployed Panel, the temperature rise time is very fast. Thus, there is little data in the transition temperatures. Figure 62 shows the variation of arc rate with cell temperature for the APSA module at all ion fluxes and both sets of days, with a bias voltage of -300V. Except for two single arc points, there is no arcing above approximately 230K. Since during operation the cells will only be operating in sunlight, there should not be arcing on this type of cell during most of the orbit. However, as the cells exit eclipse, they will still be cold and will arc. As they heat up, the cells will thermally desorb neutrals,
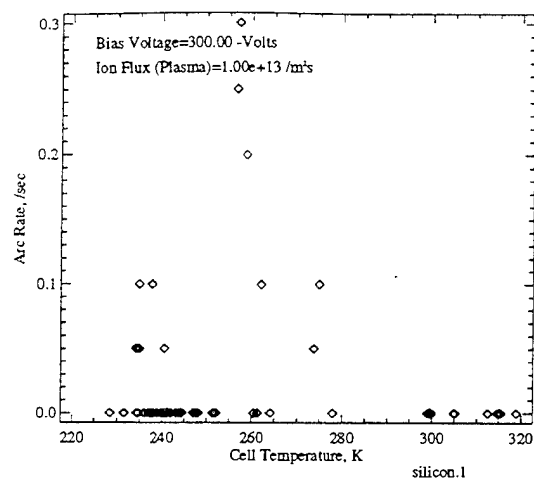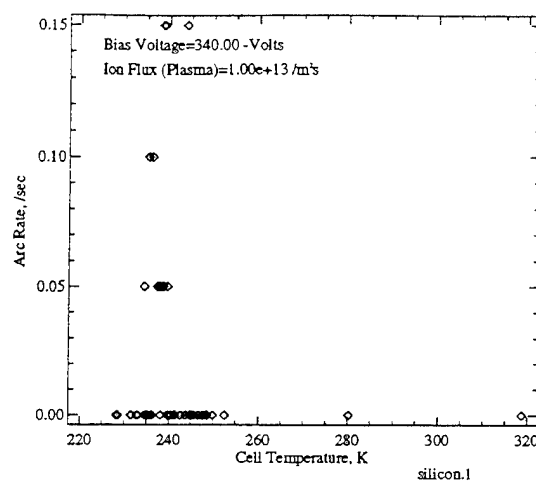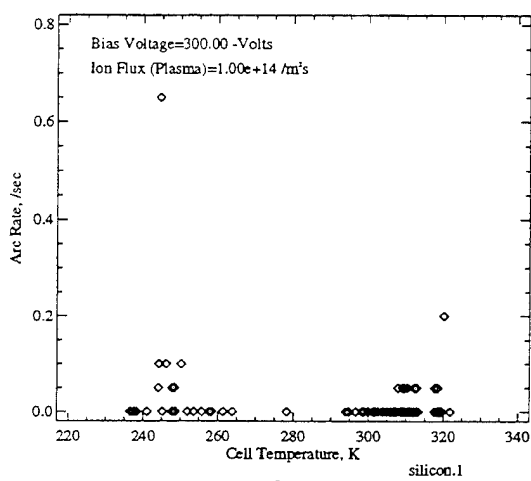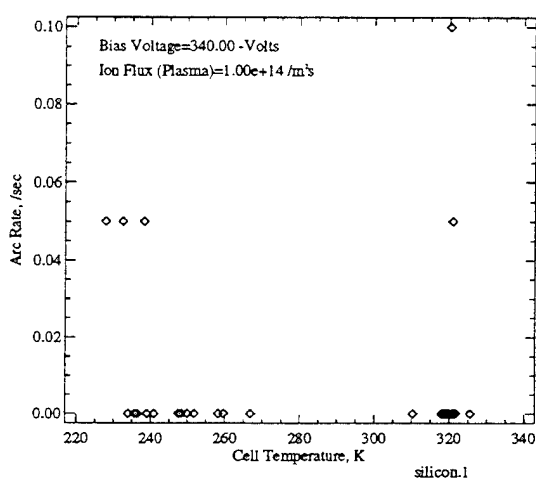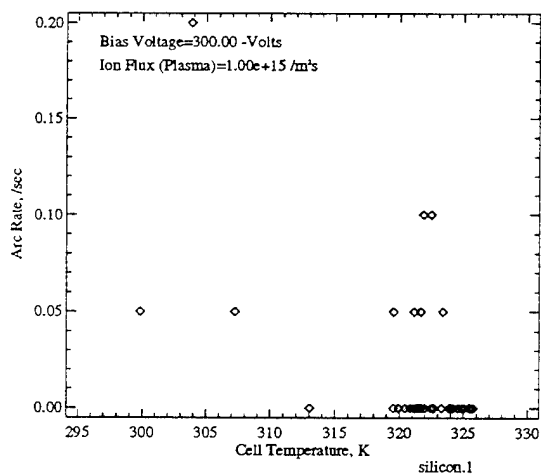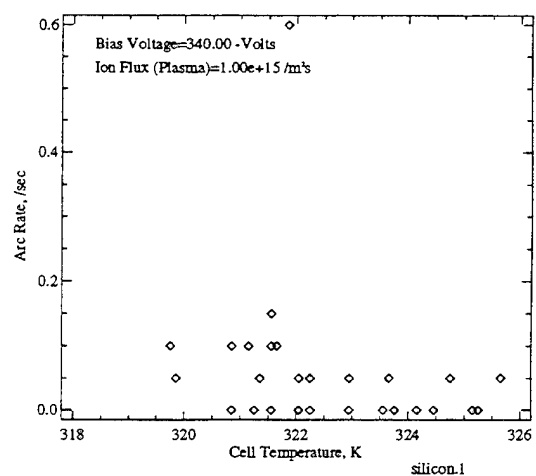
Figure 59: Arc Rate Variation with Cell Temperature on Module #1 at -300V and -340V
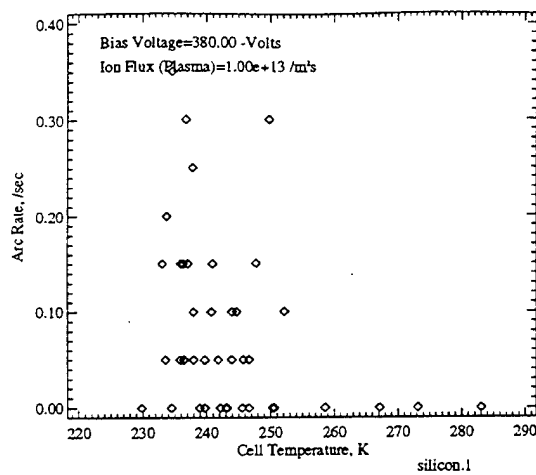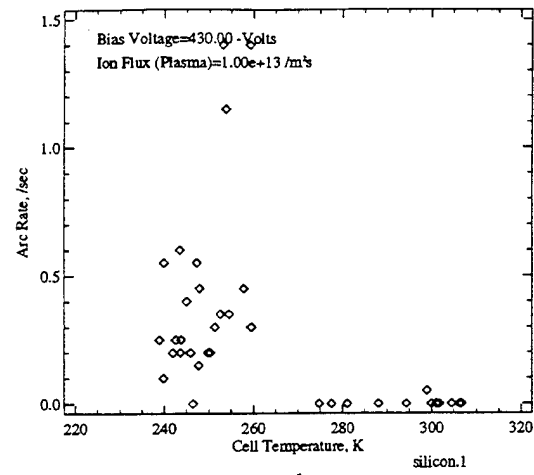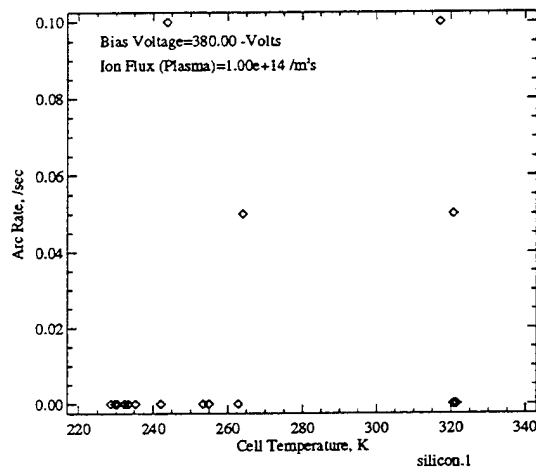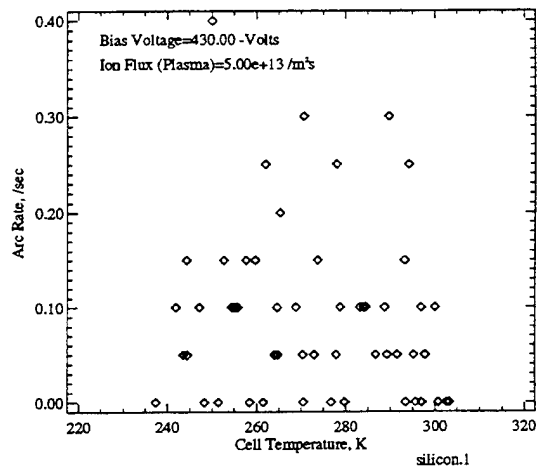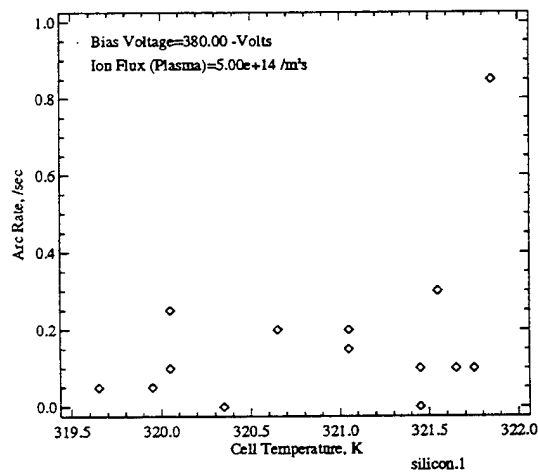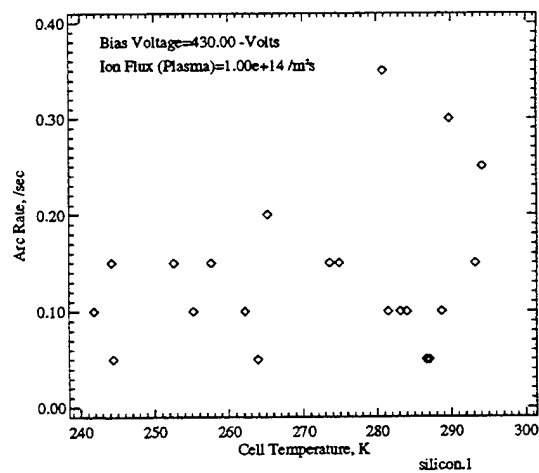
Figure 60: Arc Rate Variation with Cell Temperature on Module #1 at -380V and -430V

which will further enhance the desorbed neutral cloud over the triple junction and increase the chance of breakdown. This effect was seen during the experiment, when increased arc rates were measured on both the silicon and APSA modules during the eclipse-sunlight transition periods[76].
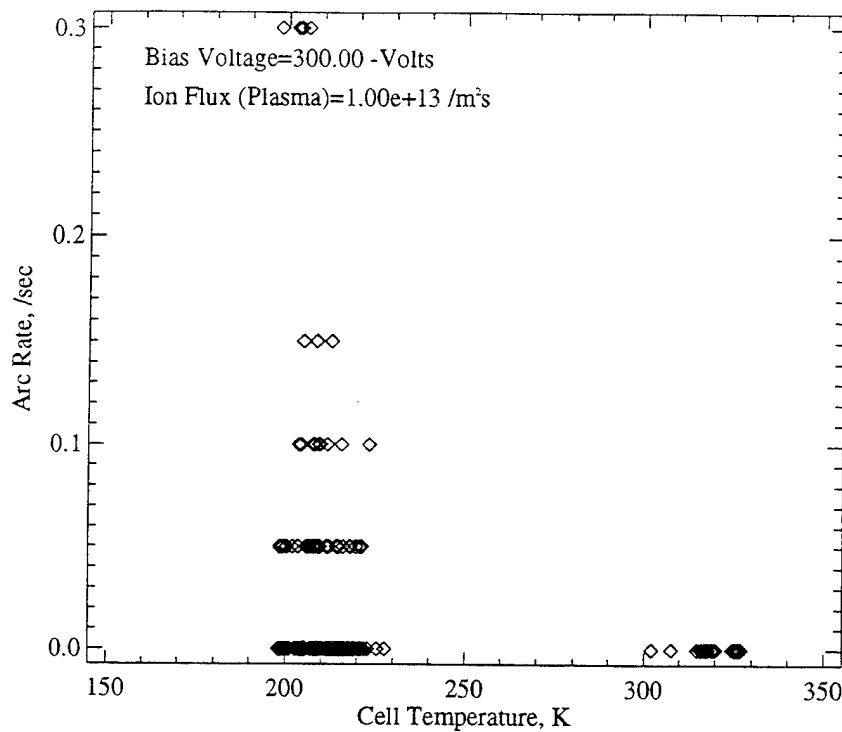
Figure 61: Arc Rate Variation with Cell Temperature on APSA Module #5 at -300V and $1 \times 10^{13}/m^2s$ ion flux (days 95033-95108)

Figure 63 shows the cell temperature variation of the averaged arc rate data for the silicon modules #2 and #5. Graph a shows the results for silicon module #2 on the low days at -300V and an ion flux of $1 \times 10^{14}/m^2s$. At low temperatures, there is a high level of arcing, which does not seem to be dependent on the temperature. At the high temperatures, the arcing rate has dropped to near zero. Graph b shows the results for the same module on the high days at -360V and an ion flux of $1 \times 10^{13}/m^2s$. This graph has the same form as seen in the simulation, shown in Figure 18. At the lowest temperatures, the arc rate is high and relatively steady with increasing temperature. At approximately 245K, however, the arc rate quickly drops, and is zero at the high temperatures. Graphs c and d show similar results for the APSA module #5 at -300V on both sets of days. Although there are fewer data points for this module, there is clearly arcing only at the low temperatures.
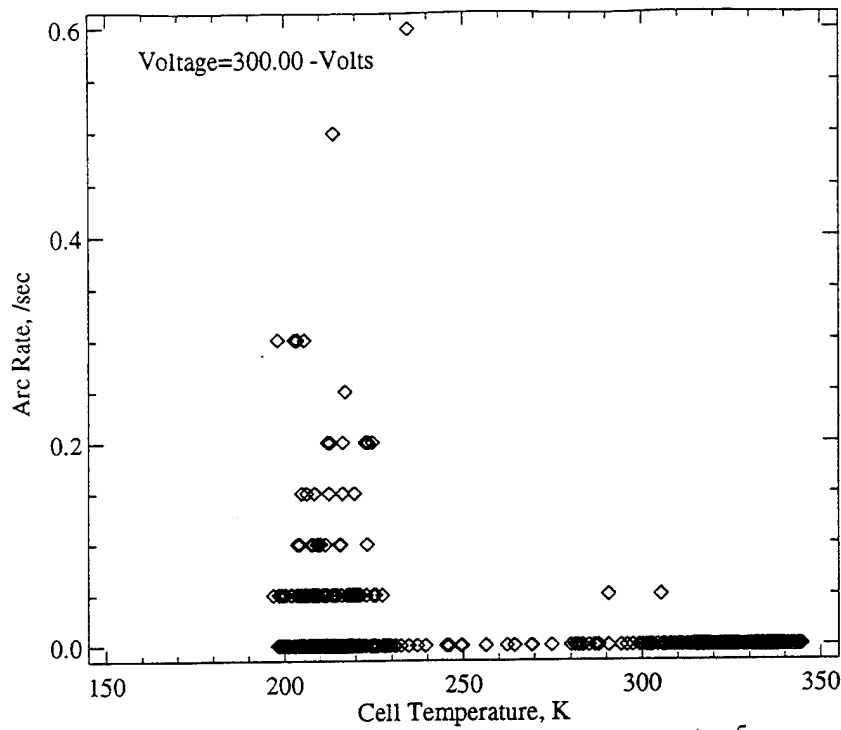
Figure 62: Arc Rate Variation with Cell Temperature on APSA Module #5 at -300V

Figure 64 shows similar results for the thin and thick GaAs/Ge modules #4 and #11. These modules also show much more arcing activity at the low cell temperatures than at the high temperatures.

The temperature dependence seen during the experiment is an important validation of the model. The other two models proposed to explain solar array arcing[78, 97] both have no cell temperature dependence. This temperature dependence supports the theory that adsorbed neutral gas is desorbed during the charging process and breaks down during the arc discharge. Because the ambient neutral density was not measured, the critical temperatures for arcing on each module cannot be properly determined. However, from Figure 62, the APSA module appears to have a critical temperature of 230K at -300V. From Figure 59, the standard silicon cells have a critical temperature of approximately 280K at -300V and an ion flux of $1 \times 10^{13}/m^2s$.
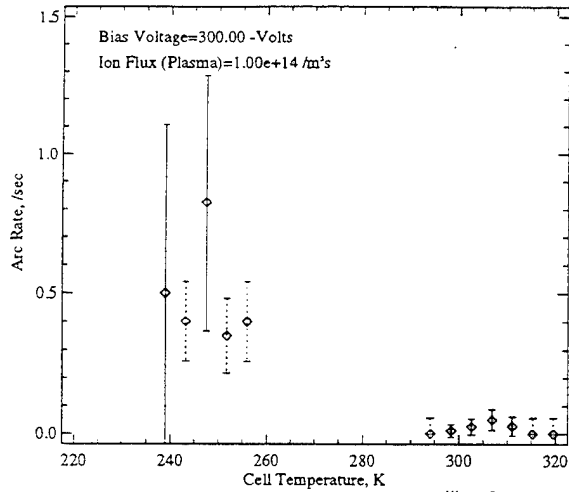
a: Low Days (94234-94308) Average
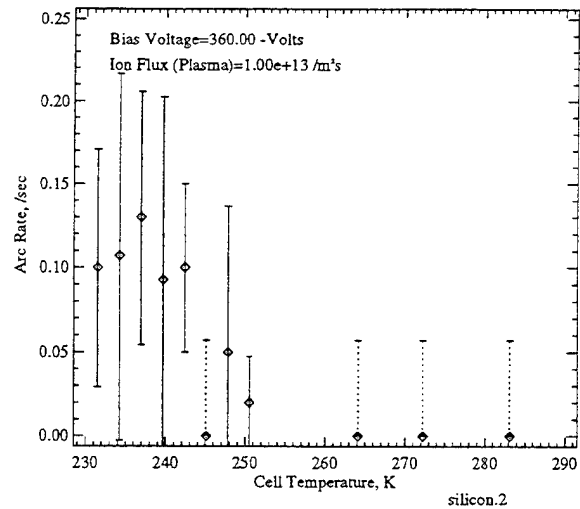
b: High Days (95033-95108) Average
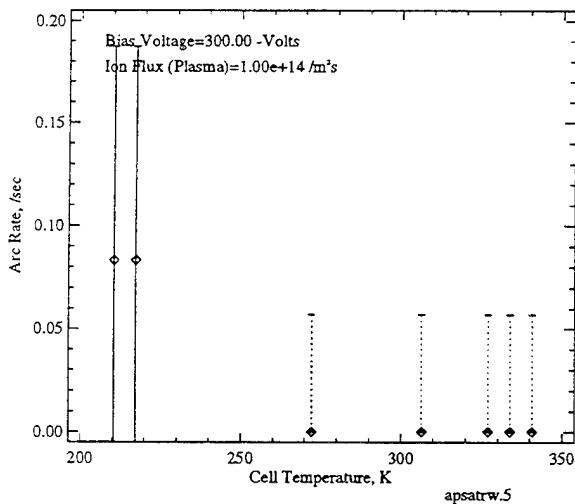
c: Low Days (94234-94308) Average
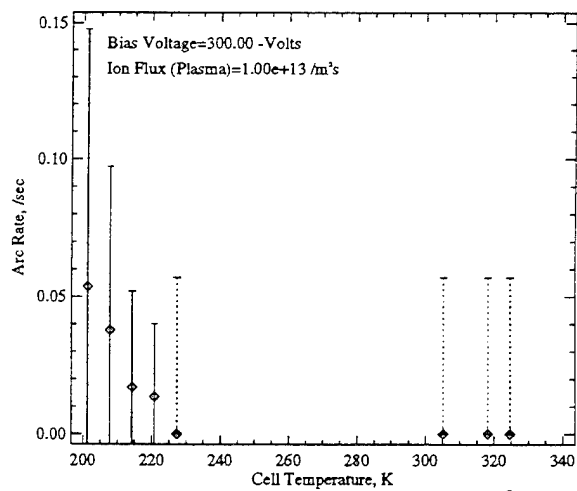
d: High Days (95033-95108) Average

Figure 63: Arc Rate Variation with Cell Temperature for Silicon Modules #2 and #5
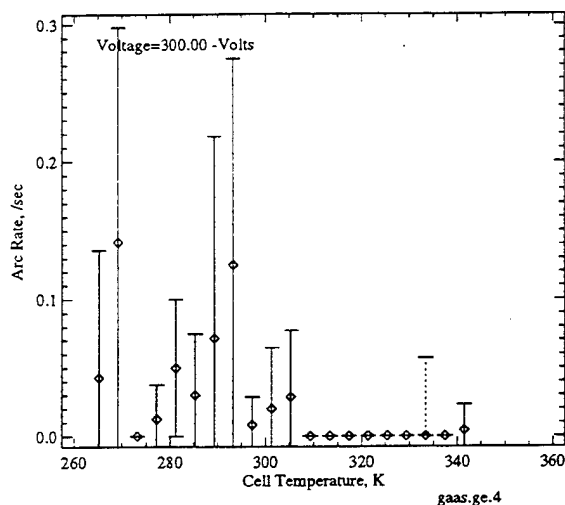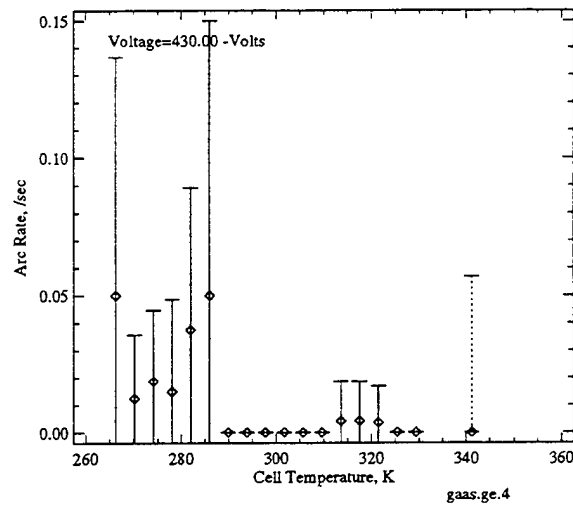
130

a: Low Days (94234-94308) Average   b: High Days (95033-95108) Average
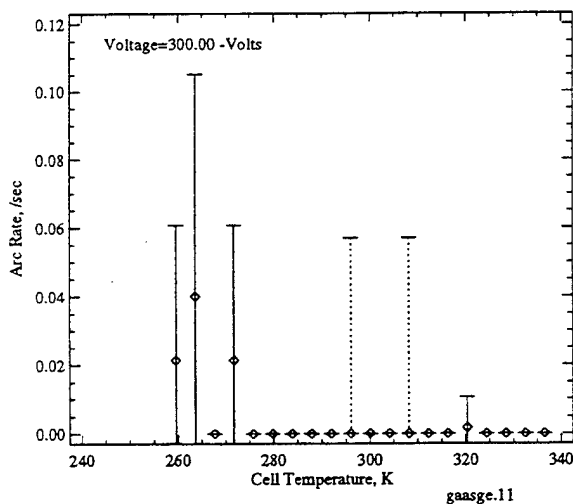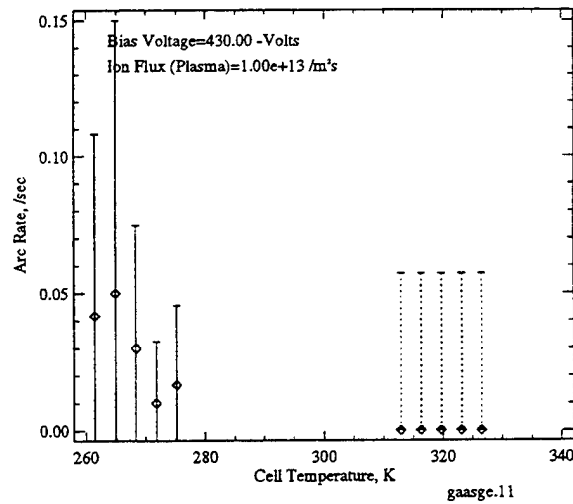
c: Low Days (94234-94308) Average   d: High Days (95033-95108) Average

Figure 64: Arc Rate Variation with Cell Temperature for GaAs/Ge Modules #4 and #11

131

6.4 Arc Rate Dependency on Ion Flux

Another important parameter in determining the arcing rate on a high voltage solar array is the ion flux to the front surface of the array. This flux determines the ion charging time, which, along with the EFEE charging time, determines the interval between successive arcs within the radius of a discharge wave. The ion charging time is given by

$$\tau_{ion} = \frac{[V_e - (V_a - \frac{\Delta Q}{C_{front}})]C_{front}}{en_e v_{ion} A_{cell} \cos \alpha} \tag{107}$$

The term $[V_e - (V_a - \frac{\Delta Q}{C_{front}})]$ is the drop in potential ΔV across the coverglass due to the arc discharge. This is the potential which must be built back up by the incoming ions. The front surface capacitance is given by

$$C_{front} = \frac{1}{d_1/(A_{cell}\epsilon_{d_1}) + d_2/(A_{cell}\epsilon_{d_2})} = \frac{A_{cell}}{(d_1/\epsilon_{d_1}) + (d_2\epsilon_{d_2})} \tag{108}$$

The ion flux is given by $\Gamma_i = n_e v_{ion} \cos \alpha$. Thus, the ion charging time can be rewritten as

$$\tau_{ion} = \frac{\Delta V}{e\Gamma_i \left(\frac{d_1}{\epsilon_{d_1}} + \frac{d_2}{\epsilon_{d_2}}\right)} \tag{109}$$

Note, the cell area cancels out in the equation, and thus the ion charging time is not a function of cell area. The implicit assumption in this is that the surface charge is discharged evenly by the discharge wave, or at least that the charge is recharged by incoming ions in the same spatial distribution as it is discharged. On average, this is a valid assumption, since otherwise charge would continue to build or be depleted, which would eventually either draw in the discharge wave, or stop the wave from spreading.

Given two arcing rate data points at different ion fluxes, but at the same bias voltage, the potential drop ΔV may be determined. Since the EFEE charging time is not a function of ion flux, the EFEE charging times for the two points will be the same. Thus, subtracting

the two total charging times yields

$$\begin{aligned}
\tau_2 - \tau_1 &= \left(\tau_{ion_2} + \tau_{efee_2}\right) - \left(\tau_{ion_1} + \tau_{efee_1}\right) \\
&= \frac{\Delta V}{e\Gamma_{i_2}\left(\frac{d_1}{\epsilon_{d_1}} + \frac{d_2}{\epsilon_{d_2}}\right)} - \frac{\Delta V}{e\Gamma_{i_1}\left(\frac{d_1}{\epsilon_{d_1}} + \frac{d_2}{\epsilon_{d_2}}\right)} \\
&= \frac{\Delta V}{e\left(\frac{d_1}{\epsilon_{d_1}} + \frac{d_2}{\epsilon_{d_2}}\right)}\left(\frac{1}{\Gamma_{i_2}} - \frac{1}{\Gamma_{i_1}}\right)
\end{aligned} \tag{110}$$

Therefore, given two charging times τ_1 and τ_2 and their corresponding ion fluxes Γ_{i_1} and Γ_{i_2}, Eq. (110) can be solved for ΔV as

$$\Delta V = \frac{e\left(\tau_2 - \tau_1\right)\left(\frac{d_1}{\epsilon_{d_1}} + \frac{d_2}{\epsilon_{d_2}}\right)}{\frac{1}{\Gamma_{i_2}} - \frac{1}{\Gamma_{i_1}}} \tag{111}$$

Figure 65 shows the arc rate variation with ion flux at a cell temperature of 245K and bias voltage of -300V. In order to determine the potential drop during an arc, two arc rates need to be chosen at different ion fluxes. A fit suggested by the model of the form

$$R = \frac{1}{C_1/\Gamma_i + C_2} \tag{112}$$

was used. However, since only points with a non-zero arcing rate (and thus a finite charging time) can be used, only the non-zero points were fit, shown in Figure 66. From this fit, at an ion flux of $1.2 \times 10^{13}/m^2 s$ the arc rate is 0.05 /sec, corresponding to a charging time of 20 seconds. At a flux of $2 \times 10^{14}/m^2 s$, the arc rate is 0.5 /sec, and the charging time is thus 2 seconds. Substituting these values into Eq. (111) yields a potential drop during the arc of 238.8V. Thus, the surface potential drops to -62.2V, which is near the measured value of on the order of -100V seen in ground experiments[35].

It should be noted that this method of estimating the potential drop is very sensitive to the arc rate and ion flux at the lower of the two ion fluxes, since these terms dominate. Typically, the point where one arc occurs is chosen, to try to make the difference in the ion fluxes greatest. Because points with only one arc have a high relative uncertainty, however, there is thus also a high uncertainty in the value of ΔV. For example, Figure 67 shows a fit to the APSA module #5 at -300V at a cell temperature of 215K. Choosing an arc rate of 0.05 /sec at an ion flux of $4.5 \times 10^{12}/m^2 s$ and 0.145 /sec at $1 \times 10^{14}/m^2 s$ results in a

ΔV of only -45.7V. Although this is not completely unrealistic, it is lower than expected. So, although this does help confirm the model, it is difficult to produce accurate estimates for ΔV without more accurate data.
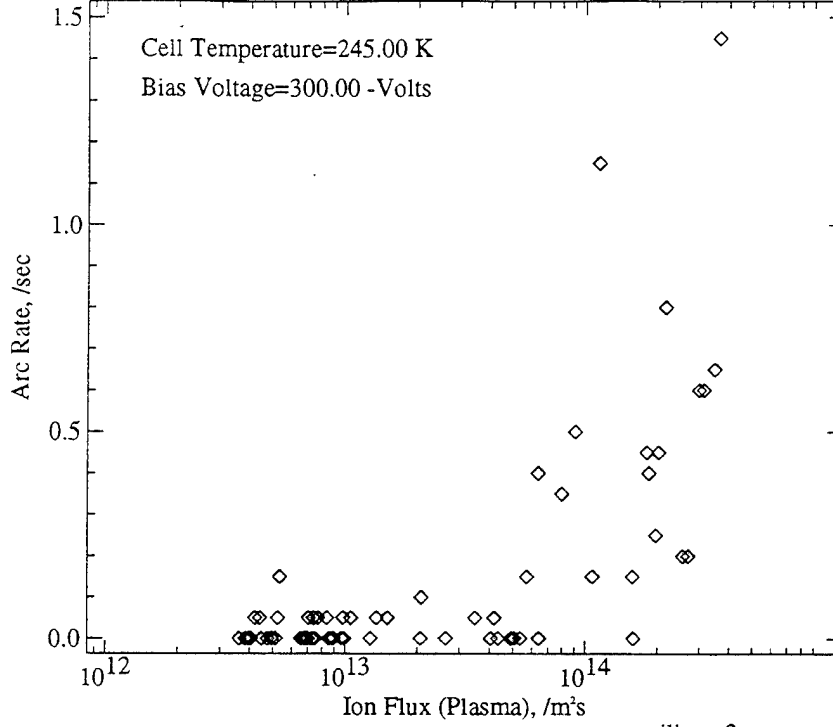
Figure 65: Arc Rate Variation with Ion Flux on Silicon Module #2 at 245K and -300V

6.4.1 Critical Ion Flux

For a finite experiment time τ_{exp}, there will exist a critical ion flux below which the ion charging time will exceed the experiment time. For ion fluxes below this critical flux, the electric field in at triple junction would not become sufficiently large to induce EFEE runaway, and no arcing would be expected. Neglecting the EFEE charging time, the critical ion flux can be determined by setting $\tau_{ion} = \tau_{exp}$ in Eq. (107), so that

$$\Gamma_{i_{crit}} = \frac{(\Delta V)C_{front}}{eA_{cell}\tau_{exp}} \tag{113}$$

Figure 68 shows a graph of the ion charging time variation with ion flux for the standard silicon cells biased to -300V, assuming that the potential drops from -300V to -100V after an arc occurs. For this case, the expected critical ion flux is approximately $1 \times 10^{13}/m^2s$.
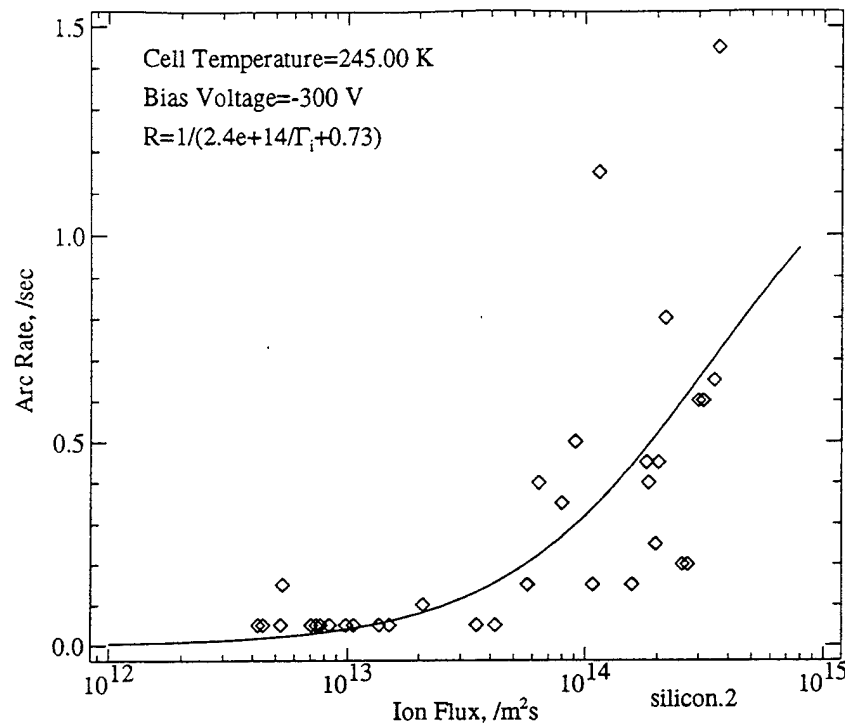
Figure 66: Ion Flux Fit for Silicon Module #2 at 245K and -300V

If the EFEE charging time is not negligible, the critical ion flux will be greater than this value. Figure 69 shows the arc rate variation with ion flux for the silicon module #2. From graph a, for the low days, the critical ion flux appears to be approximately $3 \times 10^{13}/m^2 s$, while the high days in graph c show a critical flux of approximately $4.5 \times 10^{13}/m^2 s$. Thus, since the EFEE charging time is probably not negligible, the model accurately predicts the critical ion flux. However, it should be noted that at the low ion fluxes the neutral density will also probably be low, which could also account for the lack of arcing.

It is important to emphasize that the critical ion fluxes seen in the PASP Plus experiment are for a 20 second experiment duration. If the modules are biased for a longer duration, a lower critical ion flux would be seen, as described by Eq. (113). Thus, for power systems operating in LEO, with typical sunlight durations on the order of 60 minutes, arcing could be seen at ion fluxes much lower than the critical fluxes seen in PASP Plus. From Eq. (113) with a 60 minute bias time, a critical ion flux of approximately $5 \times 10^{10}/m^2 s$ would be expected for the the standard silicon cells. During portions of the orbit, the satellite may not experience any eclipse, resulting in very long periods of continuous biasing. For these portions the orbit, infrequent arcing could be seen at very low ion fluxes. Therefore, if a

135
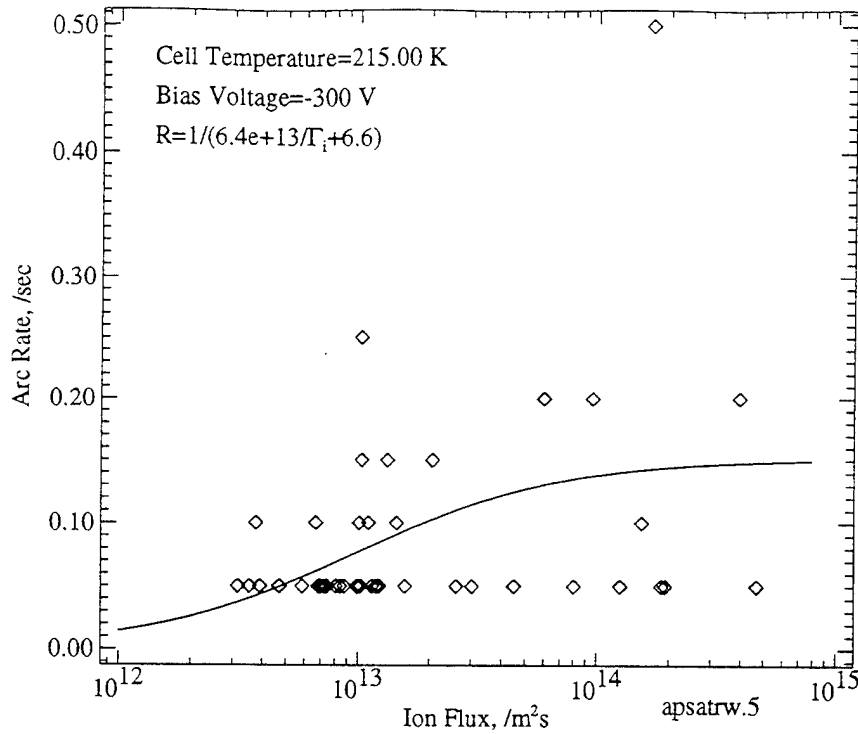
Figure 67: Ion Flux Fit for APSA Module #5 at 215K and -300V

spacecraft has a zero tolerance for arcing, the power system should be operated below the onset voltage even at high LEO orbits, which have a low ion flux.

6.4.2 Wake Effects

When the ram angle is greater than 90°, the solar array modules are in the spacecraft wake. This could result in a much lower ion flux, depending on the wake angle, which would suppress arcing. Wake current collection was studied by Wang[101] for charged plates at zero, small and large wake angles. Small wake angles are defined as $\alpha_w < \theta_0$, where θ_0 is the Mach angle given by $\theta_0 = \sin^{-1}(\frac{1}{M})$. The Mach number M is defined as $M = v_{orbit}/C_s$, where C_s is the ion acoustic velocity $C_s = \sqrt{KT_e/m_i}$. When a plate at a small wake angle ·is biased to even a low voltage, a sheath structure develops on the plate. A presheath near the leading edge is able to collect a large current, while the trailing fully developed sheath region collects a much lower current. For the APEX orbit, the Mach angle is approximately $7^o - 15^o$. Thus, if the ram angle is within approximately 15° of 90° (i.e. $\leq 105^o$) and the side of the biased module is near the edge of the panel, the resulting presheath structure is able
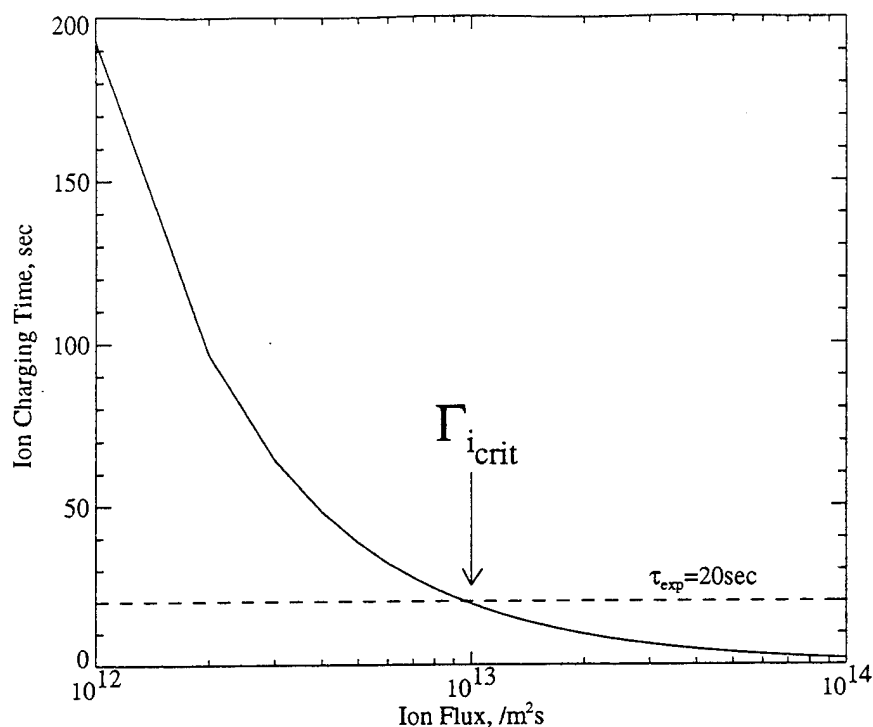
Figure 68: Ion Charging Time for the Silicon Module #2

to draw a significant flux of ions to the negatively biased array. For larger ram angles, a high voltage is required to generate a high ion flux. This is illustrated in Figure 70, which shows that the silicon module #2, which is near the edge, is able to receive a large ion flux at low voltages when slightly in the wake, and is able to receive a high ion flux at large ram angles when biased to several hundred volts. The reason that module #2 can arc in the wake at high voltages can be explained as follows[87]. In the wake, the plasma density is decreased. Thus, the potential structure generated by a high voltage module extends a considerable distance outward, crossing the wake boundary. This potential structure is able to deflect the ion trajectories, causing them to strike the module. If, at low wake angles and low bias voltages, the biased module is not near the leading edge, the collecting surface is not in the presheath as described by Wang[101], since the front portion of the plate is unbiased. Thus, the current collected by the module in this case would be much lower. At low wake angles and high voltages, the potential structure is still able to attract ions from the wake boundary to the module, shown in Figure 71a, which will result in arcing. At high angles, however, the electric field at the wake boundary is too weak to draw ions to the module, shown in Figure 71b. This is the case for the silicon module #1, which is located more than
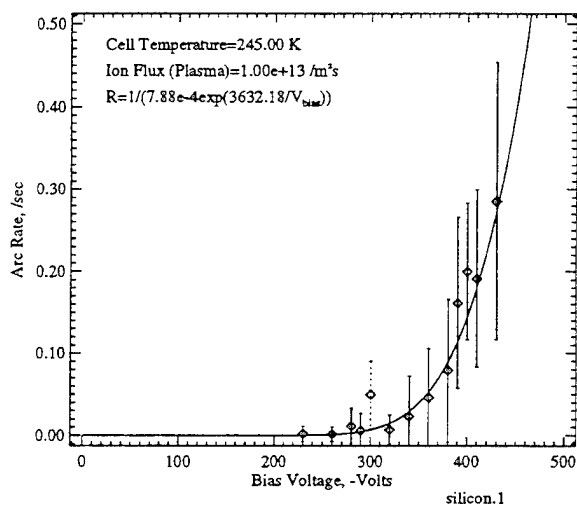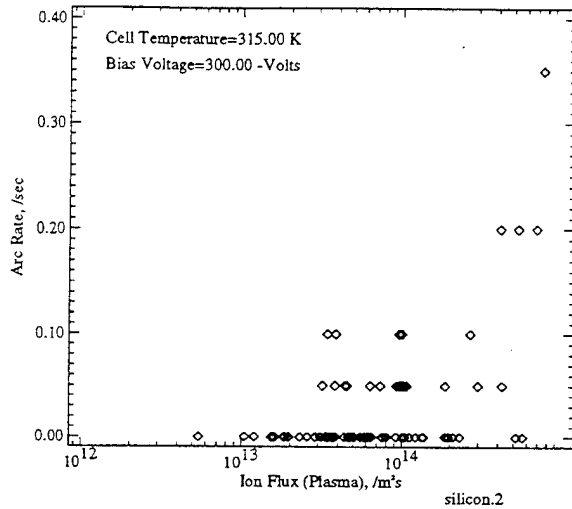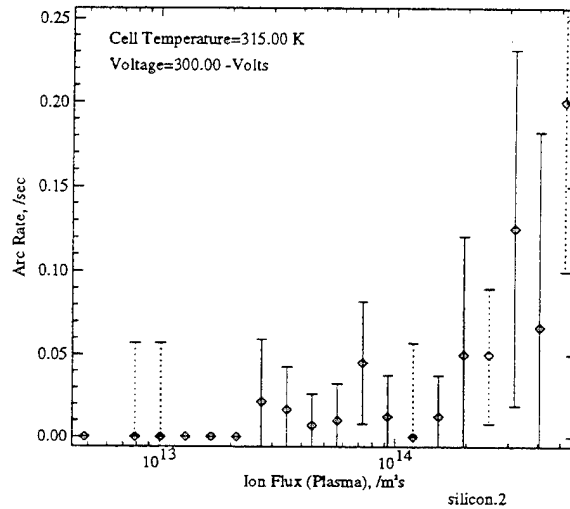
137

a: Low Days (94234-94308)
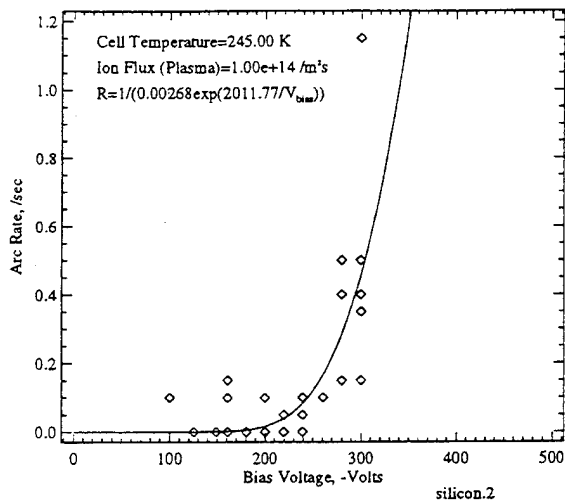
b: Low Days (94234-94308) Average
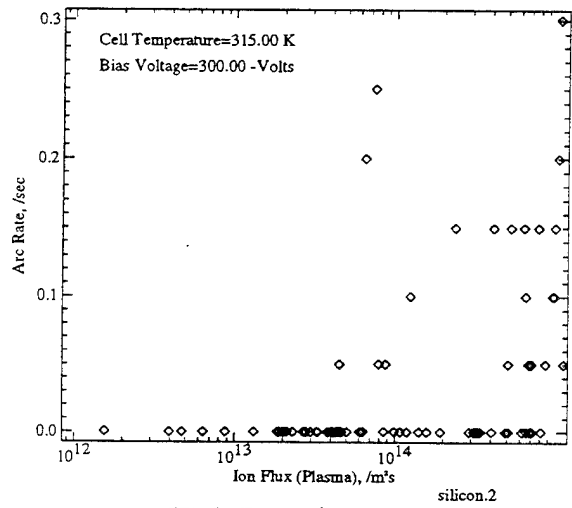
c: High Days (95038-95108)
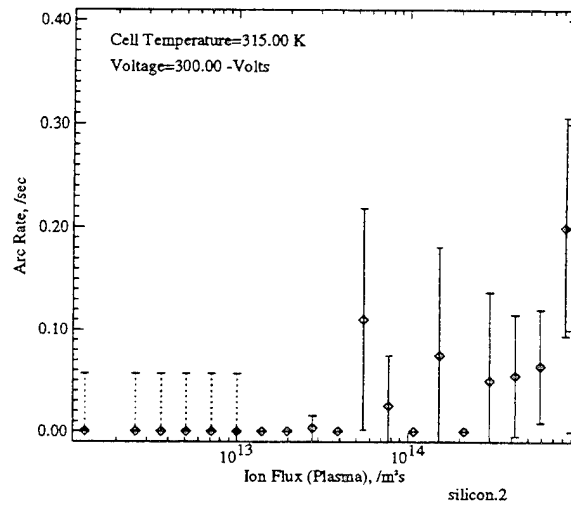
d: High Days (95038-95108) Average

Figure 69: Arc Rate Variation with Ion Flux for Silicon Module #2

half of the panel width away from the leading edge, shown in Figure 20. Thus, it would be expected that module #2 would exhibit arcing up to ram angles of approximately 105° at low voltage and higher angles at high voltage, while module #1 should arc only in ram (i.e. $\alpha \leq 90^o$) at low voltage, and slightly into wake at high voltage. This is exactly what was seen during the experiment[77]. Figure 72 shows the arcing activity on the silicon module #2 during a portion of the orbit where the panel transitions from wake to ram. The lower half of the figure shows the TPM data. The module was seen to arc heavily at ram angles up 120°, and arced to a lesser degree even beyond this angle. Beyond 120°, the spacecraft was also in sunlight, causing the cells to be hot and further suppressing arcing. Figure 73 shows a similar figure for the silicon module #1. In this case, arcing was not observed until the panel was at a low wake angle ($\alpha \leq 105^o$). Because operational solar panels on spacecraft have cells over the entire panel, the results seen for module #2 represent the expected arcing activity during wake operations. Thus, high voltage solar arrays operating in the -400V range can expect to arc heavily up to ram angles of approximately 120°, at at lower levels beyond that.

The APSA module #5, also located in the middle of the Deployed Panel, showed wake effect similar to that of module #1, as seen in Figure 74. On this module, arcing also did not begin until the ram angle less than 105°. However, another interesting phenomenon is seen in the figure. When the panel reached a ram angle of approximately 85°, the arcing rate decreased significantly. The cell temperature at this point was very cold at this point, so arcing would be expected to continue. On possible explanation for the decrease in arcing is that the ambient neutral density was low and the dielectric side surface was thus unable to recharge the surface neutral density to a level sufficient for further arcing to occur.

6.5 Radiation Effects

The electrostatic analyzer on PASP Plus measured the ion and electron spectra in the 30eV to 30keV range. The arc rate variation with both ion and electron counts were examined to test for a possible correlation between arcing and radiation flux. A hypothesis

Ion Trajectories

Presheath

Potential Contours

Panel

α_w
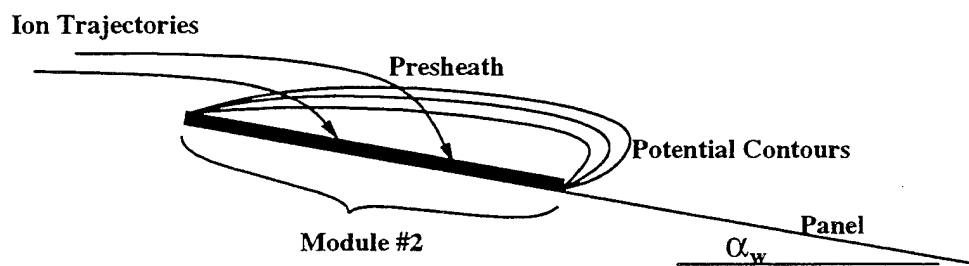
Module #2

a: Small Wake Angle and Low Voltage

Ion Trajectories

Wake Boundary

Module #2

Potential Contours

Panel

α_w
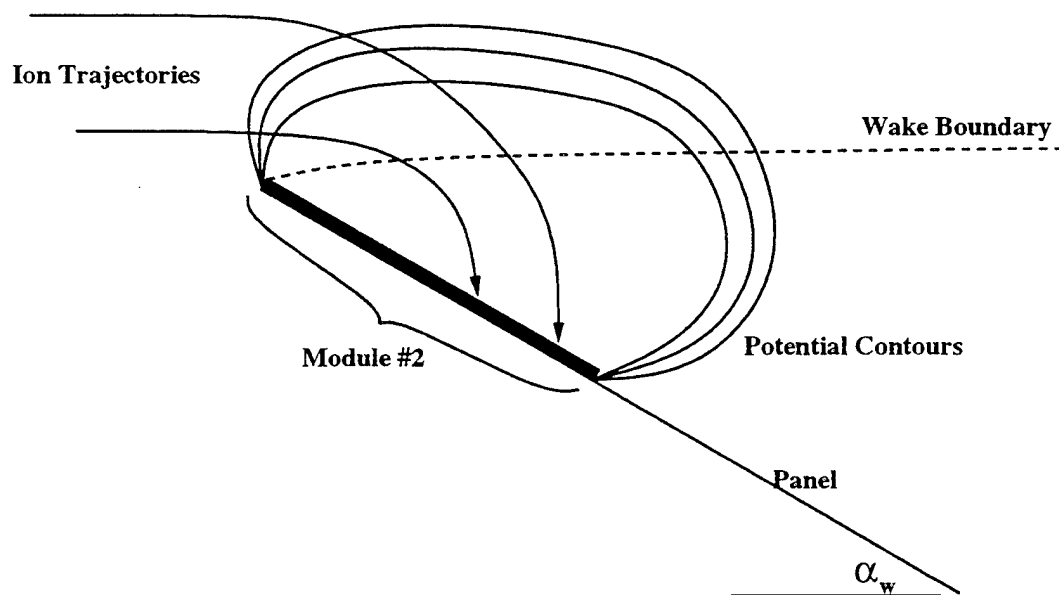
b: Large Wake Angle and High Voltage

Figure 70: Wake Current Collection by Silicon Module #2

Ion Trajectories

Presheath

Panel

Potential Contours

Module #1 α_w

a: Small Wake Angle and High Voltage

Ion Trajectories

Wake Boundary

Panel

Potential Contours

Module #1

α_w
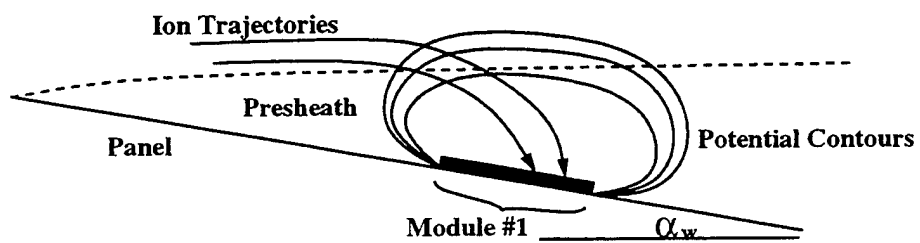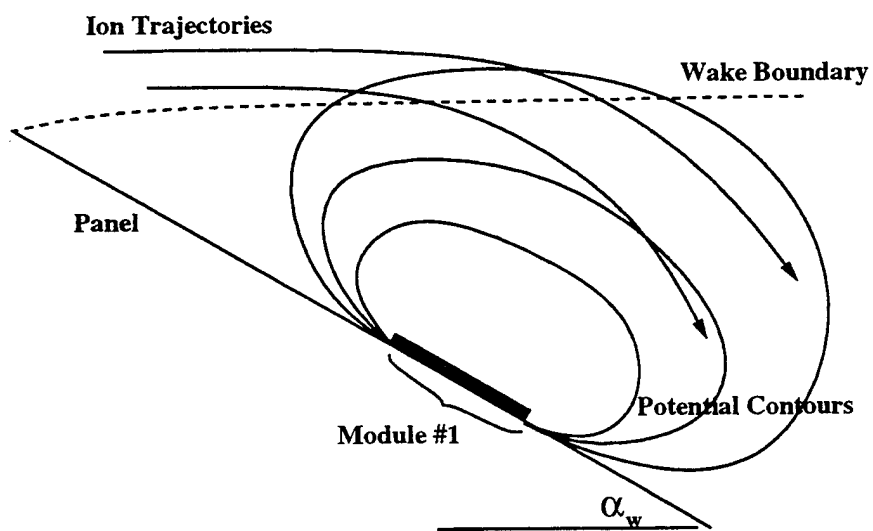
b: Large Wake Angle and High Voltage

Figure 71: Wake Current Collection by Silicon Module #1

for such a correlation is that the radiation deposits charge within the dielectrics, which would then alter the potential structure in the triple junction region and affect the arcing rate[35]. When examining the data, cell temperature, bias voltage, and plasma ion flux were all kept constant, since correlations between arcing and these parameters were all found to exist. Because the majority of the data was taken at low altitudes, where the plasma density was greatest, most of the data is at a relatively low radiation flux, making this study somewhat limited. Figure 75 shows the arc rate variation with ion and electron flux at -300V and $1 \times 10^{13}/m^2s$ on days 95033-95108 for the silicon module #2. No obvious correlation is seen to exist for either ion or electron flux. Similar results are seen in Figure 76 for the APSA module #5 under the same conditions. Thus, the limited data from the PASP Plus experiment indicates no correlation between arcing and radiation flux.

6.6   Summary of Results for Each Module

6.6.1   Standard Silicon Module #1 and #2

From the pre- and post-flight simulations, the standard silicon modules #1 and #2 were expected show moderate levels of arcing in both eclipse and sunlight, with arc rates of up to approximately 0.35 /sec and 1.0 /sec expected at -400V for modules #1 and #2 respectively. These simulations were performed assuming an emission site density of $1.5 \times 10^7 m^{-2}$, which was used for all modules. However, since these cells were produced in 1984, it is believed that the emission site density on modules #1 and #2 may be higher. When simulations were run with an emission site density of $1.5 \times 10^8 m^{-2}$, a much higher arc rate was seen. The actual site density is probably somewhere between the two values used in the simulations. During the experiment, arc rates near the simulated values were observed, with slightly higher levels of arcing being observed, most likely due to a high emission site density. Thus, this shows the importance of minimizing the number of emission sites on the interconnect. An arcing onset voltage of approximately -160V was found. The arcing on module #2 was approximately three times that of module #1, confirming an area scaling. These arrays also showed a temperature dependence for arcing, as expected. At low temperatures, high levels

of arcing were seen, while much lower arc rates were observed at high temperatures. During transition from eclipse to sunlight, when the cells are heating up and thermally desorbing neutrals and futher enhancing the neutral density above the emission site, substantially increased levels of arcing was seen. Thus, when actual satellites are operating at high negative voltages, arcing would be expected upon first entering sunlight, when the cells begin operating and are still cold. A critical temperature for arcing of approximately 280K was observed at -300V and $1 \times 10^{13}/m^2 s$ ion flux, and 260K at -360V and $1 \times 10^{13}/m^2 s$ ion flux. These arrays also showed increasing arc rates with increasing ion flux. The location of these two modules allowed the effect of wake operation to be studied. Module #1, which located near the center of the panel, arced only at ram angles less than approximately 105°. Module #2, located near the edge of the panel, however, was able to draw in ions and arc even at higher angles. Since module #2 more accurately represents the geometry of actual solar panels on spacecraft, arcing would be expected in both ram and wake on LEO high voltage solar arrays.

6.6.2 Silicon Wrap-Through-Contact Module #3

Based on results of previous experiments, the wrap-through-contact cells were expected to show much lower arcing rates than the conventional geometry cells, with a relatively high onset voltage. During the experiment, the arcing rates on this module were much lower than on the conventional cells. However, arcing was observed at an onset voltage of -160V, which is much lower than expected. This voltage is the level to be used on the Space Station, which is using these WTC cells. Thus, arcing could be observed on the Station solar arrays. Beyond the onset voltage, the arc rate did not depend strongly on the bias voltage. Higher levels of arcing were typically seen at the low temperatures, as shown in Figure 77.

6.6.3 APSA Module #5

The very thin APSA cells were expected to show high levels of arcing, with rates up to approximately 0.8 /sec at -300V. During the experiment, high arc rates were observed, but

only at very low temperatures. Above approximately 230K, almost no arcing was observed. The array also showed an increase in arcing during eclipse-sunlight transitions. An onset voltage of as low as -75V was observed, with the rate sharply increasing with bias voltage. This array has shown that arcing can occur at relatively low bias voltages on cells with thin dielectric layers. However, if this type of cell were used on a spacecraft and the arrays were artificially heated above 230K before entering sunlight, arcing could be almost completely suppressed.

6.6.4   Thin GaAs/Ge Modules #4 and #6

The thin GaAs/Ge modules #4 and #6 were expected to show arcing rates comparable to module #5. In the experiment, however, these modules showed somewhat lower arcing levels than expected. Beyond the onset voltage of approximately -125V, arcing on the modules did show a strong voltage dependence. Like the two standard silicon modules, these modules showed an area scaling for the arc rates. These cells also showed the strong temperature dependence expected, with a critical temperature of approximately 310K at -300V and 290K at -430V.

6.6.5   Thick GaAs/Ge Module #11

Because of the thick dielectric layer, this module was expected to show much lower arc rates than the thinner conventional geometry cells. This is what was seen in the experiment, with an onset voltage of -180V. This array also showed a temperature dependence, with a critical temperature of approximately 280K. This module demonstrated that by increasing the dielectric thickness, the arcing onset voltage can be increased, and the subsequent arc rates can be lowered, compared to a cell with a thin dielectric layer. This shows the trade off with the mass of the array and the allowable arcing rate.

6.6.6 GaAs/Ge Wrap-Through-Contact Module #8

Similar to the silicon WTC module, module #8 was expected to show much lower arc rates than the conventional cells, with a higher onset voltage. In the experiment, this module did show a much lower level of arcing, and with an onset voltage of approximately -260V. This onset voltage is significantly higher than that of the other modules, but is still quite low compared to previous experiments. The arc rate did increase slightly with bias voltage. The very low level of arcing made further depencies difficult to determine.

6.6.7 Concentrator Modules #14 and #15

Since the cells in these modules are shielded from the ambient plasma, these modules were not expected to show any significant arcing. The mini-cassegrainian module #14 showed possible arcs in only 24 out of 2957 experiments, all of which were only one or two arcs. There was no voltage dependence evident on this module. The mini-dome module #15 showed possible arcing in 53 of 3059 trials, with several of the trials showing rates on the order of 0.8 /sec at the higher voltages. The very low number of trials showing arcing made further dependencies impossible to study. This experiment has shown that the concentrator designs are extremely resistant to arcing, with arcing rates that were typically at a low enough level to possibly be noise.
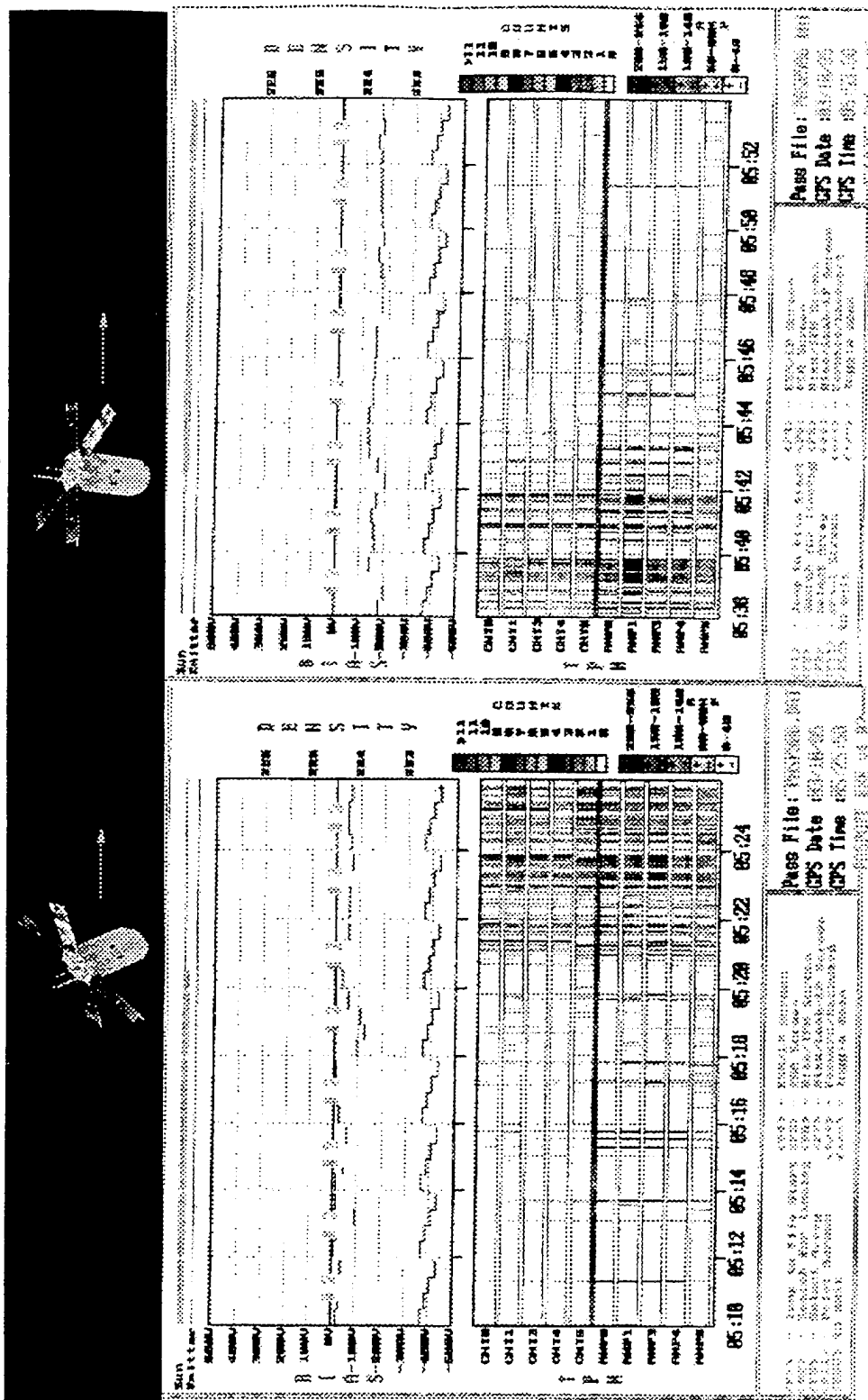
Figure 72: Silicon Module #2 Arcing During Wake Biasing

Figure 73: Silicon Module #1 Arcing During Wake Biasing

Figure 74: APSA Module #5 Arcing During Wake Biasing

148
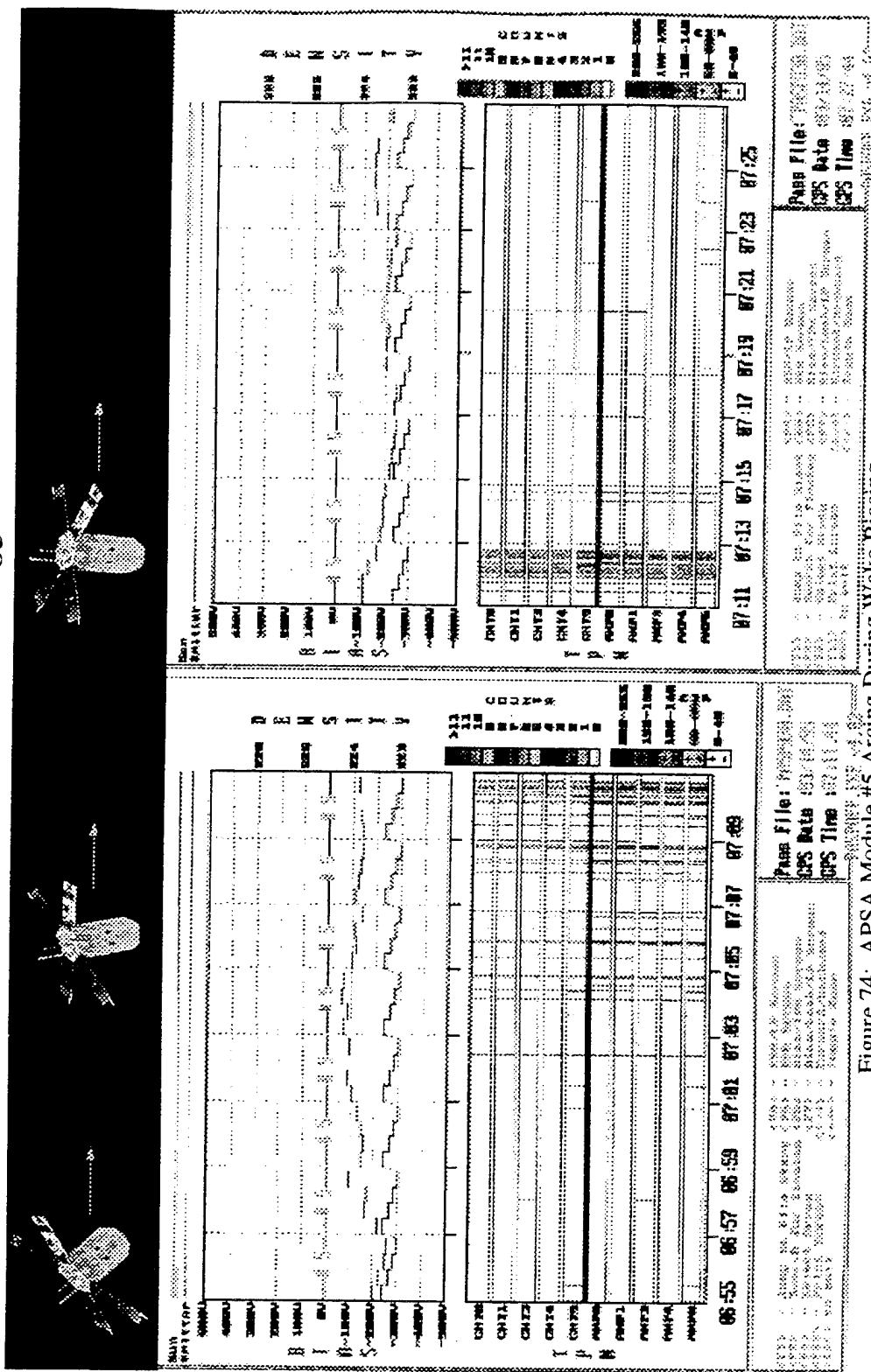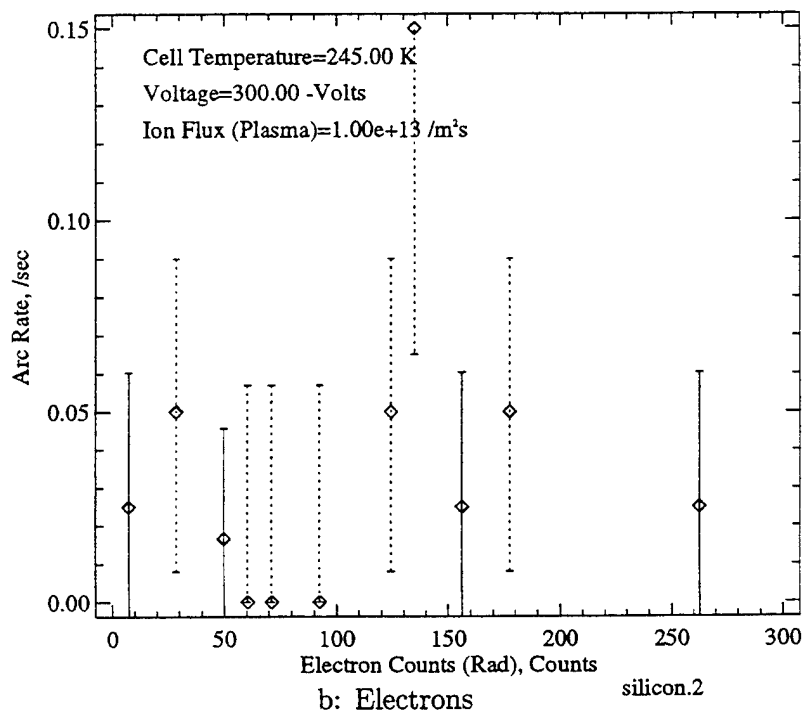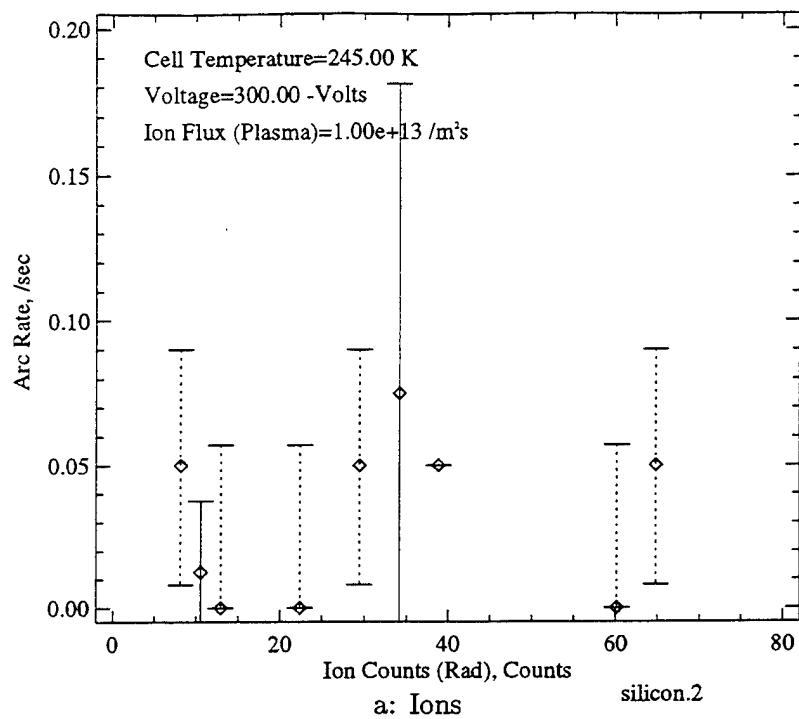
Figure 75: Arc Rate Variation with Radiation Flux for Silicon Module #2

a: Ions

apsatrw.5

b: Electrons

apsatrw.5
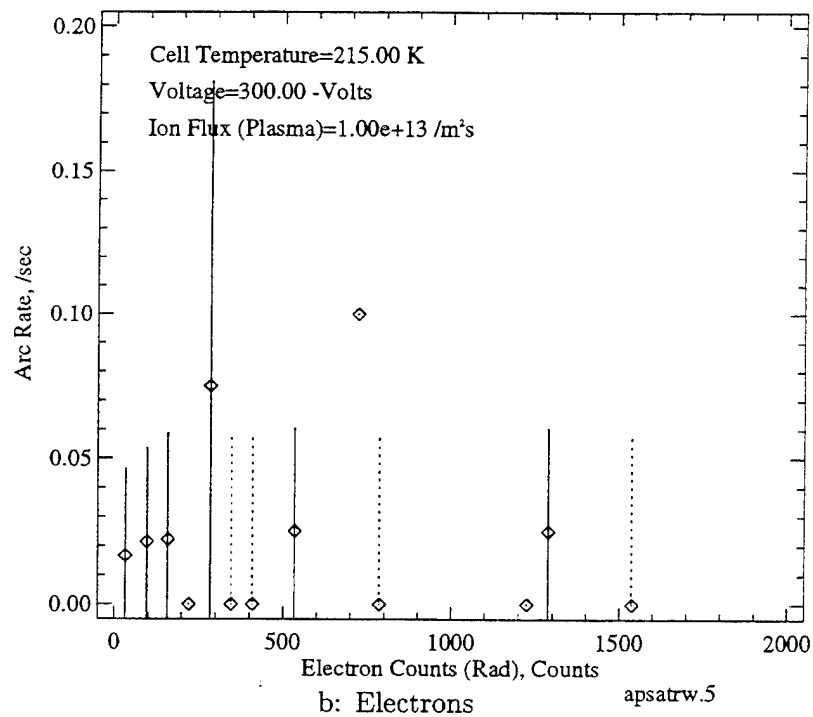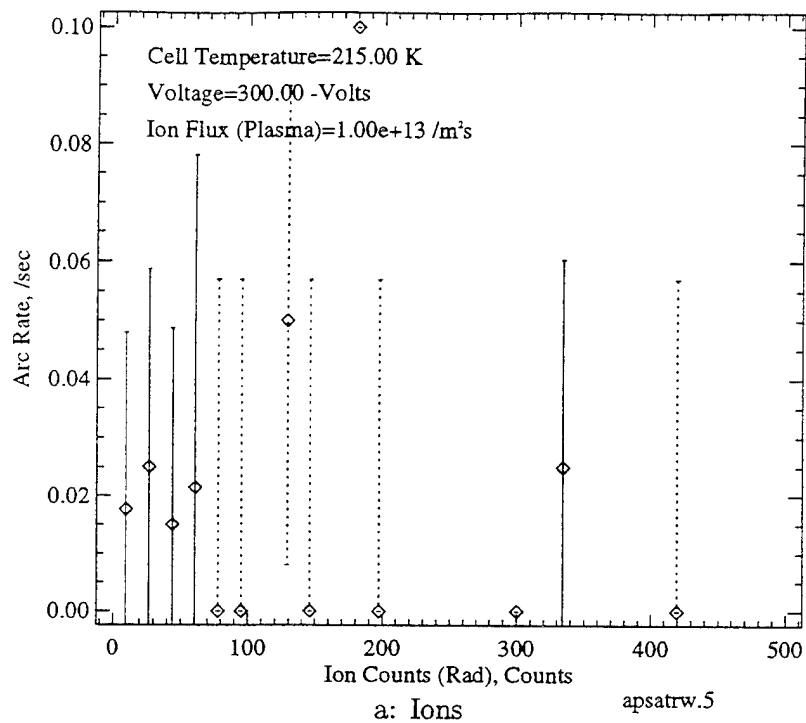
Figure 76: Arc Rate Variation with Radiation Flux for APSA Module #5

150

sil.wtc.3
Figure 77: Arc Rate Variation with Cell Temperature on Silicon WTC Module #3

Chapter 7

Conclusions

As power demands continue to increase, solar cells will be operated at higher bias voltages to minimize mass and power loss during transmission. Since positive bias operation can result in a significant current leakage and power loss, negative voltage systems are desirable. Current systems have already increased bus voltages from the -28V typically used in the past to -33V to -51V, and the Space Station design calls for the arrays to reach a potential of -160V. However, at high negative voltages, arcing on the solar cells can occur, resulting in electromagnetic and optical noise, and solar cell and power system damage. Arcing has been observed on high voltage solar cells in both ground and flight experiments at voltages on the order of hundreds of volts.

Using numerical and analytical analysis, Cho and Hastings developed a model to describe the arcing onset process[13]. In this process, ambient ions first charge the front surface of the dielectric layer (i.e. coverglass and dielectric). Electrons from enhanced field electron emission on the interconnects then strike the dielectric side surface, releasing secondary electrons. This secondary electron emission further charges the dielectric, causing the EFEE to increase and eventually runaway. As the electrons strike the side surface, neutrals adsorbed to the surface are desorbed, forming a dense cloud over the region. If the neutral cloud density exceeds a critical value (approximately $6 \times 10^{21} m^{-3}$, ionization and arcing occurs. The resulting plasma cloud then discharges the dielectric surface, resetting the process. A semi-analytic computer code was written by Cho to predict arcing rates on high voltage solar arrays using this model. A version of this code, which neglected the neutral density criterion, was used by Mong[62] to predict arcing rates on the SAMPIE and PASP Plus experiment.

In this work, the semi-analytic code developed by Cho was modified to be more physically accurate and to allow experiments to be more realistically simulated by including experiment equipment limitations and by allowing the environmental data to vary in time. The determination of the EFEE charging time is done numerically to accomodate the voltage dependence of the secondary electron yield. Also, the recharging of the neutral density is now modeled time accurately, as opposed to always using the steady state neutral density.

This code was then used to simulate the arc rates for the conventional geometry cells biased during the PASP Plus experiment. This Air Force experiment was flown aboard the APEX satellite to examine the interactions of conventional, wrap-through-contact, and concentrator cell designs with the space plasma environment. Pre-flight predictions of the arcing activity were made with parameters generated using environmental models for the baseline APEX orbit. Post-flight simulations were then conducted using the actual flight data parameters. The simulations were found to accurately predict the arcing levels seen during the experiment.

Analysis of the PASP Plus flight data was conducted to examine arc rate dependencies on the various material, environmental, and operational parameters. The results can be summaraized as follows:

(1) The wrap-though-contact cells were found to arc, as predicted by Font et al.[26], although less frequently than the conventional cells. The concentrator cells showed a much lower arc rate than either design, to the point to become almost indistinguishable from possible noise.

(2) A strong dependency on bias voltage was found, as predicted by the model. Fits based on the model form were then made, which could then be scaled to account for differences in cell area, dielectric thickness, and work function. From this, it was verified that the arc rate varies linearly with array area, and strongly with the inverse of the dielectric thickness. Onset voltages of between approximately -100V -300V were found for the conventional and wrap-through-contact cells, which is significantly lower than was previously believed[23]. This further shows the relevance of considering solar array arcing during the design of high voltage power systems.

(3) The strong dependence of arcing with cell temperature predicted by the model was also verified by the PASP Plus experiment. During eclipse, all of the conventional modules showed increased levels of arcing. The existance of a critical temperature above which no arcing is seen, for a given bias voltage and ion flux, was verified. Thus, if cells on operating power systems are kept hot, arcing can be avoided. The APSA module was mounted over a cut-out on the Deployed Panel and was exposed to space on the back, which most closely represents the configuration of actual arrays. Because of the resulting high temperatures during sunlight, this module was found to arc almost exclusively during eclipse and transition from eclipse into sunlight. Thus, if operating systems are heated prior to exited eclipse, arcing can be significantly reduced, and possibly avoided altogether.

(4) Ion flux was also verified as a factor in the arcing process, with arcing possible even during wake operations. Thus, to avoid arcing, the cells must either be kept below the onset voltage or above the critical temperature.

(5) Radiation flux, however, was not found to affect arcing levels, although only a limited amount of data was available to support this.

Thus, if a power system is to be designed for a spacecraft sensitive to arcing, concentrator arrays offer the lowest arcing levels, followed by wrap-through-contact arrays and then thick dielectric conventional arrays. Alternately, thin cells can be used provided the cell temperature is always above the critical temperature during operation, or the bias voltage is kept below the onset voltage, which can be as low as near -100V.

The dependencies found between arcing and bias voltage, cell temperature, and ion flux, as well as the arc rate scalings with array area, dielectric thickness, and work function, all strongly support the model developed by Cho and Hastings. Thus, the semi-analytic simulation has been shown to be an accurate tool for predicting solar array arcing. This tool could then be used to perform voltage/mass trade studies, or to help design new cells to mitigate arcing during high voltage operation.

7.1 Suggestions for PASP II

Currently, there is a plan to perform a second Photovoltaic Array Space Power experiment. This will allow other cell materials and designs to be flight tested and further data to be gathered on current cells. Using lessons learned from the PASP Plus experiment, the following suggests are made for the next flight:

(1) Measure the ambient neutral density. The neutral density is one of the key parameters in the Cho/hastings arcing model. Measuring the neutral density will allow critical temperatures to be more accurately characterized for varying bias voltages and ion fluxes. It will also reduce the uncertainty in the analysis of the dependence of arcing on bias voltage, ion flux and cell temperature, since points of constant neutral flux could be examined.

(2) Use an inline current sensor, similar to that used in the SAMPIE experiment, to characterize the arcs. The use of transient pulse monitors, which measure electric field variations to detect the arcs is much more susceptible to noise than inline current sensors. Also, comparison of arcing rates and arc strengths between different cells is difficult with TPMs, because of the varying distance of the modules from each TPM and electric field reflections and resonances on the spacecraft[2]. Inline current sensors do not have different sensitivies to different modules because of location and are much less succeptible to noise from external sources. If TPMs are to be used again, it is recommended that more thresholds be added near the lower end of the scale. The sensors on PASP Plus have an initial threshold (setting 1) significantly higher than necessary. The settings 2-4 were not even used during the experiment.

(3) Have several possible bias step durations. The PASP Plus experiment had one bias duration (23 seconds). Having several bias durations, such as 23 sec, 60 sec, 120 sec, and 300 sec would allow the onset voltages found during PASP Plus to be verified. A longer experiment duration would also allow the critical ion flux dependence on bias time to be examined. It is not advised to have a duration longer than 300 seconds for several reasons. First, the plasma and neutral densities will change considerably during long experiments, greatly affecting the arcing process. Second, long bias times result in few data points being

taken. As seen in PASP Plus, the large scatter in the data requires a large number of data points to allow the results to be statistical significant. Thus, it is recommended that the majority of the experiment be conducted with the same 23 second bias step used in PASP Plus, with several longer biased steps used to study the onset voltage and critical ion flux.

(4) Bias to higher voltages. Problems with the power source on PASP Plus restricted operations to -440V and below. Biasing to higher voltages would allow a better study of the dependence of arc rate on bias voltage to be made. At high voltage, the model suggests that, once the EFEE charging time becomes insignicant, the arc rate should vary linearly with the ion flux. This could not be verified at the voltage levels used on PASP Plus, but could be verified at higher voltages. Also, higher bias voltages would result in higher arc rates, increasing the statistical significance of the data.

(5) Increase the range of the Langmuir probe. The probe used on PASP Plus was only accurate up to a density of approximately $2 \times 10^{11} m^{-3}$. The density seen on orbit exceeded this level at times, resulting in some of the probe data being unreliable.

(6) Continue to bias in eclipse. The majority of arcing seen on PASP Plus was during eclipse, when the cells were cold. This resulted in a higher number of non-zero data points during these conditions. Although photovoltaic power systems on spacecraft operate only during sunlight, they are still very succeptible to arcing upon exiting eclipse, when the cells are still cold and are thermally desorbing neutrals as they heat up. Gathering data during eclipse, as well as during transitions into and out of eclipse, allow a large amount of data to be gathered over the entire range of temperatures seen by the cells.

Appendix A

Enhanced Field Electron Emission

A.1 EFEE Mechanism

The process of enhanced field electron emission is a key part of the arcing mechanism on high voltage solar arrays. A detailed study of the process was performed by Cho in Ref. [13]. Several of the important aspects of EFEE are reviewed here.

Experimentally, significant electron emission currents have been observed at applied electric fields on the order of 100 to 1000 times smaller than those expected theoretically from the Fowler-Nordheim formula for field emission. However, the currents do show the characteristic shape of the Fowler-Nordheim current by giving a straight line on a plot of $\log(I/V^2)$ vs $1/V$. For a constant gap d between two flat electrodes, the Fowler-Nordheim emission current is given by

$$I_{FN} = j_{FN}S_{FN} = A \left(\beta \frac{V}{d} \right)^2 \exp \left(-\frac{Bd}{\beta V} \right) S_{FN} \tag{114}$$

where S_{FN} is the effective emission site area. The constants A and B are given by [52]

$$A = \frac{1.54 \times 10^{-6} 10^{4.52/\sqrt{\phi_w}}}{\phi_w} \tag{115}$$

$$B = 6.53 \times 10^9 \phi_w^{1.5} \tag{116}$$

where ϕ_w is the work function of the metal in eV. If the emission is due to Fowler-Nordheim emission, the slope of the plot gives $-Bd/\beta$. The factor β is the electric field enhancement factor. The electric field on the cathode surface can be enhanced by two mechanisms:

microprotrusions and dielectric impurities.

The field enhancement due to microprotrusions was calculated by Vibrans [100]. The highest enhancement is found when the emitting point is approximated by a sphere on the tip of an infinitesimally thin wire, given by

$$\beta = 2 + \frac{h}{r_0} \tag{117}$$

where h is the height of the protrusion and r_0 is the radius of the tip. This geometrical enhancement can explain enhancement factors up to a few hundred [52].

But for higher values of β, it becomes increasingly difficult to explain the enhancement due to geometrical considerations alone, especially when examinations of the cathode surface have often shown no sign of the necessary structures. Thus, in this work, it is assumed that the field enhancement is not due primarily to microprotrusions. Latham attributed the electric field enhancement to a dielectric inclusion on the surface due to a metal impurity or chemical reaction [52, 54]. When an electric field is applied to the dielectric, electrons first tunnel from the metal-dielectric interface into the conduction band of the dielectric. The electrons start tunneling at locations on the interface where a favorable tunneling contact is made, such as would be created by a local concentration of impurity atoms [8]. These electrons are accelerated inside the dielectric and create positive holes through collisions, which then migrate toward the metal-dielectric interface and further enhance the field. Latham assumed that the electron emission from the dielectric-vacuum interface obeys a formula similar to Richardson-Dushman's formula

$$j_{d-v} = A_R T_e^2 \exp(-e\chi/\kappa T_e) \tag{118}$$

where A_R is a constant, T_e is the electron temperature at the dielectric-vacuum interface, and χ is the barrier height at the interface.

The electron temperature at the interface is approximated by $e\Delta V \simeq 3/2\kappa T_e$, where ΔV is the potential drop across the dielectric layer, assuming that electrons are rapidly thermalized through collisions with lattice atoms and the energy loss due to the collisions

160

is negligible. The potential drop is assumed to be proportional to the applied voltage by

$$\Delta V \simeq \frac{3}{2}\frac{\kappa T_e}{e} \simeq \frac{1}{\epsilon_d}\frac{\Delta d}{d}V \tag{119}$$

where ϵ_d is the relative dielectric constant of the dielectric layer and Δd is the thickness of the layer.

Substituting Eq. (119) into Eq. (118), the resulting equation gives a straight line when $\log(I/V^2)$ vs $1/V$ is plotted. The resulting field enhancement factor obtained from the plot is

$$\beta = \frac{2B\Delta d}{3\chi\epsilon_d} = \frac{4.35 \times 10^9 \phi_w^{1.5}\Delta d}{\chi\epsilon_d} \tag{120}$$

The enhancement factor is thus determined by the dielectric thickness Δd, the barrier height at the dielectric-vacuum interface χ, the dielectric constant ϵ_d, and the surface work function ϕ_w. This model is able to explain enhancement factors up to a few thousand [39] and the width of the electron energy spectrum observed in experiments [7]. It also gives an explanation for the electroluminescence observed at the electron emission sites by Hurley [45, 46].

The relationship between the currents given by Eqs. (118) and (114) will now be examined by first substituting Eqs. (119) and (120) into Eq. (118) to obtain the current density emitted from the dielectric-vacuum interface

$$\begin{aligned}
j_{d-v} &= A_R\left(\frac{e\chi\beta V}{Bd\kappa}\right)^2\exp\left(-\frac{Bd}{\beta V}\right)\\
&= A_R\left(\frac{e\chi}{B\kappa}\right)^2\left(\beta\frac{V}{d}\right)^2\exp\left(-\frac{Bd}{\beta V}\right)
\end{aligned} \tag{121}$$

The current density at the metal-dielectric interface j_{m-d} is still given by the Fowler-Nordheim equation as

$$j_{m-d} = \frac{I}{S_{FN}} = A(\beta E)^2\exp\left(-\frac{B}{\beta E}\right) \tag{122}$$

While the total currents will be equal, there is no guarantee that the two current densities will be. While the electrons are thermalized through the collisions with the lattice, the electron flow from the metal-dielectric interface suffers significant diffusion due to the collisions. Assuming an Einstein relation for the diffusion coefficient, $D/\mu_e = \kappa T_e/e$, the

diffusion distance δd can be estimated by

$$\delta d \simeq \sqrt{Dt_d} = \sqrt{D(\frac{\Delta d}{v_e})} = \sqrt{D\frac{\Delta d}{\mu_e \Delta V/\Delta d}} = \sqrt{\frac{\kappa T_e}{e\Delta V}}\Delta d \simeq \Delta d \qquad (123)$$

where t_d is the time it takes an electron to travel through the layer and Eq. (119) has been used. Thus, the electrons diffuse a distance comparable to the dielectric layer thickness. As the electrons diffuse through the dielectric layer, the current density from the dielectric-vacuum interface can be much lower than that from the dielectric-metal interface. To account for this, the areas S_{FN} and S_{real} are introduced, as discussed in the next section.

A.2 Finite Electron Emission Site Area on a Broad Area Cathode

In experiments, it is the field emission current, rather than the current density, that is measured. The emission site area cannot be directly measured when the cathode is a plane electrode. For a constant gap d, the Fowler-Nordheim current I_{FN} is given by Eq. (114). Taking the derivative of $\log_{10}(I_{FN}/V^2)$ with respect to $1/V$, we have

$$\frac{d(\log_{10}(I/V^2))}{d(1/v)} = -\log_{10} e \frac{Bd}{\beta} \qquad (124)$$

The graph of $\log_{10}(I_{FN}/V^2)$ plotted against $1/V$ is often referred to as a F-N plot. If the emission current is due to field emission, the F-N plot is a straight line with a slope of $-Bd/\beta$. If a value for the work function ϕ_w is assumed, the field enhancement factor β is determined from the slope of the line. The factor S_{FN} can then be found by dividing the experimentally measured current by the premultiplier in front of S_{FN} in Eq. (114)

$$S_{FN} = \frac{I}{A(\beta\frac{V}{d})^2 \exp(-\frac{Bd}{\beta V})} \qquad (125)$$

This value for S_{FN} can be regarded as the effective emission site area at the metal-dielectric interface. However, it is otherwise physically meaningless except that it has dimensions of area[65], because the emission site area seen from outside of the dielectric layer is the area

S_{real} at the dielectric-vacuum interface. As discussed above, S_{real} can have a different value than S_{FN} due to diffusion of electrons within the dielectric. Calculating S_{real} from the electron diffusion is very difficult, however. But, S_{real} can be calculated from consideration of the space charge effect due to electrons which appear clearly in F-N plots at high voltages.

As the voltage an current density increases, the electron density in front of the emission site increases and the space charges begin to affect the electric field at the site, causing the plot of $\log_{10}(I_{FN}/V^2)$ vs $1/V$ to become nonlinear. The points where the F-N plot departs from a straight line can be calculated from quasi-one-dimensional equations taking into account the spreading of the electron beam.

We consider electron trajectories in the cylindrical coordinate shown in Figure 78. It is assumed that electrons are emitted uniformly from an aperture of radius r_0 at $z = 0$. Neglecting collisions, the current density can be calculated by the method of characteristics, with the result given by

$$j(r, 0, d) = \int v \cos\theta f(r_o, \theta_o, z = 0, v, \theta, \varphi)v^2 dv d\Omega \qquad (126)$$

where f is the speed distribution of the emitted electrons, v is the emission speed at $z = 0$, and φ and θ are the polar and azimuthal angles of the emission velocity vector. If the speed distribution is Maxwellian, the current density can be written as

$$j(r, 0, d) = j_o \int \frac{\overline{E}}{\pi} \exp(-\overline{E}) \cos\theta d\overline{E} d\Omega \qquad (127)$$

where $\overline{E}$ is the electron emission energy normalized by the temperature as $\overline{E} = \frac{1}{2}m_e v^2/\kappa T_e$, and j_o is the uniform current density at the cathode $j_o = \frac{n_\infty}{4}\sqrt{\frac{8\kappa T_e}{\pi m_e}}$.

The x, y positions at $z = 0$ are given by

$$x_o = r - v \sin\theta \cos\varphi\tau$$
$$y_o = -v \sin\theta \sin\varphi\tau$$
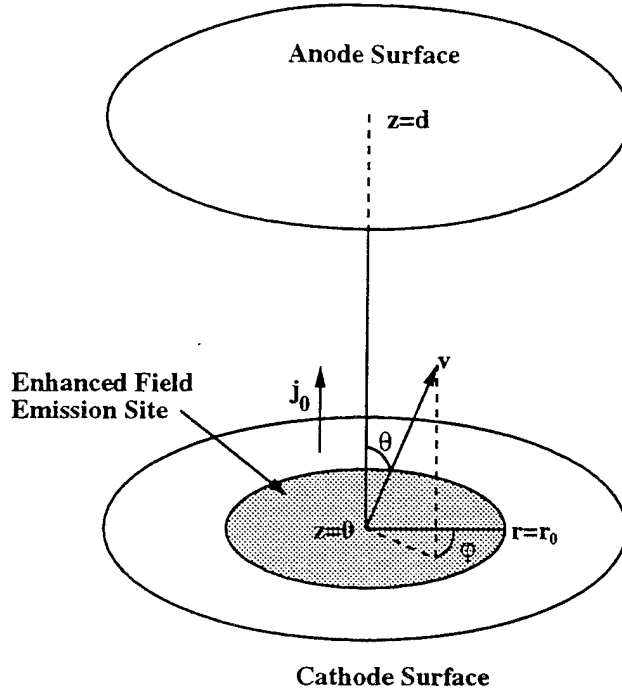
Figure 78: Electron Beam Broadening

where τ is the time for it takes electrons to reach the anode, given by

$$\tau = -\frac{v}{a}[\cos\theta - \sqrt{\cos^2\theta + \frac{2ad}{v^2}}] \tag{128}$$

and $a = eV/m_e/d$ is the uniform acceleration in the z direction neglecting any space charge effects. Since the position at $z = 0$ must be within the radius r_o, that is, $x_o^2 + y_o^2 < r_0^2$, the integration in Eq. (127) is carried out over θ and φ which satisfy

$$r^2 + v^2\tau^2\sin^2\theta - 2rv\tau\sin\theta\cos\varphi < r_o^2 \tag{129}$$

After some algebra, the current density at the center of the anode $j(0,0,d)$ is approximately given by

$$\frac{j(0,0,d)}{j_o} \approx 0.25\bar{r}_o^2\overline{V} \tag{130}$$

where $\bar{r}_o = r_o/d$ and $\overline{V} = V/\kappa T_e$.

The beam cross section at the center of a plane at z is approximated by

$$\begin{cases} A_b = S_{real} & (z < 0.25 r_o^2 \frac{(V/d)}{\kappa T_e}) \\ A_b = \frac{S_{real}}{0.25 r_o^2 \frac{(V/d)}{\kappa T_e} \frac{1}{z}} & (z \geq 0.25 r_o^2 \frac{(V/d)}{\kappa T_e}) \end{cases} \qquad (131)$$

where r_o is the radius of emission site at $z = 0$, that is, $r_o = \sqrt{S_{real}/\pi}$.

The quasi-one-dimensional equations are now given by

$$\begin{cases} e n_e v_{ez} A_b = I_e \\ v_e \frac{dv_{ez}}{dz} = \frac{e}{m_e} \frac{d\phi}{dz} \\ \frac{d^2\phi}{dz^2} = \frac{e n_e}{\epsilon_o} \end{cases} \qquad (132)$$

The boundary conditions are given by

$$\begin{cases} \phi(z = 0) = 0 \\ \phi(z = d) = V (> 0) \\ E_{c.o.} = -\frac{d\phi}{dz}|_{z=0} \\ I_e = A\beta^2 E_{c.o.}^2 \exp(-\frac{B}{\beta E_{c.o.}}) S_{FN} \\ v_{ez}(z = 0) = \sqrt{\frac{\kappa T_e}{m_e}} \end{cases} \qquad (133)$$

An electron temperature κT_e of one electron volt is chosen because this is the spread typically seen in the energy spectrum of electrons emitted due to EFEE. In the above analysis, the effect of the space charge on the electron trajectories was neglected, although the effect was included for the emission current I_e, which seems contradictory. However, the space charge effect would be more prominent on the current I_e than on the electron trajectories, because the current depends exponentially on the cathode field $E_{c.o.}$. Thus, this treatment is justified to a first order approximation.

If the emission site areas calculated from Eq. (125), which are typically between $10^{-13} m^2$ and $10^{-17} m^2$, are substituted into S_{real} in Eq. (131), this usually leads to an overestimation of the electron space charge effect and the F-N plot departs from linear much earlier than is observed in experiments. Therefore, having the same current density at both interfaces is prohibited not only from the physical nature of the field emission, *i.e.* collisional diffusion,

165

but also from the viewpoint of the space charge effect of the electrons.

Using the above analysis and data from Ref. [34], Cho studied the emission current between two plane stainless steel electrodes with a gap distance of $d = 0.76mm$ [13]. Assuming a work function of $\phi_w = 4.5eV$, the F-N plot gave a field enhancement factor of $\beta = 345$. The value for S_{FN} calculated using Eq. (125) was $S_{FN} = 2.3 \times 10^{-15}m^2$. If this value is used for S_{real} in Eq. (131), the result shows the emission current to be space charge limited at a much lower voltage than was observed in the experiment. Cho found that a value of $S_{real} = 2.8 \times 10^{-10}m^2$ gave much better agreement with the experimental data. Dielectric particles identified by experiments [9, 85] as emission sites often have the size of microns. Thus, this value of S_{real} is a reasonable value for the estimation of the diffusion distance of electrons in Eq. (123).

The Fowler-Nordheim formula is the result of a one-dimensional quantum mechanical calculation [27], and does not include these two-dimensional effects. In the model for arcing on solar arrays, a finite emission site area S_{real} on the conductor surface was assumed, and the Fowler-Nordheim coefficient A was modified to $A' = AS_{FN}/S_{real}$ in order to have the same total current as measured in experiments. The constant A' now corresponds to the premultiplier $A_R(e\chi/B)^2$ in Eq. (121).

A.3   Space Charge Limited EFEE

To examine the space charge limitation on the EFEE current, Cho [13] conducted PIC simulations, with a bias voltage of -500 V and and an emission site with field enhancement factor of 500 on the conductor surface in contact with the triple junction. For initial conditions, the front surface is charged to $\phi_s = 0$ and the side surface is uncharged. Thus, the side surface potential changes linearly from 0 to V according to the dielectric constants. The electric field at the triple junction is given by

$$E_{T.J.} = \frac{V}{\frac{\epsilon_{d2}}{\epsilon_{d1}}d_1 + d_2} \tag{134}$$

having a value of $E_{T.J.} = 5.2 \times 10^6 V/m$, and an initial emission current of $j_{ec} = I/S_{real} = 1.9 A/m^2$. First, the time history of the emission current was modeled using a space charge-free simulation, with the results shown in Figure 79. As seen, a rapid increase in the current, up to five orders of magnitude higher than its initial value, occurs. The simulation was stopped when the emission current density exceeded 10% of the space charge limited value.

The state at this point was then used as the initial conditions for a PIC simulation including the space charge effects. The time variation of the emission current for this simulation is shown in Figure 80. The time is counted from the final time in the previous simulation, with the oscillation near $t = 0$ due to numerical noise from connecting the two codes. In the first 0.2 nsec, we still see a rapid increase in the current, until the average current density over the emission site reaches $\overline{j_{ec}} = I/S_{real} = 3.2 \times 10^7 A/m^2$. At this point, the current is 0.278 mA, which is much lower than the typical arc discharge current of the order of an ampere. The current density, however, is much higher than the Child-Langmuir space charge-limited current density of $j_{sp} = 7.2 \times 10^5 A/m^2$ for a $190 \mu m$ gap with a bias voltage of -500 V. This high current is caused by the positive surface charge present on the dielectric surface near the triple junction created by secondary electron emission. This positive surface charge initially cancels the negative space charge over the conductor surface, allowing the emission current to be much higher than the Child-Langmuir current. However, this effect soon is overwhelmed by the negative space charge of the electrons which lie extensively over the dielectric side surface. The emission current then becomes quasi-steady, as seen in Figure 80.
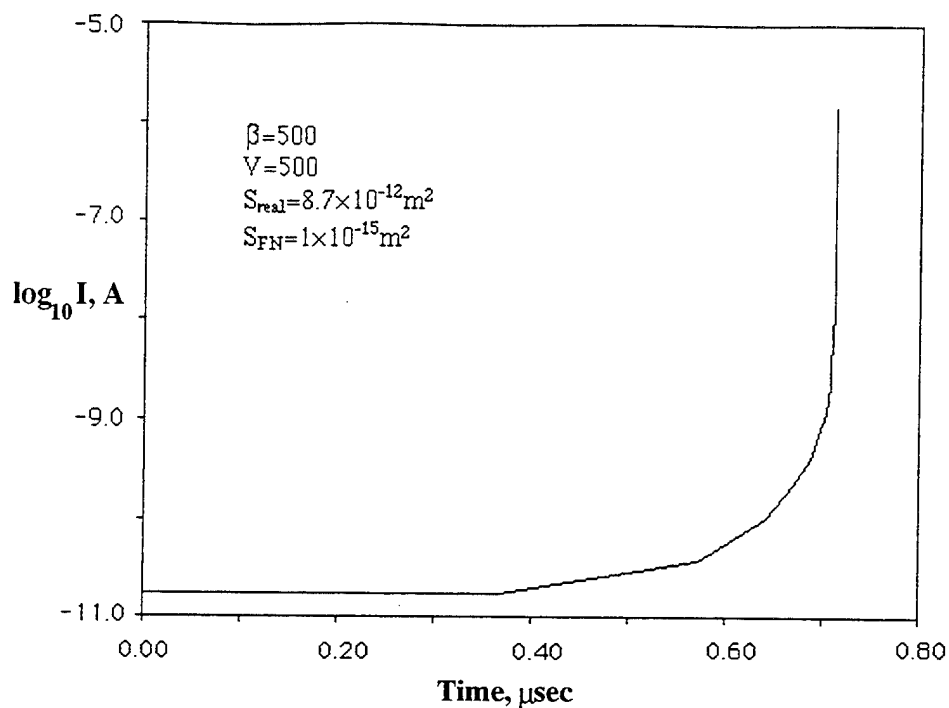
Figure 79: Electron Emission Current from Conductor Surface Calculated by Space Charge-Free Scheme
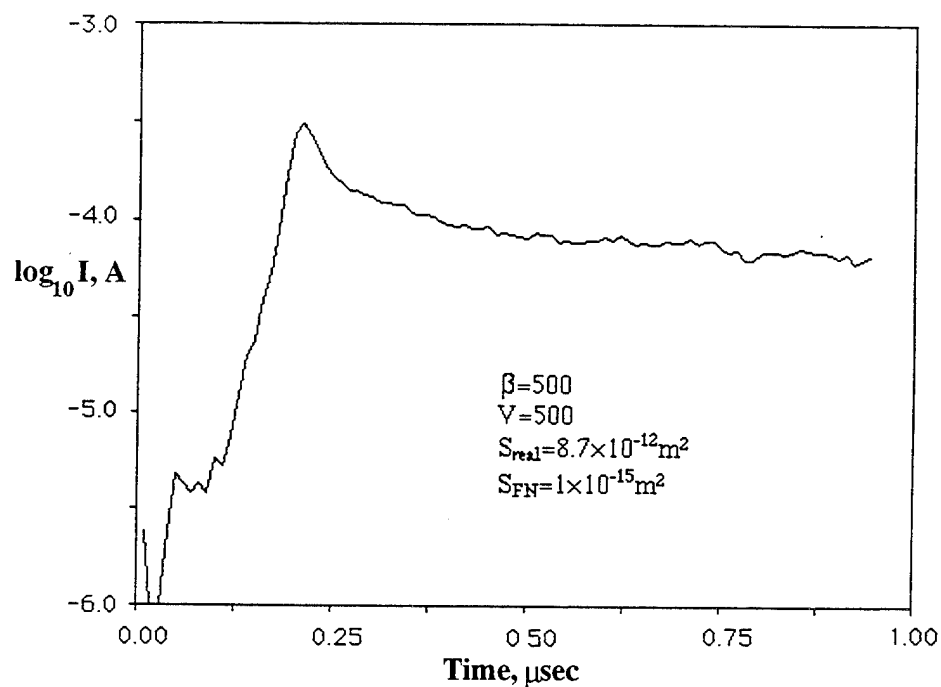
Figure 80: Electron Emission Current from Conductor Surface Calculated by PIC Code Including Space Charge Effects

168

The quasi-steady current is the result of the balance of the negative space charge of the electron current with the positive space charge on the dielectric side surface. Since the negative space charge is proportional to the emission current, and the positive space charge is proportional to the bias voltage, the steady state current density j_{ec}^* should be linearly proportional to the bias voltage V. A least squares fit to data from simulations at various voltages gives

$$j_{ec}^* = 1.39 \times 10^4 |V| A/m^2 \qquad (135)$$

with V in volts. This linear dependence on voltage was verified by Cho with the following analysis [13].

If we consider a sheet of electrons hopping along the dielectric side surface as shown in Figure 81, the current parallel to the surface can be given by

$$I_x = \sigma_- v_{ex} \qquad (136)$$

where I_x is the current per unit length, σ_- is the electron density per unit area over the side surface, and v_{ex} is the electron velocity in the x direction. This is similar to the formulation of the electron current in vacuum surface flash-over used in Reference 5, 81. Once the surface charge reaches a steady state by having a secondary electron yield of unity, this current must equal the emission current $j_{ec}^* \sqrt{S_{real}}$ for current continuity. The electron density per unit area over the side surface can then be given by

$$\sigma_- = \frac{j_{ec}^* \sqrt{S_{real}}}{v_{ex}} \qquad (137)$$

It is when this negative charge density becomes comparable to the positive surface charge density σ_+ that the negative space charge limitation on j_{ec} occurs. The positive surface charge density can be approximated by

$$\frac{\sigma_+}{2\epsilon_0} \simeq E_y \qquad (138)$$

where E_y is the electric field perpendicular to the side surface. Equating σ_- with σ_+, the
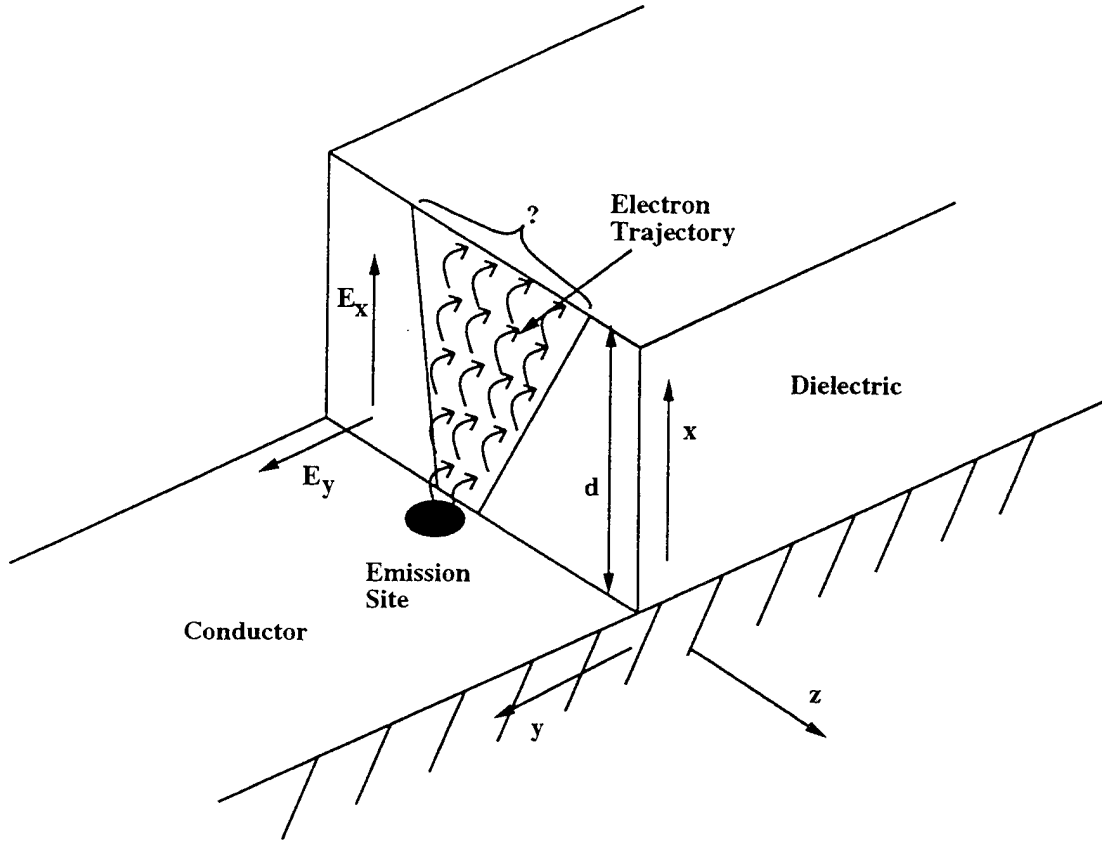
Figure 81: Electron Hopping Along Side Surface

negative space charge-limited current density is given by

$$j_{ec}^{*} = 2\epsilon_0 \frac{1}{\sqrt{S_{real}}} v_{ex} E_y \tag{139}$$

The electron velocity v_{ex} is now calculated assuming a probability distribution function given by

$$f(v, \alpha, \varphi) dv d\Omega = \frac{1}{\pi} \delta(v - v_o) \cos \alpha \sin \alpha dv d\alpha d\varphi \tag{140}$$

where v is the emission speed, α is the polar angle, and φ is the azimuthal angle of the emission velocity. For simplicity, we have assumed a mono-energetic emission with $E_{se} = \frac{1}{2} m_e v_o^2$. The emission velocities are given by

$$v_x = v_o \sin \alpha \sin \varphi$$

$$v_y = v_o \cos \alpha$$

170

$$v_z = v_o \sin\alpha\cos\varphi \tag{141}$$

Assuming E_x and E_y are uniform, the electron trajectories are parabolic, and the velocity at the top of the parabola is given by

$$v_x = v_0[\sin\alpha\sin\varphi + (\frac{E_x}{E_y})\cos\alpha]$$

where $v_0 = \sqrt{2eE_{se}/m_e}$. Taking the average over the distribution function gives

$$< v_x >= \frac{2}{3}v_o(\frac{E_x}{E_y})$$

Substituting this average into v_{ex} in Eq. (139) gives

$$j_{ec}^* = \frac{4}{3}\epsilon_o \frac{v_o}{\sqrt{S_{real}}}E_x$$

The magnitude of the electric field in the x direction is approximated by the bias voltage $|V|$ as $E_x \simeq |V|/d$. Then, the current density can then be rewritten as

$$j_{ec}^* = \frac{4}{3}\epsilon_o \frac{v_o}{\sqrt{S_{real}}d}|V| \tag{142}$$

Therefore, the quasi-steady state space charge-limited current density j_{ec}^* is linear in the bias voltage V. The PIC simulation was run and the showed good agreement with the above results. The simulation results were used to correct the premultiplier in Eq. (142), giving

$$j_{ec}^* = 1.05\epsilon_0\sqrt{\frac{2e}{m_e}}\frac{\sqrt{E_{se}}}{\sqrt{S_{real}}d}|V| \tag{143}$$

with E_{se} and E_{se1} in eV, and $|V|$ in volts. E_{se1} is the electron incident energy for a secondary electron yield of unity. Note, the current j_{ec}^* is independent of the field enhancement factor β.

In the quasi-steady state, there is also an intense electron current to the side surface, with the average current density defined by

$$\overline{j_e^*} \equiv \frac{\int_0^{d_1+d_2} j_e^*(x)dx}{d_1 + d_2} \tag{144}$$

171

where the values for $j_e^*(x)$ are obtained from numerical results. The results of the simulations are fit well by the square of the bias voltage as $\overline{j_e^*} = 14.8|V|^2$. This current can also be quantified in a manner similar to j_{ec}^*.

The incident current per unit z length, I_y, is equal to the electron current parallel to the dielectric surface, I_x, from current continuity. The incident current density is given by dividing the current by the distance which the electron travels during one hop over the surface, x_{hop},

$$j_e^* = \frac{I_y}{x_{hop}} = \frac{I_x}{x_{hop}}$$

The hopping distance must satisfy $x_{hop} = E_{se1}/E_x$ since the secondary electron yield is unity. Using this, and $I_x = j_{ec}^*\sqrt{S_{real}}$, Eq. (142) leads to

$$j_e^* = \frac{4}{3}\epsilon_o \frac{v_o}{E_{se1}d^2}V^2 \tag{145}$$

Thus, the incident current density is proportional to the square of the bias voltage. To quantify the premultiplier, we need to calculate E_{se1}. The incident energy and angle of an impacting electron are given by

$$\begin{aligned} E_i &= \frac{1}{2}m_e(v_x^2 + v_y + v_z^2) \\ \tan\theta_i &= \frac{\sqrt{v_x^2 + v_z^2}}{|v_y|} \end{aligned} \tag{146}$$

For the emission probability distribution function and the emission velocities given by Eqs. (140) and (141), the average incident energy and angle are given by

$$< E_i >= E_{se}[1 + 2(\frac{E_x}{E_y})^2] \tag{147}$$

$$< \tan\theta_i >= \frac{1}{\pi}\int_0^{\pi/2}[\int_0^{2\pi}\sqrt{\sin^2\alpha + 2(\frac{E_x}{E_y})\sin 2\alpha\sin\varphi + 4(\frac{E_x}{E_y})^2\cos^2\alpha}d\varphi]\sin\alpha d\alpha \tag{148}$$

Using Eqs. (147) and (148), the following equation can be solved for (E_x/E_y)

$$\gamma_{ee} = \gamma_{max}\frac{E_i}{E_{max}}\exp\left(2 - 2\sqrt{\frac{E_i}{E_{max}}}\right)\exp(2(1 - \cos\theta_i)) = 1 \tag{149}$$

where $\cos\theta_i$ is given by $\sqrt{1/(1+ <\tan\theta_i>^2)}$. The PIC simulations again gave good agreement with the analytic results, and the PIC results were used to correct the numerical factor in Eq. (145) to give

$$j_e^* = 0.52\epsilon_o\sqrt{\frac{2e}{m_e}}\frac{\sqrt{E_{se}}}{E_{se1}d^2}|V|^2 \tag{150}$$

The incident electron current is thus independent of any parameters regarding the EFEE site, such as β, S_{real}, or S_{FN}. It is this current that desorbs a significant amount of neutral gas from the side surface, producing a locally dense neutral cloud over the emission site.

A.4 Review of Field Enhancement Factor, β, Distributions

With increasing microscopy resolution in the 1970's, research has begun to identify field emission sites on broad-area electrodes. Broad-area electrodes have lateral dimensions comparable to or greater than the electrode separation distance, as opposed to point cathodes whose radii are comparable to or less than a micron [65]. Scanning electron microscopes and anode microprobes have been used to pin-point emission sites on the broad-area electrodes. The most important finding of these studies is that the identified emission sites often lack the geometric dimensions necessary for the field enhancement factor β observed in the experiments, as discussed in section A.1. This led to proposals of enhanced field emission mechanisms that do not rely on microprotrusions on the cathode surface. A survey by Noer of experiments prior to 1981 showed that the field enhancement factor ranged from a few tens to a few thousands, with effective emission site areas S_{FN} ranging from $10^{-18}m^2$ to $10^{-14}m^2$ [65]. The typical number density of emission sites was on the order of several times ten per cm^2 with dimensions larger than microns. These values, however, depend strongly on the surface conditions of the cathode, which were typically well polished metal surfaces. Thus, it is possible to have much higher emission site densities on untreated cathodes, such as the interconnects on solar arrays.

Since the 1980's, SEM, Auger electron spectroscopy (AES), and scanning field microscopy (SFM) have been used to study individual field emission sites. Niedermann et al. [64] found an emission site density of $1.5 \times 10^4 m^2$ on Sb samples with field enhancement

factors greater than 200 and $S_{FN} = 10^{-16} m^2$. The experiments used a movable point anode having a spatial resolution of 1 μm over a flat cathode, characterizing the emission sites by the electric field necessary to give a prescribed current of typically 40 nA. Thus, the enhancement factors calculated using the Fowler-Nordheim formula in Eq. (114) depended on the value assumed for the effective emission site are S_{FN}. AES studies done on the emission sites found a large variety of elements such as C, S, Mo, Ti, and Ag (which are typically found as dielectric oxides), at the sites. The scales of the sites were typically larger than a few μm.

Renner et al. [85] and Niedermann et al. [63] used the same apparatus as in Ref. [64] to test Al and MoS$_2$ electrodes. A fit to the data from Ref. [85] to the exponential distribution used in Chap. 2, $f(\beta) = f_o \exp(-\beta/\beta_o)$, gives $\beta_0 = 87$ and $n_{es} = 3.6 \times 10^5 m^{-2}$ [13]. A fit to the data from Ref. [63], assuming $\phi_w = 4.0 eV$ and $S_{FN} = 10^{-15} m^2$, gives an emission site density of $n_{es} = 4.1 \times 10^6 m^{-2}$ with an average value of β of 66 for sites that emitted greater than 40 nA at a given electric field strength.

Latham et al. [55] measured the spatial distribution of sites on a planar OFHC copper electrode using an optical imaging technique. Emission site densities of $n_{es} = 1.3 \times 10^4 m^{-2}$ and $5.8 \times 10^4 m^{-2}$ for applied fields of 20 and 36 MV/m, respectively, were found. Since only the total current was measured, the β distribution function cannot be deduced directly from the data. The average current measured in the experiments was $2.8 \times 10^{-7} A$. So, assuming a $\phi_w = 4.5 eV$ and $S_{FN} = 10^{-15} m^2$, a field enhancement factor of $\beta = 210$ is found. Thus, the density of emission sites with $\beta \geq 210$ is $1.3 \times 10^4 m^{-2}$.

Although there are still many unanswered questions about EFEE, the experimental results give encouraging support to the modeling used in this work. Primarily, in the emission site distributions, and in the hypothesis that the sites are generally dielectric inclusions on the interconnects, rather than microprotrusions.

Appendix B

Capacitance Matrix

Because the Poisson Equation is linear, the change in the surface potential $\delta\phi_{s,j}$ at any location due to a change in the surface charge of $\delta\sigma_i$ at location $\vec{x}_i$ is given by the solution of Poisson's Equation $\nabla^2 \delta\phi_{s,j} = \delta_{i,j}$ with $\delta_{i,j}$ zero except at the point i. Thus, we can know how one unit surface charge affects the surface potential everywhere. In a discrete system, the relation between $\delta\sigma_i$ and $\delta\phi_{s,j}$ can be expressed by a capacitance matrix A in

$$\begin{pmatrix} \delta\phi_{s,1} \\ \vdots \\ \delta\phi_{s,N} \end{pmatrix} = A \cdot \begin{pmatrix} \delta\sigma_1 \\ \vdots \\ \delta\sigma_N \end{pmatrix} \tag{151}$$

The method used to obtain the capacitance matrix is that given by Ref. [43]. In this scheme, a unit surface charge density is placed at gridpoint X_i and the Poisson Equation is solved to obtain ϕ_s at every point, giving the ith column of the matrix A

$$\begin{pmatrix} \phi_{s,1} \\ \vdots \\ \phi_{s,i} \\ \vdots \\ \phi_{s,N} \end{pmatrix} = \begin{pmatrix} \vdots & A_{1,i} & \vdots \\ \vdots & \vdots & \vdots \\ \vdots & A_{i,i} & \vdots \\ \vdots & \vdots & \vdots \\ \vdots & A_{N,i} & \vdots \end{pmatrix} \cdot \begin{pmatrix} 0 \\ \vdots \\ 1 \\ \vdots \\ 0 \end{pmatrix} \tag{152}$$

The process is then repeated for each gridpoint on the dielectric to determine each column of the capacitance matrix. A fifth order fit to the diagonal elements of the matrix is used to find the coefficients c_n for the equation relating the capacitance to the first impact

site (Eq. (30))

$$\frac{C_{diele}(d_i)}{C_{norm}} = \frac{1}{\sum_{n=1}^{n=6} c_n \left(\frac{d_i}{d}\right)^{n-1}} \tag{153}$$

where C_{norm} is the capacitance per unit area of the front surface

$$C_{norm} = \frac{1}{\frac{d_1}{\epsilon_{d_1}} + \frac{d_2}{\epsilon_{d_2}}} \tag{154}$$

To simulate the arc rates for each solar array on the PASP Plus experiment, the capacitance matrix was first determined for each cell and fit to find the coefficients for Eq. (153). A study was also performed to examine the sensitivity of the arc rate to the capacitance coefficients. This was done by simulating the PASP Plus standard silicon array module #2 with various values for the coefficients. The simulation was run using the coefficients from the silicon module #2, thick GaAs/Ge module #11, APSA module #5, and with all coefficients set to zero except c_0, which was set to either 0.001, 0.01, or 0.1. In these simulations, all of the other parameters were constant, with a plasma density of $1 \times 10^{10} m^{-3}$, neutral density of $3.177 \times 10^{14} m^{-3}$, and cell temperature of 245K.

Figure 82 shows the average arc rates at increasing voltage using the capacitance coefficients from each module and the constant c_0 of 0.01. As seen, there is virtually no difference in the rates using any of the cell's coefficients, and only a slight difference using the constant coefficient. Figure 83 shows the variation in average arc rate using the three constant coefficients ($c_0 = 0.001, 0.01$, or 0.1). This shows a larger difference, although the rates are still of the same order. The reason for the insensitivity is that the right hand side of Eq. (153) found from the coefficients is just used as the premultiplier for the front surface capacitance to find the capacitance at the impact point. This premultiplier is found from the fit to the normalized capacitance as a function of normalized distance. Since it is the normalized values that are used, this factor shows only small differences from cell to cell, as shown in Figure 84. The front surface capacitance itself, however, will have greatly differing values for the various cells, due to their dielectric constants and thicknesses, which *will* have a strong effect on the arc rates.

176
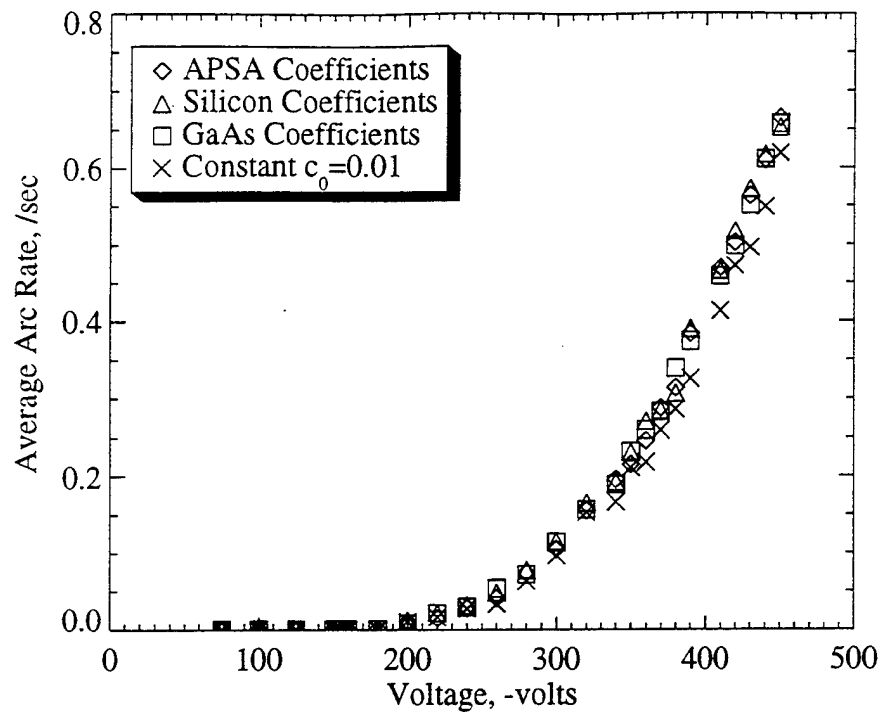
Figure 82: Arc Rate Sensitivity to Capacitance Coefficients Using Values from PASP Plus Modules
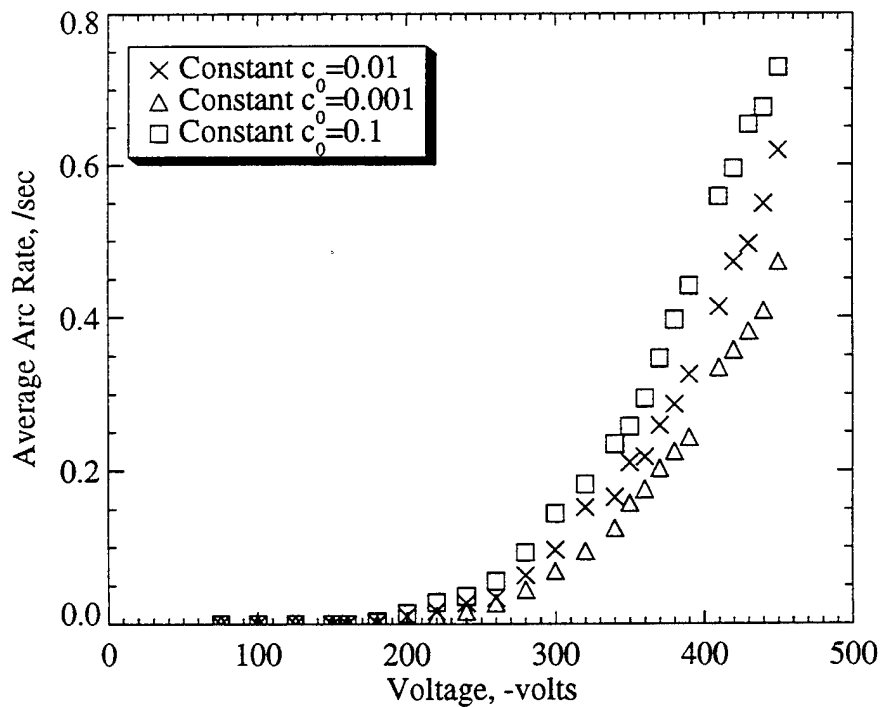
Figure 83: Arc Rate Sensitivity to Capacitance Coefficients Using Constant Values for c_0
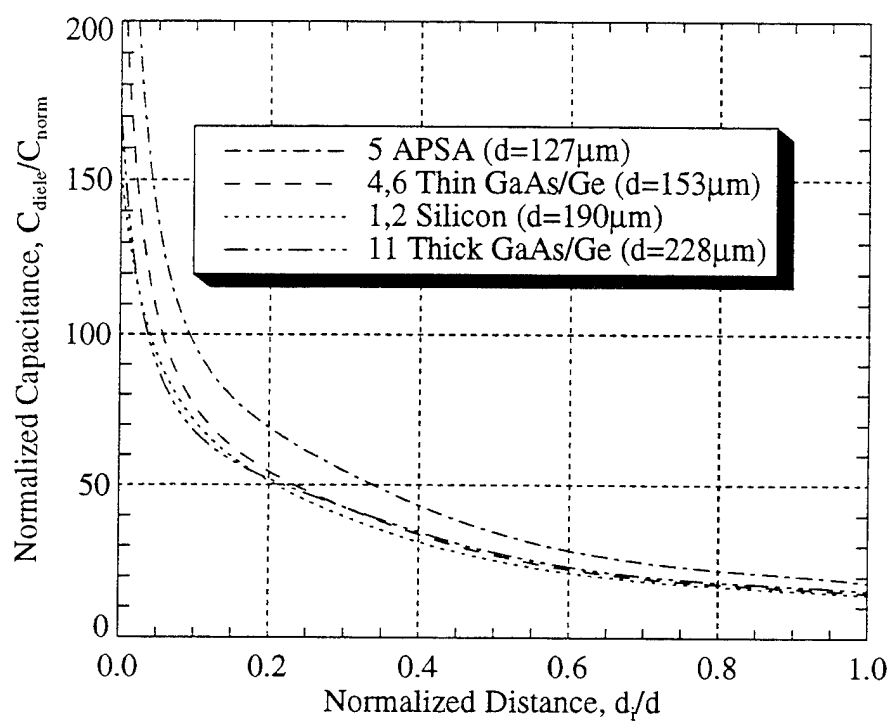
Figure 84: Comparison of Normalized Capacitance for PASP Plus Solar Cells

Appendix C

Bias Steps of PASP Plus Modules

Table 21: Bias Steps of PASP Plus Modules on Day 94234

Voltage	Module									
	1	2	3	4	5	6	8	11	14	15
-75V	21	21	0	21	0	22	0	22	0	0
-100V	21	21	0	20	0	22	0	22	0	0
-125V	20	21	0	21	0	22	0	22	0	0
-150V	19	21	0	21	0	21	0	22	0	0
-160V	0	0	0	0	0	0	0	0	0	0
-180V	0	0	0	0	0	0	0	0	0	0
-200V	0	0	0	0	0	0	0	0	0	0
-220V	0	0	0	0	0	0	0	0	0	0
-240V	0	0	0	0	0	0	0	0	0	0
-260V	0	0	0	0	0	0	0	0	0	0
-280V	0	0	0	0	0	0	0	0	0	0
-290V	0	0	0	0	0	0	0	0	0	0
-300V	0	0	0	0	0	0	0	0	0	0
-310V	0	0	0	0	0	0	0	0	0	0
-320V	0	0	0	0	0	0	0	0	0	0
-330V	0	0	0	0	0	0	0	0	0	0
-340V	0	0	0	0	0	0	0	0	0	0
-350V	0	0	0	0	0	0	0	0	0	0
-360V	0	0	0	0	0	0	0	0	0	0
-370V	0	0	0	0	0	0	0	0	0	0
-380V	0	0	0	0	0	0	0	0	0	0
-390V	0	0	0	0	0	0	0	0	0	0
-400V	0	0	0	0	0	0	0	0	0	0
-410V	0	0	0	0	0	0	0	0	0	0
-420V	0	0	0	0	0	0	0	0	0	0
-430V	0	0	0	0	0	0	0	0	0	0
-440V	0	0	0	0	0	0	0	0	0	0
-450V	0	0	0	0	0	0	0	0	0	0

Table 22: Bias Steps of PASP Plus Modules on Day 94235

Voltage	Module									
	1	2	3	4	5	6	8	11	14	15
-75V	32	32	18	32	18	31	18	31	18	18
-100V	32	32	18	32	18	31	18	31	18	18
-125V	32	32	18	32	18	31	18	31	18	18
-150V	30	32	18	32	18	32	18	31	18	18
-160V	0	0	0	0	0	0	0	0	0	0
-180V	0	0	0	0	0	0	0	0	0	0
-200V	0	0	0	0	0	0	0	0	0	0
-220V	0	0	0	0	0	0	0	0	0	0
-240V	0	0	0	0	0	0	0	0	0	0
-260V	0	0	0	0	0	0	0	0	0	0
-280V	0	0	0	0	0	0	0	0	0	0
-290V	0	0	0	0	0	0	0	0	0	0
-300V	0	0	0	0	0	0	0	0	0	0
-310V	0	0	0	0	0	0	0	0	0	0
-320V	0	0	0	0	0	0	0	0	0	0
-330V	0	0	0	0	0	0	0	0	0	0
-340V	0	0	0	0	0	0	0	0	0	0
-350V	0	0	0	0	0	0	0	0	0	0
-360V	0	0	0	0	0	0	0	0	0	0
-370V	0	0	0	0	0	0	0	0	0	0
-380V	0	0	0	0	0	0	0	0	0	0
-390V	0	0	0	0	0	0	0	0	0	0
-400V	0	0	0	0	0	0	0	0	0	0
-410V	0	0	0	0	0	0	0	0	0	0
-420V	0	0	0	0	0	0	0	0	0	0
-430V	0	0	0	0	0	0	0	0	0	0
-440V	0	0	0	0	0	0	0	0	0	0
-450V	0	0	0	0	0	0	0	0	0	0

Table 23: Bias Steps of PASP Plus Modules on Day 94236

Voltage	Module									
	1	2	3	4	5	6	8	11	14	15
-75V	0	0	28	0	28	0	28	0	28	28
-100V	0	0	28	0	28	0	28	0	28	28
-125V	0	0	27	0	28	0	28	0	28	28
-150V	0	0	26	0	28	0	28	0	28	28
-160V	22	22	0	22	0	22	0	22	0	0
-180V	22	22	0	22	0	22	0	22	0	0
-200V	21	22	0	22	0	22	0	22	0	0
-220V	21	22	0	22	0	22	0	22	0	0
-240V	0	0	0	0	0	0	0	0	0	0
-260V	0	0	0	0	0	0	0	0	0	0
-280V	0	0	0	0	0	0	0	0	0	0
-290V	0	0	0	0	0	0	0	0	0	0
-300V	0	0	0	0	0	0	0	0	0	0
-310V	0	0	0	0	0	0	0	0	0	0
-320V	0	0	0	0	0	0	0	0	0	0
-330V	0	0	0	0	0	0	0	0	0	0
-340V	0	0	0	0	0	0	0	0	0	0
-350V	0	0	0	0	0	0	0	0	0	0
-360V	0	0	0	0	0	0	0	0	0	0
-370V	0	0	0	0	0	0	0	0	0	0
-380V	0	0	0	0	0	0	0	0	0	0
-390V	0	0	0	0	0	0	0	0	0	0
-400V	0	0	0	0	0	0	0	0	0	0
-410V	0	0	0	0	0	0	0	0	0	0
-420V	0	0	0	0	0	0	0	0	0	0
-430V	0	0	0	0	0	0	0	0	0	0
-440V	0	0	0	0	0	0	0	0	0	0
-450V	0	0	0	0	0	0	0	0	0	0

Table 24: Bias Steps of PASP Plus Modules on Day 94237

Voltage	Module									
	1	2	3	4	5	6	8	11	14	15
-75V	0	0	0	0	0	0	0	0	0	0
-100V	0	0	0	0	0	0	0	0	0	0
-125V	0	0	0	0	0	0	0	0	0	0
-150V	0	0	0	0	0	0	0	0	0	0
-160V	35	35	10	35	10	35	10	35	10	10
-180V	35	35	10	35	10	35	10	35	10	10
-200V	36	35	10	35	10	35	10	35	10	10
-220V	33	35	10	35	10	35	10	35	10	10
-240V	0	0	0	0	0	0	0	0	0	0
-260V	0	0	0	0	0	0	0	0	0	0
-280V	0	0	0	0	0	0	0	0	0	0
-290V	0	0	0	0	0	0	0	0	0	0
-300V	0	0	0	0	0	0	0	0	0	0
-310V	0	0	0	0	0	0	0	0	0	0
-320V	0	0	0	0	0	0	0	0	0	0
-330V	0	0	0	0	0	0	0	0	0	0
-340V	0	0	0	0	0	0	0	0	0	0
-350V	0	0	0	0	0	0	0	0	0	0
-360V	0	0	0	0	0	0	0	0	0	0
-370V	0	0	0	0	0	0	0	0	0	0
-380V	0	0	0	0	0	0	0	0	0	0
-390V	0	0	0	0	0	0	0	0	0	0
-400V	0	0	0	0	0	0	0	0	0	0
-410V	0	0	0	0	0	0	0	0	0	0
-420V	0	0	0	0	0	0	0	0	0	0
-430V	0	0	0	0	0	0	0	0	0	0
-440V	0	0	0	0	0	0	0	0	0	0
-450V	0	0	0	0	0	0	0	0	0	0

Table 25: Bias Steps of PASP Plus Modules on Day 94238

Voltage	Module									
	1	2	3	4	5	6	8	11	14	15
-75V	0	0	0	0	0	0	0	0	0	0
-100V	0	0	0	0	0	0	0	0	0	0
-125V	0	0	0	0	0	0	0	0	0	0
-150V	0	0	0	0	0	0	0	0	0	0
-160V	0	0	20	0	20	0	20	0	20	20
-180V	0	0	20	0	20	0	20	0	20	20
-200V	0	0	20	0	20	0	20	0	20	20
-220V	0	0	18	0	20	0	20	0	20	20
-240V	0	0	0	0	0	0	0	0	0	0
-260V	0	0	0	0	0	0	0	0	0	0
-280V	0	0	0	0	0	0	0	0	0	0
-290V	0	0	0	0	0	0	0	0	0	0
-300V	0	0	0	0	0	0	0	0	0	0
-310V	0	0	0	0	0	0	0	0	0	0
-320V	0	0	0	0	0	0	0	0	0	0
-330V	0	0	0	0	0	0	0	0	0	0
-340V	0	0	0	0	0	0	0	0	0	0
-350V	0	0	0	0	0	0	0	0	0	0
-360V	0	0	0	0	0	0	0	0	0	0
-370V	0	0	0	0	0	0	0	0	0	0
-380V	0	0	0	0	0	0	0	0	0	0
-390V	0	0	0	0	0	0	0	0	0	0
-400V	0	0	0	0	0	0	0	0	0	0
-410V	0	0	0	0	0	0	0	0	0	0
-420V	0	0	0	0	0	0	0	0	0	0
-430V	0	0	0	0	0	0	0	0	0	0
-440V	0	0	0	0	0	0	0	0	0	0
-450V	0	0	0	0	0	0	0	0	0	0

Table 26: Bias Steps of PASP Plus Modules on Day 94239

Voltage	Module									
	1	2	3	4	5	6	8	11	14	15
-75V	0	0	0	0	0	0	0	0	0	0
-100V	0	0	0	0	0	0	0	0	0	0
-125V	0	0	0	0	0	0	0	0	0	0
-150V	0	0	0	0	0	0	0	0	0	0
-160V	0	0	0	0	0	0	0	0	0	0
-180V	0	0	0	0	0	0	0	0	0	0
-200V	0	0	0	0	0	0	0	0	0	0
-220V	0	0	0	0	0	0	0	0	0	0
-240V	3	3	0	4	0	4	0	4	0	0
-260V	3	3	0	4	0	4	0	4	0	0
-280V	3	3	0	3	0	4	0	4	0	0
-290V	0	0	0	0	0	0	0	0	0	0
-300V	3	3	0	3	0	4	0	4	0	0
-310V	0	0	0	0	0	0	0	0	0	0
-320V	0	0	0	0	0	0	0	0	0	0
-330V	0	0	0	0	0	0	0	0	0	0
-340V	0	0	0	0	0	0	0	0	0	0
-350V	0	0	0	0	0	0	0	0	0	0
-360V	0	0	0	0	0	0	0	0	0	0
-370V	0	0	0	0	0	0	0	0	0	0
-380V	0	0	0	0	0	0	0	0	0	0
-390V	0	0	0	0	0	0	0	0	0	0
-400V	0	0	0	0	0	0	0	0	0	0
-410V	0	0	0	0	0	0	0	0	0	0
-420V	0	0	0	0	0	0	0	0	0	0
-430V	0	0	0	0	0	0	0	0	0	0
-440V	0	0	0	0	0	0	0	0	0	0
-450V	0	0	0	0	0	0	0	0	0	0

Table 27: Bias Steps of PASP Plus Modules on Day 94240

Voltage	Module									
	1	2	3	4	5	6	8	11	14	15
-75V	0	0	0	0	0	0	0	0	0	0
-100V	0	0	0	0	0	0	0	0	0	0
-125V	0	0	0	0	0	0	0	0	0	0
-150V	0	0	0	0	0	0	0	0	0	0
-160V	0	0	0	0	0	0	0	0	0	0
-180V	0	0	0	0	0	0	0	0	0	0
-200V	0	0	0	0	0	0	0	0	0	0
-220V	0	0	0	0	0	0	0	0	0	0
-240V	43	43	0	43	0	46	0	48	0	0
-260V	43	43	0	42	0	43	0	48	0	0
-280V	43	43	0	43	0	43	0	48	0	0
-290V	0	0	0	0	0	0	0	0	0	0
-300V	43	42	0	43	0	43	0	48	0	0
-310V	0	0	0	0	0	0	0	0	0	0
-320V	0	0	0	0	0	0	0	0	0	0
-330V	0	0	0	0	0	0	0	0	0	0
-340V	0	0	0	0	0	0	0	0	0	0
-350V	0	0	0	0	0	0	0	0	0	0
-360V	0	0	0	0	0	0	0	0	0	0
-370V	0	0	0	0	0	0	0	0	0	0
-380V	0	0	0	0	0	0	0	0	0	0
-390V	0	0	0	0	0	0	0	0	0	0
-400V	0	0	0	0	0	0	0	0	0	0
-410V	0	0	0	0	0	0	0	0	0	0
-420V	0	0	0	0	0	0	0	0	0	1
-430V	0	0	0	0	0	0	0	0	0	0
-440V	0	0	0	0	0	0	0	0	0	0
-450V	0	0	0	0	0	0	0	0	0	0

Table 28: Bias Steps of PASP Plus Modules on Day 94241

Voltage	Module									
	1	2	3	4	5	6	8	11	14	15
-75V	0	0	0	0	0	0	0	0	0	0
-100V	0	0	0	0	0	0	0	0	0	0
-125V	0	0	0	0	0	0	0	0	0	0
-150V	0	0	0	0	0	0	0	0	0	0
-160V	0	0	0	0	0	0	0	0	0	0
-180V	0	0	0	0	0	0	0	0	0	0
-200V	0	0	0	0	0	0	0	0	0	0
-220V	0	0	0	0	0	0	0	0	0	0
-240V	39	40	43	40	44	40	44	45	45	50
-260V	39	40	44	40	44	40	44	45	45	50
-280V	39	39	44	40	44	40	44	45	45	48
-290V	0	0	0	0	0	0	0	0	0	0
-300V	39	39	44	40	43	40	44	44	45	46
-310V	0	0	0	0	0	0	0	0	0	0
-320V	0	0	0	0	0	0	0	0	0	0
-330V	0	0	0	0	0	0	0	0	0	0
-340V	0	0	0	0	0	0	0	0	0	0
-350V	0	0	0	0	0	0	0	0	0	0
-360V	0	0	0	0	0	0	0	0	0	0
-370V	0	0	0	0	0	0	0	0	0	0
-380V	0	0	0	0	0	0	0	0	0	0
-390V	0	0	0	0	0	0	0	0	0	0
-400V	0	0	0	0	0	0	0	0	0	0
-410V	0	0	0	0	0	0	0	0	0	0
-420V	0	0	0	0	0	0	0	0	0	0
-430V	0	0	0	0	0	0	0	0	0	0
-440V	0	0	0	0	0	0	0	0	0	0
-450V	0	0	0	0	0	0	0	0	0	0

Table 29: Bias Steps of PASP Plus Modules on Day 94242

Voltage	Module									
	1	2	3	4	5	6	8	11	14	15
-75V	0	0	0	0	0	0	0	0	0	0
-100V	0	0	0	0	0	0	0	0	0	0
-125V	0	0	0	0	0	0	0	0	0	0
-150V	0	0	0	0	0	0	0	0	0	0
-160V	0	0	0	0	0	0	0	0	0	0
-180V	0	0	0	0	0	0	0	0	0	0
-200V	0	0	0	0	0	0	0	0	0	0
-220V	0	0	0	0	0	0	0	0	0	0
-240V	0	0	66	0	65	0	67	0	66	76
-260V	0	0	66	0	66	0	65	0	67	70
-280V	0	0	66	0	66	0	65	0	67	68
-290V	0	0	0	0	0	0	0	0	0	0
-300V	0	0	66	0	66	0	66	0	67	65
-310V	0	0	0	0	0	0	0	0	0	0
-320V	1	1	0	1	0	1	0	1	0	0
-330V	0	0	0	0	0	0	0	0	0	0
-340V	1	1	0	1	0	1	0	1	0	0
-350V	0	0	0	0	0	0	0	0	0	0
-360V	1	1	0	1	0	1	0	1	0	0
-370V	0	0	0	0	0	0	0	0	0	0
-380V	1	1	0	1	0	1	0	1	0	0
-390V	0	0	0	0	0	0	0	0	0	0
-400V	0	0	0	0	0	0	0	0	0	0
-410V	0	0	0	0	0	0	0	0	0	0
-420V	0	0	0	0	0	0	0	0	0	0
-430V	0	0	0	0	0	0	0	0	0	0
-440V	0	0	0	0	0	0	0	0	0	0
-450V	0	0	0	0	0	0	0	0	0	0

Table 30: Bias Steps of PASP Plus Modules on Day 94243

Voltage	Module									
	1	2	3	4	5	6	8	11	14	15
-75V	0	0	0	0	0	0	0	0	0	0
-100V	0	0	0	0	0	0	0	0	0	0
-125V	0	0	0	0	0	0	0	0	0	0
-150V	0	0	0	0	0	0	0	0	0	0
-160V	0	0	0	0	0	0	0	0	0	0
-180V	0	0	0	0	0	0	0	0	0	0
-200V	0	0	0	0	0	0	0	0	0	0
-220V	0	0	0	0	0	0	0	0	0	0
-240V	0	0	41	0	41	0	42	0	43	46
-260V	0	0	41	0	41	0	42	0	43	43
-280V	0	0	41	0	41	0	41	0	42	43
-290V	1	1	0	0	41	0	0	0	0	0
-300V	0	0	40	0	82	0	41	0	42	43
-310V	1	1	0	0	0	0	0	0	0	0
-320V	0	0	41	1	0	2	43	2	43	43
-330V	1	1	0	0	0	0	0	0	0	0
-340V	0	0	41	1	0	2	43	2	43	43
-350V	0	0	0	0	0	0	0	0	0	0
-360V	0	0	41	1	0	2	42	2	43	43
-370V	0	0	0	0	0	0	0	0	0	0
-380V	0	0	41	1	0	2	42	2	43	43
-390V	0	0	0	0	0	0	0	0	0	0
-400V	0	0	0	0	0	0	0	0	0	0
-410V	0	0	0	0	0	0	0	0	0	0
-420V	0	0	0	0	0	0	0	0	0	0
-430V	0	0	0	0	0	0	0	0	0	0
-440V	0	0	0	0	0	0	0	0	0	0
-450V	0	0	0	0	0	0	0	0	0	0

Table 31: Bias Steps of PASP Plus Modules on Day 94244

Voltage	Module									
	1	2	3	4	5	6	8	11	14	15
-75V	0	0	0	0	0	0	0	0	0	0
-100V	0	0	0	0	0	0	0	0	0	0
-125V	0	0	0	0	0	0	0	0	0	0
-150V	0	0	0	0	0	0	0	0	0	0
-160V	0	0	0	0	0	0	0	0	0	0
-180V	0	0	0	0	0	0	0	0	0	0
-200V	0	0	0	0	0	0	0	0	0	0
-220V	0	0	0	0	0	0	0	0	0	0
-240V	0	0	0	0	0	0	0	0	0	0
-260V	0	0	0	0	0	0	0	0	0	0
-280V	0	0	0	0	0	0	0	0	0	0
-290V	46	46	0	0	39	0	0	0	0	0
-300V	0	0	0	0	39	0	0	0	0	0
-310V	40	46	0	0	0	0	0	0	0	0
-320V	0	0	39	46	0	47	39	47	39	39
-330V	40	46	0	0	0	0	0	0	0	0
-340V	0	0	39	46	0	47	39	47	39	39
-350V	0	0	0	0	0	0	0	0	0	0
-360V	0	0	39	46	0	47	39	47	39	39
-370V	0	0	0	0	0	0	0	0	0	0
-380V	0	0	38	46	0	46	39	47	39	39
-390V	0	0	0	0	0	0	0	0	0	0
-400V	0	0	0	0	0	0	0	0	0	0
-410V	0	0	0	0	0	0	0	0	0	0
-420V	0	0	0	0	0	0	0	0	0	0
-430V	0	0	0	0	0	0	0	0	0	0
-440V	0	0	0	0	0	0	0	0	0	0
-450V	0	0	0	0	0	0	0	0	0	0

Table 32: Bias Steps of PASP Plus Modules on Day 94245

Voltage	Module									
	1	2	3	4	5	6	8	11	14	15
-75V	0	0	0	0	0	0	0	0	0	0
-100V	0	0	0	0	0	0	0	0	0	0
-125V	0	0	0	0	0	0	0	0	0	0
-150V	0	0	0	0	0	0	0	0	0	0
-160V	0	0	0	0	0	0	0	0	0	0
-180V	0	0	0	0	0	0	0	0	0	0
-200V	0	0	0	0	0	0	0	0	0	0
-220V	0	0	0	0	0	0	0	0	0	0
-240V	0	0	0	0	0	0	0	0	0	0
-260V	0	0	0	0	0	0	0	0	0	0
-280V	0	0	0	0	0	0	0	0	0	0
-290V	69	77	0	0	6	0	0	0	0	0
-300V	0	0	0	0	6	0	0	0	0	0
-310V	67	75	0	0	0	0	0	0	0	0
-320V	0	0	0	78	0	79	0	80	0	0
-330V	67	75	0	0	0	0	0	0	0	0
-340V	0	0	0	78	0	79	0	79	0	0
-350V	0	0	0	0	0	0	0	0	0	0
-360V	0	0	0	78	0	79	0	79	0	0
-370V	0	0	0	0	0	0	0	0	0	0
-380V	0	0	0	77	0	78	0	79	0	0
-390V	0	0	6	0	0	0	6	0	6	6
-400V	0	0	0	0	0	0	0	0	0	0
-410V	0	0	6	0	0	0	6	0	6	6
-420V	0	0	0	0	0	0	0	0	0	0
-430V	0	0	6	0	0	0	6	0	6	6
-440V	0	0	0	0	0	0	0	0	0	0
-450V	0	0	6	0	0	0	6	0	6	6

Table 33: Bias Steps of PASP Plus Modules on Day 94246

Voltage	Module									
	1	2	3	4	5	6	8	11	14	15
-75V	0	0	0	0	0	0	0	0	0	0
-100V	0	0	0	0	0	0	0	0	0	0
-125V	0	0	0	0	0	0	0	0	0	0
-150V	0	0	0	0	0	0	0	0	0	0
-160V	0	0	0	0	0	0	0	0	0	0
-180V	0	0	0	0	0	0	0	0	0	0
-200V	0	0	0	0	0	0	0	0	0	0
-220V	0	0	0	0	0	0	0	0	0	0
-240V	0	0	0	0	0	0	0	0	0	0
-260V	0	0	0	0	0	0	0	0	0	0
-280V	0	0	0	0	0	0	0	0	0	0
-290V	3	5	0	0	46	0	0	0	0	0
-300V	0	0	0	0	46	0	0	0	0	0
-310V	3	5	0	0	0	0	0	0	0	0
-320V	0	0	0	4	0	4	0	4	0	0
-330V	3	5	0	0	0	0	0	0	0	0
-340V	11	11	0	6	0	6	0	6	0	0
-350V	11	11	0	2	0	2	0	2	0	0
-360V	11	11	0	6	0	6	0	6	0	0
-370V	10	11	0	2	0	2	0	2	0	0
-380V	0	0	0	4	0	4	0	4	0	0
-390V	0	0	45	9	0	9	46	10	46	48
-400V	0	0	0	0	0	0	0	0	0	0
-410V	0	0	40	9	0	9	46	10	46	48
-420V	0	0	41	9	0	9	46	10	46	47
-430V	0	0	41	9	0	9	46	10	46	48
-440V	0	0	0	0	0	0	0	0	0	0
-450V	0	0	0	0	0	0	0	0	0	0

Table 34: Bias Steps of PASP Plus Modules on Day 94290

Voltage	Module									
	1	2	3	4	5	6	8	11	14	15
-75V	0	0	0	0	0	0	0	0	0	0
-100V	0	0	0	0	0	0	0	0	0	0
-125V	0	0	0	0	0	0	0	0	0	0
-150V	0	0	0	0	0	0	0	0	0	0
-160V	57	58	0	58	0	58	0	58	0	0
-180V	57	58	0	58	0	58	0	58	0	0
-200V	57	57	0	58	0	58	0	58	0	0
-220V	57	58	0	58	0	58	0	58	0	0
-240V	0	0	0	0	0	0	0	0	0	0
-260V	0	0	0	0	0	0	0	0	0	0
-280V	0	0	0	0	0	0	0	0	0	0
-290V	0	0	0	0	0	0	0	0	0	0
-300V	0	0	0	0	0	0	0	0	0	0
-310V	0	0	0	0	0	0	0	0	0	0
-320V	0	0	0	0	0	0	0	0	0	0
-330V	0	0	0	0	0	0	0	0	0	0
-340V	0	0	0	0	0	0	0	0	0	0
-350V	0	0	0	0	0	0	0	0	0	0
-360V	0	0	0	0	0	0	0	0	0	0
-370V	0	0	0	0	0	0	0	0	0	0
-380V	0	0	0	0	0	0	0	0	0	0
-390V	0	0	0	0	0	0	0	0	0	0
-400V	0	0	0	0	0	0	0	0	0	0
-410V	0	0	0	0	0	0	0	0	0	0
-420V	0	0	0	0	0	0	0	0	0	0
-430V	0	0	0	0	0	0	0	0	0	0
-440V	0	0	0	0	0	0	0	0	0	0
-450V	0	0	0	0	0	0	0	0	0	0

Table 35: Bias Steps of PASP Plus Modules on Day 94291

Voltage	Module									
	1	2	3	4	5	6	8	11	14	15
-75V	0	0	0	0	0	0	0	0	0	0
-100V	0	0	0	0	0	0	0	0	0	0
-125V	0	0	0	0	0	0	0	0	0	0
-150V	0	0	0	0	0	0	0	0	0	0
-160V	83	83	0	84	0	85	0	85	0	0
-180V	83	83	0	83	0	85	0	85	0	0
-200V	84	83	0	83	0	85	0	85	0	0
-220V	84	83	0	83	0	85	0	85	0	0
-240V	0	0	30	0	31	0	31	0	32	32
-260V	0	0	30	0	30	0	31	0	32	31
-280V	0	0	30	0	30	0	31	0	32	32
-290V	0	0	0	0	0	0	0	0	0	0
-300V	0	0	30	0	30	0	31	0	31	32
-310V	0	0	0	0	0	0	0	0	0	0
-320V	0	0	0	0	0	0	0	0	0	0
-330V	0	0	0	0	0	0	0	0	0	0
-340V	0	0	0	0	0	0	0	0	0	0
-350V	0	0	0	0	0	0	0	0	0	0
-360V	0	0	0	0	0	0	0	0	0	0
-370V	0	0	0	0	0	0	0	0	0	0
-380V	0	0	0	0	0	0	0	0	0	0
-390V	0	0	0	0	0	0	0	0	0	0
-400V	0	0	0	0	0	0	0	0	0	0
-410V	0	0	0	0	0	0	0	0	0	0
-420V	0	0	0	0	0	0	0	0	0	0
-430V	0	0	0	0	0	0	0	0	0	0
-440V	0	0	0	0	0	0	0	0	0	0
-450V	0	0	0	0	0	0	0	0	0	0

Table 36: Bias Steps of PASP Plus Modules on Day 94292

Voltage	Module									
	1	2	3	4	5	6	8	11	14	15
-75V	0	0	0	0	0	0	0	0	0	0
-100V	0	0	0	0	0	0	0	0	0	0
-125V	0	0	0	0	0	0	0	0	0	0
-150V	0	0	0	0	0	0	0	0	0	0
-160V	0	0	0	0	0	0	0	0	0	0
-180V	0	0	0	0	0	0	0	0	0	0
-200V	0	0	0	0	0	0	0	0	0	0
-220V	0	0	0	0	0	0	0	0	0	0
-240V	36	36	108	37	108	37	108	37	108	110
-260V	36	36	108	37	107	37	108	37	108	107
-280V	36	36	108	36	108	37	108	37	108	108
-290V	0	0	0	0	0	0	0	0	0	0
-300V	36	36	108	36	108	37	108	36	108	108
-310V	0	0	0	0	0	0	0	0	0	0
-320V	0	0	0	0	0	0	0	0	0	0
-330V	0	0	0	0	0	0	0	0	0	0
-340V	0	0	0	0	0	0	0	0	0	0
-350V	0	0	0	0	0	0	0	0	0	0
-360V	0	0	0	0	0	0	0	0	0	0
-370V	0	0	0	0	0	0	0	0	0	0
-380V	0	0	0	0	0	0	0	0	0	0
-390V	0	0	0	0	0	0	0	0	0	0
-400V	0	0	0	0	0	0	0	0	0	0
-410V	0	0	0	0	0	0	0	0	0	0
-420V	0	0	0	0	0	0	0	0	0	0
-430V	0	0	0	0	0	0	0	0	0	0
-440V	0	0	0	0	0	0	0	0	0	0
-450V	0	0	0	0	0	0	0	0	0	0

Table 37: Bias Steps of PASP Plus Modules on Day 94293

Voltage	Module									
	1	2	3	4	5	6	8	11	14	15
-75V	0	0	0	0	0	0	0	0	0	0
-100V	0	0	0	0	0	0	0	0	0	0
-125V	0	0	0	0	0	0	0	0	0	0
-150V	0	0	0	0	0	0	0	0	0	0
-160V	0	0	0	0	0	0	0	0	0	0
-180V	0	0	0	0	0	0	0	0	0	0
-200V	0	0	0	0	0	0	0	0	0	0
-220V	0	0	0	0	0	0	0	0	0	0
-240V	90	90	0	92	0	92	0	92	0	0
-260V	90	90	0	92	0	92	0	92	0	0
-280V	90	90	0	91	0	92	0	92	0	0
-290V	0	0	0	0	54	0	0	0	0	0
-300V	90	90	0	90	0	92	0	92	0	0
-310V	0	0	54	0	0	0	54	0	54	54
-320V	0	0	0	0	0	0	0	0	0	0
-330V	0	0	54	0	0	0	54	0	54	54
-340V	0	0	0	0	0	0	0	0	0	0
-350V	0	0	54	0	0	0	54	0	54	54
-360V	0	0	0	0	0	0	0	0	0	0
-370V	0	0	53	0	0	0	54	0	54	54
-380V	0	0	0	0	0	0	0	0	0	0
-390V	0	0	0	0	0	0	0	0	0	0
-400V	0	0	0	0	0	0	0	0	0	0
-410V	0	0	0	0	0	0	0	0	0	0
-420V	0	0	0	0	0	0	0	0	0	0
-430V	0	0	0	0	0	0	0	0	0	0
-440V	0	0	0	0	0	0	0	0	0	0
-450V	0	0	0	0	0	0	0	0	0	0

Table 38: Bias Steps of PASP Plus Modules on Day 94294

Voltage	Module									
	1	2	3	4	5	6	8	11	14	15
-75V	0	0	0	0	0	0	0	0	0	0
-100V	0	0	0	0	0	0	0	0	0	0
-125V	0	0	0	0	0	0	0	0	0	0
-150V	0	0	0	0	0	0	0	0	0	0
-160V	0	0	0	0	0	0	0	0	0	0
-180V	0	0	0	0	0	0	0	0	0	0
-200V	0	0	0	0	0	0	0	0	0	0
-220V	0	0	0	0	0	0	0	0	0	0
-240V	0	0	0	0	0	0	0	0	0	0
-260V	0	0	0	0	0	0	0	0	0	0
-280V	0	0	0	0	0	0	0	0	0	0
-290V	0	0	0	0	95	0	0	0	0	0
-300V	0	0	0	0	0	0	0	0	0	0
-310V	0	0	95	0	0	0	97	0	98	98
-320V	31	31	0	34	0	35	0	35	0	0
-330V	0	0	95	0	0	0	97	0	98	98
-340V	31	31	0	31	0	35	0	35	0	0
-350V	0	0	95	0	0	0	97	0	98	98
-360V	31	31	0	31	0	35	0	35	0	0
-370V	0	0	95	0	0	0	97	0	97	98
-380V	31	31	0	31	0	35	0	33	0	0
-390V	0	0	0	0	0	0	0	0	0	0
-400V	0	0	0	0	0	0	0	0	0	0
-410V	0	0	0	0	0	0	0	0	0	0
-420V	0	0	0	0	0	0	0	0	0	0
-430V	0	0	0	0	0	0	0	0	0	0
-440V	0	0	0	0	0	0	0	0	0	0
-450V	0	0	0	0	0	0	0	0	0	0

Table 39: Bias Steps of PASP Plus Modules on Day 94295

Voltage	Module									
	1	2	3	4	5	6	8	11	14	15
-75V	0	0	0	0	0	0	0	0	0	0
-100V	0	0	0	0	0	0	0	0	0	0
-125V	0	0	0	0	0	0	0	0	0	0
-150V	0	0	0	0	0	0	0	0	0	0
-160V	0	0	0	0	0	0	0	0	0	0
-180V	0	0	0	0	0	0	0	0	0	0
-200V	0	0	0	0	0	0	0	0	0	0
-220V	0	0	0	0	0	0	0	0	0	0
-240V	0	0	0	0	37	0	0	0	0	0
-260V	0	0	0	0	37	0	0	0	0	0
-280V	0	0	0	0	36	0	0	0	0	0
-290V	0	0	0	0	0	0	0	0	0	0
-300V	0	0	0	0	36	0	0	0	0	0
-310V	0	0	0	0	0	0	0	0	0	0
-320V	62	64	0	71	0	71	0	72	0	0
-330V	0	0	0	0	0	0	0	0	0	0
-340V	62	64	37	67	0	71	41	72	41	41
-350V	0	0	0	0	0	0	0	0	0	0
-360V	61	64	37	64	0	71	38	72	40	41
-370V	0	0	0	0	0	0	0	0	0	0
-380V	61	64	37	64	0	71	38	71	41	41
-390V	0	0	0	0	0	0	0	0	0	0
-400V	0	0	36	0	0	0	36	0	41	41
-410V	0	0	0	0	0	0	0	0	0	0
-420V	0	0	0	0	0	0	0	0	0	0
-430V	0	0	0	0	0	0	0	0	0	0
-440V	0	0	0	0	0	0	0	0	0	0
-450V	0	0	0	0	0	0	0	0	0	0

Table 40: Bias Steps of PASP Plus Modules on Day 94304

Voltage	Module									
	1	2	3	4	5	6	8	11	14	15
-75V	0	0	0	0	0	0	0	0	0	0
-100V	0	0	0	0	0	0	0	0	0	0
-125V	0	0	0	0	0	0	0	0	0	0
-150V	0	0	0	0	0	0	0	0	0	0
-160V	0	0	0	140	98	2	0	2	0	0
-180V	0	0	0	140	98	2	0	2	0	0
-200V	0	0	0	139	97	2	0	2	0	0
-220V	0	0	0	139	97	2	0	2	0	0
-240V	0	0	0	0	0	0	0	0	0	0
-260V	0	0	0	0	0	0	0	0	0	0
-280V	0	0	0	0	0	0	0	0	0	0
-290V	0	0	0	0	0	0	0	0	0	0
-300V	0	0	0	0	0	0	0	0	0	0
-310V	0	0	0	0	0	0	0	0	0	0
-320V	0	0	0	0	0	0	0	0	0	0
-330V	0	0	0	0	0	0	0	0	0	0
-340V	0	0	0	0	0	0	0	0	0	0
-350V	0	0	0	0	0	0	0	0	0	0
-360V	0	0	0	0	0	0	0	0	0	0
-370V	0	0	0	0	0	0	0	0	0	0
-380V	0	0	0	0	0	0	0	0	0	0
-390V	0	0	0	0	0	0	0	0	0	0
-400V	0	0	0	0	0	0	0	0	0	0
-410V	0	0	0	0	0	0	0	0	0	0
-420V	0	0	0	0	0	0	0	0	0	0
-430V	0	0	0	0	0	0	0	0	0	0
-440V	0	0	0	0	0	0	0	0	0	0
-450V	0	0	0	0	0	0	0	0	0	0

Table 41: Bias Steps of PASP Plus Modules on Day 94305

Voltage	Module									
	1	2	3	4	5	6	8	11	14	15
-75V	0	0	0	0	0	0	0	0	0	0
-100V	0	0	0	0	0	0	0	0	0	0
-125V	0	0	0	0	0	0	0	0	0	0
-150V	0	0	0	0	0	0	0	0	0	0
-160V	197	14	2	0	91	171	2	205	0	0
-180V	197	13	2	0	91	172	2	205	0	0
-200V	195	13	2	0	90	170	2	204	0	0
-220V	196	13	2	0	90	170	2	202	0	0
-240V	0	0	0	0	0	0	0	0	0	0
-260V	0	0	0	0	0	0	0	0	0	0
-280V	0	0	0	0	0	0	0	0	0	0
-290V	0	0	0	0	0	0	0	0	0	0
-300V	0	0	0	0	0	0	0	0	0	0
-310V	0	0	0	0	0	0	0	0	0	0
-320V	0	0	0	0	0	0	0	0	0	0
-330V	0	0	0	0	0	0	0	0	0	0
-340V	0	0	0	0	0	0	0	0	0	0
-350V	0	0	0	0	0	0	0	0	0	0
-360V	0	0	0	0	0	0	0	0	0	0
-370V	0	0	0	0	0	0	0	0	0	0
-380V	0	0	0	0	0	0	0	0	0	0
-390V	0	0	0	0	0	0	0	0	0	0
-400V	0	0	0	0	0	0	0	0	0	0
-410V	0	0	0	0	0	0	0	0	0	0
-420V	0	0	0	0	0	0	0	0	0	0
-430V	0	0	0	0	0	0	0	0	0	0
-440V	0	0	0	0	0	0	0	0	0	0
-450V	0	0	0	0	0	0	0	0	0	0

Table 42: Bias Steps of PASP Plus Modules on Day 94306

Voltage	Module									
	1	2	3	4	5	6	8	11	14	15
-75V	0	0	0	0	0	0	0	0	0	0
-100V	0	0	0	0	0	0	0	0	0	0
-125V	0	0	0	0	0	0	0	0	0	0
-150V	0	0	0	0	0	0	0	0	0	0
-160V	3	172	172	0	0	0	160	0	0	0
-180V	3	172	171	0	0	0	160	0	0	0
-200V	2	171	171	0	0	0	159	0	0	0
-220V	2	171	171	0	0	0	158	0	0	0
-240V	0	0	0	197	2	2	0	2	0	0
-260V	0	0	0	197	2	2	0	2	0	0
-280V	0	0	0	197	2	2	0	2	0	0
-290V	0	0	0	0	0	0	0	0	0	0
-300V	0	0	0	196	2	2	0	2	0	0
-310V	0	0	0	0	0	0	0	0	0	0
-320V	0	0	0	0	0	0	0	0	0	0
-330V	0	0	0	0	0	0	0	0	0	0
-340V	0	0	0	0	0	0	0	0	0	0
-350V	0	0	0	0	0	0	0	0	0	0
-360V	0	0	0	0	0	0	0	0	0	0
-370V	0	0	0	0	0	0	0	0	0	0
-380V	0	0	0	0	0	0	0	0	0	0
-390V	0	0	0	0	0	0	0	0	0	0
-400V	0	0	0	0	0	0	0	0	0	0
-410V	0	0	0	0	0	0	0	0	0	0
-420V	0	0	0	0	0	0	0	0	0	0
-430V	0	0	0	0	0	0	0	0	0	0
-440V	0	0	0	0	0	0	0	0	0	0
-450V	0	0	0	0	0	0	0	0	0	0

Table 43: Bias Steps of PASP Plus Modules on Day 94307

Voltage	Module									
	1	2	3	4	5	6	8	11	14	15
-75V	0	0	0	0	0	0	0	0	0	0
-100V	0	0	0	0	0	0	0	0	0	0
-125V	0	0	0	0	0	0	0	0	0	0
-150V	0	0	0	0	0	0	0	0	0	0
-160V	0	0	0	0	0	0	0	0	0	0
-180V	0	0	0	0	0	0	0	0	0	0
-200V	0	0	0	0	0	0	0	0	0	0
-220V	0	0	0	0	0	0	0	0	0	0
-240V	149	2	2	30	172	138	2	193	0	0
-260V	149	2	2	30	172	138	2	192	0	0
-280V	149	2	2	29	171	136	2	192	0	0
-290V	0	0	0	0	0	0	0	0	0	0
-300V	149	2	2	29	171	136	2	191	0	0
-310V	0	0	0	0	0	0	0	0	0	0
-320V	0	0	0	0	0	0	0	0	0	0
-330V	0	0	0	0	0	0	0	0	0	0
-340V	0	0	0	0	0	0	0	0	0	0
-350V	0	0	0	0	0	0	0	0	0	0
-360V	0	0	0	0	0	0	0	0	0	0
-370V	0	0	0	0	0	0	0	0	0	0
-380V	0	0	0	0	0	0	0	0	0	0
-390V	0	0	0	0	0	0	0	0	0	0
-400V	0	0	0	0	0	0	0	0	0	0
-410V	0	0	0	0	0	0	0	0	0	0
-420V	0	0	0	0	0	0	0	0	0	0
-430V	0	0	0	0	0	0	0	0	0	0
-440V	0	0	0	0	0	0	0	0	0	0
-450V	0	0	0	0	0	0	0	0	0	0

Table 44: Bias Steps of PASP Plus Modules on Day 94308

Voltage	Module									
	1	2	3	4	5	6	8	11	14	15
-75V	0	0	0	0	0	0	0	0	0	0
-100V	0	0	0	0	0	0	0	0	0	0
-125V	0	0	0	0	0	0	0	0	0	0
-150V	0	0	0	0	0	0	0	0	0	0
-160V	0	0	0	0	0	0	0	0	0	0
-180V	0	0	0	0	0	0	0	0	0	0
-200V	0	0	0	0	0	0	0	0	0	0
-220V	0	0	0	0	0	0	0	0	0	0
-240V	57	172	172	0	2	0	216	0	0	0
-260V	56	172	172	0	2	0	215	0	0	0
-280V	56	172	171	0	2	0	213	0	0	0
-290V	0	0	0	0	0	0	0	0	0	0
-300V	56	171	171	0	2	0	213	0	0	0
-310V	0	0	0	3	0	1	0	2	0	0
-320V	0	0	0	0	0	0	0	0	0	0
-330V	0	0	0	3	0	2	0	2	0	0
-340V	0	0	0	0	0	0	0	0	0	0
-350V	0	0	0	2	0	2	0	2	0	0
-360V	0	0	0	0	0	0	0	0	0	0
-370V	0	0	0	2	0	2	0	2	0	0
-380V	0	0	0	0	0	0	0	0	0	0
-390V	0	0	0	0	0	0	0	0	0	0
-400V	0	0	0	0	0	0	0	0	0	0
-410V	0	0	0	0	0	0	0	0	0	0
-420V	0	0	0	0	0	0	0	0	0	0
-430V	0	0	0	0	0	0	0	0	0	0
-440V	0	0	0	0	0	0	0	0	0	0
-450V	0	0	0	0	0	0	0	0	0	0

Table 45: Bias Steps of PASP Plus Modules on Day 95033

Voltage	Module									
	1	2	3	4	5	6	8	11	14	15
-75V	0	0	0	0	0	0	0	0	0	0
-100V	0	0	0	0	0	0	0	0	0	0
-125V	0	0	0	0	0	0	0	0	0	0
-150V	0	0	0	0	0	0	0	0	0	0
-160V	0	0	0	0	0	0	0	0	0	0
-180V	0	0	0	0	0	0	0	0	0	0
-200V	0	0	0	0	0	0	0	0	0	0
-220V	0	0	0	0	0	0	0	0	0	0
-240V	20	40	0	0	0	0	0	0	0	0
-260V	20	40	0	0	0	0	0	0	0	0
-280V	20	40	0	0	0	0	0	0	0	0
-290V	0	0	0	0	0	0	0	0	0	0
-300V	20	40	0	0	0	0	0	0	0	0
-310V	0	0	0	0	0	0	0	0	0	0
-320V	0	0	0	0	0	0	0	0	0	0
-330V	0	0	0	0	0	0	0	0	0	0
-340V	0	0	0	0	0	0	0	0	0	0
-350V	0	0	0	0	0	0	0	0	0	0
-360V	0	0	0	0	0	0	0	0	20	0
-370V	0	0	0	0	0	0	0	0	0	0
-380V	0	0	0	0	0	0	0	0	20	0
-390V	0	0	0	0	0	0	0	0	0	0
-400V	0	0	0	0	0	0	0	0	19	0
-410V	0	0	0	0	0	0	0	0	0	0
-420V	0	0	0	0	0	0	0	0	19	0
-430V	0	0	0	0	0	0	0	0	0	0
-440V	0	0	0	0	0	0	0	0	0	0
-450V	0	0	0	0	0	0	0	0	0	0

Table 46: Bias Steps of PASP Plus Modules on Day 95034

Voltage	Module									
	1	2	3	4	5	6	8	11	14	15
-75V	0	0	0	0	0	0	0	0	0	0
-100V	0	0	0	0	0	0	0	0	0	0
-125V	0	0	0	0	0	0	0	0	0	0
-150V	0	0	0	0	0	0	0	0	0	0
-160V	0	0	0	0	0	0	0	0	0	0
-180V	0	0	0	0	0	0	0	0	0	0
-200V	0	0	0	0	0	0	0	0	0	0
-220V	0	0	0	0	0	0	0	0	0	0
-240V	0	0	0	0	0	0	0	0	0	0
-260V	0	0	0	0	0	0	0	0	0	0
-280V	0	0	0	0	0	0	0	0	0	0
-290V	0	0	0	0	0	0	0	0	0	0
-300V	0	0	0	0	0	0	0	0	0	0
-310V	0	0	0	0	0	0	0	0	0	0
-320V	0	0	0	0	0	0	0	0	0	0
-330V	0	0	0	0	0	0	0	0	0	0
-340V	0	0	0	0	0	0	0	0	0	0
-350V	0	0	0	0	0	0	0	0	0	0
-360V	0	0	0	0	0	14	172	40	20	0
-370V	0	0	0	0	0	0	0	0	0	0
-380V	0	0	0	0	0	14	172	40	20	0
-390V	0	0	0	0	0	0	0	0	0	0
-400V	0	0	0	0	0	14	171	40	20	0
-410V	0	0	0	0	0	0	0	0	0	0
-420V	0	0	0	0	0	14	168	38	19	0
-430V	0	0	0	0	0	0	0	0	0	0
-440V	0	0	0	0	0	0	0	0	0	0
-450V	0	0	0	0	0	0	0	0	0	0

Table 47: Bias Steps of PASP Plus Modules on Day 95035

Voltage	Module									
	1	2	3	4	5	6	8	11	14	15
-75V	0	0	0	0	0	0	0	0	0	0
-100V	0	0	0	0	0	0	0	0	0	0
-125V	0	0	0	0	0	0	0	0	0	0
-150V	0	0	0	0	0	0	0	0	0	0
-160V	0	0	0	0	0	0	0	0	0	0
-180V	0	0	0	0	0	0	0	0	0	0
-200V	0	0	0	0	0	0	0	0	0	0
-220V	0	0	0	0	0	0	0	0	0	0
-240V	0	0	0	0	0	0	0	0	0	0
-260V	0	0	0	0	0	0	0	0	0	0
-280V	0	0	0	0	0	0	0	0	0	0
-290V	0	42	186	0	0	0	0	0	0	0
-300V	0	0	0	0	0	0	0	0	0	0
-310V	0	42	185	0	0	0	0	0	0	0
-320V	0	0	0	0	0	0	0	0	0	0
-330V	0	41	185	0	0	0	0	0	0	0
-340V	0	0	0	0	0	0	0	0	0	0
-350V	0	41	182	0	0	0	0	0	0	0
-360V	0	0	0	23	0	167	0	0	0	0
-370V	0	0	0	0	0	0	0	0	0	0
-380V	0	0	0	23	0	166	0	0	0	0
-390V	0	0	0	0	0	0	0	0	0	0
-400V	0	0	0	22	0	166	0	0	0	0
-410V	0	0	0	0	0	0	0	0	0	0
-420V	0	0	0	23	0	165	0	0	0	0
-430V	0	0	0	0	0	0	0	0	0	0
-440V	0	0	0	0	0	0	0	0	0	0
-450V	0	0	0	0	0	0	0	0	0	0

Table 48: Bias Steps of PASP Plus Modules on Day 95036

Voltage	Module									
	1	2	3	4	5	6	8	11	14	15
-75V	0	0	0	0	0	0	0	0	0	0
-100V	0	0	0	0	0	0	0	0	0	0
-125V	0	0	0	0	0	0	0	0	0	0
-150V	0	0	0	0	0	0	0	0	0	0
-160V	0	0	0	0	0	0	0	0	0	0
-180V	0	0	0	0	0	0	0	0	0	0
-200V	0	0	0	0	0	0	0	0	0	0
-220V	0	0	0	0	0	0	0	0	0	0
-240V	0	0	0	0	0	0	0	0	0	0
-260V	0	0	0	0	0	0	0	0	0	0
-280V	0	0	0	0	0	0	0	0	0	0
-290V	173	145	0	0	0	0	0	0	0	0
-300V	0	0	0	0	0	0	0	0	0	0
-310V	173	144	0	0	0	0	0	0	0	0
-320V	0	0	0	0	0	0	0	0	0	0
-330V	170	140	0	0	0	0	0	0	0	0
-340V	0	0	0	0	0	0	0	0	0	0
-350V	169	141	0	0	0	0	0	0	0	0
-360V	0	0	0	0	0	0	0	0	0	0
-370V	0	0	0	0	0	0	0	0	0	0
-380V	0	0	0	0	0	0	0	0	0	0
-390V	0	0	0	0	0	0	0	0	0	0
-400V	0	0	0	0	0	0	0	0	0	0
-410V	0	0	0	0	0	0	0	0	0	0
-420V	0	0	0	0	0	0	0	0	0	0
-430V	0	0	0	0	0	0	0	0	0	0
-440V	0	0	0	0	0	0	0	0	0	0
-450V	0	0	0	0	0	0	0	0	0	0

Table 49: Bias Steps of PASP Plus Modules on Day 95037

Voltage	Module									
	1	2	3	4	5	6	8	11	14	15
-75V	0	0	0	0	0	0	0	0	0	0
-100V	0	0	0	0	0	0	0	0	0	0
-125V	0	0	0	0	0	0	0	0	0	0
-150V	0	0	0	0	0	0	0	0	0	0
-160V	0	0	0	0	0	0	0	0	0	0
-180V	0	0	0	0	0	0	0	0	0	0
-200V	0	0	0	0	0	0	0	0	0	0
-220V	0	0	0	0	0	0	0	0	0	0
-240V	0	0	0	0	0	0	0	0	0	0
-260V	0	0	0	0	0	0	0	0	0	0
-280V	0	0	0	0	0	0	0	0	0	0
-290V	0	0	0	0	0	0	0	0	0	0
-300V	0	0	0	0	0	0	0	0	0	0
-310V	0	0	0	0	0	0	0	0	0	0
-320V	0	0	0	0	0	0	0	0	0	0
-330V	0	0	42	0	0	0	56	57	0	61
-340V	0	0	0	0	0	0	0	0	0	0
-350V	0	0	42	0	0	0	56	57	0	60
-360V	0	0	0	0	0	0	0	0	0	0
-370V	0	0	41	0	0	0	57	57	0	60
-380V	0	0	0	0	0	0	0	0	0	0
-390V	0	0	41	0	0	0	56	56	0	59
-400V	0	0	0	0	0	0	0	0	0	0
-410V	0	0	0	0	0	0	0	0	0	0
-420V	0	0	0	0	0	0	0	0	0	0
-430V	0	0	0	0	0	0	0	0	0	0
-440V	0	0	0	0	0	0	0	0	0	0
-450V	0	0	0	0	0	0	0	0	0	0

Table 50: Bias Steps of PASP Plus Modules on Day 95038

Voltage	Module									
	1	2	3	4	5	6	8	11	14	15
-75V	0	0	0	0	0	0	0	0	0	0
-100V	0	0	0	0	0	0	0	0	0	0
-125V	0	0	0	0	0	0	0	0	0	0
-150V	0	0	0	0	0	0	0	0	0	0
-160V	0	0	0	0	0	0	0	0	0	0
-180V	0	0	0	0	0	0	0	0	0	0
-200V	0	0	0	0	0	0	0	0	0	0
-220V	0	0	0	0	0	0	0	0	0	0
-240V	0	0	0	0	0	0	0	0	0	0
-260V	0	0	0	0	0	0	0	0	0	0
-280V	0	0	0	0	0	0	0	0	0	0
-290V	0	0	0	0	0	0	0	0	0	0
-300V	0	0	0	0	0	0	0	0	0	0
-310V	0	0	0	0	0	0	0	0	0	0
-320V	0	0	0	0	0	0	0	0	0	0
-330V	26	49	129	57	0	57	85	92	0	86
-340V	0	0	0	0	0	0	0	0	0	0
-350V	26	48	129	57	0	57	85	93	0	89
-360V	0	0	0	0	0	0	0	0	0	0
-370V	24	47	127	57	0	57	83	92	1	90
-380V	0	0	0	0	0	0	0	0	0	0
-390V	24	47	127	56	0	56	85	93	0	86
-400V	0	0	0	0	0	0	0	0	0	0
-410V	0	0	0	0	0	0	0	0	0	0
-420V	0	0	0	0	0	0	0	0	0	0
-430V	0	0	0	0	0	0	0	0	0	0
-440V	0	0	0	0	0	0	0	0	0	0
-450V	0	0	0	0	0	0	0	0	0	0

Table 51: Bias Steps of PASP Plus Modules on Day 95039

Voltage	Module									
	1	2	3	4	5	6	8	11	14	15
-75V	0	0	0	0	0	0	0	0	0	0
-100V	0	0	0	0	0	0	0	0	0	0
-125V	0	0	0	0	0	0	0	0	0	0
-150V	0	0	0	0	0	0	0	0	0	0
-160V	0	0	0	0	0	0	0	0	0	0
-180V	0	0	0	0	0	0	0	0	0	0
-200V	0	0	0	0	0	0	0	0	0	0
-220V	0	0	0	0	0	0	0	0	0	0
-240V	0	0	0	0	0	0	0	0	0	0
-260V	0	0	0	0	0	0	0	0	0	0
-280V	0	0	0	0	0	0	0	0	0	0
-290V	0	0	0	0	0	0	0	0	0	0
-300V	0	0	0	0	0	0	0	0	0	0
-310V	0	0	0	0	0	0	0	0	0	0
-320V	0	0	0	0	0	0	0	0	0	0
-330V	144	98	0	98	0	98	0	0	0	0
-340V	0	0	0	0	0	0	0	0	0	0
-350V	143	97	0	96	0	97	0	0	0	0
-360V	0	0	0	0	0	0	0	0	0	0
-370V	143	96	0	95	0	96	0	0	0	0
-380V	0	0	0	0	0	0	0	57	61	98
-390V	142	95	0	94	0	95	0	0	0	0
-400V	0	0	0	0	0	0	0	57	61	97
-410V	0	0	0	0	0	0	0	0	0	0
-420V	0	0	0	0	0	0	0	57	61	96
-430V	0	0	0	0	0	0	0	0	0	0
-440V	0	0	0	0	0	0	0	56	59	95
-450V	0	0	0	0	0	0	0	0	0	0

Table 52: Bias Steps of PASP Plus Modules on Day 95040

Voltage	Module									
	1	2	3	4	5	6	8	11	14	15
-75V	0	0	0	0	0	0	0	0	0	0
-100V	0	0	0	0	0	0	0	0	0	0
-125V	0	0	0	0	0	0	0	0	0	0
-150V	0	0	0	0	0	0	0	0	0	0
-160V	0	0	0	0	0	0	0	0	0	0
-180V	0	0	0	0	0	0	0	0	0	0
-200V	0	0	0	0	0	0	0	0	0	0
-220V	0	0	0	0	0	0	0	0	0	0
-240V	0	0	0	0	0	0	0	0	0	0
-260V	0	0	0	0	0	0	0	0	0	0
-280V	0	0	0	0	0	0	0	0	0	0
-290V	0	0	0	0	0	0	0	0	0	0
-300V	0	0	0	0	0	0	0	0	0	0
-310V	0	0	0	0	0	0	0	0	0	0
-320V	0	0	0	0	0	0	0	0	0	0
-330V	0	0	0	0	0	0	0	0	0	0
-340V	0	0	0	0	0	0	0	0	0	0
-350V	0	0	0	0	0	0	0	0	0	0
-360V	0	0	0	0	0	0	0	0	0	0
-370V	0	0	0	0	0	0	0	0	0	0
-380V	0	0	0	57	0	87	103	153	143	97
-390V	0	0	0	0	0	0	0	0	0	0
-400V	0	0	0	57	0	85	103	153	144	97
-410V	0	0	0	0	0	0	0	0	0	0
-420V	0	0	0	57	0	85	101	153	144	97
-430V	0	0	0	0	0	0	0	0	0	0
-440V	0	0	0	56	0	84	101	150	141	95
-450V	0	0	0	0	0	0	0	0	0	0

Table 53: Bias Steps of PASP Plus Modules on Day 95041

Voltage	Module									
	1	2	3	4	5	6	8	11	14	15
-75V	0	0	0	0	0	0	0	0	0	0
-100V	0	0	0	0	0	0	0	0	0	0
-125V	0	0	0	0	0	0	0	0	0	0
-150V	0	0	0	0	0	0	0	0	0	0
-160V	0	0	0	0	0	0	0	0	0	0
-180V	0	0	0	0	0	0	0	0	0	0
-200V	0	0	0	0	0	0	0	0	0	0
-220V	0	0	0	0	0	0	0	0	0	0
-240V	0	0	0	0	0	0	0	0	0	0
-260V	0	0	0	0	0	0	0	0	0	0
-280V	61	98	0	0	0	0	0	0	0	0
-290V	0	0	0	0	0	0	0	0	0	0
-300V	61	97	0	0	0	0	0	0	0	0
-310V	0	0	0	0	0	0	0	0	0	0
-320V	61	97	0	0	0	0	0	0	0	0
-330V	0	0	0	0	0	0	0	0	0	0
-340V	60	95	0	0	0	0	0	0	0	0
-350V	0	0	0	0	0	0	0	0	0	0
-360V	0	0	0	0	0	0	0	0	0	0
-370V	0	0	0	0	0	0	0	0	0	0
-380V	0	0	114	154	0	123	97	0	0	0
-390V	0	0	0	0	0	0	0	0	0	0
-400V	0	0	114	154	0	122	97	0	0	0
-410V	0	0	0	0	0	0	0	0	0	0
-420V	0	0	113	153	0	123	97	0	0	0
-430V	0	0	0	0	0	0	0	0	0	0
-440V	0	0	111	150	0	121	95	0	0	0
-450V	0	0	0	0	0	0	0	0	0	0

Table 54: Bias Steps of PASP Plus Modules on Day 95042

Voltage	Module									
	1	2	3	4	5	6	8	11	14	15
-75V	0	0	0	0	0	0	0	0	0	0
-100V	0	0	0	0	0	0	0	0	0	0
-125V	0	0	0	0	0	0	0	0	0	0
-150V	0	0	0	0	0	0	0	0	0	0
-160V	0	0	0	0	0	0	0	0	0	0
-180V	0	0	0	0	0	0	0	0	0	0
-200V	0	0	0	0	0	0	0	0	0	0
-220V	0	0	0	0	0	0	0	0	0	0
-240V	0	0	0	0	0	0	0	0	0	0
-260V	0	0	0	0	0	0	0	0	0	0
-280V	144	98	0	0	0	0	0	0	0	0
-290V	0	0	0	0	0	0	0	0	0	0
-300V	142	97	0	0	0	0	0	0	0	0
-310V	0	0	0	0	0	0	0	0	0	0
-320V	142	97	0	0	0	0	0	0	0	0
-330V	0	0	0	0	0	0	0	0	0	0
-340V	140	95	0	0	0	0	0	0	0	0
-350V	0	0	0	0	0	0	0	0	0	0
-360V	0	0	0	0	0	0	0	0	0	0
-370V	0	0	0	0	0	0	0	0	0	0
-380V	0	0	98	0	0	0	0	0	0	0
-390V	0	0	0	0	0	0	0	0	0	0
-400V	0	0	97	0	0	0	0	0	0	0
-410V	0	0	0	0	0	0	0	0	0	0
-420V	0	0	97	0	0	0	0	0	0	0
-430V	0	0	0	0	0	0	0	0	0	0
-440V	0	0	95	0	0	0	0	0	0	0
-450V	0	0	0	0	0	0	0	0	0	0

Table 55: Bias Steps of PASP Plus Modules on Day 95062

Voltage	Module									
	1	2	3	4	5	6	8	11	14	15
-75V	0	0	0	0	0	0	0	0	0	0
-100V	0	0	0	0	0	0	0	0	0	0
-125V	0	0	0	0	0	0	0	0	0	0
-150V	0	0	0	0	0	0	0	0	0	0
-160V	0	0	0	0	0	0	0	0	0	0
-180V	0	0	0	0	0	0	0	0	0	0
-200V	0	0	0	0	0	0	0	0	0	0
-220V	0	0	0	0	0	0	0	0	0	0
-240V	27	0	0	27	0	17	0	0	0	0
-260V	27	0	0	27	0	17	0	0	0	0
-280V	27	0	0	27	0	17	0	0	0	0
-290V	0	0	0	0	0	0	0	0	0	0
-300V	26	0	0	27	0	17	0	0	0	0
-310V	0	0	0	0	0	0	0	0	0	0
-320V	0	0	0	0	0	0	0	0	0	0
-330V	0	0	0	0	0	0	0	0	0	0
-340V	0	0	0	0	0	0	0	0	0	0
-350V	0	0	0	0	0	0	0	0	0	0
-360V	0	0	0	0	0	0	0	0	0	0
-370V	0	0	0	0	0	0	0	0	0	0
-380V	0	0	0	0	0	0	0	0	0	0
-390V	0	0	0	0	0	0	0	0	0	0
-400V	0	0	0	0	0	0	0	0	0	0
-410V	0	0	0	0	0	0	0	0	0	0
-420V	0	0	0	0	0	0	0	0	0	0
-430V	0	0	0	0	0	0	0	0	0	0
-440V	0	0	0	0	0	0	0	0	0	0
-450V	0	0	0	0	0	0	0	0	0	0

Table 56: Bias Steps of PASP Plus Modules on Day 95063

Voltage	Module									
	1	2	3	4	5	6	8	11	14	15
-75V	0	0	0	0	0	0	0	0	0	0
-100V	0	0	0	0	0	0	0	0	0	0
-125V	0	0	0	0	0	0	0	0	0	0
-150V	0	0	0	0	0	0	0	0	0	0
-160V	0	0	0	0	0	0	0	0	0	0
-180V	0	0	0	0	0	0	0	0	0	0
-200V	0	0	0	0	0	0	0	0	0	0
-220V	0	0	0	0	0	0	0	0	0	0
-240V	54	54	54	53	80	51	0	0	0	0
-260V	54	54	53	53	79	51	0	0	0	0
-280V	53	54	53	53	79	52	0	0	0	0
-290V	0	0	0	0	0	0	0	0	0	0
-300V	53	54	53	53	78	51	0	0	0	0
-310V	0	0	0	0	0	0	0	0	0	0
-320V	0	0	0	0	0	0	0	0	0	0
-330V	0	0	0	0	0	0	0	0	0	0
-340V	0	0	0	0	0	0	0	0	0	0
-350V	0	0	0	0	0	0	0	0	0	0
-360V	0	0	0	0	0	0	0	0	0	0
-370V	0	0	0	0	0	0	0	0	0	0
-380V	0	0	0	0	0	0	0	0	0	0
-390V	0	0	0	0	0	0	0	0	0	0
-400V	0	0	0	0	0	0	0	0	0	0
-410V	0	0	0	0	0	0	0	0	0	0
-420V	0	0	0	0	0	0	0	0	0	0
-430V	0	0	0	0	0	0	0	0	0	0
-440V	0	0	0	0	0	0	0	0	0	0
-450V	0	0	0	0	0	0	0	0	0	0

Table 57: Bias Steps of PASP Plus Modules on Day 95064

Voltage	Module									
	1	2	3	4	5	6	8	11	14	15
-75V	0	0	0	0	0	0	0	0	0	0
-100V	0	0	0	0	0	0	0	0	0	0
-125V	0	0	0	0	0	0	0	0	0	0
-150V	0	0	0	0	0	0	0	0	0	0
-160V	0	0	0	0	0	0	0	0	0	0
-180V	0	0	0	0	0	0	0	0	0	0
-200V	0	0	0	0	0	0	0	0	0	0
-220V	0	0	0	0	0	0	0	0	0	0
-240V	0	0	108	0	157	0	0	0	0	0
-260V	0	0	107	0	158	0	0	0	0	0
-280V	0	0	107	0	157	0	0	0	0	0
-290V	0	0	0	0	0	0	0	0	0	0
-300V	0	0	106	0	156	0	0	0	0	0
-310V	0	0	0	0	0	0	0	0	0	0
-320V	0	0	79	0	0	0	0	0	0	0
-330V	0	0	0	0	0	0	0	0	0	0
-340V	0	0	79	0	0	0	0	0	0	0
-350V	0	0	0	0	0	0	0	0	0	0
-360V	0	0	80	0	0	0	0	0	0	0
-370V	0	0	0	0	0	0	0	0	0	0
-380V	0	0	76	0	0	0	0	0	0	0
-390V	0	0	0	0	0	0	0	0	0	0
-400V	0	0	0	0	0	0	0	0	0	0
-410V	0	0	0	0	0	0	0	0	0	0
-420V	0	0	0	0	0	0	0	0	0	0
-430V	0	0	0	0	0	0	0	0	0	0
-440V	0	0	0	0	0	0	0	0	0	0
-450V	0	0	0	0	0	0	0	0	0	0

Table 58: Bias Steps of PASP Plus Modules on Day 95065

Voltage	Module									
	1	2	3	4	5	6	8	11	14	15
-75V	0	0	0	0	0	0	0	0	0	0
-100V	0	0	0	0	0	0	0	0	0	0
-125V	0	0	0	0	0	0	0	0	0	0
-150V	0	0	0	0	0	0	0	0	0	0
-160V	0	0	0	0	0	0	0	0	0	0
-180V	0	0	0	0	0	0	0	0	0	0
-200V	0	0	0	0	0	0	0	0	0	0
-220V	0	0	0	0	0	0	0	0	0	0
-240V	0	0	0	0	99	0	0	0	0	0
-260V	0	0	0	0	100	0	0	0	0	0
-280V	0	0	0	0	100	0	0	0	0	0
-290V	0	0	0	0	0	0	0	0	0	0
-300V	0	0	0	0	99	0	0	0	0	0
-310V	0	0	0	0	0	0	0	0	0	0
-320V	0	0	81	0	0	0	0	0	0	0
-330V	0	0	0	0	0	0	0	0	0	0
-340V	0	0	80	0	0	0	0	0	0	0
-350V	0	0	0	0	0	0	0	0	0	0
-360V	0	0	81	0	0	0	0	0	0	0
-370V	0	0	0	27	0	27	53	53	0	0
-380V	0	0	80	0	0	0	0	0	0	0
-390V	0	0	0	27	0	27	54	53	0	0
-400V	0	0	0	0	0	0	0	0	0	0
-410V	0	0	0	27	0	27	53	54	0	0
-420V	0	0	0	0	0	0	0	0	0	0
-430V	0	0	0	27	0	27	52	54	0	0
-440V	0	0	0	0	0	0	0	0	0	0
-450V	0	0	0	0	0	0	0	0	0	0

Table 59: Bias Steps of PASP Plus Modules on Day 95066

Voltage	Module									
	1	2	3	4	5	6	8	11	14	15
-75V	0	0	0	0	0	0	0	0	0	0
-100V	0	0	0	0	0	0	0	0	0	0
-125V	0	0	0	0	0	0	0	0	0	0
-150V	0	0	0	0	0	0	0	0	0	0
-160V	0	0	0	0	0	0	0	0	0	0
-180V	0	0	0	0	0	0	0	0	0	0
-200V	0	0	0	0	0	0	0	0	0	0
-220V	0	0	0	0	0	0	0	0	0	0
-240V	0	0	0	0	0	0	0	0	0	0
-260V	0	0	0	0	0	0	0	0	0	0
-280V	0	0	0	0	0	0	0	0	0	0
-290V	0	0	0	0	0	0	0	0	0	0
-300V	0	0	0	0	0	0	0	0	0	0
-310V	0	0	0	0	0	0	0	0	0	0
-320V	0	0	0	0	0	0	0	0	0	0
-330V	0	0	0	0	0	0	0	0	0	0
-340V	0	0	0	0	0	0	0	0	0	0
-350V	0	0	0	0	0	0	0	0	0	0
-360V	0	0	0	0	0	0	0	0	0	0
-370V	27	54	54	54	0	54	27	27	54	0
-380V	0	0	0	0	0	0	0	0	0	0
-390V	27	54	54	54	0	54	27	27	53	0
-400V	0	0	0	0	0	0	0	0	0	0
-410V	27	54	54	54	0	54	27	27	54	0
-420V	0	0	0	0	0	0	0	0	0	0
-430V	27	53	53	53	0	53	26	27	54	0
-440V	0	0	0	0	0	0	0	0	0	0
-450V	0	0	0	0	0	0	0	0	0	0

Table 60: Bias Steps of PASP Plus Modules on Day 95067

Voltage	Module									
	1	2	3	4	5	6	8	11	14	15
-75V	0	0	0	0	0	0	0	0	0	0
-100V	0	0	0	0	0	0	0	0	0	0
-125V	0	0	0	0	0	0	0	0	0	0
-150V	0	0	0	0	0	0	0	0	0	0
-160V	0	0	0	0	0	0	0	0	0	0
-180V	0	0	0	0	0	0	0	0	0	0
-200V	0	0	0	0	0	0	0	0	0	0
-220V	0	0	0	0	0	0	0	0	0	0
-240V	0	0	0	0	0	0	0	0	0	0
-260V	0	0	0	0	0	0	0	0	0	0
-280V	0	0	0	0	0	0	0	0	0	0
-290V	0	0	0	0	0	0	0	0	0	0
-300V	0	0	0	0	0	0	0	0	0	0
-310V	0	0	0	0	0	0	0	0	0	0
-320V	0	0	0	0	0	0	0	0	0	0
-330V	0	0	0	0	0	0	0	0	0	0
-340V	0	0	0	0	0	0	0	0	0	0
-350V	0	0	0	0	0	0	0	0	0	0
-360V	0	0	0	0	0	0	0	0	0	0
-370V	54	40	26	29	0	54	54	54	27	0
-380V	0	0	0	0	0	0	0	0	0	0
-390V	54	41	27	28	0	54	54	54	27	0
-400V	0	0	0	0	0	0	0	0	0	0
-410V	54	41	27	28	0	54	54	54	27	0
-420V	0	0	0	0	0	0	0	0	0	0
-430V	54	40	26	28	0	53	53	54	27	0
-440V	0	0	0	0	0	0	0	0	0	0
-450V	0	0	0	0	0	0	0	0	0	0

Table 61: Bias Steps of PASP Plus Modules on Day 95068

Voltage	Module									
	1	2	3	4	5	6	8	11	14	15
-75V	0	0	0	0	0	0	0	0	0	0
-100V	0	0	0	0	0	0	0	0	0	0
-125V	0	0	0	0	0	0	0	0	0	0
-150V	0	0	0	0	0	0	0	0	0	0
-160V	0	0	0	0	0	0	0	0	0	0
-180V	0	0	0	0	0	0	0	0	0	0
-200V	0	0	0	0	0	0	0	0	0	0
-220V	0	0	0	0	0	0	0	0	0	0
-240V	0	0	0	0	0	0	0	0	0	0
-260V	0	0	0	0	0	0	0	0	0	0
-280V	0	0	0	0	0	0	0	0	0	0
-290V	0	0	0	0	0	0	0	0	0	0
-300V	0	0	0	0	0	0	0	0	0	0
-310V	0	0	0	0	0	0	0	0	0	0
-320V	0	0	0	0	0	0	0	0	0	0
-330V	0	0	0	0	0	0	0	0	0	0
-340V	0	0	0	0	0	0	0	0	0	0
-350V	0	0	0	0	0	0	0	0	0	0
-360V	0	0	0	0	0	0	0	0	0	0
-370V	54	54	54	54	0	27	27	27	0	54
-380V	0	0	0	0	0	0	0	0	0	0
-390V	54	54	54	54	0	27	27	27	0	54
-400V	0	0	0	0	0	0	0	0	0	0
-410V	54	54	54	54	0	27	27	27	0	54
-420V	0	0	0	0	0	0	0	0	0	0
-430V	53	54	54	53	0	26	27	27	0	54
-440V	0	0	0	0	0	0	0	0	0	0
-450V	0	0	0	0	0	0	0	0	0	0

Table 62: Bias Steps of PASP Plus Modules on Day 95069

Voltage	Module									
	1	2	3	4	5	6	8	11	14	15
-75V	0	0	0	0	0	0	0	0	0	0
-100V	0	0	0	0	0	0	0	0	0	0
-125V	0	0	0	0	0	0	0	0	0	0
-150V	0	0	0	0	0	0	0	0	0	0
-160V	0	0	0	0	0	0	0	0	0	0
-180V	0	0	0	0	0	0	0	0	0	0
-200V	0	0	0	0	0	0	0	0	0	0
-220V	0	0	0	0	0	0	0	0	0	0
-240V	0	0	0	0	0	0	0	0	0	0
-260V	0	0	0	0	0	0	0	0	0	0
-280V	0	0	0	0	0	0	0	0	0	0
-290V	0	0	0	0	0	0	0	0	0	0
-300V	0	0	0	0	0	0	0	0	0	0
-310V	0	0	0	0	0	0	0	0	0	0
-320V	0	0	0	0	0	0	0	0	0	0
-330V	0	0	0	0	0	0	0	0	0	0
-340V	0	0	0	0	0	0	0	0	0	0
-350V	0	0	0	0	0	0	0	0	0	0
-360V	0	0	0	0	0	0	0	0	0	0
-370V	36	27	27	0	0	0	0	0	0	54
-380V	0	0	0	0	0	0	0	0	0	0
-390V	36	27	27	0	0	0	0	0	0	27
-400V	0	0	0	0	0	0	61	0	81	0
-410V	36	27	27	0	0	0	60	0	81	108
-420V	0	0	0	0	0	0	60	0	81	81
-430V	35	27	27	0	0	0	58	0	80	107
-440V	0	0	0	0	0	0	0	0	0	0
-450V	0	0	0	0	0	0	0	0	0	0

Table 63: Bias Steps of PASP Plus Modules on Day 95070

Voltage	Module									
	1	2	3	4	5	6	8	11	14	15
-75V	0	0	0	0	0	0	0	0	0	0
-100V	0	0	0	0	0	0	0	0	0	0
-125V	0	0	0	0	0	0	0	0	0	0
-150V	0	0	0	0	0	0	0	0	0	0
-160V	0	0	0	0	0	0	0	0	0	0
-180V	0	0	0	0	0	0	0	0	0	0
-200V	0	0	0	0	0	0	0	0	0	0
-220V	0	0	0	0	0	0	0	0	0	0
-240V	0	0	0	0	0	0	0	0	0	0
-260V	0	0	0	0	0	0	0	0	0	0
-280V	0	0	0	0	0	0	0	0	0	0
-290V	0	0	0	0	0	0	0	0	0	0
-300V	0	0	0	0	0	0	0	0	0	0
-310V	0	0	0	0	0	0	0	0	0	0
-320V	0	0	0	0	0	0	0	0	0	0
-330V	0	0	0	0	0	0	0	0	0	0
-340V	0	0	0	0	0	0	0	0	0	0
-350V	0	0	0	0	0	0	0	0	0	0
-360V	0	0	0	0	0	0	0	0	0	0
-370V	0	0	0	0	0	0	0	0	0	0
-380V	0	0	0	0	0	0	0	0	0	0
-390V	0	0	0	0	0	0	0	0	0	0
-400V	0	0	0	81	0	80	54	81	27	0
-410V	0	0	0	81	0	81	54	81	27	27
-420V	0	0	0	81	0	81	54	81	27	27
-430V	0	0	0	80	0	80	52	81	27	27
-440V	0	0	0	0	0	0	0	0	0	0
-450V	0	0	0	0	0	0	0	0	0	0

Table 64: Bias Steps of PASP Plus Modules on Day 95071

Voltage	Module									
	1	2	3	4	5	6	8	11	14	15
-75V	0	0	0	0	0	0	0	0	0	0
-100V	0	0	0	0	0	0	0	0	0	0
-125V	0	0	0	0	0	0	0	0	0	0
-150V	0	0	0	0	0	0	0	0	0	0
-160V	0	0	0	0	0	0	0	0	0	0
-180V	0	0	0	0	0	0	0	0	0	0
-200V	0	0	0	0	0	0	0	0	0	0
-220V	0	0	0	0	0	0	0	0	0	0
-240V	0	0	0	0	0	0	0	0	0	0
-260V	0	0	0	0	0	0	0	0	0	0
-280V	0	0	0	0	0	0	0	0	0	0
-290V	0	0	0	0	0	0	0	0	0	0
-300V	0	0	0	0	0	0	0	0	0	0
-310V	0	0	0	0	0	0	0	0	0	0
-320V	0	0	0	0	0	0	0	0	0	0
-330V	0	0	0	0	0	0	0	0	0	0
-340V	0	0	0	0	0	0	0	0	0	0
-350V	0	0	0	0	0	0	0	0	0	0
-360V	0	0	0	0	0	0	0	0	0	0
-370V	0	0	0	0	0	0	0	0	0	0
-380V	0	0	0	0	0	0	0	0	0	0
-390V	0	0	0	0	0	0	0	0	0	0
-400V	81	81	92	31	0	27	0	27	0	0
-410V	81	81	92	32	0	27	0	27	0	0
-420V	81	81	92	32	0	27	0	27	0	0
-430V	79	80	92	30	0	26	0	26	0	0
-440V	0	0	0	0	0	0	0	0	0	0
-450V	0	0	0	0	0	0	0	0	0	0

Table 65: Bias Steps of PASP Plus Modules on Day 95072

Voltage	Module									
	1	2	3	4	5	6	8	11	14	15
-75V	0	0	0	0	0	0	0	0	0	0
-100V	0	0	0	0	0	0	0	0	0	0
-125V	0	0	0	0	0	0	0	0	0	0
-150V	0	0	0	0	0	0	0	0	0	0
-160V	0	0	0	0	0	0	0	0	0	0
-180V	0	0	0	0	0	0	0	0	0	0
-200V	0	0	0	0	0	0	0	0	0	0
-220V	0	0	0	0	0	0	0	0	0	0
-240V	81	81	108	0	0	0	0	0	0	0
-260V	81	81	108	0	0	0	0	0	0	0
-280V	81	81	108	0	0	0	0	0	0	0
-290V	0	0	0	0	0	0	0	0	0	0
-300V	80	79	108	0	0	0	0	0	0	0
-310V	0	0	0	0	0	0	0	0	0	0
-320V	0	0	0	0	0	0	0	0	0	0
-330V	0	0	0	0	0	0	0	0	0	0
-340V	0	0	0	0	0	0	0	0	0	0
-350V	0	0	0	0	0	0	0	0	0	0
-360V	0	0	0	0	0	0	0	0	0	0
-370V	0	0	0	0	0	0	0	0	0	0
-380V	0	0	0	0	0	0	0	0	0	0
-390V	0	0	0	0	0	0	0	0	0	0
-400V	27	27	27	0	0	0	0	0	0	0
-410V	27	27	27	0	0	0	0	0	0	0
-420V	27	27	27	0	0	0	0	0	0	0
-430V	27	27	27	0	0	0	0	0	0	0
-440V	0	0	0	0	0	0	0	0	0	0
-450V	0	0	0	0	0	0	0	0	0	0

Table 66: Bias Steps of PASP Plus Modules on Day 95073

Voltage	Module									
	1	2	3	4	5	6	8	11	14	15
-75V	0	0	0	0	0	0	0	0	0	0
-100V	0	0	0	0	0	0	0	0	0	0
-125V	0	0	0	0	0	0	0	0	0	0
-150V	0	0	0	0	0	0	0	0	0	0
-160V	0	0	0	0	0	0	0	0	0	0
-180V	0	0	0	0	0	0	0	0	0	0
-200V	0	0	0	0	0	0	0	0	0	0
-220V	0	0	0	0	0	0	0	0	0	0
-240V	27	27	0	81	96	107	0	0	0	0
-260V	27	27	0	81	96	107	0	0	0	0
-280V	27	27	0	81	95	106	0	0	0	0
-290V	0	0	0	0	0	0	0	0	0	0
-300V	26	27	0	81	93	106	0	0	0	0
-310V	0	0	0	0	0	0	0	0	0	0
-320V	0	0	0	0	0	0	0	0	0	0
-330V	0	0	0	0	0	0	0	0	0	0
-340V	0	0	0	0	0	0	0	0	0	0
-350V	0	0	0	0	0	0	0	0	0	0
-360V	0	0	0	0	0	0	0	0	0	0
-370V	0	0	0	0	0	0	0	0	0	0
-380V	0	0	0	0	0	0	0	0	0	0
-390V	0	0	0	0	0	0	0	0	0	0
-400V	0	0	0	0	0	0	0	0	0	0
-410V	0	0	0	0	0	0	0	0	0	0
-420V	0	0	0	0	0	0	0	0	0	0
-430V	0	0	0	0	0	0	0	0	0	0
-440V	0	0	0	0	0	0	0	0	0	0
-450V	0	0	0	0	0	0	0	0	0	0

Table 67: Bias Steps of PASP Plus Modules on Day 95074

Voltage	Module									
	1	2	3	4	5	6	8	11	14	15
-75V	0	0	0	0	0	0	0	0	0	0
-100V	0	0	0	0	0	0	0	0	0	0
-125V	0	0	0	0	0	0	0	0	0	0
-150V	0	0	0	0	0	0	0	0	0	0
-160V	0	0	0	0	0	0	0	0	0	0
-180V	0	0	0	0	0	0	0	0	0	0
-200V	0	0	0	0	0	0	0	0	0	0
-220V	0	0	0	0	0	0	0	0	0	0
-240V	0	0	0	27	26	0	54	81	81	81
-260V	0	0	0	27	26	0	54	81	81	81
-280V	0	0	0	27	26	0	54	81	81	81
-290V	0	0	0	0	0	0	0	0	0	0
-300V	0	0	0	27	26	0	52	81	81	80
-310V	0	0	0	0	0	0	0	0	0	0
-320V	0	0	0	0	0	0	0	0	0	0
-330V	0	0	0	0	0	0	0	0	0	0
-340V	0	0	0	0	0	0	0	0	0	0
-350V	0	0	0	0	0	0	0	0	0	0
-360V	0	0	0	0	0	0	0	0	0	0
-370V	0	0	0	0	0	0	0	0	0	0
-380V	0	0	0	0	0	0	0	0	0	0
-390V	0	0	0	0	0	0	0	0	0	0
-400V	0	0	0	0	0	0	0	0	0	0
-410V	0	0	0	0	0	0	0	0	0	0
-420V	0	0	0	0	0	0	0	0	0	0
-430V	0	0	0	0	0	0	0	0	0	0
-440V	0	0	0	0	0	0	0	0	0	0
-450V	0	0	0	0	0	0	0	0	0	0

Table 68: Bias Steps of PASP Plus Modules on Day 95075

Voltage	Module									
	1	2	3	4	5	6	8	11	14	15
-75V	0	0	0	0	0	0	0	0	0	0
-100V	0	0	0	0	0	0	0	0	0	0
-125V	0	0	0	0	0	0	0	0	0	0
-150V	0	0	0	0	0	0	0	0	0	0
-160V	0	0	0	0	0	0	0	0	0	0
-180V	0	0	0	0	0	0	0	0	0	0
-200V	0	0	0	0	0	0	0	0	0	0
-220V	0	0	0	0	0	0	0	0	0	0
-240V	0	0	0	0	0	0	27	0	0	0
-260V	0	0	0	0	0	0	27	0	0	0
-280V	0	0	0	0	0	0	27	0	0	0
-290V	0	0	0	0	0	0	0	0	0	0
-300V	0	0	0	0	0	0	26	0	0	0
-310V	0	0	0	0	0	0	0	0	0	0
-320V	102	108	108	0	0	0	0	0	0	0
-330V	0	0	0	0	0	0	0	0	0	0
-340V	102	108	108	0	0	0	0	0	0	0
-350V	0	0	0	0	0	0	0	0	0	0
-360V	102	108	108	0	0	0	0	0	0	0
-370V	0	0	0	0	0	0	0	0	0	0
-380V	100	107	106	0	0	0	0	0	0	0
-390V	0	0	0	0	0	0	0	0	0	0
-400V	0	0	0	0	0	0	0	0	0	0
-410V	0	0	0	0	0	0	0	0	0	0
-420V	0	0	0	0	0	0	0	0	0	0
-430V	0	0	0	0	0	0	0	0	0	0
-440V	0	0	0	0	0	0	0	0	0	0
-450V	0	0	0	0	0	0	0	0	0	0

Table 69: Bias Steps of PASP Plus Modules on Day 95076

Voltage	Module									
	1	2	3	4	5	6	8	11	14	15
-75V	0	0	0	0	0	0	0	0	0	0
-100V	0	0	0	0	0	0	0	0	0	0
-125V	0	0	0	0	0	0	0	0	0	0
-150V	0	0	0	0	0	0	0	0	0	0
-160V	0	0	0	0	0	0	0	0	0	0
-180V	0	0	0	0	0	0	0	0	0	0
-200V	0	0	0	0	0	0	0	0	0	0
-220V	0	0	0	0	0	0	0	0	0	0
-240V	0	0	0	0	108	0	0	0	0	0
-260V	0	0	0	0	108	0	0	0	0	0
-280V	0	0	0	0	108	0	0	0	0	0
-290V	0	0	0	0	0	0	0	0	0	0
-300V	0	0	0	0	108	0	0	0	0	0
-310V	0	0	0	0	0	0	0	0	0	0
-320V	21	0	0	108	0	108	0	0	0	0
-330V	0	0	0	0	0	0	0	0	0	0
-340V	21	0	0	107	0	108	0	0	0	0
-350V	0	0	0	0	0	0	0	0	0	0
-360V	21	0	0	108	0	108	0	0	0	0
-370V	0	0	0	0	0	0	0	0	0	0
-380V	22	0	0	107	0	106	0	0	0	0
-390V	0	0	0	0	0	0	0	0	0	0
-400V	0	0	0	0	0	0	0	0	0	0
-410V	0	0	0	0	0	0	0	0	0	0
-420V	0	0	0	0	0	0	0	0	0	0
-430V	0	0	0	0	0	0	0	0	0	0
-440V	0	0	0	0	0	0	0	0	0	0
-450V	0	0	0	0	0	0	0	0	0	0

Table 70: Bias Steps of PASP Plus Modules on Day 95077

Voltage	Module									
	1	2	3	4	5	6	8	11	14	15
-75V	0	0	0	0	0	0	0	0	0	0
-100V	0	0	0	0	0	0	0	0	0	0
-125V	0	0	0	0	0	0	0	0	0	0
-150V	0	0	0	0	0	0	0	0	0	0
-160V	0	0	0	0	0	0	0	0	0	0
-180V	0	0	0	0	0	0	0	0	0	0
-200V	0	0	0	0	0	0	0	0	0	0
-220V	0	0	0	0	0	0	0	0	0	0
-240V	0	0	30	0	0	0	0	0	0	0
-260V	0	0	30	0	0	0	0	0	0	0
-280V	0	0	29	0	0	0	0	0	0	0
-290V	0	0	0	0	0	0	0	0	0	0
-300V	0	0	29	0	0	0	0	0	0	0
-310V	0	0	0	0	0	0	0	0	0	0
-320V	0	0	0	0	0	0	81	81	81	81
-330V	0	0	0	0	0	0	0	0	0	0
-340V	0	0	0	0	0	0	81	81	81	81
-350V	0	0	0	0	0	0	0	0	0	0
-360V	0	0	0	0	0	0	81	81	81	81
-370V	0	0	0	0	0	0	0	0	0	0
-380V	0	0	0	0	0	0	81	80	79	80
-390V	0	0	0	0	0	0	0	0	0	0
-400V	0	0	0	0	0	0	0	0	0	0
-410V	0	0	0	0	0	0	0	0	0	0
-420V	0	0	0	0	0	0	0	0	0	0
-430V	0	0	0	0	0	0	0	0	0	0
-440V	0	0	0	0	0	0	0	0	0	0
-450V	0	0	0	0	0	0	0	0	0	0

Table 71: Bias Steps of PASP Plus Modules on Day 95078

Voltage	Module									
	1	2	3	4	5	6	8	11	14	15
-75V	0	0	0	0	0	0	0	0	0	0
-100V	0	0	0	0	0	0	0	0	0	0
-125V	0	0	0	0	0	0	0	0	0	0
-150V	0	0	0	0	0	0	0	0	0	0
-160V	0	0	0	0	27	0	0	0	0	0
-180V	0	0	0	0	26	0	0	0	0	0
-200V	0	0	0	0	26	0	0	0	0	0
-220V	0	0	0	0	26	0	0	0	0	0
-240V	112	117	99	0	3	0	0	0	0	0
-260V	112	117	99	0	3	0	0	0	0	0
-280V	112	116	99	0	3	0	0	0	0	0
-290V	0	0	0	0	0	0	0	0	0	0
-300V	110	115	98	0	3	0	0	0	0	0
-310V	0	0	0	0	0	0	0	0	0	0
-320V	0	0	0	0	0	0	0	0	0	0
-330V	0	0	0	0	0	0	0	0	0	0
-340V	0	0	0	0	0	0	0	0	0	0
-350V	0	0	0	0	0	0	0	0	0	0
-360V	0	0	0	0	0	0	0	0	0	0
-370V	0	0	0	0	0	0	0	0	0	0
-380V	0	0	0	0	0	0	0	0	0	0
-390V	0	0	0	0	0	0	0	0	0	0
-400V	0	0	0	0	0	0	0	0	0	0
-410V	0	0	0	0	0	0	0	0	0	0
-420V	0	0	0	0	0	0	0	0	0	0
-430V	0	0	0	0	0	0	0	0	0	0
-440V	0	0	0	0	0	0	0	0	0	0
-450V	0	0	0	0	0	0	0	0	0	0

Table 72: Bias Steps of PASP Plus Modules on Day 95079

Voltage	Module									
	1	2	3	4	5	6	8	11	14	15
-75V	0	0	0	0	0	0	0	0	0	0
-100V	0	0	0	0	0	0	0	0	0	0
-125V	0	0	0	0	0	0	0	0	0	0
-150V	0	0	0	0	0	0	0	0	0	0
-160V	0	0	0	0	134	0	0	0	0	0
-180V	0	0	0	0	131	0	0	0	0	0
-200V	0	0	0	0	129	0	0	0	0	0
-220V	0	0	0	0	129	0	0	0	0	0
-240V	0	0	0	0	189	25	0	0	0	0
-260V	0	0	0	0	187	25	0	0	0	0
-280V	0	0	0	0	185	25	0	0	0	0
-290V	0	0	0	0	0	0	0	0	0	0
-300V	0	0	0	0	183	25	0	0	0	0
-310V	0	0	0	0	0	0	0	0	0	0
-320V	0	0	0	0	0	0	0	0	0	0
-330V	0	0	0	0	0	0	0	0	0	0
-340V	0	0	0	0	0	0	0	0	0	0
-350V	0	0	0	0	0	0	0	0	0	0
-360V	0	0	0	0	0	0	0	0	0	0
-370V	0	0	0	0	0	0	0	0	0	0
-380V	0	0	0	0	0	0	0	0	0	0
-390V	0	0	0	0	0	0	0	0	0	0
-400V	0	0	0	0	0	0	0	0	0	0
-410V	0	0	0	0	0	0	0	0	0	0
-420V	0	0	0	0	0	0	0	0	0	0
-430V	0	0	0	0	0	0	0	0	0	0
-440V	0	0	0	0	0	0	0	0	0	0
-450V	0	0	0	0	0	0	0	0	0	0

Table 73: Bias Steps of PASP Plus Modules on Day 95080

Voltage	Module									
	1	2	3	4	5	6	8	11	14	15
-75V	0	0	0	0	0	0	0	0	0	0
-100V	0	0	0	0	0	0	0	0	0	0
-125V	0	0	0	0	0	0	0	0	0	0
-150V	0	0	0	0	0	0	0	0	0	0
-160V	0	0	0	0	0	0	0	0	0	0
-180V	0	0	0	0	0	0	0	0	0	0
-200V	0	0	0	0	0	0	0	0	0	0
-220V	0	0	0	0	0	0	0	0	0	0
-240V	0	0	0	110	90	73	0	9	30	27
-260V	0	0	0	110	89	72	0	8	30	27
-280V	0	0	0	109	90	73	0	8	30	26
-290V	0	0	0	0	0	0	0	0	0	0
-300V	0	0	0	108	89	70	0	8	29	26
-310V	0	0	0	0	0	0	0	0	0	0
-320V	0	0	0	0	0	0	0	0	0	0
-330V	0	0	0	0	0	0	0	0	0	0
-340V	0	0	0	0	0	0	0	0	0	0
-350V	0	0	0	0	0	0	0	0	0	0
-360V	0	0	0	0	0	0	0	0	0	0
-370V	0	0	0	0	0	0	0	0	0	0
-380V	0	0	0	0	0	0	0	0	0	0
-390V	0	0	0	0	0	0	0	0	0	0
-400V	0	0	0	0	0	0	0	0	0	0
-410V	0	0	0	0	0	0	0	0	0	0
-420V	0	0	0	0	0	0	0	0	0	0
-430V	0	0	0	0	0	0	0	0	0	0
-440V	0	0	0	0	0	0	0	0	0	0
-450V	0	0	0	0	0	0	0	0	0	0

Table 74: Bias Steps of PASP Plus Modules on Day 95081

Voltage	Module									
	1	2	3	4	5	6	8	11	14	15
-75V	0	0	0	0	0	0	0	0	0	0
-100V	0	0	0	0	0	0	0	0	0	0
-125V	0	0	0	0	0	0	0	0	0	0
-150V	0	0	0	0	0	0	0	0	0	0
-160V	0	0	0	0	0	0	0	0	0	0
-180V	0	0	0	0	0	0	0	0	0	0
-200V	0	0	0	0	0	0	0	0	0	0
-220V	0	0	0	0	0	0	0	0	0	0
-240V	0	0	0	0	0	0	79	81	53	53
-260V	0	0	0	0	0	0	79	80	53	53
-280V	0	0	0	0	0	0	78	79	53	53
-290V	0	0	0	0	0	0	0	0	0	0
-300V	0	0	0	0	0	0	76	78	52	52
-310V	0	0	0	0	0	0	0	0	0	0
-320V	30	26	29	0	0	0	0	0	0	0
-330V	0	0	0	0	0	0	0	0	0	0
-340V	30	25	29	0	0	0	0	0	0	0
-350V	0	0	0	0	0	0	0	0	0	0
-360V	30	25	29	0	0	0	0	0	0	0
-370V	0	0	0	0	0	0	0	0	0	0
-380V	29	25	28	0	0	0	0	0	0	0
-390V	0	0	0	0	0	0	0	0	0	0
-400V	0	0	0	0	0	0	0	0	0	0
-410V	0	0	0	0	0	0	0	0	0	0
-420V	0	0	0	0	0	0	0	0	0	0
-430V	0	0	0	0	0	0	0	0	0	0
-440V	0	0	0	0	0	0	0	0	0	0
-450V	0	0	0	0	0	0	0	0	0	0

Table 75: Bias Steps of PASP Plus Modules on Day 95082

Voltage	Module									
	1	2	3	4	5	6	8	11	14	15
-75V	0	0	0	0	0	0	0	0	0	0
-100V	0	0	0	0	0	0	0	0	0	0
-125V	0	0	0	0	0	0	0	0	0	0
-150V	0	0	0	0	0	0	0	0	0	0
-160V	0	0	0	0	0	0	0	0	0	0
-180V	0	0	0	0	0	0	0	0	0	0
-200V	0	0	0	0	0	0	0	0	0	0
-220V	0	0	0	0	0	0	0	0	0	0
-240V	0	0	0	0	30	0	0	0	0	0
-260V	0	0	0	0	30	0	0	0	0	0
-280V	0	0	0	0	30	0	0	0	0	0
-290V	0	0	0	0	0	0	0	0	0	0
-300V	0	0	0	0	29	0	0	0	0	0
-310V	0	0	0	0	0	0	0	0	0	0
-320V	85	72	75	28	0	41	0	0	0	0
-330V	0	0	0	0	0	0	0	0	0	0
-340V	85	72	74	28	0	41	0	0	0	0
-350V	0	0	0	0	0	0	0	0	0	0
-360V	85	71	74	27	0	40	0	0	0	0
-370V	0	0	0	0	0	0	0	0	0	0
-380V	83	68	71	27	0	40	0	0	0	0
-390V	0	0	0	0	0	0	0	0	0	0
-400V	0	0	0	0	0	0	0	0	0	0
-410V	0	0	0	0	0	0	0	0	0	0
-420V	0	0	0	0	0	0	0	0	0	0
-430V	0	0	0	0	0	0	0	0	0	0
-440V	0	0	0	0	0	0	0	0	0	0
-450V	0	0	0	0	0	0	0	0	0	0

Table 76: Bias Steps of PASP Plus Modules on Day 95083

Voltage	Module									
	1	2	3	4	5	6	8	11	14	15
-75V	0	0	0	0	0	0	0	0	0	0
-100V	0	0	0	0	0	0	0	0	0	0
-125V	0	0	0	0	0	0	0	0	0	0
-150V	0	0	0	0	0	0	0	0	0	0
-160V	0	0	0	0	0	0	0	0	0	0
-180V	0	0	0	0	0	0	0	0	0	0
-200V	0	0	0	0	0	0	0	0	0	0
-220V	0	0	0	0	0	0	0	0	0	0
-240V	0	0	0	0	80	0	0	0	0	0
-260V	0	0	0	0	80	0	0	0	0	0
-280V	0	0	0	0	78	0	0	0	0	0
-290V	0	0	0	0	0	0	0	0	0	0
-300V	0	0	0	0	78	0	0	0	0	0
-310V	0	0	0	0	0	0	0	0	0	0
-320V	0	0	0	75	0	83	30	26	26	26
-330V	0	0	0	0	0	0	0	0	0	0
-340V	0	0	0	72	0	82	30	25	27	26
-350V	0	0	0	0	0	0	0	0	0	0
-360V	0	0	0	71	0	81	30	25	27	25
-370V	0	0	0	0	0	0	0	0	0	0
-380V	0	0	0	70	0	81	30	25	27	25
-390V	0	0	0	0	0	0	0	0	0	0
-400V	0	0	0	0	0	0	0	0	0	0
-410V	0	0	0	0	0	0	0	0	0	0
-420V	0	0	0	0	0	0	0	0	0	0
-430V	0	0	0	0	0	0	0	0	0	0
-440V	0	0	0	0	0	0	0	0	0	0
-450V	0	0	0	0	0	0	0	0	0	0

Table 77: Bias Steps of PASP Plus Modules on Day 95084

Voltage	Module									
	1	2	3	4	5	6	8	11	14	15
-75V	0	0	0	0	0	0	0	0	0	0
-100V	0	0	0	0	0	0	0	0	0	0
-125V	0	0	0	0	0	0	0	0	0	0
-150V	0	0	0	0	0	0	0	0	0	0
-160V	0	0	0	0	72	0	0	0	0	0
-180V	0	0	0	0	72	0	0	0	0	0
-200V	0	0	0	0	72	0	0	0	0	0
-220V	0	0	0	0	71	0	0	0	0	0
-240V	0	0	0	0	57	0	0	0	0	0
-260V	0	0	0	0	57	0	0	0	0	0
-280V	0	0	0	0	57	0	0	0	0	0
-290V	0	0	0	0	0	0	0	0	0	0
-300V	0	0	0	0	55	0	0	0	0	0
-310V	0	0	0	0	0	0	0	0	0	0
-320V	0	0	0	0	0	0	50	53	53	53
-330V	0	0	0	0	0	0	0	0	0	0
-340V	0	0	0	0	0	0	51	52	52	53
-350V	0	0	0	0	0	0	0	0	0	0
-360V	0	0	0	0	0	0	49	51	51	51
-370V	0	0	0	0	0	0	0	0	0	0
-380V	0	0	0	0	0	0	49	51	51	50
-390V	0	0	0	0	0	0	0	0	0	0
-400V	0	0	0	0	0	0	0	0	0	0
-410V	0	0	0	0	0	0	0	0	0	0
-420V	0	0	0	0	0	0	0	0	0	0
-430V	0	0	0	0	0	0	0	0	0	0
-440V	0	0	0	0	0	0	0	0	0	0
-450V	0	0	0	0	0	0	0	0	0	0

Table 78: Bias Steps of PASP Plus Modules on Day 95085

Voltage	Module									
	1	2	3	4	5	6	8	11	14	15
-75V	0	0	0	0	0	0	0	0	0	0
-100V	0	0	0	0	0	0	0	0	0	0
-125V	0	0	0	0	0	0	0	0	0	0
-150V	0	0	0	0	0	0	0	0	0	0
-160V	0	0	0	0	103	0	0	0	0	0
-180V	0	0	0	0	100	0	0	0	0	0
-200V	0	0	0	0	99	0	0	0	0	0
-220V	0	0	0	0	98	0	0	0	0	0
-240V	17	16	36	0	81	0	0	0	0	0
-260V	17	16	36	0	78	0	0	0	0	0
-280V	17	16	35	0	77	0	0	0	0	0
-290V	0	0	0	0	0	0	0	0	0	0
-300V	16	15	34	0	77	0	0	0	0	0
-310V	0	0	0	0	0	0	0	0	0	0
-320V	0	0	0	0	0	0	0	0	0	0
-330V	0	0	0	0	0	0	0	0	0	0
-340V	0	0	0	0	0	0	0	0	0	0
-350V	0	0	0	0	0	0	0	0	0	0
-360V	0	0	0	0	0	0	0	0	0	0
-370V	0	0	0	0	0	0	0	0	0	0
-380V	0	0	0	0	0	0	0	0	0	0
-390V	0	0	0	0	0	0	0	0	0	0
-400V	0	0	0	0	0	0	0	0	0	0
-410V	0	0	0	0	0	0	0	0	0	0
-420V	0	0	0	0	0	0	0	0	0	0
-430V	0	0	0	0	0	0	0	0	0	0
-440V	0	0	0	0	0	0	0	0	0	0
-450V	0	0	0	0	0	0	0	0	0	0

Table 79: Bias Steps of PASP Plus Modules on Day 95089

Voltage	Module									
	1	2	3	4	5	6	8	11	14	15
-75V	0	0	0	0	0	0	0	0	0	0
-100V	0	0	0	0	0	0	0	0	0	0
-125V	0	0	0	0	0	0	0	0	0	0
-150V	0	0	0	0	0	0	0	0	0	0
-160V	0	0	0	0	0	0	0	0	0	0
-180V	0	0	0	0	0	0	0	0	0	0
-200V	0	0	0	0	0	0	0	0	0	0
-220V	0	0	0	0	0	0	0	0	0	0
-240V	30	30	58	0	28	0	0	0	0	0
-260V	30	29	58	0	28	0	0	0	0	0
-280V	30	28	57	0	27	0	0	0	0	0
-290V	0	0	0	0	0	0	0	0	0	0
-300V	30	28	57	0	27	0	0	0	0	0
-310V	0	0	0	0	0	0	0	0	0	0
-320V	0	0	0	0	0	0	0	0	0	0
-330V	0	0	0	0	0	0	0	0	0	0
-340V	0	0	0	0	0	0	0	0	0	0
-350V	0	0	0	0	0	0	0	0	0	0
-360V	0	0	0	0	0	0	0	0	0	0
-370V	0	0	0	0	0	0	0	0	0	0
-380V	0	0	0	0	0	0	0	0	0	0
-390V	0	0	0	0	0	0	0	0	0	0
-400V	0	0	0	0	0	0	0	0	0	0
-410V	0	0	0	0	0	0	0	0	0	0
-420V	0	0	0	0	0	0	0	0	0	0
-430V	0	0	0	0	0	0	0	0	0	0
-440V	0	0	0	0	0	0	0	0	0	0
-450V	0	0	0	0	0	0	0	0	0	0

Table 80: Bias Steps of PASP Plus Modules on Day 95090

Voltage	Module									
	1	2	3	4	5	6	8	11	14	15
-75V	0	0	0	0	0	0	0	0	0	0
-100V	0	0	0	0	0	0	0	0	0	0
-125V	0	0	0	0	0	0	0	0	0	0
-150V	0	0	0	0	0	0	0	0	0	0
-160V	0	0	0	0	0	0	0	0	0	0
-180V	0	0	0	0	0	0	0	0	0	0
-200V	0	0	0	0	0	0	0	0	0	0
-220V	0	0	0	0	0	0	0	0	0	0
-240V	22	33	22	0	4	0	0	0	0	0
-260V	22	32	22	0	4	0	0	0	0	0
-280V	20	30	20	0	4	0	0	0	0	0
-290V	0	0	0	0	0	0	0	0	0	0
-300V	20	29	20	0	4	0	0	0	0	0
-310V	0	0	0	0	0	0	0	0	0	0
-320V	0	0	0	0	0	0	0	0	0	0
-330V	0	0	0	0	0	0	0	0	0	0
-340V	0	0	0	0	0	0	0	0	0	0
-350V	0	0	0	0	0	0	0	0	0	0
-360V	0	0	0	0	0	0	0	0	0	0
-370V	0	0	0	0	0	0	0	0	0	0
-380V	0	0	0	0	0	0	0	0	0	0
-390V	0	0	0	0	0	0	0	0	0	0
-400V	0	0	0	0	0	0	0	0	0	0
-410V	0	0	0	0	0	0	0	0	0	0
-420V	0	0	0	0	0	0	0	0	0	0
-430V	0	0	0	0	0	0	0	0	0	0
-440V	0	0	0	0	0	0	0	0	0	0
-450V	0	0	0	0	0	0	0	0	0	0

Table 81: Bias Steps of PASP Plus Modules on Day 95091

Voltage	Module									
	1	2	3	4	5	6	8	11	14	15
-75V	0	0	0	0	0	0	0	0	0	0
-100V	0	0	0	0	0	0	0	0	0	0
-125V	0	0	0	0	0	0	0	0	0	0
-150V	0	0	0	0	0	0	0	0	0	0
-160V	0	0	0	0	0	0	0	0	0	0
-180V	0	0	0	0	0	0	0	0	0	0
-200V	0	0	0	0	0	0	0	0	0	0
-220V	0	0	0	0	0	0	0	0	0	0
-240V	30	28	37	72	55	52	0	0	0	28
-260V	30	28	37	70	54	51	0	0	0	28
-280V	30	27	37	69	54	51	0	0	0	27
-290V	0	0	0	0	0	0	0	0	0	0
-300V	30	27	35	68	54	49	0	0	0	27
-310V	0	0	0	0	0	0	0	0	0	0
-320V	0	0	0	0	0	0	0	0	0	0
-330V	0	0	0	0	0	0	0	0	0	0
-340V	0	0	0	0	0	0	0	0	0	0
-350V	0	0	0	0	0	0	0	0	0	0
-360V	0	0	0	0	0	0	0	0	0	0
-370V	0	0	0	0	0	0	0	0	0	0
-380V	0	0	0	0	0	0	0	0	0	0
-390V	0	0	0	0	0	0	0	0	0	0
-400V	0	0	0	0	0	0	0	0	0	0
-410V	0	0	0	0	0	0	0	0	0	0
-420V	0	0	0	0	0	0	0	0	0	0
-430V	0	0	0	0	0	0	0	0	0	0
-440V	0	0	0	0	0	0	0	0	0	0
-450V	0	0	0	0	0	0	0	0	0	0

Table 82: Bias Steps of PASP Plus Modules on Day 95103

Voltage	Module									
	1	2	3	4	5	6	8	11	14	15
-75V	0	0	0	0	0	0	0	0	0	0
-100V	0	0	0	0	0	0	0	0	0	0
-125V	0	0	0	0	0	0	0	0	0	0
-150V	0	0	0	0	0	0	0	0	0	0
-160V	0	0	0	0	0	0	0	0	0	0
-180V	0	0	0	0	0	0	0	0	0	0
-200V	0	0	0	0	0	0	0	0	0	0
-220V	0	0	0	0	0	0	0	0	0	0
-240V	0	0	0	17	27	44	0	0	0	0
-260V	0	0	0	16	27	43	0	0	0	0
-280V	0	0	0	16	27	43	0	0	0	0
-290V	0	0	0	0	0	0	0	0	0	0
-300V	0	0	0	15	27	42	0	0	0	0
-310V	0	0	0	0	0	0	0	0	0	0
-320V	0	0	0	0	0	0	0	0	0	0
-330V	0	0	0	0	0	0	0	0	0	0
-340V	0	0	0	0	0	0	0	0	0	0
-350V	0	0	0	0	0	0	0	0	0	0
-360V	0	0	0	0	0	0	0	0	0	0
-370V	0	0	0	0	0	0	0	0	0	0
-380V	0	0	0	0	0	0	0	0	0	0
-390V	0	0	0	0	0	0	0	0	0	0
-400V	0	0	0	0	0	0	0	0	0	0
-410V	0	0	0	0	0	0	0	0	0	0
-420V	0	0	0	0	0	0	0	0	0	0
-430V	0	0	0	0	0	0	0	0	0	0
-440V	0	0	0	0	0	0	0	0	0	0
-450V	0	0	0	0	0	0	0	0	0	0

Table 83: Bias Steps of PASP Plus Modules on Day 95104

Voltage	Module									
	1	2	3	4	5	6	8	11	14	15
-75V	0	0	0	0	0	0	0	0	0	0
-100V	0	0	0	0	0	0	0	0	0	0
-125V	0	0	0	0	0	0	0	0	0	0
-150V	0	0	0	0	0	0	0	0	0	0
-160V	0	0	0	0	0	0	0	0	0	0
-180V	0	0	0	0	0	0	0	0	0	0
-200V	0	0	0	0	0	0	0	0	0	0
-220V	0	0	0	0	0	0	0	0	0	0
-240V	0	0	0	0	0	3	72	74	71	72
-260V	0	0	0	0	0	2	71	74	70	71
-280V	0	0	0	0	0	2	71	73	69	70
-290V	0	0	0	0	0	0	0	0	0	0
-300V	0	0	0	0	0	2	70	72	68	70
-310V	0	0	0	0	0	0	0	0	0	0
-320V	0	0	7	0	0	0	0	0	0	0
-330V	0	0	0	0	0	0	0	0	0	0
-340V	0	0	7	0	0	0	0	0	0	0
-350V	0	0	0	0	0	0	0	0	0	0
-360V	0	0	7	0	0	0	0	0	0	0
-370V	0	0	0	0	0	0	0	0	0	0
-380V	0	0	6	0	0	0	0	0	0	0
-390V	0	0	0	0	0	0	0	0	0	0
-400V	0	0	0	0	0	0	0	0	0	0
-410V	0	0	0	0	0	0	0	0	0	0
-420V	0	0	0	0	0	0	0	0	0	0
-430V	0	0	0	0	0	0	0	0	0	0
-440V	0	0	0	0	0	0	0	0	0	0
-450V	0	0	0	0	0	0	0	0	0	0

Table 84: Bias Steps of PASP Plus Modules on Day 95105

Voltage	Module									
	1	2	3	4	5	6	8	11	14	15
-75V	0	0	0	0	0	0	0	0	0	0
-100V	0	0	0	0	0	0	0	0	0	0
-125V	0	0	0	0	0	0	0	0	0	0
-150V	0	0	0	0	0	0	0	0	0	0
-160V	0	0	0	0	18	0	0	0	0	0
-180V	0	0	0	0	18	0	0	0	0	0
-200V	0	0	0	0	17	0	0	0	0	0
-220V	0	0	0	0	17	0	0	0	0	0
-240V	0	0	0	0	0	0	0	0	0	0
-260V	0	0	0	0	0	0	0	0	0	0
-280V	0	0	0	0	0	0	0	0	0	0
-290V	0	0	0	0	0	0	0	0	0	0
-300V	0	0	0	0	0	0	0	0	0	0
-310V	0	0	0	0	0	0	0	0	0	0
-320V	87	100	100	0	0	0	0	0	0	0
-330V	0	0	0	0	0	0	0	0	0	0
-340V	86	100	100	0	0	0	0	0	0	0
-350V	0	0	0	0	0	0	0	0	0	0
-360V	86	100	100	0	0	0	0	0	0	0
-370V	0	0	0	0	0	0	0	0	0	0
-380V	85	99	98	0	0	0	0	0	0	0
-390V	0	0	0	0	0	0	0	0	0	0
-400V	0	0	0	0	0	0	0	0	0	0
-410V	0	0	0	0	0	0	0	0	0	0
-420V	0	0	0	0	0	0	0	0	0	0
-430V	0	0	0	0	0	0	0	0	0	0
-440V	0	0	0	0	0	0	0	0	0	0
-450V	0	0	0	0	0	0	0	0	0	0

Table 85: Bias Steps of PASP Plus Modules on Day 95106

Voltage	Module									
	1	2	3	4	5	6	8	11	14	15
-75V	0	0	0	0	0	0	0	0	0	0
-100V	0	0	0	0	0	0	0	0	0	0
-125V	0	0	0	0	0	0	0	0	0	0
-150V	0	0	0	0	0	0	0	0	0	0
-160V	0	0	0	0	138	0	0	0	0	0
-180V	0	0	0	0	138	0	0	0	0	0
-200V	0	0	0	0	137	0	0	0	0	0
-220V	0	0	0	0	137	0	0	0	0	0
-240V	0	0	0	0	159	0	0	0	0	0
-260V	0	0	0	0	158	0	0	0	0	0
-280V	0	0	0	0	157	0	0	0	0	0
-290V	0	0	0	0	0	0	0	0	0	0
-300V	0	0	0	0	154	0	0	0	0	0
-310V	0	0	0	0	0	0	0	0	0	0
-320V	0	0	0	16	0	18	0	0	0	0
-330V	0	0	0	0	0	0	0	0	0	0
-340V	0	0	0	16	0	18	0	0	0	0
-350V	0	0	0	0	0	0	0	0	0	0
-360V	0	0	0	16	0	17	0	0	0	0
-370V	0	0	0	0	0	0	0	0	0	0
-380V	0	0	0	16	0	17	0	0	0	0
-390V	0	0	0	0	0	0	0	0	0	0
-400V	0	0	0	0	0	0	0	0	0	0
-410V	0	0	0	0	0	0	0	0	0	0
-420V	0	0	0	0	0	0	0	0	0	0
-430V	0	0	0	0	0	0	0	0	0	0
-440V	0	0	0	0	0	0	0	0	0	0
-450V	0	0	0	0	0	0	0	0	0	0

Table 86: Bias Steps of PASP Plus Modules on Day 95107

Voltage	Module									
	1	2	3	4	5	6	8	11	14	15
-75V	0	0	0	0	0	0	0	0	0	0
-100V	0	0	0	0	0	0	0	0	0	0
-125V	0	0	0	0	0	0	0	0	0	0
-150V	0	0	0	0	0	0	0	0	0	0
-160V	0	0	0	0	0	0	0	0	0	0
-180V	0	0	0	0	0	0	0	0	0	0
-200V	0	0	0	0	0	0	0	0	0	0
-220V	0	0	0	0	0	0	0	0	0	0
-240V	0	0	0	0	108	0	0	0	0	0
-260V	0	0	0	0	108	0	0	0	0	0
-280V	0	0	0	0	108	0	0	0	0	0
-290V	0	0	0	0	0	0	0	0	0	0
-300V	0	0	0	0	106	0	0	0	0	0
-310V	0	0	0	0	0	0	0	0	0	0
-320V	0	0	0	107	0	79	0	0	18	18
-330V	0	0	0	0	0	0	0	0	0	0
-340V	0	0	0	107	0	79	0	0	17	18
-350V	0	0	0	0	0	0	0	0	0	0
-360V	0	0	0	107	0	79	0	0	17	17
-370V	0	0	0	0	0	0	0	0	0	0
-380V	0	0	0	105	0	76	0	0	17	17
-390V	0	0	0	0	0	0	0	0	0	0
-400V	0	0	0	0	0	0	0	0	0	0
-410V	0	0	0	0	0	0	0	0	0	0
-420V	0	0	0	0	0	0	0	0	0	0
-430V	0	0	0	0	0	0	0	0	0	0
-440V	0	0	0	0	0	0	0	0	0	0
-450V	0	0	0	0	0	0	0	0	0	0

Table 87: Bias Steps of PASP Plus Modules on Day 95108

Voltage	Module									
	1	2	3	4	5	6	8	11	14	15
-75V	0	0	0	0	0	0	0	0	0	0
-100V	0	0	0	0	0	0	0	0	0	0
-125V	0	0	0	0	0	0	0	0	0	0
-150V	0	0	0	0	0	0	0	0	0	0
-160V	0	0	0	0	0	0	0	0	0	0
-180V	0	0	0	0	0	0	0	0	0	0
-200V	0	0	0	0	0	0	0	0	0	0
-220V	0	0	0	0	0	0	0	0	0	0
-240V	0	0	0	0	0	0	0	0	0	0
-260V	0	0	0	0	0	0	0	0	0	0
-280V	0	0	0	0	0	0	0	0	0	0
-290V	0	0	0	0	0	0	0	0	0	0
-300V	0	0	0	0	0	0	0	0	0	0
-310V	0	0	0	0	0	0	0	0	0	0
-320V	0	0	0	0	0	0	78	78	60	60
-330V	0	0	0	0	0	0	0	0	0	0
-340V	0	0	0	0	0	0	78	77	60	60
-350V	0	0	0	0	0	0	0	0	0	0
-360V	0	0	0	0	0	0	77	77	60	60
-370V	0	0	0	0	0	0	0	0	0	0
-380V	0	0	0	0	0	0	76	77	60	60
-390V	0	0	0	0	0	0	0	0	0	0
-400V	0	0	0	0	0	0	0	0	0	0
-410V	0	0	0	0	0	0	0	0	0	0
-420V	0	0	0	0	0	0	0	0	0	0
-430V	0	0	0	0	0	0	0	0	0	0
-440V	0	0	0	0	0	0	0	0	0	0
-450V	0	0	0	0	0	0	0	0	0	0

Appendix D

Environmental Parameter/Voltage Data Space

This appendix contains all of the negative biasing data for the PASP Plus experiment gathered while the arrays were in ram. The graphs show the data space for the cell temperature, ion flux, and bias voltage for each module. Each point on the graph represents a bias step and shows the values of the two parameters at the time of the biasing.

As can be seen, the PASP Plus experiment filled in most of the voltage/ion flux and voltage/cell temperature parameter spaces for all modules. At voltages between -75V and -150V, there is data mainly at only the high and low temperatures, corresponding to near steady state in sunlight and eclipse, since limited biasing was down at the low voltages, and was done in the early portion of the experiment when biasing was not done during transition between sunlight and eclipse. The APSA module 5 and the Space Station WTC module 3 has a more sparsely filled in voltage/cell temperature space than the other cells. Both of these arrays were mounted over cut-outs on the deployed panel, which resulted in very fast rise/drop times for the temperatures as the spacecraft went into and out of sunlight. Therefore, these cells spent less time at the intermediate temperatures, and thus had fewer data points in this regime.

The ion flux/cell temperature spaces are also fairly well filled in for most cells, again with the exceptions of the APSA module 5 and the Space Station WTC module 3. From Fig. 89c, the heating of the spacecraft with time is evident. Horizontal bands of data points are seen at the high temperatures, corresponding to the distinct sets of days when negative biasing was done (94234-94246, 94290-94308, and 95062-95108).
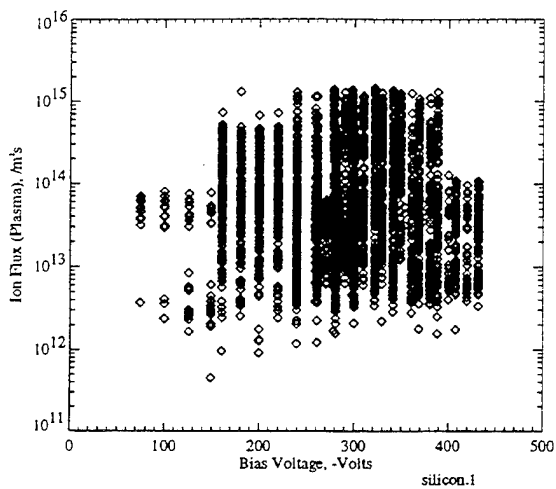
a: Voltage/Ion Flux Data Space for
Silicon Module 1
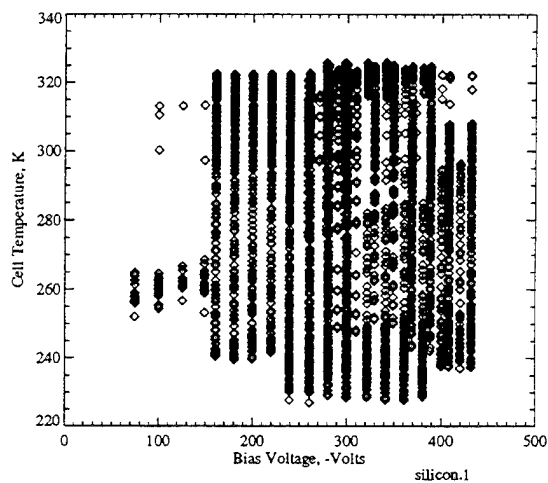
b: Voltage/Cell Temperature Data
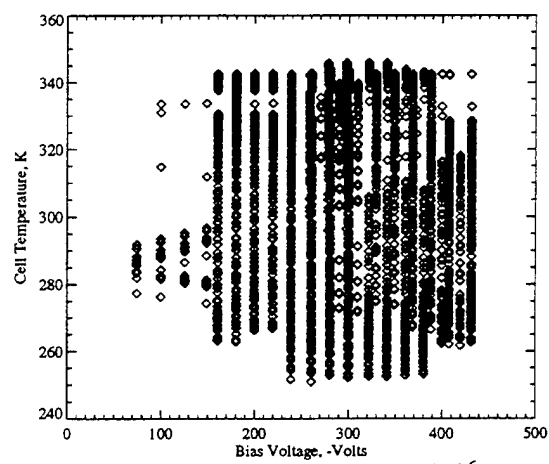Space for Silicon Module 1
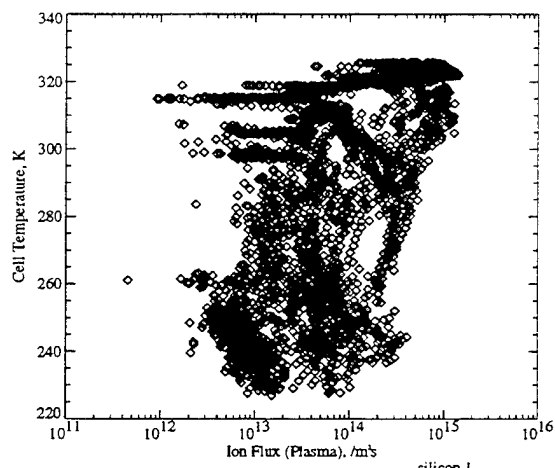
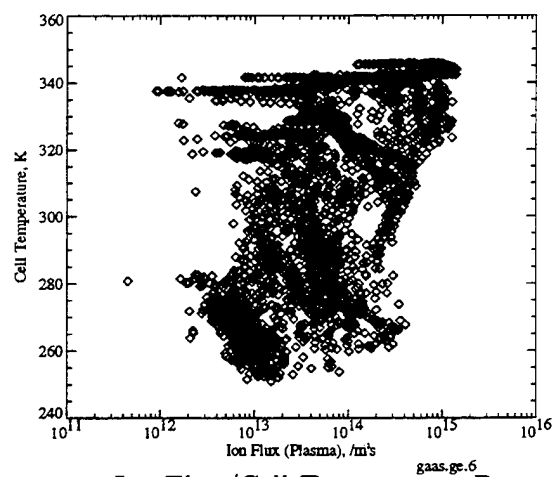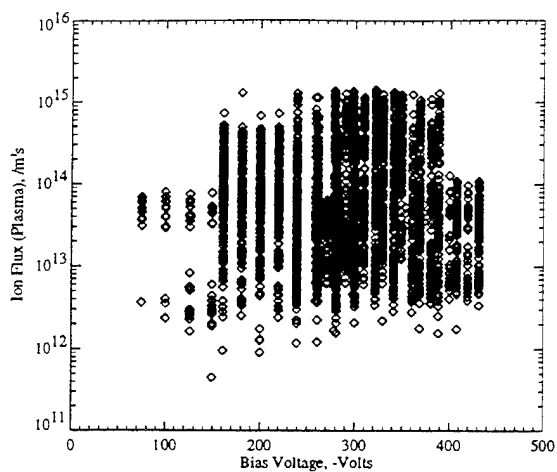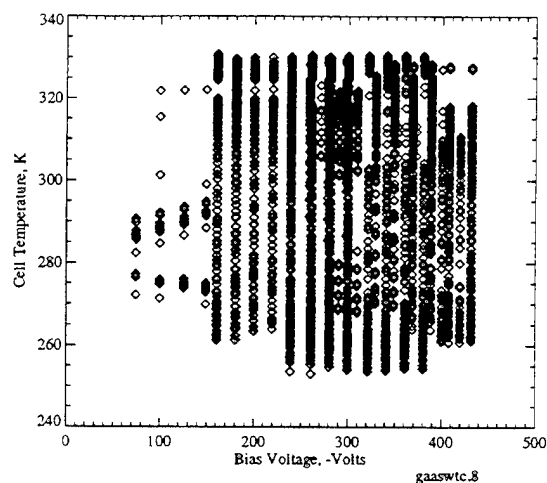c: Ion Flux/Cell Temperature Data
Space for Silicon Module 1

Figure 85: Environmental Parameter/Voltage Data Space for Silicon Module 1
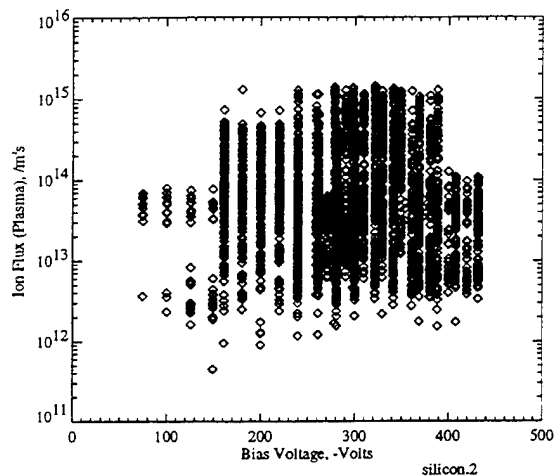
a: Voltage/Ion Flux Data Space for Silicon Module 2
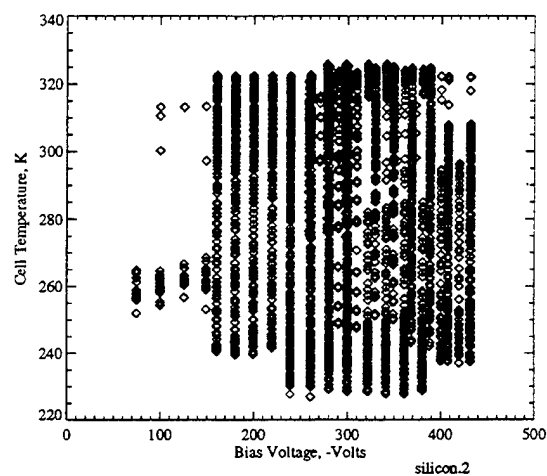
b: Voltage/Cell Temperature Data Space for Silicon Module 2
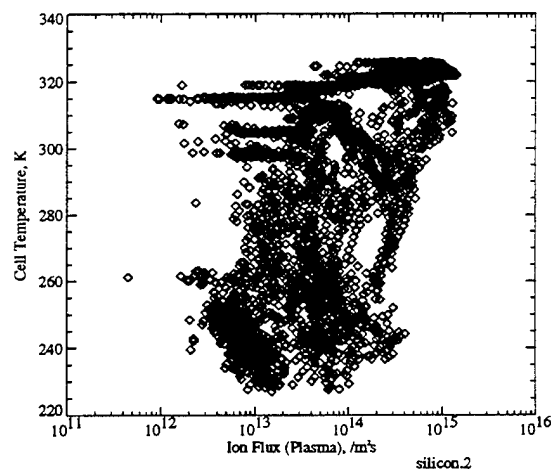
c: Ion Flux/Cell Temperature Data Space for Silicon Module 2

Figure 86: Environmental Parameter/Voltage Data Space for Silicon Module 2
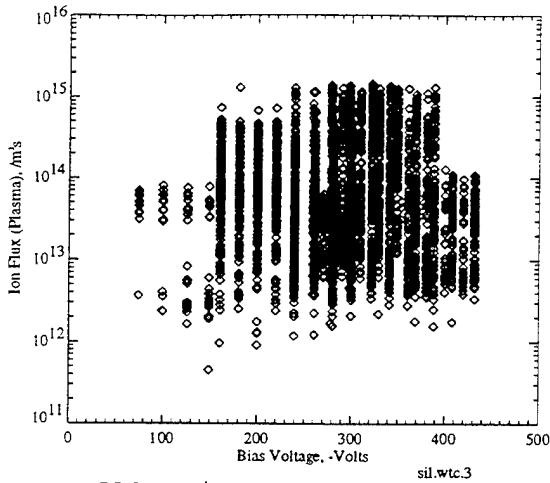
a: Voltage/Ion Flux Data Space for
Silicon Wrap-Through-Contact
Module 3
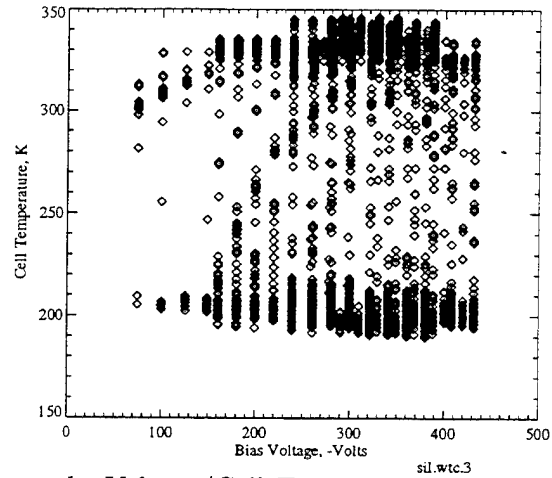
b: Voltage/Cell Temperature Data
Space for Silicon
Wrap-Through-Contact Module 3
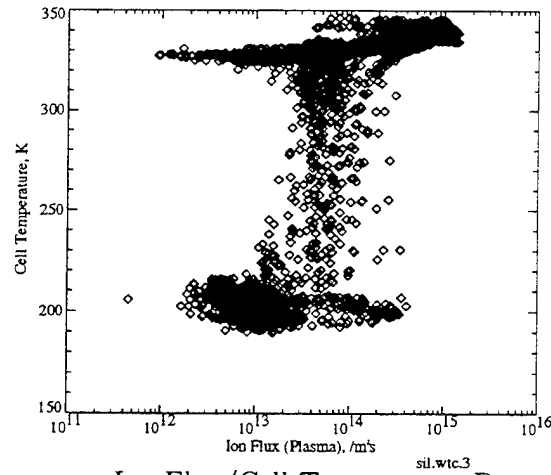
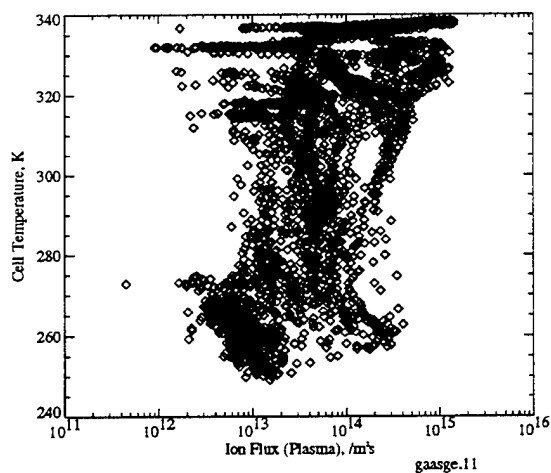c: Ion Flux/Cell Temperature Data
Space for Silicon
Wrap-Through-Contact Module 3

Figure 87: Environmental Parameter/Voltage Data Space for Silicon Wrap-Through-Contact Module 3
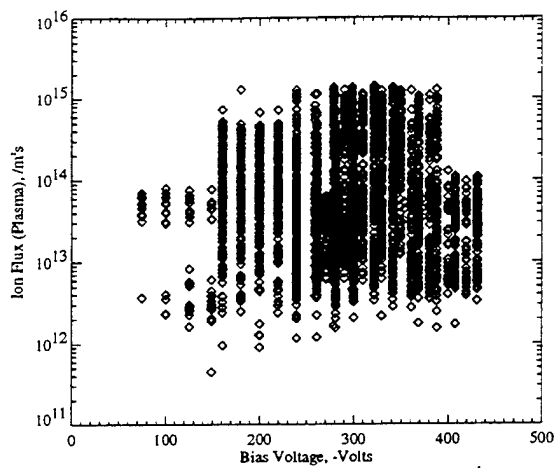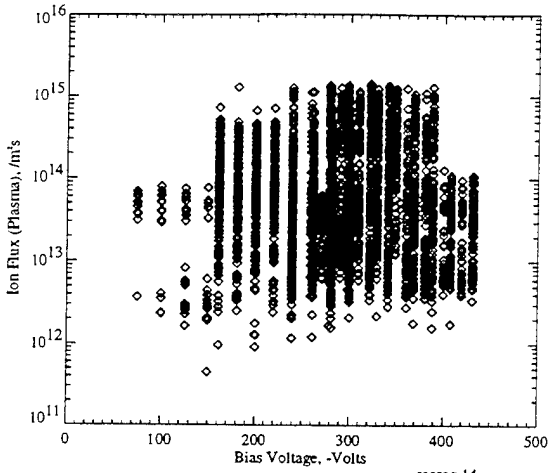
a: Voltage/Ion Flux Data Space for
Thin GaAs/Ge Module 4
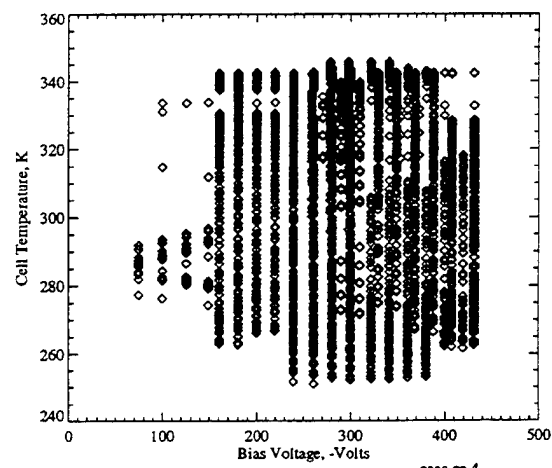
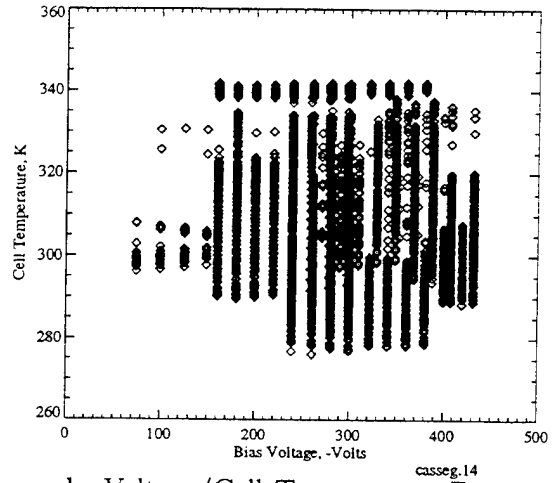b: Voltage/Cell Temperature Data
Space for Thin GaAs/Ge Module 4
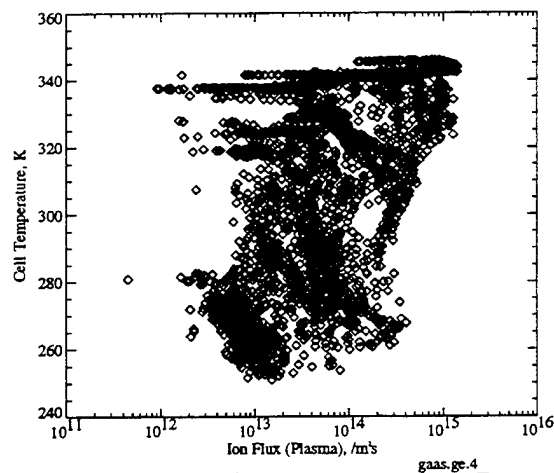
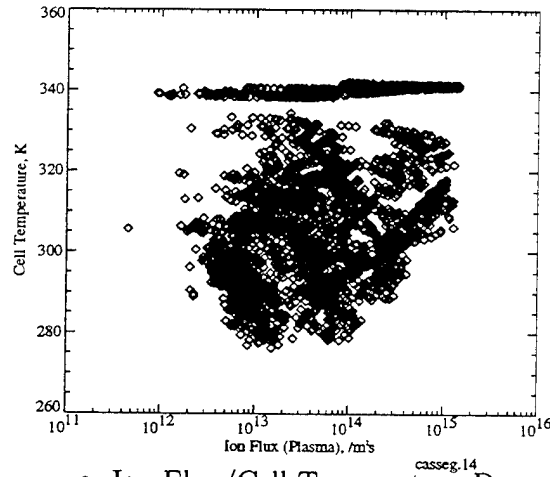c: Ion Flux/Cell Temperature Data
Space for Thin GaAs/Ge Module 4

Figure 88: Environmental Parameter/Voltage Data Space for Thin GaAs/Ge Module 4

251
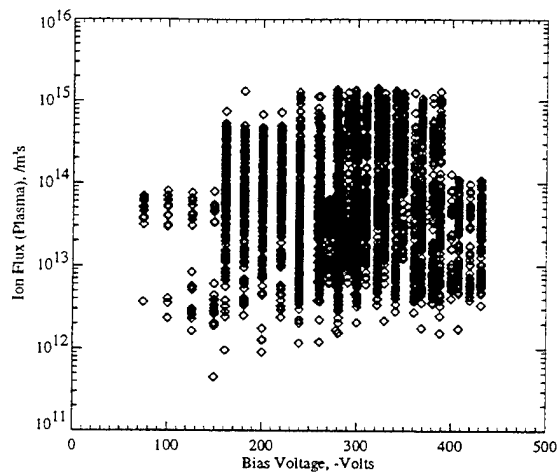
a: Voltage/Ion Flux Data Space for APSA Module 5
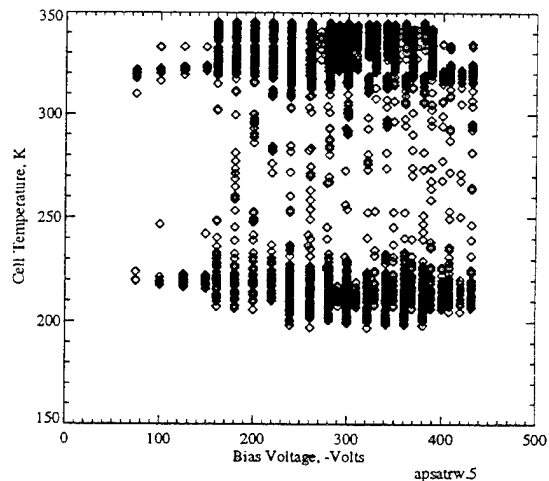
b: Voltage/Cell Temperature Data Space for APSA Module 5
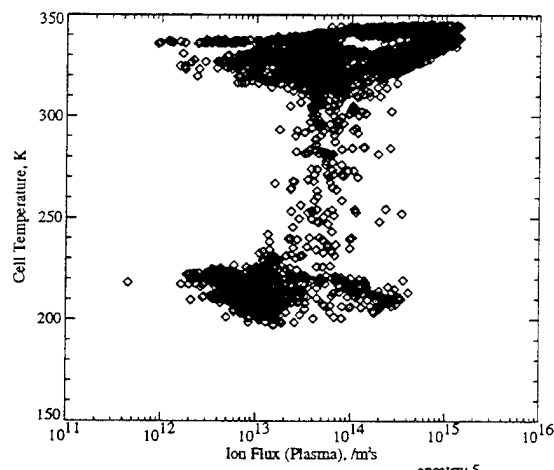
c: Ion Flux/Cell Temperature Data Space for APSA Module 5

Figure 89: Environmental Parameter/Voltage Data Space for APSA Module 5
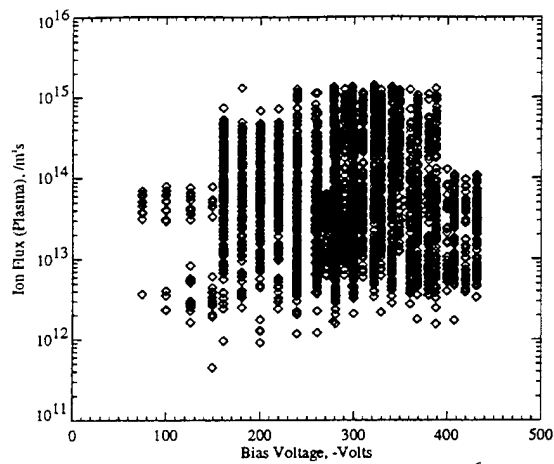
a: Voltage/Ion Flux Data Space for
Thin GaAs/Ge Module 6

b: Voltage/Cell Temperature Data
Space for Thin GaAs/Ge Module 6

c: Ion Flux/Cell Temperature Data
Space for Thin GaAs/Ge Module 6

Figure 90: Environmental Parameter/Voltage Data Space for Thin GaAs/Ge Module 6
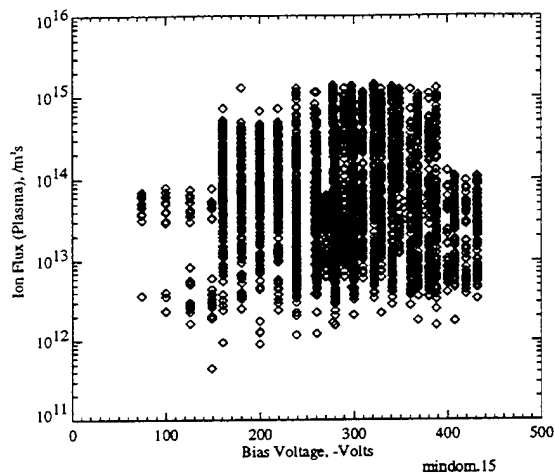
a: Voltage/Ion Flux Data Space for GaAs/Ge Wrap-Through-Contact Module 8

b: Voltage/Cell Temperature Data Space for GaAs/Ge Wrap-Through-Contact Module 8
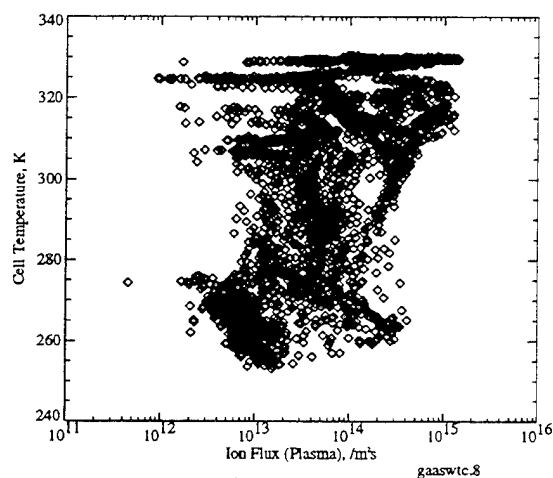
c: Ion Flux/Cell Temperature Data Space for GaAs/Ge Wrap-Through-Contact Module 8

Figure 91: Environmental Parameter/Voltage Data Space for GaAs/Ge Wrap-Through-Contact Module 8
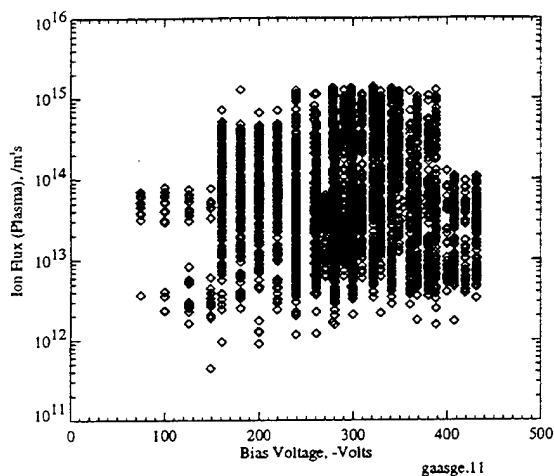
a: Voltage/Ion Flux Data Space for
Thick GaAs/Ge Module 11
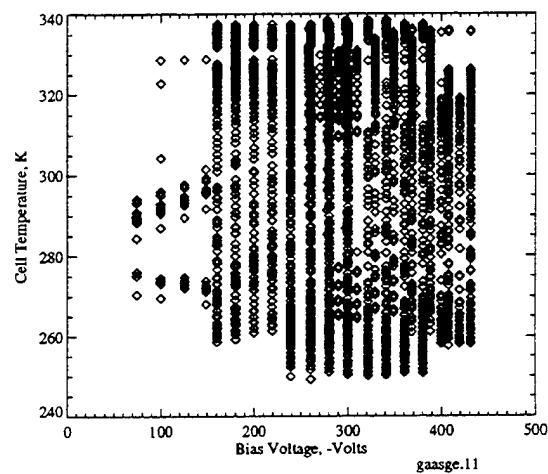
b: Voltage/Cell Temperature Data
Space for Thick GaAs/Ge Module 11

c: Ion Flux/Cell Temperature Data
Space for Thick GaAs/Ge Module 11

Figure 92: Environmental Parameter/Voltage Data Space for Thick GaAs/Ge Module 11

a: Voltage/Ion Flux Data Space for Mini-Cassegrainian Module 14

b: Voltage/Cell Temperature Data Space for Mini-Cassegrainian Module 14

c: Ion Flux/Cell Temperature Data Space for Mini-Cassegrainian Module 14

Figure 93: Environmental Parameter/Voltage Data Space for Mini-Cassegrainian Module 14

a: Voltage/Ion Flux Data Space for
Mini-Dome Module 15
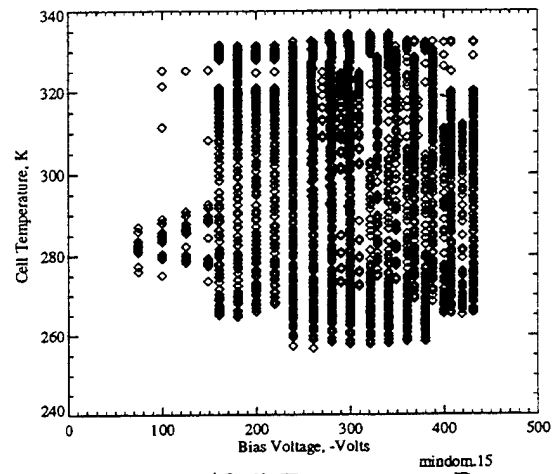
b: Voltage/Cell Temperature Data
Space for Mini-Dome Module 15
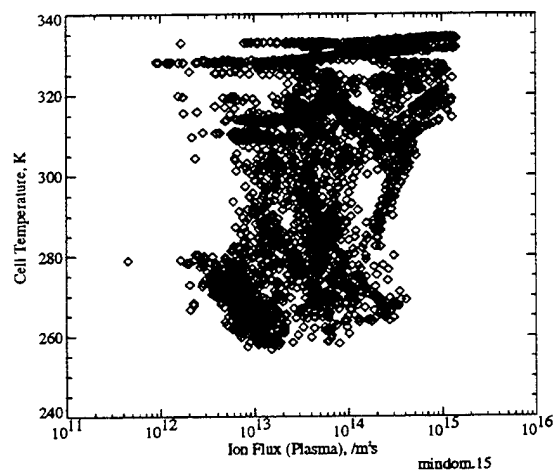
c: Ion Flux/Cell Temperature Data
Space for Mini-Dome Module 15

Figure 94: Environmental Parameter/Voltage Data Space for Mini-Dome Module 15

Bibliography

[1] S. F. Adams, "Photovoltaic Array Space Power Plus Diagnostics Flight Experiment: Pre-Flight Description of Experimental Photovoltaic Modules", Technical Report WL-TR-92-2080, Wright Laboratory, 1992.

[2] R. C. Adamo, K. L. Gion, and D. R. Dana, "PASP Plus/Transient Pulse Monitor (TPM)-Preflight Characterization Technical Report," PL-TR-94-2131, ADA282582, Phillips Laboratory, Hanscom AFB, MA, 1994.

[3] Advanced Photovoltaic and Electronics Experiment Biweekily Engineering Report, 8-21 May, 1995, Phillips Laboratory, Hanscom AFB, MA.

[4] YA. L. Al'Pert, *The Near-Earth and Interplanetary Plasma*, Vol. 1, Cambridge University Press, 1983, pp. 22-24.

[5] R. A. Anderson and J. P. Brainard, "Mechanism of Pulsed Surface Flashover Involving Electron-Stimulated Desorption," Journal of Applied Physics, Vol. 51, No. 3, pp. 1414-1421, March 1980.

[6] C. Ashley, "A Case for a 50 Volt Bus," Hughes Aircraft Co., presented at the Space Power Workshop, Albuquerque, NM, 1995.

[7] C. S. Athwal and R. V. Latham, "The Effect of the Applied Field on the Energy Spectra of Electrons Field Emitted from Microscopic Sites on Broad-Area Copper Electrodes," Physica, Vol. 104 C, pp. 189-195, 1981.

[8] K. H. Bayliss and R. V. Latham, "An Analysis of Field-Induced Hot-Electron Emission from Metal-Insulator Microstructures on Broad-Area High-Voltage Electrodes," Proc. R. Soc. Lond., Vol. A 403, pp. 285-311, 1986.

[9] K. H. Bayliss and R. V. Latham, "The Spatial Distribution and Spectral Characteristics of Field-Induced Electron Emission Sites on Broad-Area High-Voltage Electrodes," Vacuum, Vol. 35, No. 6, pp. 211-217, 1985.

[10] P. R. Bevington and D. K. Robinson, *Data Reduction and Error Analysis for the Physical Sciences*, 2nd Edition, McGraw-Hill, 1992.

[11] W. S. Boyle, P. Kisliuk, and L. H. Germer, "Electrical Beakdown in High Vacuum," Journal of Applied Physics, Vol. 26, pp. 720-725, 1955.

[12] F. F. Chen, *Introduction to Plasma Physics and Controlled Fusion Volume 1: Plasma Physics*. Plenum Press, US, 1984.

[13] M. Cho, "Arcing on High Voltage Solar Arrays in Low Earth Orbit: Theory and Computer Particle Simulation," Ph.D. Thesis, M.I.T., 1992.

[14] M. Cho and D. E. Hastings, "Dielectric Charging Processes and Arcing Rates of High Voltage Solar Arrays," Journal of Spacecraft and Rockets, Vol. 28, pp. 698-706, 1991.

[15] H. Curtis, D. Guidice, P. Severance, and M. Piszczor, "Results of Thermal Vacuum Tests for the PASP Plus Flight Modules," Proceedings of XII Space Photovoltaic Research and Technology Conference, NASA Conference Publication 3210, pp. 2889-297, May 1993.

[16] H. Curtis, M. Piszczor, P. Severance, D. Guidice, and D. Olson, "Early Results from the PASP Plus Flight Experiment," presented at the First World Conference on Photovoltaic Energy Conversion, Waikoloa, HI. Dec. 5-9, 1994.

[17] H.Curtis, "Overview of PASP-Plus Solar Cell Data," NASA Lewis Research Center, presented at the Space Power Workshop, Albuquerque, NM, 1995.

[18] D. Dana, "Diagnostics-TPM," presented at the PASP Plus Data Processing and Analysis Meeting, Phillips Laboratory, Hanscom AFB, MA, January 20, 1994.

[19] V. Davis, "Parasitic Current Collection by Solar Arrays in LEO," S-Cubed, presented at the Space Power Workshop, Albuquerque, NM, 1995.

[20] D. E. Delorey, "PASP Plus Time History Data Base File Structures," PL-TR-94-2242, Phillips Laboratory, Hanscom AFB, MA, September 24, 1994. ADA290587

[21] W. F. Denig, "Diagnostics-LP, ESA, Emitter," presented at the PASP Plus Data Processing and Analysis Meeting, Phillips Laboratory, Hanscom AFB, MA, January 20, 1994.

[22] M. J. Drinkwine and D. Lichtman, "Electron Stimulated Desorption: A Critical Review," Progress in Surface Science, Vol. 8, pp. 123-142, 1977.

[23] D. C. Ferguson, "Current Collection by the SSF Solar Array - Comparison of PASP-Plus and Sampie Results," presented at Space Power Workshop, Albuquerque, New Mexico, 1995.

[24] D. C. Ferguson, "Solar Array Arcing in Plasma," Third Annual Workshop on Space Operations Automation and Robotics (Soar 1989), NASA CP-3059, pp. 509-513, Mar. 1990.

[25] D. C. Ferguson, "The Voltage Threshold for Arcing for Solar Cells in LEO-Flight and Ground Test Results", NASA TM-87259, March 1986.

[26] G. I. Font, J. D. Soldi, C. Perez de la Cruz, and D. E. Hastings, "Arcing Mechanism of Wrap-Through-Contact Solar Cells," AIAA 95-0597 presented at the 33rd Aerospace Sciences Meeting, Reno, NV, 1995.

[27] R. H. Fowler and L. Nordheim, "Electron Emission on Intense Electric Fields," Proc. R. Soc. London A, Vol. 119, pp. 173-181, 1928.

[28] H. Fujii, Y. Shibuya, T. Abe, K. Ijichi, R. Kasai, and K. Kuriki, "Laboratory Simulation of Plasma Interaction with High Voltage Solar Arrays", Proceedings of the 15th International Symposium on Space Technology Science, Kanagawa, Japan, 1986.

[29] N. T. Grier and N. J. Stevens, "Plasma Interaction Experiment (PIX) Flight Results", Spacecraft Charging Technology 1978 NASA CP-2071, pp. 295-314.

[30] N. T. Grier, "Plasma Interaction Experiment II: Laboratory and Flight Results", Spacecraft Environment Interactions Technology Conference, 1983, NASA CP-2359, pp. 333-348.

[31] N. T. Grier and V. A. Davis, fax memo from S-Cubed, La Jolla, CA, October 29, 1993.

[32] D. A. Guidice, P. S. Severance, H. B. Curtis, and M. F. Piszczor, "Investigation of Space-Environment Effects on Photovoltaic Technologies by the PASP Plus Experiment," AIAA 95-0371, presented at the 33rd Aerospace Sciences Meeting, Reno, NV, 1995.

[33] O. Hachenberg and W. Brauer, "Secondary Electron Emission from Solids", Advancement in Electronics and Electron Physics, Vol. 11, pp. 413-499, 1959.

[34] R. Hackam and S. K. Salman, "Effects of Electrode Curvature, Distance from Glass Insulator, and Addition of Hydrogen on Field-Emission Currents and Breakdown Voltage in Vacuum," Journal of Applied Physics, Vol. 45, No. 10, pp. 4384-4392, 1974.

[35] D.E. Hastings, personal communication.

[36] D.E. Hastings and M. Cho, "Ion Drag for a Negatively Biased Solar Array in Low Earth Orbit", Journal of Spacecraft and Rockets, Vol. 27, pp. 279-284, 1990.

[37] D. E. Hastings, M. Cho, and H. Kuninaka, "The Arcing Rate for a High Voltage Solar Array: Theory, Experiments and Predictions", Journal of Spacecraft and Rockets, Vol. 29, pp. 538-554, 1992.

[38] D. E. Hastings, G. Weyl and D. Kaufman, "The Threshold Voltage for Arcing on Negatively Biased Solar Arrays", Journal of Spacecraft and Rockets, Vol. 27, pp. 539-544, 1990.

[39] P. He and M. K. Sinha, "Prebreakdown Characteristics of Thin Film-Coated Molybdenum Electrodes," Journal of Applied Physics, Vol. 66, No. 12, pp. 6184-6186, 1989.

[40] B. G. Herron, J. R. Bayless and J. D. Worden, "High Voltage Solar Array Technology", Journal of Spacecraft and Rockets, Vol. 10, pp. 457, 1973.

[41] G. B. Hillard and D. C. Ferguson, "The Solar Array Module Plasma Interaction Experiment: Technical Requirements Document", NASA TM-105660, 1992.

[42] G. B. Hillard and D. C. Ferguson, "The Solar Array Module Plasma Interactions Experiment (SAMPIE): Science and Technology Objectives", Journal of Spacecraft and Rockets,Vol. 30, No. 4, pp. 484-494, 1993..

[43] R. W. Hockney and J. W. Eastwood. *Computer Simulation Using Particles*. McGraw-Hill, USA, 1981.

[44] A. M. Howatson, *An Introduction to Gas Discharge*. Pergamon Press, Oxford, 1965.

[45] R. E. Hurley, "Electrical Phenomena Occuring at the Surface of Electrically Stressed Metal Cathodes. I. Electroluminescence and Breakdown Phenomena with Medium Gap Spaceings (2-8mm)," Journal of Physics D: Applied Physics, Vol. 12, pp. 2229-2246, 1979.

[46] R. E. Hurley, "Electrical Phenomena Occuring at the Surface of Electrically Stressed Metal Cathodes. II. Identification of Electroluminescent (k-spot) radiation with Electron Emission on Broad Area Cathodes," Journal of Physics D: Applied Physics, Vol. 12, pp. 2247-2252, 1979.

[47] G. T. Inouye and R. C. Chaky, "Enhanced Electron Emission from Positive Dielectric/Negative Metal Configurations on Spacecraft", IEEE Trans. Nuc. Sci., Vol. NS-29, No. 6, pp. 1589-1593, December 1982.

[48] G. A. Jongeward, I. Katz, M. J. Mandell and D. E. Parks, "The Role of Unneutralized Surface Ions in Negative Potential Arcing", presented at the 1985 IEEE 22nd Annual Conference, NSRE.

[49] F. L. Knight, "The Space Test Program APEX Mission Satellite," The Aerospace Corporation, Los Angeles, CA.

[50] H. Kuninaka, "Space Experiment on Plasma Interaction Caused by High Voltage Photovoltaic Power Generation," presented at the 25th AIAA Plasmadynamics and Lasers Conference, 1994.

[51] H. Kuninaka, "Qualitative Experiment on Arc Discharge on Negatively Biased Solar Cell," Journal of Spacecraft and Rockets, Vol. 27, pp. 665-668, 1990.

[52] R. V. Latham, *High Voltage Vacuum Insulation: The Physical Basis*. Academic Press, London, England, 1981.

[53] R. V. Latham, "Prebreakdown Electron Emission", IEEE Trans. Elec. Insul., Vol. EI-18, June 1983.

[54] R. V. Latham, "The Origin of Prebreakdown Electron Emission from Vacuum-Insulated High Voltage Cathodes," Vacuum, Vol. 32, No. 3, pp. 137-140, 1982.

[55] R. V. Latham, K. H. Bayliss, and B. M. Cox, "Spatially Correlated Breakdown Events Initiated by Field Emission in Vacuum and High Pressure SF_6," Journal of Physics D: Applied Physics, Vol. 19, pp. 219-231, February 1986.

[56] P. Leung, "Characterization of EMI Generated by the Discharge of a 'Volt' Solar Array", Technical Report CR-176537, NASA, November 1985.

[57] L. Malter, "Thin Film Field Emission," Physical Review, Vol. 50, pp. 40-58, 1936.

[58] D. Marvin, "Degradation of PASP-Plus Solar Cells," The Aerospace Corporation, presented at the Space Power Workshop, Albuquerque, NM, 1995.

[59] B. McNeil, memo to Phillips Laboratory from Radex, Inc., March 24, 1995.

[60] S. A. Merryman, A. J. Brandy, and L. B. Gordon, "The Breakdown Characteristics of Outgassing Dominated Vacuum Regions," Proceedings of the 23rd Intersociety Energy Conversion Engineering Conference, pp. 763-765, 1988.

[61] W. L. Miller, "An Investigation of Arc Discharging on Negatively Biased Dielectric-Conductor Samples in a Plasma", Spacecraft Environment Interactions Technology Conference, 1983, NASA CP-2359, pp. 333-348.

[62] R. L. Mong, "Arcing Mitigation and Predictions for High Voltage Solar Arrays", S.M. Thesis, M.I.T., 1993.

[63] P. Niedermann, N. Sankarraman, and O. Fischer, "Enhanced Field Emission from Molybdenum Disulfide," IEEE Trans. Elec. Insul., Vol. 23, No. 1, pp. 3-8, 1988.

[64] P. Niedermann, N. Sankarraman, R. J. Noer, and O. Fischer, "Field Emission from Broad-Area Niobium Cathode: Effect of High-Temperature treatment," Journal of Applied Physics, Vol. 59, No. 3, pp. 892-901, 1986.

[65] R. J. Noer, "Electron Emission From Broad-Area Electrodes," Applied Physics, Vol. A28, pp. 1-24, May 1982.

[66] R. Papoular, *Electrical Phenomena in Gases. English Translation.* Univeristy Microfilm International, Ann Arbor MI, 1977.

[67] "PASP Plus Data Processing and Analysis Meeting", Phillips Laboratory, US Air Force, Jan 20, 1994.

[68] "PASP Plus Experiment Specification," Phillips Laboratory, US Air Force, Jan 17, 1991.

[69] "PASP Plus Comprehensive Performance Test Procedures, Rev.4 17 March 1993," PL/GPSP Space Physics Division, Phillips Laboratory, Hanscom AFB, MA, March 26, 1993.

[70] "PASP Plus Comprehensive Performance Test Procedures, PASP-CPT-06, 15 October 1993," PL/GPSP Space Physics Division, Phillips Laboratory, Hanscom AFB, MA, Decmber 4, 1993.

[71] "PASP Plus Comprehensive Performance Test Procedures, PASP-CPT-06, Post-Environmental Test, April 4, 1994," PL/GPSP Space Physics Division, Phillips Laboratory, Hanscom AFB, MA, April 8, 1994.

[72] "PASP Plus Limited Performance Test Procedures, PASP-LPT-06, November 1, 1993," PL/GPSP Space Physics Division, Phillips Laboratory, Hanscom AFB, MA, January 20-21, 1994.

[73] "PASP Plus Limited Performance Test Procedures, PASP-LPT-06 Pre-Thermal Vacuum Version, February 8, 1994," PL/GPSP Space Physics Division, Phillips Laboratory, Hanscom AFB, MA, February 15, 1994.

[74] "PASP Plus Limited Performance Test Procedures, PASP-LPT-06 Pre-Vibration, March 1, 1994," PL/GPSP Space Physics Division, Phillips Laboratory, Hanscom AFB, MA, March 12-14, 1994.

[75] "PASP Plus Limited Performance Test Procedures, PASP-LPT-06 March 1, 1994," PL/GPSP Space Physics Division, Phillips Laboratory, Hanscom AFB, MA, May 26-June 25, 1994.

[76] "PASP On-Orbit Log, Book 1," Phillips Laboratory, Hanscom AFB, MA.

[77] "PASP On-Orbit Log, Book 2," Phillips Laboratory, Hanscom AFB, MA.

[78] D. E. Parks, G. Jongeward, I. Katz and V. A. Davis, "Threshold-Determining Mechanisms for Discharges in High-Voltage Solar Arrays", Journal of Spacecraft and Rockets, Vol. 24, pp. 367-371, 1987.

[79] C. Perez de la Cruz, "Arc Rate Predictions and Flight Data Analyis for the Solar Array Module Plasma Interactions Experiment (SAMPIE)," S.M. Thesis, M.I.T., 1995.

[80] C. Perez de la Cruz, D. E. Hastings, D. Ferguson, and B. Hillard, "Arc Rate Predictions and Flight Data Analyis for the SAMPIE Experiment," to be presented at the 34th Aerospace Sciences Meeting, Reno, NV, 1996.

[81] A. S. Pillai and R. Hackam, "Surface Flashover of Solid Dielectric in Vacuum," Journal of Applied Physics, Vol. 53, No. 4, pp. 2983-2987, April 1982.

[82] W. H. Press, B. P. Flannery, S. A. Teukolsky, and W. T. Vetterling, *Numerical Recipes: The Art of Scientific Computing*, Cambridge University Press, Cambridge, Englasnd, 1986.

[83] K. P. Ray and D. A. Guidice, personal communication, Phillips Laboratory, Hanscom AFB, MA, June 23, 1995.

[84] P. A. Redhead, J. P. Hobson, and E. V. Kornelsen, *The Physical Basis of Ultra High Vacuum*, Chapman Hall Ltd., London, 1968.

[85] C. Renner, P. Niedermann, and O. Fisher, "Enhanced Field Emission Investigation of Aluminum," IEEE Trans. Elec. Insul., Vol. 24, pp. 911-916, Dec. 1989.

[86] P. S. Severance and D. A. Guidice, "Investigation of Space Environmental Effects on Advanced Solar Arrays", Phillips Laboratory, US Air Force.

[87] G. B. Shaw, "Analysis of the Ion Current Collection in the Plasma Wake During the Charging Hazards and Wake Studies (CHAWS) Experiment," S.M. Thesis, M.I.T., 1995.

[88] D. B. Snyder, "Discharges on a Negatively Biased Solar Cell Array in a Charged Particle Environment", *Spacecraft Environment Interactions Technology Conference*, NASA CP-2359, pp. 379-388, 1983

[89] D. B. Snyder, "Characteristics of Arc Currents on a Negatively Biased Solar Cell Array in a Plasma," Technical Report NASA TM-83728, 1984.

[90] D. B. Snyder and E. Tyree, "The Effect of Plasma on Solar Cell Array Arc Characteristics", Technical Report NASA TM-86887, 1985.

[91] J. D. Soldi and D. E. Hastings, "Arcing Predictions for PASP Plus Solar Arrays," PL-TR-94-2234, ADA 292230, Phillips Laboratory, Hanscom AFB, MA, August 2, 1994.

[92] J. D. Soldi, C. Perez de la Cruz, G. I. Font, and D. E. Hastings, "Arc Rate Predictions and Flight Data Analysis for the SAMPIE and PASP Plus Experiments," AIAA 95-0373, presented at the 33rd Aerospace Sciences Meeting, Reno, NV, 1995.

[93] N. J. Stevens, "Review of Interactions of Large Space Structures with the Environment, Space Systems and their Interactions with Earth's Space Environment", Progress in Aeronautics and Astronautics", Vol. 71, AIAA, Washington D. C., pp. 437-454, 1980.

[94] N. J. Stevens, C. S. Underwood, and M. R. Jones, "Interpretation of High Voltage Solar Array Discharge Experiments," IEEE Trans. Nuc. Sci., Vol. NS-37, No. 6, pp. 2120-2127, 1990.

[95] D. Stewart, "Determination of an Optimum Bus Voltage for Geosynchronous Spacecraft," Lockheed-Martin Astrospace, presented at the Space Power Workshop, Albuquerque, NM, 1995.

[96] H. Thiemann and K. Bogus, "Anomalous Current Collection and Arcing of Solar-Cell Modules in a Simulated High-Density Low-Earth-Orbit Plasma, ESA Journal, Vol. 10, pp. 43-57, 1986.

[97] H. Thiemann and R. W. Schunk, "Computer Experiments on Arcing Processes as Observed in Ground Tests," Journal of Spacecraft and Rockets, Vol. 31, No. 6, pp. 929-936.

[98] H. Thieman, R. W. Schunk and K. Bogus, "Where do negatively biased solar arrays arc?", Journal of Spacecraft and Rockets, Vol. 27, pp. 563-565, 1990.

[99] B. L. Upschulte, G.. M. Weyl, W. J. Marinelli, E. Aifer, D. E. Hastings, and D. Snyder, "Significant Reduction in Arc Frequency of Negatively Biased Solar Cells: Observations, Diagnostics, and Mitigation Techniques," presented at the Space Photovoltaic Research and Technology conference, Cleveland, OH, NASA CP-3121, 1991

[100] G. E. Vibrans, "Field Emission in Vacuum Voltage Breakdown," Technical Report 353, ESD-TR-64-327, AD 602844, Lincoln Lab. M.I.T., 1964.

[101] J. J. Wang, "Electrodynamic Interactions Between Charged Space Systems and the Ionospheric Plasma Environment," Ph.D Thesis, M.I.T., 1993.

[102] E. Wulf and U. von Zahn, "The Shuttle Environment: Effects of Thruster Firings on Gas Density and Composition in the Payload Bay," Journal of Geophysical Research, Vol. 91, No. A3, pp. 3270-3278, 1986.